



# Cerebral connectivity study by functional and diffusion MRI in intelligence

Ilaria Suprano

## ► To cite this version:

Ilaria Suprano. Cerebral connectivity study by functional and diffusion MRI in intelligence. Medical Imaging. Université de Lyon, 2019. English. NNT : 2019LYSE1282 . tel-02499621

**HAL Id: tel-02499621**

**<https://theses.hal.science/tel-02499621>**

Submitted on 5 Mar 2020

**HAL** is a multi-disciplinary open access archive for the deposit and dissemination of scientific research documents, whether they are published or not. The documents may come from teaching and research institutions in France or abroad, or from public or private research centers.

L'archive ouverte pluridisciplinaire **HAL**, est destinée au dépôt et à la diffusion de documents scientifiques de niveau recherche, publiés ou non, émanant des établissements d'enseignement et de recherche français ou étrangers, des laboratoires publics ou privés.



N° d'ordre NNT : 2019LYSE1282

**THÈSE DE DOCTORAT DE L'UNIVERSITÉ DE LYON**  
opérée au sein de  
**l'Université Claude Bernard Lyon 1**

**Ecole Doctorale ED205 - Interdisciplinaire Sciences Santé**

**Spécialité de doctorat :**  
**Recherche clinique, innovation technologique, santé publique**

Soutenue publiquement le 02 decembre 2019, par :  
**Ilaria Suprano**

---

**Etude de la connectivité cérébrale  
par IRM fonctionnelle et de diffusion  
dans l'intelligence**

---

Devant le jury composé de :

<b>M. Maxime Guye</b> <i>Professeur des Universités - Praticien Hospitalier, Aix-Marseille Université</i>	Rapporteur
<b>M. François Lazeyras</b> <i>Professeur associé, Université de Genève</i>	Rapporteur
<b>M. Pierre Fourneret</b> <i>Professeur des Universités - Praticien Hospitalier, Université Lyon 1</i>	Examinateur
<b>Mme. Lucie Hertz-Pannier</b> <i>Directrice de Recherche CEA, Université Paris Descartes</i>	Examinatrice
<b>M. Olivier Koenig</b> <i>Professeur des universités, Université Lumière Lyon 2</i>	Examinateur
<b>Mme. Fanny Nusbaum</b> <i>Chercheuse associée - Directrice du Centre PSYRENE, Université Lyon 1</i>	Examinatrice
<b>Mme. Sophie Achard</b> <i>Directrice de Recherche CNRS, Université Grenoble Alpes</i>	Invitée
<b>M. Olivier Revol</b> <i>Praticien Hospitalier, Hospices Civils de Lyon</i>	Invité
<b>M. Dominique Sappey-Marinier</b> <i>Maître de Conférence des Universités - Praticien Hospitalier, Université Lyon 1</i>	Directeur
<b>Mme. Chantal Delon-Martin</b> <i>Chargée de Recherche INSERM, Université Grenoble Alpes</i>	Co-Directrice



# Acknowledgements

Je remercie très sincèrement les Professeurs Professor Maxime Guy et François Lazeyras d'avoir accepté d'être rapporteur de ce travail.

Je remercie l'ensemble des membres du jury d'avoir accepté de juger ce travail de thèse : Professeur Pierre Fourneret, Docteure Lucie Hertz-Panier, Professeur Olivier Koenig, Docteure Fanny Nusbaum, Docteure Chantal Delon-Martin, et Docteur Dominique Sappey-Marinier.

Je suis très reconnaissante à mes superviseurs, le Docteur Dominique Sappey-Marinier et la Docteure Chantal Delon-Martin, pour leurs suggestions, conseils et encouragements tout au long de cette thèse.

Je remercie le Docteur Olivier Beuf, directeur du laboratoire CREATIS, ainsi que la responsable de l'équipe 5 "RMN et optique : De la mesure au biomarqueur", la Docteure Hélène Ratiney, de m'avoir accueillis au sein du laboratoire.

Je remercie les différents directeurs du CERMEP-Imagerie du Vivant, les Professeurs Gerard Gimenez, Didier Revel et Luc Zimmer, pour leur accueil au CERMEP durant toutes ces années. Je remercie également les Docteurs Danielle Ibarolla et Franck Lamberton pour leur aide lors des acquisition IRM.

Un merci très special à Jamila Lagha, assistante de direction du CERMEP, pour sa disponibilité et son soutien quotidien, en particulier pour surmonter les difficultés lors de mon arrivée en France.

Je tiens à remercier tous mes collègues avec qui j'ai partagé d'excellents moments plus ou moins longues au CERMEP.

In particolare il mio risolutore di problemi preferito, Aldo, gentile e disponibile in ogni situazione.

Enfin, un immense merci à Gabriel pour son soutien tout au long de cette thèse, avec qui j'ai passé trois années, a partager nos expériences quotidiennes, a s'enrichir mutuellement et a surmonter nos difficultés scientifiques.



Un grande grazie a tutti i miei amici di sempre, che nonostante la distanza sono rimasti al mio fianco. Indipendentemente da dove siamo nel mondo, o in quale punto delle nostre vite ci troviamo, so che potrò sempre contare su di voi.

Grazie ai miei amici lionesi, con i quali ho condiviso questi tre anni. Siete stati la mia casa e la mia famiglia all'estero. Un grazie particolare va a Bruna e Giacomo, con i quali ho condiviso ogni singolo momento del dottorato. Gli ultimi mesi di scrittura della tesi sono stati a dir poco intensi ma, sostenendoci a vicenda, siamo riusciti ad affrontarli e superarli al meglio.

Infine vorrei ringraziare la mia famiglia, i miei genitori e mia sorella Alessia. Loro più di tutti hanno sentito il peso della distanza, ma nonostante ciò mi hanno sempre sostenuta e trasmesso la loro fiducia, incoraggiandomi giorno per giorno.

E per concludere, grazie Giò!

# Abstract

The idea that intelligence is embedded not only in specific brain regions, but also in efficient brain networks has grown up. Indeed, human brain organization is believed to rely on complex and dynamic networks in which the communication between cerebral regions guarantees an efficient transfer of information. These recent concepts have led us to explore the neural bases of intelligence using advanced MRI techniques in combination with graph analysis. On one hand, advanced MRI techniques, such as resting-state functional MRI (rs-fMRI) and diffusion MRI (dMRI) allow the exploration of respectively the functional and the structural brain connectivity while on the other hand, graph theory models allow the characterization of brain networks properties at different scales, thanks to global and local metrics.

The aim of this thesis is to characterize the topology of functional and structural brain networks in children and in adults with high intelligence quotient (HIQ) compared to standard intelligence quotient (SIQ).

First, we focused our attention on a children population with different cognitive characteristics. Two HIQ profiles, namely homogeneous (Hom-HIQ) and heterogeneous HIQ (Het-HIQ), have been defined based on clinical observations and Intelligence Quotient (IQ) sub-tests. Using resting-state fMRI techniques, we examined the functional network topology changes, estimating the "hub disruption index" ( $\kappa$ ), in these two HIQ profiles. We found significant topological differences in the integration and segregation properties of brain networks in HIQ compared to SIQ children, for the whole brain graph, for each hemispheric graph, and for the homotopic connectivity. These brain networks changes resulted to be more pronounced in the Het-HIQ subgroup. Finally, we found significant correlations between the graph networks' changes and the full-scale IQ, as well as some IQ subscales. These results demonstrated for the first time, that the two HIQ profiles are related to different neural substrate organizations. Then, the structural brain network connectivity was measured by dMRI. We found strong correlations between the children brain networks density and their intelligence scores. Furthermore, several correlations were found between integration graph metrics suggesting that intelligence performances are related to a homogeneous network organization. These findings demonstrated that intelligence neural substrate is based on a strong white matter microarchitecture of the major fiber-bundles and a well-balanced network organization between local and global scales. This children population was finally studied using a memory-word task in fMRI. Significant changes were observed between both HIQ and SIQ groups. This study confirmed our hypothesis that both HIQ profiles are characterized by a different brain activity, with again stronger changes in Het-HIQ children.

Second, we investigated both functional and structural connectivity in a popula-

tion of adults. We found several correlations between graph metrics and intelligence sub-scores. As well as for the children population, high cognitive abilities of adults seemed to be related with different organization of brain structural and functional networks.

In conclusion, this work has demonstrated that the sensitivity of graph metrics based on advanced connectomic MRI techniques, such as rs-fMRI and dMRI, can provide a better characterization of children and adult HIQ, and further, distinguish different intelligence profiles in children.

# Résumé

L'idée que l'intelligence s'appuie non seulement sur des régions spécifiques du cerveau, mais également sur des réseaux cérébraux efficaces s'est récemment affirmée. En effet, on pense que l'organisation du cerveau humain repose sur des réseaux complexes et dynamiques au sein desquels une bonne communication entre les régions cérébrales garantit un transfert efficace d'informations. Ces concepts récents nous ont amené à explorer les bases neurales de l'intelligence en combinant des techniques avancées d'IRM et la théorie des graphes. D'un côté, les techniques avancées d'IRM, telles que l'IRM fonctionnelle de repos (IRMf-rs) et l'IRM de diffusion (IRMd), permettent d'explorer respectivement la connectivité cérébrale fonctionnelle et structurale, tandis que les modèles de la théorie des graphes permettent la caractérisation des propriétés des réseaux à différentes échelles, grâce à des métriques globales et locales.

L'objectif de cette thèse est de caractériser la topologie des réseaux cérébraux fonctionnels et structurels chez les enfants et les adultes avec un quotient intellectuel supérieur (HIQ) par rapport aux sujets de niveau standard (SIQ).

Premièrement, nous avons concentré notre attention sur une population d'enfants présentant différentes caractéristiques cognitives. Deux profils HIQ, à savoir homogène (Hom-HIQ) et hétérogène HIQ (Het-HIQ), ont été définis sur la base d'observations cliniques et de sous-tests du quotient intellectuel (QI). En utilisant des techniques d'IRMf au repos, nous avons examiné les modifications topologiques du réseau fonctionnel par « l'index de perturbation des nœuds » ( $\kappa$ ). Nous avons trouvé des différences topologiques significatives dans les propriétés d'intégration et de ségrégation des réseaux, chez les enfants HIQ par rapport aux enfants SIQ, pour le graphe cérébral entier, pour chaque graphe hémisphérique et pour la connectivité homotopique. De plus, ces changements de topologie sont plus prononcés dans le sous-groupe Het-HIQ. Enfin, nous avons trouvé des corrélations significatives entre les métriques de graphes et le QI total ainsi que d'autres sous indices du QI. Ces résultats ont démontré pour la première fois que les deux profils HIQ sont liés à des organisations différentes du substrat neuronal. Ensuite, la connectivité structurale du réseau cérébral, mesurée par IRMd chez l'ensemble des enfants HIQ, est significativement différente de celle des enfants SIQ. Nous avons également constaté de fortes corrélations entre la densité des réseaux cérébraux des enfants et leurs scores d'intelligence. De plus, plusieurs corrélations ont été trouvées entre les métriques de graphe d'intégration et les scores d'intelligence suggérant que les performances intellectuelles sont probablement liées à une organisation uniforme des réseaux. Ces résultats ont démontré que le substrat neuronal de l'intelligence repose sur une solide microarchitecture des principaux faisceaux de fibres de la substance blanche et sur

une organisation de réseau bien équilibrée entre les échelles locale et globale. Cette population d'enfants a finalement été étudiée par IRMf à l'aide d'une tâche de mémorisation de mots. Des changements significatifs ont été observés entre les groupes HIQ et SIQ. Cette étude confirme notre hypothèse selon laquelle les deux profils HIQ sont caractérisés par une activité cérébrale différente, avec un effet plus prononcé chez les enfants Het-HIQ.

Deuxièmement, nous avons étudié la connectivité fonctionnelle et structurale dans une population d'adultes. Nous avons trouvé plusieurs corrélations entre les métriques de graphe et les sous-scores d'intelligence. De même que pour la population d'enfants, les capacités cognitives élevées des adultes sont corrélées à une organisation uniforme des réseaux structurels et fonctionnels et un moindre fonctionnement en clusters.

En conclusion, ce travail a démontré que la sensibilité des métriques de graphes basées sur des techniques d'IRM avancées de connectivité, telles que l'IRM de repos et l'IRM de diffusion, permettent de mieux caractériser les réseaux cérébraux des enfants et des adultes, et de distinguer différents profils d'intelligence.

# Contents

<b>Abstract</b>	<b>v</b>
<b>Résumé</b>	<b>vii</b>
<b>Index</b>	<b>xii</b>
<b>List of figures</b>	<b>xxii</b>
<b>List of symbols and abbreviations</b>	<b>xxiii</b>
<b>Introduction</b>	<b>1</b>
<b>I State of the Art</b>	<b>5</b>
<b>1 Magnetic Resonance Imaging</b>	<b>7</b>
1 Introduction . . . . .	8
2 From signal to images . . . . .	8
2.1 The Nuclear Magnetic Resonance (NMR) phenomenon . . . . .	9
2.2 Imaging . . . . .	10
2.3 Conventional MRI sequences . . . . .	12
3 Functional MRI . . . . .	15
3.1 BOLD signal . . . . .	15
3.2 Acquisition sequences . . . . .	18
3.3 From functional localisationism to connectionism . . . . .	19
3.4 Task fMRI . . . . .	21
3.5 Resting-state fMRI . . . . .	22
4 Diffusion MRI . . . . .	24
4.1 Physic principle . . . . .	24
4.2 Acquisition sequences . . . . .	25
4.3 Diffusion Tensor Imaging (DTI) . . . . .	26
4.4 Tractography technique . . . . .	29
<b>2 Brain connectivity</b>	<b>33</b>
1 Introduction . . . . .	34
2 Graph theory . . . . .	35
2.1 Graph definition . . . . .	36

2.2	Graph properties . . . . .	36
3	Graph metrics . . . . .	38
3.1	Nodal metrics . . . . .	38
3.2	Global metrics . . . . .	40
3.3	Hub disruption index . . . . .	41
4	Matrix notation . . . . .	42
5	Brain graph topology . . . . .	43
6	Brain connectivity with MRI . . . . .	45
6.1	Brain parcellation . . . . .	45
6.2	Connectivity matrix . . . . .	45
<b>3</b>	<b>Intelligence</b>	<b>51</b>
1	Introduction . . . . .	52
2	g-Factor Model . . . . .	52
3	Other Models . . . . .	53
4	Intelligence Quotient (IQ) measure . . . . .	54
5	Wechsler Intelligence Scales . . . . .	55
5.1	WISC-IV . . . . .	55
5.2	WAIS-IV . . . . .	56
6	MRI application to intelligence . . . . .	57
6.1	Early MRI studies . . . . .	57
6.2	The Parieto-Frontal Integration Theory (P-FIT) . . . . .	61
6.3	The role of brain connectivity in intelligence . . . . .	62
<b>4</b>	<b>Aim of the thesis</b>	<b>69</b>
<b>II</b>	<b>Research project on HIQ children</b>	<b>73</b>
<b>5</b>	<b>Functional connectivity: a resting-state fMRI study</b>	<b>79</b>
1	Introduction . . . . .	82
2	Development of the pre-processing of rs-fMRI . . . . .	84
2.1	Signal to noise ratio . . . . .	84
2.2	Subjects' motion . . . . .	84
2.3	fMRI signal processing . . . . .	87
2.4	Anatomical atlas . . . . .	90
2.5	Wavelet decomposition scale . . . . .	91
2.6	Graph's cost . . . . .	93
3	Materials and Methods . . . . .	93
3.1	Participants . . . . .	93
3.2	MRI acquisition . . . . .	94
3.3	Data preprocessing . . . . .	94
3.4	Wavelets decomposition . . . . .	95
3.5	Graph construction . . . . .	96
3.6	Hub Disruption Index ( $\kappa$ ) estimation . . . . .	96
3.7	Statistical analysis . . . . .	98
4	Results . . . . .	99

4.1	Modifications of FC organization with intelligence . . . . .	99
4.2	Correlations between FC organization and intelligence . . . . .	103
5	Discussion . . . . .	104
5.1	Brain networks changes with high intelligence . . . . .	104
5.2	Correlation between brain networks changes and IQ subscales . . . . .	109
6	Conclusion . . . . .	110
<b>6</b>	<b>Structural connectivity: a DTI study</b>	<b>111</b>
1	Introduction . . . . .	113
2	Materials and Methods . . . . .	114
2.1	Participants . . . . .	114
2.2	Intelligence scores . . . . .	115
2.3	MRI acquisition and processing . . . . .	115
2.4	Fiber-Bundle Analysis . . . . .	116
2.5	Graph analysis . . . . .	116
2.6	Statistical analysis . . . . .	119
3	Results . . . . .	120
3.1	Correlation with WISC scores and graph metrics . . . . .	120
3.2	Correlation with intelligence domains using factor analysis . . . . .	123
4	Discussion . . . . .	129
5	Conclusion . . . . .	132
<b>7</b>	<b>Brain activation during semantic tasks</b>	<b>135</b>
1	Introduction . . . . .	136
2	Materials and Methods . . . . .	137
2.1	Subjects . . . . .	137
2.2	MRI acquisition . . . . .	138
2.3	Verbal semantic memory task . . . . .	138
2.4	MRI processing . . . . .	139
2.5	First level analysis . . . . .	140
2.6	Second level analysis . . . . .	140
2.7	Task paradigm . . . . .	140
3	Results . . . . .	141
3.1	Task performance . . . . .	141
3.2	fMRI activation . . . . .	143
4	Discussion . . . . .	145
5	Conclusion . . . . .	148
<b>III</b>	<b>Research project on HIQ Adults</b>	<b>151</b>
<b>8</b>	<b>Functional and structural connectivity</b>	<b>153</b>
1	Introduction . . . . .	154
2	Materials and Methods . . . . .	155
2.1	Population . . . . .	155
2.2	MRI acquisition . . . . .	155
2.3	Intelligence scores . . . . .	156



2.4	Data preprocessing . . . . .	156
2.5	Connectivity measurement . . . . .	158
2.6	Graph metrics . . . . .	159
2.7	Statistical analysis . . . . .	159
3	Results . . . . .	159
3.1	Behavioral observations . . . . .	159
3.2	Functional connectivity . . . . .	160
3.3	Structural connectivity . . . . .	161
4	Discussion . . . . .	163
5	Conclusion . . . . .	164

<b>Conclusion</b>	<b>167</b>
-------------------	------------

<b>Limitations and perspectives</b>	<b>171</b>
-------------------------------------	------------

<b>Bibliography</b>	<b>195</b>
---------------------	------------

<b>Annex</b>	<b>199</b>
--------------	------------

<i>Curriculum Vitae</i>	<b>207</b>
-------------------------	------------

<b>Publications and Communications</b>	<b>209</b>
--	------------

# List of Figures

<b>I State of the Art</b>	<b>7</b>
<b>1 Magnetic Resonance Imaging</b>	<b>8</b>
1.1 (A) Magnetic field gradient in z direction. (B) Spatial slice in a real object selected by a selected pulse with the application of a gradient [De Graaf (1998)]. . . . .	11
1.2 Illustration of k-space with its 4 quadrants. Adapted from <a href="https://www.radiologycafe.com">https://www.radiologycafe.com</a> . . . . .	12
1.3 Spin-echo imaging sequence diagram. TR is the repetition time between two 90° pulses. TE is the echo time between the first 90° and the echo signal registration. Adapted from [McRobbie <i>et al.</i> (2006)]. .	13
1.4 Gradient-echo sequence diagram. TR is the repetition time measured between two RF pulses. TE is the echo time between the first 90° and the echo signal registration. Adapted from [McRobbie <i>et al.</i> (2006)].	14
1.5 Haemodynamic response phenomenon. The neuronal activity consumes the oxygen from the blood, causing an increase of deoxyhaemoglobin concentration. In response to neuronal activity, the blood flow increases leading to an increase of oxygen concentration in blood. The difference of oxygenated and deoxygenated haemoglobin results in a decrease of deoxyhaemoglobin. From Oxford Sparks. . . .	16
1.6 Blood oxygenated level dependent (BOLD) timecourse. . . . .	17
1.7 BOLD, CBF and CBV temporal trend for: (A) a short stimulus, and (B) a long stimulus. . . . .	17
1.8 EPI imaging sequence diagram. Adapted from [McRobbie <i>et al.</i> (2006)].	18
1.9 Example of k-space sampling: it starts from the point $(-k_{f,max}, -k_{p,max})$ and goes on with a zig-zag trajectory. . . . .	19
1.10 Brain regions classified with primary areas name on the left (localisationism), and Brodmann nomenclature on the right. . . . .	20
1.11 Illustration of connectionism: a complex network analysis reflecting whole-brain connectivity. . . . .	21
1.12 Three task fMRI experimental designs: Block, Event-Related and Mixed. (Courtesy of Allen D. Elster, MRIquestions.com). . . . .	22

1.13	Two functional networks: nodes in warm colors are significantly correlated with task-positive seeds and significantly anticorrelated with task-negative seeds, while nodes in cold colors are significantly correlated with task-negative seed regions and significantly anticorrelated with task-positive seed regions. [Fox <i>et al.</i> (2005)] . . . . .	23
1.14	The most important resting-state networks [Raichle (2011)]. . . . .	24
1.15	(A) Spin-echo imaging sequence diagram and (B) phase evolution of the spins at different locations along the gradient direction. $\delta$ is the gradient diffusion duration and the $\Delta$ is the diffusion time. The $180^\circ$ pulse inverts the phase wrap produced by the first gradient pulse and the second gradient pulse, which is now identical to the first one in amplitude and length, completely refocuses this phase wrap. . . . .	26
1.16	Isotropic diffusion versus anisotropic diffusion. The anisotropic diffusion is represented by an ellipsoid with three eigenvalues $\lambda_1 \gg \lambda_2 > \lambda_3$ , while for isotropic diffusion the ellipsoid becomes a sphere with $\lambda_1 \sim \lambda_2 \sim \lambda_3$ . . . . .	28
1.17	Examples of images acquired with DTI. From left to right FA, AD, RD, and MD weighted images. Data acquired at CERMEP. . . . .	28
1.18	Diagram of a neuron with a myelinated axon (adapted from wikipedia). . . . .	29
1.19	Examples of different possible fiber configurations in white matter and for each configuration the following information are showed: diffusion probability (p) along the three directions, diffusion tensor (DT), principal direction obtained from DT, fODF, and diffusion signal (adapted from [Johansen-Berg and Behrens (2009)]) . . . . .	30
1.20	Spherical convolution illustration: voxel diffusion signal ( $S_{tot}$ is composed by signals of multiple fibre populations ( $S_1$ and $S_2$ ) within it. Under the assumption of a common fibre signal profile (fODF), it is also the convolution of fODF with the fiber response function (R) (adapted from wikipedia). . . . .	31

## 2 Brain connectivity 34

2.1	Representation of the Euler's problem. (A) The map of the ancient Prussian city of Königsberg with its seven bridges across the river Pregel. (B) Euler's representation of the problem by a graph that helps to realize that it is not possible to visit all the nodes passing on each edge only once. Figure adapted from [Toroczkai (2005)]. . . . .	35
2.2	Example of a simple graph $G=(V,E)$ , with five nodes $V=A, B, C, D, E$ and eight edges that link the nodes $E=AB, AC, BC, BD, BE, CD, DE, EA$ . . . . .	36
2.3	Example of undirected graph (on the left), and directed graph (on the right). . . . .	37
2.4	Example of unweighted graph (on the left), and weighted graph with a different weight for each connection (on the right). . . . .	37
2.5	Example of fully connected graph, with all nodes having at least one connection. . . . .	38

2.6	Graphical representation of two integration metrics: the degree (blue), and the minimum path length (green). Adapted from [Sporns]. . . . .	39
2.7	Graphical representation of segregation and hubs metrics. Two modules, that are limited by red lines, communicate between them thanks to a hub node that is highlighted in blue. In the second module, the clustering coefficient is coloured in orange. Adapted from [Sporns]. . . . .	40
2.8	Hub disruption index $\kappa$ computation for nodal degree metric: nodal degree of an individual subject in relation to the degree average of the standard intelligence quotient (SIQ) group (A) for one standard intelligence quotient (SIQ) child and (B) for one high intelligence quotient (HIQ) child. The mean nodal degree of the SIQ group is subtracted from the degree of the corresponding node in an individual subject and then this individual difference is plotted against the SIQ group mean. $\kappa$ is the slope of the regression line computed on this scatter plot. Based on this definition, the data for a SIQ child (C) will be scattered around a horizontal line ( $\kappa \sim 0$ ), whereas the data for a HIQ child (D) will be scattered around a negatively sloping line ( $\kappa < 0$ ). . . . .	42
2.9	Example of a graph $G=(V,E)$ on the left of the image and its adjacency matrix on the right. . . . .	43
2.10	Graphical representation of three different graph topologies. A regular graph (on the left), a random graph (on the right), and a small-world graph (in the middle). Image taken from [Watts and Strogatz (1998)]. . . . .	44
2.11	Three brain connectivity measures. First, in morphological connectivity, the connections between the nodes are obtained from cortical GM thickness correlations. Second, functional connectivity is estimated from temporal correlations of BOLD signals between regions. Third, structural connectivity is calculated from WM fibers obtained from tractography. . . . .	46
2.12	Example of a pipeline for obtaining morphological connectivity matrix from [He <i>et al.</i> (2007)]. (A) Cortical thickness estimation from the anatomical MRI: the inner and outer surfaces were extracted and finally cortical thickness was measured at each vertex; (B) cerebral cortex segmentation; (C) Significant correlations between cortical thickness measurement of two brain regions; (D) Correlation matrix across all the population; (E) Anatomical correlation matrix obtained from the thresholded correlation matrix; (F) Graph representation of morphological correlation matrix. Adapted from [He <i>et al.</i> (2007)]. . . . .	47
2.13	Representation of graph generation from functional connectivity. After brain parcellation (A), time-series of brain regions are extracted (B), each time-series is decomposed using wavelet transformation (C), and finally, the Pearson correlation between each pair of nodes is computed for all the wavelets scales (D). . . . .	48

2.14	Representation of graph generation from structural connectivity. First, (1) the nodes are defined from an anatomical parcellation of the anatomical image. Second, (2) diffusion images are preprocessed and the tractography is generated. Third, (3) the connectivity matrix is created using the number of fibers that connect each pairs of nodes. From this matrix, structural connectivity graph of the brain is generated (4).	49
------	---	----

### 3 Intelligence 52

3.1	Structure of mental abilities. On the bottom, from 1 to 15, the different tests. In the middle, 5 mental abilities from the tests. On the top, $g$ that is common to all abilities. Numbers represent the correlations between tests, mental abilities and $g$ . [Haier (2016)]	52
3.2	Schematic representation of changes in crystallized and fluid intelligence during the life span. Adapted from [Horn (1982)].	53
3.3	Page from the Binet-Simon Intelligence Scale: children were asked which face, of each pair, was prettier. Adapted from [Binet and Simon (1916)].	54
3.4	Normal distribution of IQ scores. The average IQ is 100 and 68% of the population has a normal IQ in the range between 85 and 115. Only the 2.5% of the population has a very high IQ ( $IQ > 130$ ). Adapted from <a href="https://www.iqtestforfree.net">https://www.iqtestforfree.net</a> .	55
3.5	Structure of Wechsler Intelligence Scale for Children (WISC-IV) and Wechsler Adult Intelligence Scale (WAIS-IV). The 10 principal subtests are distributed in four groups, each for a different intelligence score.	56
3.6	Evolution of cortex thickness difference between high and standard intelligence group from 7 to 16 years old. In early childhood, high intelligence group presents a thinner cortex that increases. The most significant result is obtained at age 13 when an elevated increase in cortical thickness is measured in high intelligence group. Adapted from [Shaw <i>et al.</i> (2006)].	58
3.7	Regions with significant greater AD when comparing the homogeneous HIQ group (Top) and heterogeneous HIQ group (Bottom) with the standard IQ group. Adapted from [Nusbaum <i>et al.</i> (2017)].	59
3.8	Example of frontal and parietal regions ((A) and (C) PFC, prefrontal cortex; (B) ACC, anterior cingulate cortex; (D) and (E) PPC, posterior parietal cortex) with their activation level in two different intelligence group: Average intelligence and Superior intelligence groups. Activation levels are represented by changes in BOLD signal during reasoning task. Adapted from [Lee <i>et al.</i> (2006)b].	60

3.9	The Parieto-Frontal Integration Theory (PFIT) network: blue circles indicate PFIT regions located in the left hemisphere, while pink regions are located in both hemispheres. The yellow arrow represents the transfer of information through the major white matter tracts of fiber-bundles that connects the regions. The regions numbers refer to the Brodmann area (BA) nomenclature. Adapted from [Eggermont (2012)]. . . . .	62
3.10	Results obtained from functional connectivity analysis on HCP population that are located mainly in default mode network (DMN) and fronto-parietal network (FPN). Functional connections significantly associated with intelligence scores are represented (A) in anatomical space, and (B) outside the anatomical space. Correlations between the average functional connectivity values in the whole implicated network showed in panel (C) and general intelligence scores. Adapted from [Hearne <i>et al.</i> (2016)]. . . . .	63
3.11	Correlations between local efficiency and IQ changes in adolescents: purple and blue nodes present a significant correlation in cortical and subcortical regions respectively. On the bottom, example of correlation scatterplots in left inferior orbitofrontal cortex, left cuneus, and right thalamus. Adapted from [Koenis <i>et al.</i> (2015)]. . . . .	65
3.12	Nodes showing significant associations between intelligence and nodal efficiency. In red, (A) dorsal anterior cingulate cortex (dACC), and (B) insula (AI) present a positive association while, in blue (C) temporo-parietal junction (TPJ) presents a negative association. Adapted from [Hilger <i>et al.</i> (2017)a]. . . . .	66
<b>4</b>	<b>Aim of the thesis</b>	<b>69</b>
<b>II</b>	<b>Research project on HIQ children</b>	<b>75</b>
<b>5</b>	<b>Functional connectivity: a resting-state fMRI study</b>	<b>81</b>
5.1	Example of distribution of signal to noise ratio for a subject of our population. . . . .	85
5.2	Example of a child presenting only 4 scans with a high head motion. Data from our children population. . . . .	86
5.3	Example of a child presenting more than 24% of scans suffering by high head motion that affects resting-state fMRI signal. . . . .	87
5.4	Percentage of significant correlation in the correlation matrix derived from the subjects who did not present any significant head motion, obtained using four procedures to extract time-series. Method 1: time-series extraction regressing both WM and CSF signals; Method 2: time-series extraction regressing only WM signal; Method 3: time-series extraction regressing only CSF signal; Method 4: time-series extraction without any nuisance signal regression. . . . .	89

5.5	Representation of parcellation schemes: on the left, the Harvard-Oxford parcellation and on the right, the Desikan Killiany parcellation.	90
5.6	Percentage of significant correlation in each subject of the reference group (SIQ) for the two anatomical atlases: in red, Desikan Killiany parcellation and in green, Harvard-Oxford parcellation. . . . .	91
5.7	Percentage of significant correlations in the correlation matrices derived for each subject of the reference group (SIQ) for the two wavelet scales: in red, wavelet scale 2 and in blue, wavelet scale 3. . . . .	92
5.8	Pipeline used in rs-fMRI study detailing all the steps from subject movement to graph cost. . . . .	93
5.9	Hub disruption index $\kappa$ computation for nodal degree metric. Given a set of nodes from an atlas $N_i, i \in [1, n]$ , and a nodal metric $M$ , each node $i$ presents a value $M_i, i \in [1, n]$ for a given subject. Across a set of reference subjects $R_j, j \in [1, m]$ , the averaged nodal metric can be computed $\langle M_i \rangle_R$ . For each individual $I_k, k \in [1, \rho]$ , whatever its status (patient, HIQ child, or healthy subject), its metric in each node is $M_{i,I_k}$ and the difference in nodal metric with the reference group is $M_{i,I_k} - \langle M_i \rangle_R$ . The scatterplot with all nodes is computed with $\langle M_i \rangle_R$ in abscissa and $M_{i,I_k} - \langle M_i \rangle_R$ in ordinates. For each node $i$ , if the nodal metric is close to the reference's nodal metric, then the linear trend of this plot is about 0. Conversely, if the nodal metrics are reduced in some nodes and increased in others, then the linear trend will differ from 0. $\kappa$ is the slope of the regression line computed on this scatter plot. Example for the nodal degree (D) as metric of interest. $D_{i,I}$ vs. $\langle D_i \rangle_R$ for a standard intelligence quotient (SIQ) child (A) and for a high intelligence quotient (HIQ) child (B), $D_{i,I} - \langle D_i \rangle_R$ vs. $\langle D_i \rangle_R$ for a SIQ child (C) is scattered around a horizontal line ( $\kappa \sim 0$ ), whereas for a HIQ child (D) is scattered around a negatively sloping line ( $\kappa < 0$ ). . . . .	97
5.10	Boxplot (first quartile, median and third quartile) of $\kappa$ values in Standard Intelligence Quotient (SIQ), High Intelligence Quotient (HIQ) groups, and its Homogeneous HIQ (Hom-HIQ), and Heterogeneous HIQ (Het-HIQ) subgroups for each graph metrics in the whole brain networks: A) Degree (D), B) Betweenness Centrality (BC), C) Local Efficiency (LE), and D) Clustering Coefficient (CC). p<0.05; ** p<0.01; when testing significance of $\kappa$ values in HIQ, Hom-HIQ or Het-HIQ groups compared to SIQ group using permutation test (number of permutations = 1000). . . . .	100
5.11	Local results: (A) significant decreased nodal degree metric in left dorsolateral prefrontal nodes when comparing all High Intelligence Quotient (All-HIQ) and Heterogeneous High Intelligence Quotient (Het-HIQ) to Standard Intelligence Quotient (SIQ) groups in whole brain networks analysis; (B) trend for decreased nodal degree metric in left inferior parietal cortex when comparing Het-HIQ to SIQ. . . .	100



5.12	Local results: (A) significant decreased nodal degree metric in left dorsolateral prefrontal nodes when comparing all High Intelligence Quotient (All-HIQ) and Heterogeneous High Intelligence Quotient (Het-HIQ) to Standard Intelligence Quotient (SIQ) groups in hemispherical network analysis; (B) trend for increased functional connectivity in amygdala nodes when comparing All-HIQ, and Het-HIQ to SIQ. . . .	101
5.13	Boxplot of $\kappa$ values of the left (A, C, E, G) and the right (B, D, F, H) hemispheres networks in SIQ, HIQ groups, and its Hom-HIQ, and Het-HIQ subgroups for each graph metrics: A-B) Degree (D); C-D) Betweenness Centrality (BC); E-F) Local Efficiency (LE), and G-H) Clustering Coefficient (CC). $*p < 0.05$ ; $**p < 0.01$ ; when testing significance of $\kappa$ values in HIQ, Hom-HIQ or Het-HIQ compared to SIQ group using permutation test (number of permutations = 1000). . . .	102
5.14	Boxplot of $\kappa$ values of functional connectivity between homotopic regions network in SIQ, HIQ groups, and its Hom-HIQ, and Het-HIQ subgroups. p<0.05 when testing significance of $\kappa$ values in HIQ, Hom-HIQ or Het-HIQ groups compared to SIQ group using permutation test (number of permutations = 1000). . . . .	103
5.15	Correlations between Full Scale Intelligence Quotient (FSIQ) and reorganization indices ( $\kappa$ ) of graph metrics measured in: (A) the whole brain networks, (B) the left hemisphere networks, (C) the right hemisphere networks and (D) the homotopic nodes. Significant correlations were measured for $\kappa$ describing hubs ( $\kappa_{BC}$ ) and integration properties ( $\kappa_D$ ) in the whole brain network, for integration and segregation properties in the left hemisphere network ( $\kappa_D^L$ and $\kappa_{LE}^L$ ) and for homotopic connectivity ( $\kappa_{HC}$ ). No significant correlations were found in the right hemisphere network. . . . .	105
5.16	Correlations between Verbal Comprehension Index (VCI) and reorganization indices ( $\kappa$ ) of graph metrics measured in: (A) the whole brain networks, (B) the left hemisphere networks, (C) the right hemisphere networks and (D) the homotopic nodes. Significant correlations were measured for $\kappa$ describing hubs properties in the whole brain networks ( $\kappa_{BC}$ ), for integration properties in the whole brain network ( $\kappa_D$ ) and for segregation properties in the whole brain networks ( $\kappa_{CC}$ and $\kappa_{LE}$ ), in the left ( $\kappa_{CC}^L$ and $\kappa_{LE}^L$ ) and right hemisphere networks ( $\kappa_{CC}^R$ , $\kappa_{LE}^R$ ) and for homotopic connectivity ( $\kappa_{HC}$ ). . . . .	106
5.17	Correlations between Perceptual Reasoning Index (PRI) and reorganization indices ( $\kappa$ ) of graph metrics measured in: (A) the whole brain networks, (B) the left hemisphere networks, (C) the right hemisphere networks and (D) the homotopic nodes. Significant correlations were measured for $\kappa$ describing hubs properties in the whole brain networks ( $\kappa_{BC}$ ), for integration ( $\kappa_D^L$ ) and segregation properties in the left hemisphere networks ( $\kappa_{LE}^L$ ) and for homotopic connectivity ( $\kappa_{HC}$ ). . . . .	107



5.18	Correlations between Working Memory Index (WMI) and reorganization indices ( $\kappa$ ) of graph metrics measured in: (A) the whole brain networks, (B) the left hemisphere networks, (C) the right hemisphere networks and (D) the homotopic nodes. Significant correlations were measured for $\kappa$ describing hubs properties in the whole brain networks ( $\kappa_{BC}$ ), for integration properties in the left hemisphere networks ( $\kappa_D$ .	108
------	--	-----

## 6 Structural connectivity: a DTI study 112

6.1	Overview of the pipeline used for data processing. On top, the pipeline for graph generation: graph nodes are generated through anatomical parcellation on T1 image (1) and probabilistic anatomically constrained streamline tractography is generated from diffusion images (2). Then, the numbers of streamlines connecting each pair of nodes are used to define edges in the weighted graph and generate the connectivity matrices. (3) Finally, a proportional threshold ( $\tau=0.25$ ) was applied to remove the weakest connections before generating adjacency matrices (4). On bottom, the pipeline for fiber-bundles extraction. Computation of FA, MD, AD, and RD (5) from diffusion images. Registration of the atlas on the subject space (6) and extraction of the mean value inside WM masks. . . . .	117
6.2	Schematic representation of the connectivity matrix subdivision in different networks, including left-, right-, and inter- hemispheres networks and lobes networks. The cortical regions in each lobe are also reported. . . . .	118
6.3	Significant positive correlations obtained between the graph density of the whole brain networks and the full-scale intelligence quotient (FSIQ) the verbal comprehension index (VCI), the perceptual reasoning index (PRI), and the working memory index (WMI). . . . .	121
6.4	Significant correlations obtained between the full-scale intelligence quotient (FSIQ) and the local graph metrics in the left precuneus and the left middle temporal networks. . . . .	124
6.5	Significant correlations obtained between the verbal comprehension index (VCI) and the local graph metrics in the left superior and middle temporal networks. . . . .	124
6.6	A significant positive correlation obtained between the perceptual reasoning index (PRI) and degree metric in the right caudate. . . . .	125
6.7	The g-score, obtained using a factor analysis of the ten WISC subtests, was composed of three major broad domains, named “fluid intelligence” (PA1), “classification ability” (PA2), and “crystallized intelligence” (PA3). . . . .	126
6.8	Significant positive correlations measured between graph density in the whole brain networks and the g-score ( $p<0.01$ ), the fluid intelligence domain (PA1; $p<0.001$ ), and the classification ability domain (PA2; $p<0.05$ ). . . . .	128

6.9	Correlations between PA1-g intelligence domain and local graph metrics in the right precuneus node. . . . .	130
<b>7</b>	<b>Brain activation during semantic tasks</b>	<b>136</b>
7.1	Illustration of the task. The Encoding and the Retrieval phases constitute a block . . . . .	139
7.2	Boxplots of response time measured in seconds for three different factors. (A) for Intelligence group: Standard Intelligence Quotient (SIQ), Homogeneous High Intelligence Quotient (Hom-HIQ), and Heterogeneous High Intelligence Quotient (Het-HIQ); (B) for task factor: words with semantic link (SL), words without semantic link (WL), and non-sense words (NS); (C) for response factor: incorrect, miss, and correct. *** $p < 0.001$ . . . . .	142
7.3	Illustration of regions that showed significant higher activation during encoding phase of words without semantic link (WL): (A) left inferior occipital cortex in standard intelligence group compared to the heterogenous HIQ profile, (B) left prefrontal cortex in homogeneous HIQ profile compared to heterogeneous profile. . . . .	144
7.4	Illustration of the regions that showed higher activation in Het-HIQ profile compared to reference group (SIQ), (A) in the left thalamus in the difference between the retrieving of words without link (WL) and word with semantic link (SL), and (B) & (C) in the left occipital cortex for the difference between the retrieving of non-sense words (NS) and all sense words (SL+WL). . . . .	145
7.5	Illustration of the regions that showed higher activation in the Het-HIQ profile compared to the Hom-HIQ profile, (A) in the left middle frontal gyrus for the difference between the retrieving of non-sense words (NS) and both sense words (SL+WL). During the retrieving of non sense (NS) and words with semantic link (SL), (B) in the left posterior cingulate gyrus, (C) in the right posterior central gyrus, and (D) in the right pre-central gyrus. . . . .	146
<b>IV</b>	<b>Research project on HIQ adults</b>	<b>153</b>
<b>8</b>	<b>Functional and structural connectivity</b>	<b>154</b>
8.1	Steps of the fMRIVolume HCP Pipeline. Starting from gradient distortion correction to the intensity normalization [Glasser <i>et al.</i> (2013)].	157
8.2	Significant correlation obtained between graph transitivity and the perceptual reasoning index (PRI) of the functional connectivity. . . .	160
8.3	Significant correlations obtained between graph assortativity and full scale intelligence quotient (FSIQ), perceptual reasoning index (PRI), and working memory index (WMI) for structural connectivity. . . .	161

8.4	Significant correlations obtained between graph clustering coefficient (CC) and perceptual reasoning index (PRI) in the right inferior temporal cortex. Clustering Coefficient increases in high PRI values. . . .	162
8.5	Significant correlations obtained between both degree and betweenness centrality (BC) graph metrics and full scale intelligence quotient (FSIQ) in the right anterior cingulate cortex. Both graph metric decrease in high FSIQ. . . . .	163

# List of symbols and abbreviations

## Latin letters

$\vec{s}$	Static spin moment
$B_0$	Magnetic field
$M_z$	Longitudinal magnetization
$M_{xy}$	Tranverse magnetization

## Greek letters

$\vec{\mu}$	Nuclear magnetic moment
$\gamma$	Gyromagnetic ratio
$\vec{\omega}$	Larmor angular frequency
$\vec{\nu}$	Larmor frequency
$\delta$	Gradient diffusion duration
$\Delta$	Diffusion time between the two gradients
$\lambda_{1,2,3}$	Eigenvalues of diffusion tensor
$\vec{\epsilon}_{1,2,3}$	Eigenvectors of diffusion tensor

## Abbreviations

<i>2DFT</i>	2D Fourier transform
<i>AD</i>	Axial Diffusivity
<i>BOLD</i>	Blood Oxygenation level dependent
<i>deoxyHb</i>	Deoxygenated Haemoglobin
<i>CBF</i>	Cerebral Blood Flow
<i>CBV</i>	Cerebral Blood Volume
<i>CEN</i>	Central Executive Network
<i>CMRO<sub>2</sub></i>	Cerebral metabolic rate of oxygen
<i>CSF</i>	Cerebrospinal fluid
<i>DMN</i>	Default Mode Network

---

<i>DT</i>	Diffusion Tensor
<i>DTI</i>	Diffusion Tensor Imaging
<i>EPI</i>	Echo Planar Imaging
<i>FA</i>	Fractional Anisotropy
<i>FC</i>	Functional Connectivity
<i>fMRI</i>	functional Magnetic Resonance Imaging
<i>FOD</i>	Fiber Orientation Density
<i>FSIQ</i>	Full Scale Intelligence Quotient
<i>GM</i>	Gray Matter
<i>HCP</i>	Human Connectome Project
<i>HIQ</i>	High Intelligence Quotient
<i>Het-HIQ</i>	Heterogeneous High Intelligence Quotient
<i>Hom-HIQ</i>	Homogeneous High Intelligence Quotient
<i>HR</i>	Haemodynamic response
<i>IQ</i>	Intelligence Quotient
<i>IIT</i>	Illinois Institute of Technology
<i>MD</i>	Mean Diffusivity
<i>MODWT</i>	Mean Overlap discrete wavelet transform
<i>MRI</i>	Magnetic Resonance Imaging
<i>NMR</i>	Nuclear Magnetic Resonance
<i>ODF</i>	Orientation Distribution Function
<i>oxyHb</i>	Oxygenated Haemoglobin
<i>PRI</i>	Perceptual Reasoning Index
<i>PSI</i>	Processing Speed Index
<i>RD</i>	Radial diffusion
<i>RF</i>	Radio Frequency
<i>ROI</i>	Region of Interest
<i>RSN</i>	Resting state Network
<i>SIQ</i>	Standard Intelligence Quotient
<i>SMN</i>	Sensory Motor Network
<i>SNR</i>	Signal to Noise Ratio
<i>TE</i>	Echo Time
<i>TR</i>	Repetition Time
<i>VCI</i>	Verbal Comprehension Index
<i>VBM</i>	Voxel Based morphometry
<i>WAIS</i>	Wechsler Adult Intelligence Scale
<i>WISC</i>	Wechsler Intelligence scale for children
<i>WM</i>	White Matter
<i>WMI</i>	Working Memory Index

# Introduction

Human intelligence has always been a subject of interest for the humanity. The percentage of High Intelligence Quotient (HIQ) people is about of 2-3% of the total population, representing in childhood an average of one child per two classes. Despite of HIQ persons are usually characterized by better cognitive abilities, they may present simultaneously some disabilities. Indeed, they can be unable to manage their attention and emotions and these difficulties may cause social difficulties. A HIQ person may feel out of place, and then may suffer from this, until presenting some psychological troubles. In order to improve our understanding of their mental abilities, we investigated new markers characterizing the neural correlates of intelligence and to explain their behaviour difference with scientific grounds.

Magnetic resonance imaging (MRI) is a powerful technology to non-invasively investigate multiple aspects of the brain. Indeed, with the evolution of MRI, non-conventional acquisition protocols have been developed and two main techniques have been spread: functional MRI (fMRI) and diffusion MRI (dMRI). On one hand, the first technique allows to measure the activity of the brain in two different situations. With task fMRI, the activity of the brain during the performance of a task can be studied. Instead, resting-state fMRI provides information about the brain activity at rest, without any task performance. On the other hand, dMRI allows to obtain quantitative information about the structure of white matter at microscopic scale. From these two techniques, we can measure how the brain regions are connected among them on two different levels. With fMRI, the functional connectivity between regions can be measured, while dMRI provides information about the structural connectivity, or rather how the white matter (WM) fibers link the cortical regions. Since brain connectivity can be modeled as a network in which the brain regions are connected, a natural technique to explore it is the graph analysis. Indeed, the brain network can be represented as a graph in which the gray matter (GM) regions represent the nodes of the graph and structural or functional connectivity represent the edges between the nodes.

In this work, we will take advantage from the specificity of these modern MRI

---

techniques to characterize the neural bases of intelligence, based on both functional and structural brain connectivity measured in children and in adults.

This thesis is composed of three principal parts. The first part presents the state of the art of MRI, graph theory, and MRI studies of intelligence. In the second part, we explored the neural substrate of intelligence in children with three complementary MR approaches. Finally, in the third part, the structural and functional connectivity networks related to intelligence have been characterized in adults.

In the first chapter of the part I, MRI is illustrated starting from the physical mechanisms at the origin of nuclear magnetic resonance till the generation of the images, passing through the imaging sequences used in conventional MRI. Then, we introduced functional MRI. Starting from the neuro-physiological mechanism that is beyond this technique, we explained two different fMRI measures: task fMRI and resting-state fMRI. Finally, we present the principles of diffusion MRI technique. We begin by recalling the diffusion phenomenon. We then present the diffusion MRI sequence and the major diffusion technique namely diffusion tensor imaging (DTI). We concluded this chapter with the illustration of this technique that can, on one hand, generate parametric maps characterizing the tissue architecture and, on the other hand, reconstruct by tractography the fibers of white substance bundles from the main direction of diffusion.

In the second chapter, the brain connectivity concept is introduced. We started with the description of the graph theory and its metrics. Then, we explained the different graph types and the topology of the brain network. Finally, the process to measure brain connectivity, using an anatomical parcellation and a connectivity matrix, from different MRI techniques is discussed. The state of the art section is concluded with the presentation of the Intelligence. In this chapter, the history of neuroscience researches in Intelligence concept has been introduced. From the most ancient to the most recent models and intelligence tests used in research are presented. This chapter is concluded by the description of the different investigation of the intelligence by MRI. The literature review starts from the early MRI studies till the modern studies that explore the connectivity of brain network related to intelligence.

The second part of this work is dedicated to the study of brain correlates of intelligence in HIQ children. The participants of this research project are a group of children between 8-12 years that undergo the fourth edition of Wechsler Intelligence scale for Children (WISC-IV), and a complete MRI protocol. Based on the results of the WISC-IV test, children were divided into three groups: a group of children with

---

a standard full scale intelligence quotient (SIQ), a group of children with a Full Scale Intelligence Quotient (FSIQ) higher than 130 called homogeneous HIQ (Hom-HIQ), and a group of children with a Verbal Comprehension Index (VCI) or a Perceptual Reasoning Index (PRI) higher than 130 and a significant difference between VCI and PRI, called heterogeneous HIQ (Het-HIQ). The first and the second chapters of the second section, are dedicated to the characterization of cerebral connectivity through two advanced MRI techniques: rs-fMRI and DTI respectively. The first chapter starts with the methodological description to optimize the pipeline for functional connectivity measures. Then, we explore the functional brain connectivity with the graph theory, and its topological modification using the "hub disruption index". With this metric, we evaluate how the functional brain topology changes according to different intelligence scores and different HIQ profiles. The structural brain connectivity measured with DTI is then described in the second chapter. The last study on the same children population is presented in the third chapter of this section. A task fMRI study was performed in children using a memory semantic task. Brain performances and activations during this task were analyzed in correlation with the children cognitive abilities.

In the last part of this work, our research project was applied to investigate the intelligence in adults. As well as for the children population, we performed a connectivity study with rs-fMRI and DTI techniques. In this chapter, we report the results obtained with the application of graph theory on both functional and structural connectivity matrices and their relationship with intellectual abilities in adult age.

Finally, we will draw the main conclusions of this work and highlight the most interesting perspectives for further investigations.





## I State of the Art

---



# Chapter 1

---

## Magnetic Resonance Imaging

---

### Contents

---

<b>1</b>	<b>Introduction</b>	<b>8</b>
<b>2</b>	<b>From signal to images</b>	<b>8</b>
2.1	The Nuclear Magnetic Resonance (NMR) phenomenon	9
2.2	Imaging	10
2.3	Conventional MRI sequences	12
<b>3</b>	<b>Functional MRI</b>	<b>15</b>
3.1	BOLD signal	15
3.2	Acquisition sequences	18
3.3	From functional localisationism to connectionism	19
3.4	Task fMRI	21
3.5	Resting-state fMRI	22
<b>4</b>	<b>Diffusion MRI</b>	<b>24</b>
4.1	Physic principle	24
4.2	Acquisition sequences	25
4.3	Diffusion Tensor Imaging (DTI)	26
4.4	Tractography technique	29

---

# 1 Introduction

In 1946, the Nuclear Magnetic Resonance (NMR) was independently but simultaneously discovered by Purcell, Torrey and Pound at Cambridge MIT, and Bloch, Hansen and Packard at Stanford. In 1952, Bloch and Purcell were both awarded with the Nobel Prize for physics for their important discovery. At the beginning, NMR was an experimental technique for physicist to explore the nuclear magnetic moments of nuclei.

The first to use NMR technique on living systems was Felix Bloch who analyzed water contained in his finger, and only in 1971 the first disease study by NMR was realized. With this technique, it is possible to investigate several properties of the matter described by different parameters and to obtain images weighted by different contrasts.

In contrast with other physical techniques used in medicine, NMR uses radio waves, a nonionizing radiation. Their frequency band (MHz) is too low to release the electrons and to create ionization. For this property, NMR is a non-invasive and non-destructive technique, ideal for *in vivo* analysis.

# 2 From signal to images

The application of NMR in neuroscience involves mainly spectroscopy, functional imaging, and diffusion imaging. Therefore, NMR is considered a great diagnostic technique that studies the magnetic proprieties of the matter using the intrinsic nuclear moment, the spin. A nucleus with an odd number of protons and neutrons has a non-zero nuclear magnetic spin and a kinetic moment defined as follow:

$$\| \vec{s} \| = \sqrt{s(s+1)} * \hbar \quad (1.1)$$

where  $\vec{s}$  is the dipolar kinetic moment,  $s$  the spin, and  $\hbar$  the Planck constant normalized on  $2\pi$ . In its ground state, a nucleus with a kinetic momentum  $\vec{s}$  has a nuclear magnetic momentum  $\vec{\mu}$ :

$$\vec{\mu} = \gamma \vec{s} \quad (1.2)$$

where  $\gamma$  is the gyromagnetic ratio.

Being a constant defined as the ratio between nuclear magnetic momentum and intrinsic angular magnetic spin momentum, the magnetic momentum is specific for each nucleus. The most studied nucleus is the hydrogen nucleus, fundamental in

medical studies thanks to its high isotopic abundance and its easier detection due to its large gyromagnetic ratio ( $42.58 \text{ MHz/T}$ ).

Due to their paramagnetic property, when placed in an external magnetic field, these magnetic momenta will be aligned to the field direction and the nuclear state is splitted into two levels called "Zeeman levels". The difference between the population of the two energetic levels leads to the macroscopic magnetization  $\vec{M}$ :

$$\vec{M} = \sum \vec{\mu} \quad (1.3)$$

During this alignment, the spins experience a precession motion whose frequency depends on the angular frequency  $\vec{\omega}$ , the fundamental parameter of NMR.

$$\vec{\omega} = -\gamma \vec{B}_0 \quad (1.4)$$

where  $\vec{\omega}$  is named Larmor angular frequency and depends on Larmor frequency (for hydrogen nucleus  $\nu = 42.58 \text{ MHz}$  for  $B_0 = 1T$ ) with  $\omega = 2\pi\nu$ .

## 2.1 The Nuclear Magnetic Resonance (NMR) phenomenon

The macroscopic magnetization relaxation gives information about the sample. In order to have a signal, the equilibrium state must be perturbed by a magnetic field  $\vec{B}_1$ , perpendicular to  $\vec{B}_0$  that is along the  $z$  axis, rotating with the Larmor frequency. The system of spins is then on resonance with the field and two phenomena happen:

- microscopically: the spins receive an amount of energy enough to transit from a level to the other;
- macroscopically: the magnetization will have a precessional motion around  $B_0$  and  $B_1$ .

When the magnetic field  $B_1$  is turned off, the three magnetization components come back into an equilibrium position through the relaxation process. This motion is described by the following Bloch's equations:

$$\begin{cases} \frac{dM_x(t)}{dt} = -\frac{M_x(t)}{T_2} \\ \frac{dM_y(t)}{dt} = -\frac{M_y(t)}{T_2} \\ \frac{dM_z(t)}{dt} = -\frac{M_z(t)-M_0}{T_1} \end{cases} \quad (1.5)$$

where  $T_1$  and  $T_2$  are the relaxation time needed to return to the equilibrium, and  $M_0$  is the initial magnetization.

$T_1$  is the *Longitudinal Relaxation Time* or *spin-lattice* that describes the temporal evolution of the longitudinal magnetization as mathematically expressed by the following equation:

$$M_z(t) = M_z(0)(1 - e^{-\frac{t}{T_1}}) \quad (1.6)$$

During this process, the spins give their energy to the lattice. The characteristic time of the exchanged energy between the spins themselves is  $T_2$  named *spin-spin* or *Transverse relaxation time*.  $T_2$  measures how fast the spins lost their phase coherence because of spin-spin interactions, and during this time-frame the transverse magnetization comes back to the equilibrium state. The temporal evolution of the transverse magnetization is described by:

$$M_{xy}(t) = M_{xy}(0)e^{-\frac{t}{T_2}} \quad (1.7)$$

In practice,  $B_0$  in-homogeneity, due to the magnet and/or heterogeneities of the sample, increases the decay rate of the transverse magnetization. This signal decay is then dependent on the apparent relaxation time  $T_2^*$  defined by:

$$\frac{1}{T_2^*} = \frac{1}{T_2} + \frac{1}{T_2'} \quad (1.8)$$

where  $T_2'$  characterizes the relaxation time induced by this loss of coherence due to local variations of magnetic field.

## 2.2 Imaging

In 1973, Lauterbur reached for the first time density distribution by NMR Imaging. The spatial coding is supplied by the introduction of magnetic fields variation through a gradient application. Field gradients describe the variation of longitudinal components of magnetic field along the three axes (x, y, z):

$$\vec{G}(t) = (G_x(t), G_y(t), G_z(t)) = \left( \frac{\partial B_z}{\partial x}, \frac{\partial B_z}{\partial y}, \frac{\partial B_z}{\partial z} \right) \quad (1.9)$$

Figure 1.1 shows the trend of the magnetic field along z axis depending on z position. A selective RF pulse in the range  $\Delta\omega$  excites the rate of z ( $\Delta z$ ) (area of figure colored in gray). The slice thickness depends on the gradient intensity and on the bandwidth of the radio frequency pulse: a larger bandwidth ( $\Delta\omega$ ) means a greater thickness of the excited slice range ( $\Delta z$ ).

k-space is a formalism used in MRI to interpret images. Indeed, the 2D Fourier

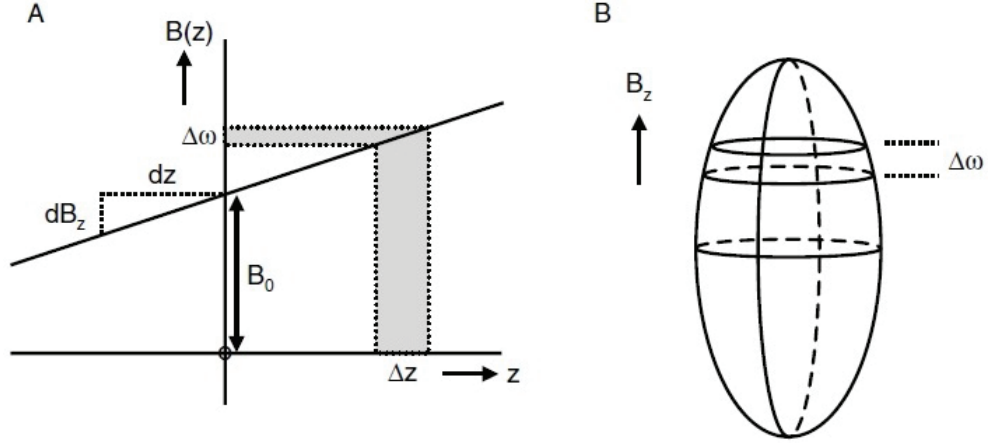


Figure 1.1: (A) Magnetic field gradient in  $z$  direction. (B) Spatial slice in a real object selected by a selected pulse with the application of a gradient [De Graaf (1998)].

transform (2DFT) method provides a  $k$ -space sampling for the formation of the images. In order to have a 3D image, the sample is divided in 2D slices along a third direction. Once a slice is selected, in order to distinguish the signal from spins that have a different position in the slice, the second step of the image acquisition is to apply two new gradients. The first gradient applied after the selective pulse is named *Phase-encoding Gradient* and it is usually along  $y$  direction. When  $G_y$  is turned on, spins along this direction feel a different magnetic field and consequently they acquire a specific phase  $\Phi = \gamma G_y t y$ . So, spins of the selective slice, that were in phase, now become dephased.

During the signal acquisition, a gradient along  $x$  axis named *Frequency-encoding Gradient* or *Readout Gradient* is turned on. It modifies Larmor frequency depending on the gradient duration along the other transverse direction to the slice. Finally, the signal in the  $k$ -space  $S(k_x, k_y)$  is obtained by the following equation:

$$S(k_x, k_y) = \iint \rho(x, y) e^{i\gamma(G_x x t + G_y y t)} dx dy = \iint \rho(x, y) e^{i2\pi(k_x x + k_y y)} dx dy \quad (1.10)$$

where  $k_x = \gamma \frac{G_x t x}{2\pi}$  and  $k_y = \gamma \frac{G_y t y}{2\pi}$

From these expressions, it is obvious that the phase-encoding gradient causes a dephasing in  $k_y$  direction while the readout gradient moves along  $k_x$  axis. Furthermore,  $k$ -space sampling depends on the values of the phase-encoding, the frequency-encoding gradient, and by their combinations.

As example, the I and IV quadrants sampling of the  $k$ -space for  $k_x > 0$  are described below:



- $k_y = 0$  line is achieved putting  $G_y=0$  ( $k_x$  axis);
- $k_y > 0$  line is achieved putting  $G_y>0$  (I quadrant);
- $k_y < 0$  line is achieved putting  $G_y<0$  (IV quadrant).

K-space central points have low k-coordinate values (low spatial frequencies) and they correspond to the image contrast, while points with high spatial frequency (on k-space edges) have information about image details (Figure 1.2).

Finally, the 2D image is obtained through the Inverse Fourier Transform and the image in the real space is obtained.

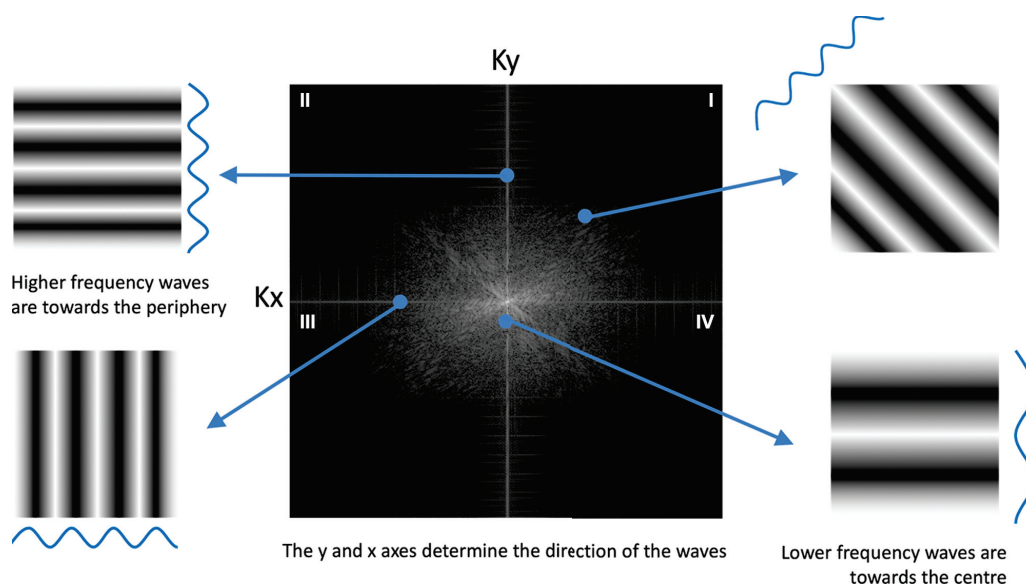


Figure 1.2: Illustration of k-space with its 4 quadrants. Adapted from <https://www.radiologycafe.com>.

## 2.3 Conventional MRI sequences

Several acquisition sequences have been developed to measure NMR signal and they are based on two main sequences that use different methods to refocus the signal. The NMR signal can be measured by a *Spin-Echo* sequence using two RF pulses, one  $90^\circ$  and one  $180^\circ$ , or with one  $90^\circ$  pulse in conjunction with a gradient reversal (see next section), named *Gradient-Echo*.

### 2.3.1 Spin-Echo

The spin-echo sequence was introduced in the 50s by Erwin Hahn and it is based on a  $180^\circ$  pulse that refocuses the magnetization after a time  $t$  called *Echo Time* (TE). This sequence starts with a  $90^\circ$  pulse that moves the magnetization from the

longitudinal to transverse plane. During a period of half echo-time ( $TE/2$ ), spins groups may precess with a different speed from others because of their different  $T_2$  and of local field inhomogeneities leading to the  $T_2^*$ . The following  $180^\circ$  pulse rotates the magnetization components reversing the phase difference and allowing the spins re-phasing during an other  $TE/2$  period. At the end, the echo signal is generated after a TE time from the selective pulse and a line of the k-space is acquired. After a repetition time (TR), the sequence is repeated several times until the k-space is filled.

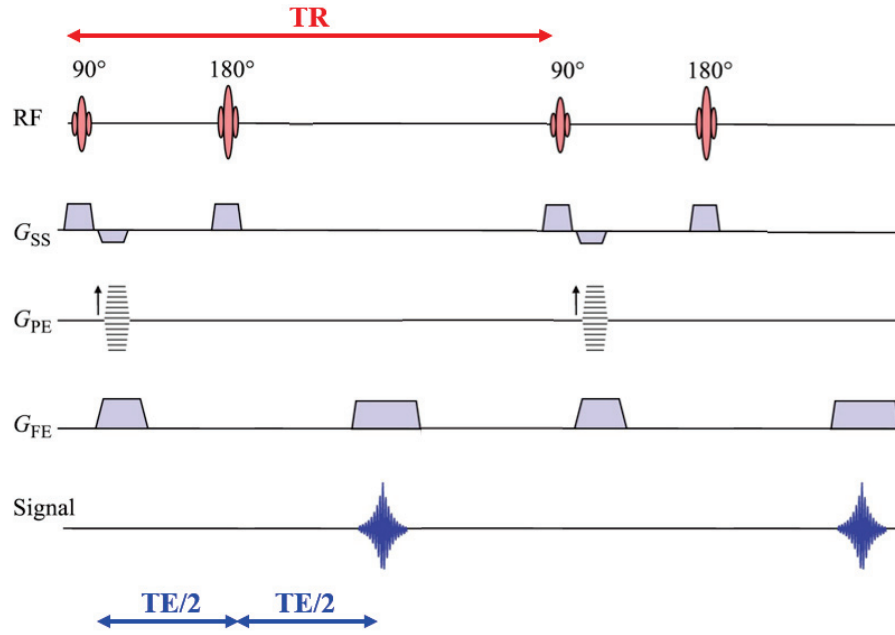


Figure 1.3: Spin-echo imaging sequence diagram. TR is the repetition time between two  $90^\circ$  pulses. TE is the echo time between the first  $90^\circ$  and the echo signal registration. Adapted from [McRobbie *et al.* (2006)].

The contrast of the image obtained with a spin-echo sequence can be changed modifying the two main parameters of the sequence TR and TE. When the time between the excitation and the echo signal (TE) is short, the echo signal is measured too early to differentiate the tissues based on their  $T_2$ . In this case, with a short TR the longitudinal magnetization differences between tissue are stronger and the contrast of the image is T1-weighted, while with a long TR the T1 effect disappears and the image is proton density weighted. With a similar reasoning, with long TR the longitudinal magnetization is recovered and with a long TE difference in  $T_2$  are more visible and the image is  $T_2$ -weighted.

### 2.3.2 Gradient-Echo

The second sequence that allows to refocus the NMR signal is called "gradient-echo". In this case the echo signal is produced with the application of a gradient reversal at the center of the acquisition period. After an initial RF pulse that is typically in the range of  $10^\circ$  to  $40^\circ$ , a negative gradient is applied to dephase the spins because of changes in local magnetic fields. This process is then reversed applying a second gradient with the same strength but opposite polarity to the first one and the spins are refocused to produce an echo signal. Since the absence of a  $180^\circ$  RF pulse, this sequence does not erase the static tissue susceptibility gradients producing an image contrast of  $T_2^*$  that depends on these factors. In order to minimize the influence of these susceptibility artefacts on the images, a short TE is often used. Moreover, the small initial RF causes a faster magnetization recovering allowing to use a shorter TR. In these conditions, the images exhibit  $T_1$ -weighting in which tissues with short  $T_1$  appear brighter than those with long  $T_1$ .

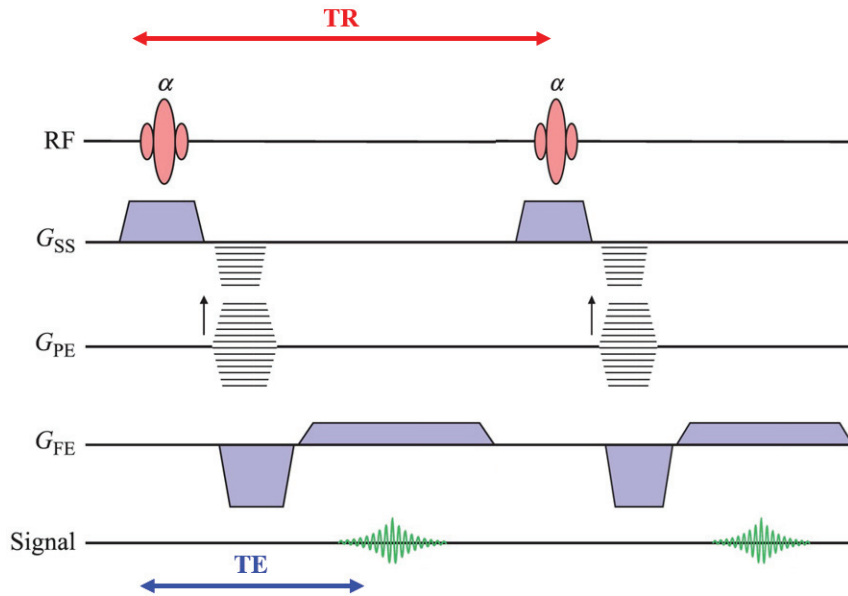


Figure 1.4: Gradient-echo sequence diagram. TR is the repetition time measured between two RF pulses. TE is the echo time between the first  $90^\circ$  and the echo signal registration. Adapted from [McRobbie *et al.* (2006)].

### 3 Functional MRI

Functional Magnetic Resonance Imaging (*fMRI*) is one of the functional neuroimaging techniques that describes physiological changes accompanying brain activity. Despite it was known that regional cerebral blood flow increased in areas of neuronal activity since the end of 1980's, Belliveau and colleagues [Belliveau *et al.* (1991)] were the first in 1991 to use MRI to observe cerebral activation. They showed an increased brain activity in primary visual cortex during photic stimulation measuring blood volume changes of this area thanks to the susceptibility changes from a gadolinium bolus. A new technique named *Blood oxygenation level dependent (BOLD)* was introduced by [Ogawa *et al.* (1990)], allowing two groups from Minnesota and MGH to measure the brain activation without the use of any exogenous contrast. They were able to create the neuronal activation maps detecting changes in blood flow exploiting different magnetic properties of oxygenated and deoxygenated blood [Ogawa *et al.* (1992), Kwong *et al.* (1992)].

#### 3.1 BOLD signal

Like all organs, the brain requires high level of energy metabolism for its activity. More in detail, it is responsible for the 20% of the energy consumption. Because brain energy production is joined with the oxydative metabolism, an amount of oxygen increment is needed to increase brain activity. BOLD signal was measured for the first time in 1990 by Ogawa *et al.* on rats [Ogawa *et al.* (1990)]. It is based on the variation of deoxyhaemoglobin concentration in blood. In living organisms, there are two types of haemoglobin: the oxygenated one (oxyHb) and the haemoglobin without oxygen (deoxyHb). When the neural activity increases, a greater deoxyHb amount is generated. This phenomenon is modeled by the haemodynamic response.

Due to its paramagnetic property, the deoxyHb creates local magnetic field distortions within and around blood vessels. In 1992, Ogawa demonstrated that local field gradients cause changes in nearby spins that achieve different resonance frequencies [Ogawa *et al.* (1992)]. This phenomenon is reflected in a  $T_2^*$  decrease in tissue around the blood vessels. In 1998, Thulborn *et al.* demonstrated that these susceptibility gradients produce measurable changes in  $T_2$  contrast [Thulborn (1998)]. These distinct experiments allow to conclude that both  $T_2$  and  $T_2^*$  changes contribute to BOLD contrast.

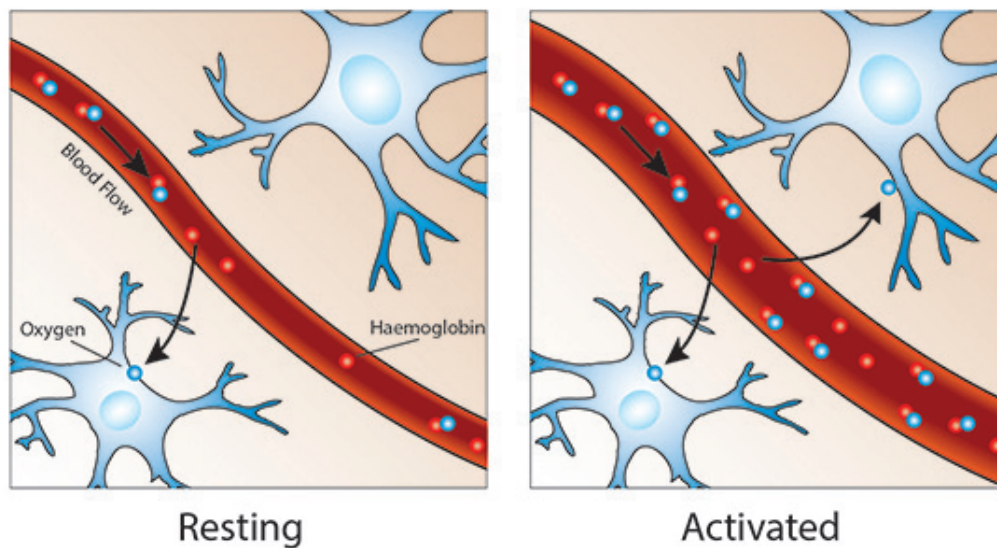


Figure 1.5: Haemodynamic response phenomenon. The neuronal activity consumes the oxygen from the blood, causing an increase of deoxyhaemoglobin concentration. In response to neuronal activity, the blood flow increases leading to an increase of oxygen concentration in blood. The difference of oxygenated and deoxygenated haemoglobin results in a decrease of deoxyhaemoglobin. From Oxford Sparks.

### 3.1.1 Temporal dynamic of BOLD signal

It may seem paradoxical, but during a neuronal activation an increased BOLD signal is measured and a more intense image is obtained [Jezzard (2001)]. This is due to the fact that BOLD signal reflects neurovascular coupling modeled by the *Haemodynamic response* (HR) to activation [Buxton (2009)] that depends on different phenomena: cerebral metabolic rate of oxygen ( $CMRO_2$ ), cerebral blood flow (CBF) and cerebral blood volume (CBV) changes. During a neuronal activation, these three events happen simultaneously, and BOLD timecourse is the combination of  $CMRO_2$ , CBF and CBV temporal signals as shown in Figure 1.7.

The typical fMRI BOLD response is composed of three steps (Figure 1.6):

- **Initial dip:** an initial dip lasting 1s before the positive BOLD signal has been reported [Menon *et al.* (1995)]. This effect is visible only in high magnetic field and it corresponds to an increase of deoxyhaemoglobin. It reflects the rapid  $CMRO_2$  increase that starts before the blood flow changes.
- **Positive response:** after 5-8s from the beginning of the stimulus, the signal increases by 2-3 % from the baseline. The positive response is often composed of an overshoot followed by an exponential decay. Mandeville and colleagues in 1999 demonstrated that this amplification is due to CBV increase that, starting

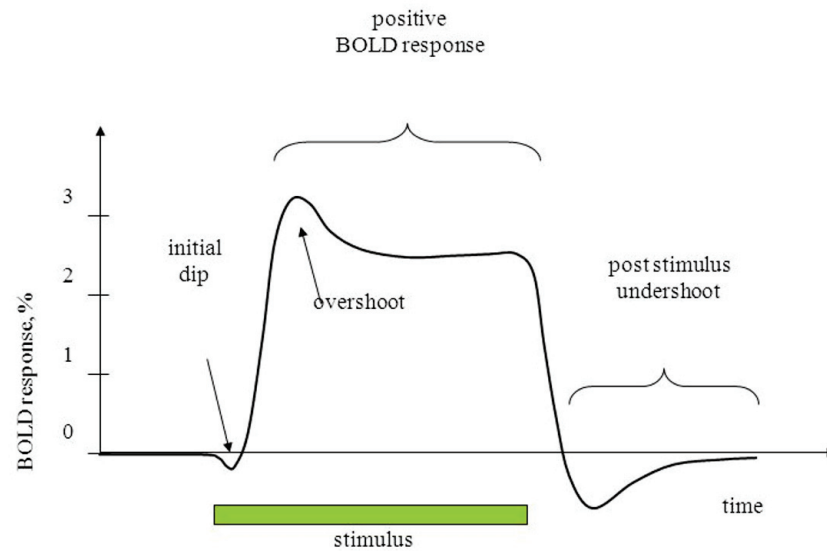


Figure 1.6: Blood oxygenated level dependent (BOLD) timecourse.

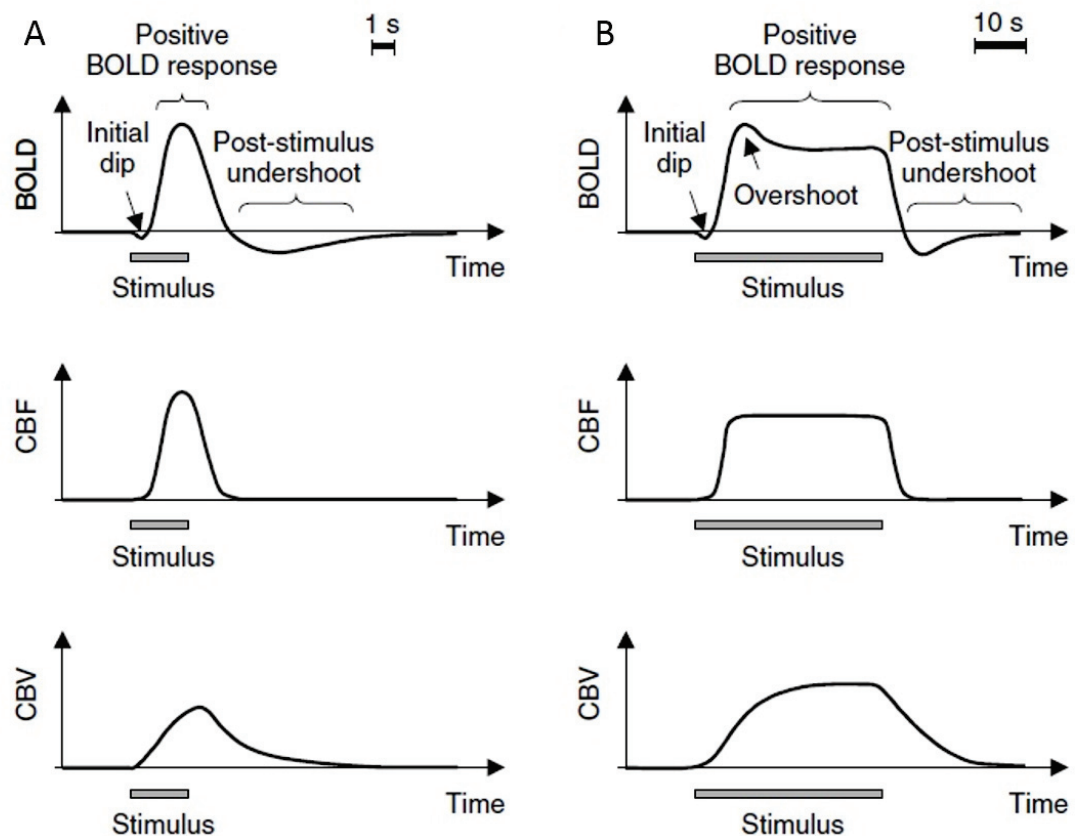


Figure 1.7: BOLD, CBF and CBV temporal trend for: (A) a short stimulus, and (B) a long stimulus.

later than CBF, reduces the BOLD signal during the plateau phase [Mandeville *et al.* (1999)].

- **Post-stimulus undershoot:** the BOLD signal ends with a post-stimulus undershoot that lasts for approximately 30 s. As for the overshoot, it is caused by the CBV changes because when the blood flow falls dramatically, CBV levels are still elevated and a reduced BOLD signal is measured.

## 3.2 Acquisition sequences

The most used imaging method in fMRI is the gradient-echo sequence for its sensitivity to BOLD effect with an encoding echo-planar imaging (EPI) for fast k-space acquisition (Figure 1.8). Compared to the conventional imaging, EPI most important advantage is the speed for obtaining the image. While the duration of the conventional MRI sequences previously described is about  $N \times TR$  because each k-space row is filled after a selective pulse, the total duration of an EPI acquisition is about one TR. This short duration is obtained because EPI sequence allows to sample the entire k-space with only one initial RF pulse (Figure 1.8). For functional imaging, this spatial encoding scheme is used with gradient-echo sequences that offer a  $T_2^*$  contrast. Since the signal intensity decay is measured after the excitation determined by local field inhomogeneities, this technique is ideal for BOLD contrast imaging.

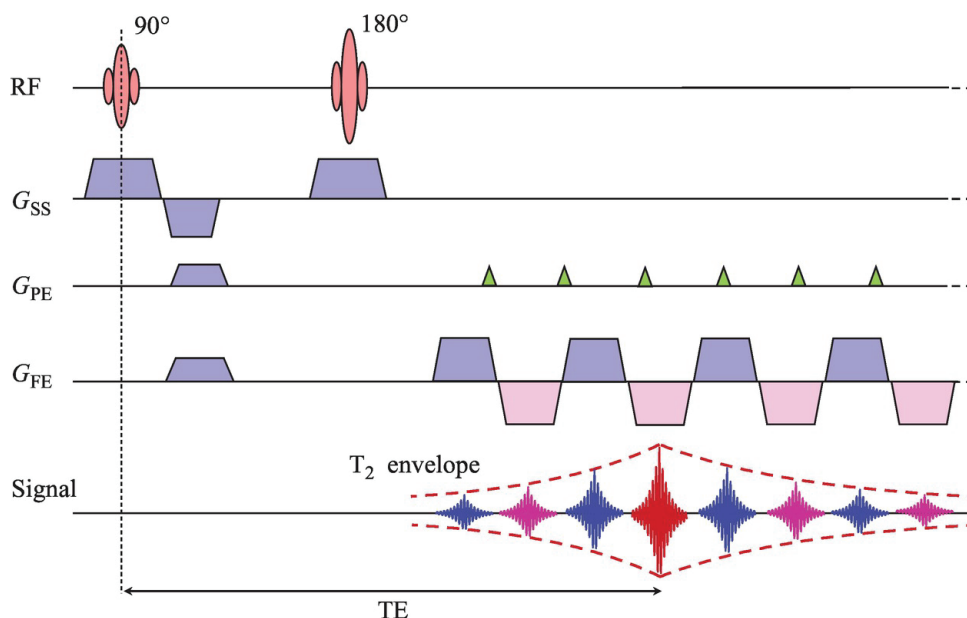


Figure 1.8: EPI imaging sequence diagram. Adapted from [McRobbie *et al.* (2006)].

Figure 1.8 shows a typical EPI sequence and figure 1.9 its k-space trajectory. The k-space sampling starts in the point  $(-k_{f,max}, -k_{p,max})$  and when  $G_{freq}$  is turned on, the first gradient-echo is acquired along k-space line  $k_p = -k_{p,max}$ . A



so called blip phase-encoding gradient changes the position in k-space till the point  $(k_{f,max}, -k_{p,max} + \Delta k_p)$ . After another refocusing ( $-G_{freq}$ ), the second acquisition starts. Iterating this process, the k-space is completely sampled.

Maximum echo formation is achieved in k-space origin where the initial negative phase-encoding gradient is completely refocused by the sum of all blip gradients.

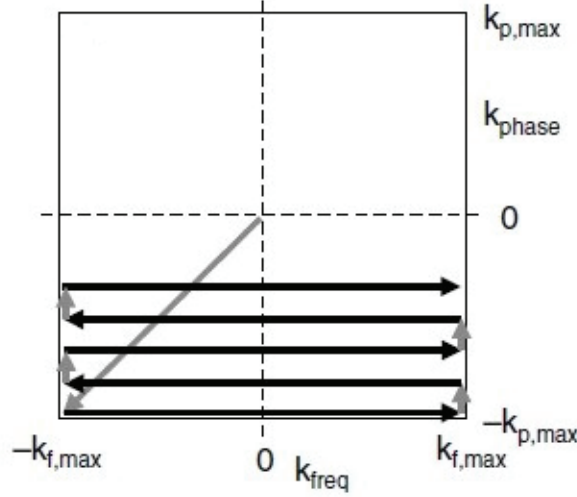


Figure 1.9: Example of k-space sampling: it starts from the point  $(-k_{f,max}, -k_{p,max})$  and goes on with a zig-zag trajectory.

While the most important EPI advance is the shortness of the acquisition time, it has two fundamental drawbacks:

- the magnetic field inhomogeneities are not re-focalized because absence of a  $180^\circ$  pulse. For this reason the images are deformed and, since  $T_2^*$  is smaller, the signal intensity is lower;
- transverse magnetization is created once and the signal is given by echo gradients when the  $G_{phase}$  areas are compensated.

### 3.3 From functional localisationism to connectionism

The major goal of functional MRI is to understand brain function. Since its introduction, fMRI was mainly used to spatially localize brain function [Friston *et al.* (1994)]. This localisationism approach was introduced with the formulation of phrenology by Franz Joseph Gall at the end of the XVIII century. Starting from this, a central assumption in neuroscience was the association between particular regions and specific functions. Despite this theory was not confirmed by Fluorens in



1815, later experiments supported the idea of localisationism. In particular Broca and later Wernicke localized regions respectively involved in language processing and in comprehension of speech. Nowadays, two main theories about brain's cognitive function have been developed. The first one supports functional specialization of brain regions based on the concept that neural activity can be revealed by localized changes in metabolism. Furthermore, several studies have demonstrated the functional specialization of distinct regions. For instance, all the primary cortices are involved in brain's input and output and they have different spatial locations:

- primary visual cortex is in the occipital lobe;
- primary auditory cortex is located in the temporal lobe;
- somatosensory cortex is in parietal lobe;
- primary motor cortex is in frontal lobe;
- olfactory bulb is located on the inferior surface of the frontal lobe;
- gustatory cortex is located on the inferior surface of the temporal lobe.

Nowadays, the most used standardized nomenclature in neuroimaging is *Brodman classification* of brain areas (Figure 1.10). In 1909, the German anatomist Korbinian Brodmann numerated cortical areas in humans, monkeys, and other species based on the cytoarchitectural organization of neurons. The Brodmann classification divides the cortex into 52 areas, numbered sequentially, that have been discussed, and renamed for a century. However, the neuroimaging studies still refer to this nomenclature to identify the function of each brain area.

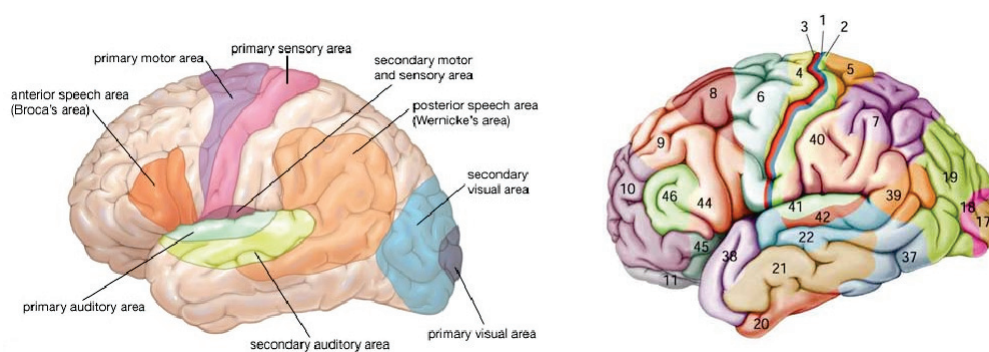


Figure 1.10: Brain regions classified with primary areas name on the left (localisationism), and Brodmann nomenclature on the right.

The second modern theory, instead, considers the brain as an interactive network in which the regions are functionally interconnected rather than specialized. This idea is named connectionism theory and refers to methods aiming at identifying and quantifying inter-regional relationships [Friston *et al.* (1994)]. In particular,

functional connectivity is the statistical correlation among neural activity measurements [Friston (2011)].

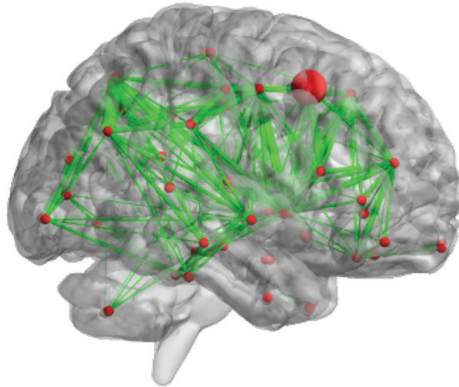


Figure 1.11: Illustration of connectionism: a complex network analysis reflecting whole-brain connectivity.

These two approaches are mainly based on two functional MRI techniques: task fMRI and resting-state fMRI measuring brain activation during a task and at rest, respectively. Task and rs-fMRI are presented in details in the next sections.

### 3.4 Task fMRI

Since the discovery that brain activation can be indirectly measured throughout the BOLD effect, a number of imaging approaches have been used to measure it and to obtain an image of activation areas. The prototype brain mapping of task fMRI experiment consists of alternating periods of a stimulus task and a control task during which the signal changes are measured. Two experimental paradigms are used: the Block Design and the Event-Related Design.

#### 3.4.1 Block Design

Block Design is the first paradigm used for fMRI experiments [Bandettini *et al.* (1993), Ogawa *et al.* (1992)] and for statistical analysis [Bandettini *et al.* (1993), Friston *et al.* (1994)]. It consists in a succession of time interval blocks with continuous stimuli from 16 s to a minute, named epoch, interleaved with control condition. These repeated measures with the same functional condition increase the image signal to noise ratio (SNR). Typically tasks with different functional properties are performed in order to obtain a BOLD signal. The time between two epochs with the same task defines a cycle.

The advantage of this paradigm is to obtain an intense BOLD signal but the subject could predict the stimulus because the repetition of the same task. Generally, a fMRI acquisition is composed of 120 volumes or more.

### 3.4.2 Event-Related Design

This paradigm provides a rapid succession of different random functional tasks. It allows to obtain temporal information of the haemodynamic response eliminating routine effects, thanks to the random distribution of the tasks. It investigates the BOLD response to each individual task.

### 3.4.3 Mixed Design

In mixed paradigms, semi-randomized events take place during the task blocks, with rest periods in between them. This method preserves the positive aspects of the two methods: high SNR of blocked methods, and the flexibility of event-related ones.

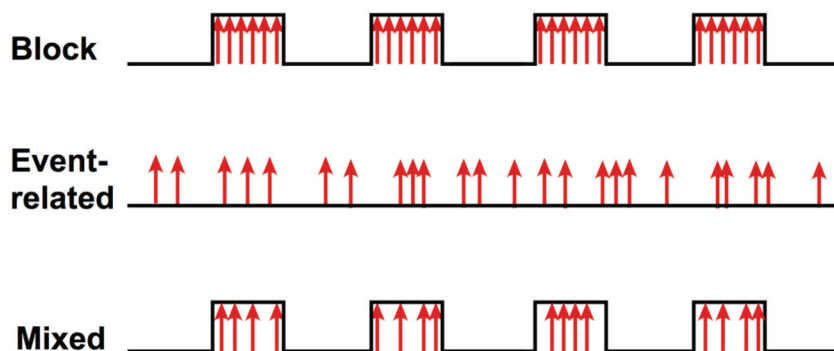


Figure 1.12: Three task fMRI experimental designs: Block, Event-Related and Mixed. (Courtesy of Allen D. Elster, MRIquestions.com).

## 3.5 Resting-state fMRI

As opposed to task-based fMRI, resting-state fMRI is acquired without a paradigm when the subject is at rest. The first evidence that the brain presents spontaneous activity at rest, was observed in 1995 by Biswal and colleagues [Biswal *et al.* (1995)]. They measured a correlation of low frequency time courses ( $<0.1$  Hz), between sensorimotor cortex and supplementary motor cortices at rest. Some years later, Raichle *et al.* observed during a mental task a brain energy consumption less than 5% more of its baseline energy [Raichle *et al.* (2001), Raichle and Gusnard (2001)]. This low

activity suggests the existence of a default brain function that is constantly active while this activity is diminished during specific tasks.

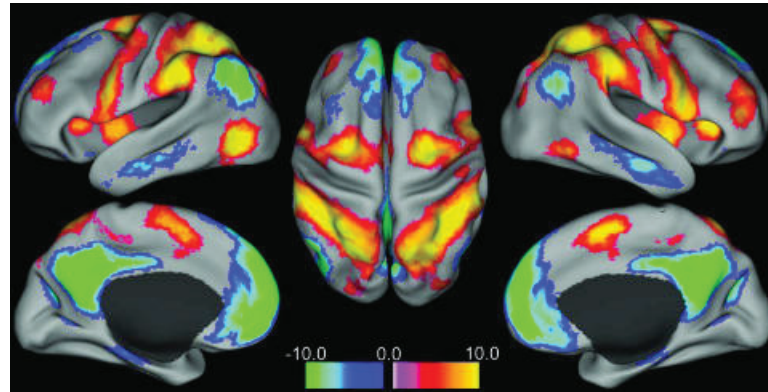


Figure 1.13: Two functional networks: nodes in warm colors are significantly correlated with task-positive seeds and significantly anticorrelated with task-negative seeds, while nodes in cold colors are significantly correlated with task-negative seed regions and significantly anticorrelated with task-positive seed regions. [Fox *et al.* (2005)]

In 2005, Fox *et al.* demonstrated that two anticorrelated functional networks, normally observed during cognitive tasks, are present also in the absence of any other task. This dichotomy is then intrinsic to the brain: one network is named task-positive network because composed of regions exhibiting activation during a task while the other is the task-negative network because consisting in regions that exhibit deactivation during a task. Resting-state network is composed of at least 20 distinct patterns of brain connections similar to networks of task-induced activations and deactivations. The most important include the default mode network (DMN) (involved with introspection and mind wandering), the salience network (involved in detecting and filtering salient stimuli), the central executive network (involved in high level cognitive functions), the dorsal attention network, the sensory motor network (SMN), and the visual and the auditory networks.

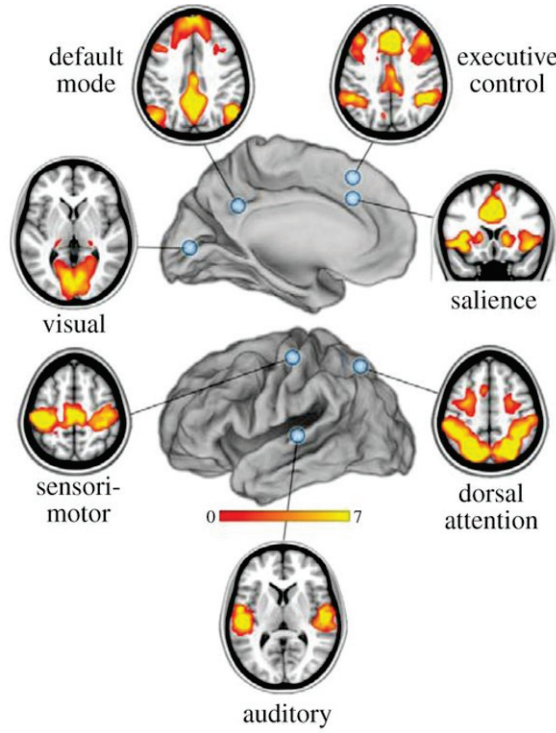


Figure 1.14: The most important resting-state networks [Raichle (2011)].

## 4 Diffusion MRI

### 4.1 Physic principle

Diffusion is the spontaneous movement of the water molecules when they are agitated by thermal energy. This phenomenon is also named *Brownian motion*, in honor of Robert Brown, the first to describe this movement in 1828 [Brown (1828)] observing spontaneous movement of pollen particles in water. The mathematical formalization of the diffusion was introduced in the 19th century by Adolph Fick's laws. For the first law, the flux of particles ( $J$ ) is directly proportional to the concentration gradient ( $\nabla C$ ) by the diffusion coefficient  $D$ .

$$J = -D\nabla C \quad (1.11)$$

Fick's second law is a partial differential equation describing the spatio-temporal evolution of the concentration:

$$\frac{\partial C}{\partial t} = D \frac{\partial^2 C}{\partial x^2} \quad (1.12)$$

In 1905, Albert Einstein demonstrated these laws by connecting Fick's diffusion coefficient ( $D$ ) with the statistics of Brownian motion. He also defined the diffusion

coefficient ( $D$ ) as being directly proportional to the absolute temperature ( $T$ ) and Boltzmann constant ( $k_B$ ):

$$D = \frac{k_B T}{6\pi\eta r} \quad (1.13)$$

where  $\eta$  is the viscosity of the medium and  $r$  is the radius of the particles.

## 4.2 Acquisition sequences

Measuring the Brownian movement of water in a tissue, we can obtain diffusion-weighted images (DWI). In the mid-1960's, Edward Stejskal and John Tanner introduced the pulsed gradient spin-echo (PSGE) sequence [Stejskal and Tanner (1965)], applying to a spin-echo sequence two symmetric diffusion gradients on either side of the  $180^\circ$ -pulse. These diffusion gradients can take three encoding directions providing a specific diffusion-weighted direction, corresponding to the encoding coordinate system. The first of these gradients changes the phase of the spins by an amount that depends on their location. If the spins have not moved during the diffusion time  $\Delta$  which is the time between the application of the two gradients ( $\delta$ ), the second gradient will completely rephase them and their signal will not be changed. If the spins have diffused, they will be not rephased with the second gradient: the more they have moved, the less they are rephased (Figure 1.15).

The signal ( $S(b)$ ) will be attenuated following the equation:

$$S(b) = S_0 e^{-bD} \quad (1.14)$$

where  $S_0$  is the initial signal,  $S(b)$  the intensity of the signal at echo time,  $D$  the diffusion coefficient. Finally,  $b$  is the measure of the gradient diffusion intensity that depends on the gyromagnetic ratio ( $\gamma$ ), the gradient diffusion duration ( $\delta$ ), and the diffusion time between the two gradients ( $\Delta$ ):

$$b = \gamma^2 G^2 \delta^2 \left( \Delta - \frac{\delta}{3} \right) \quad (1.15)$$

The measured diffusion coefficient  $D$ , also named Apparent Diffusion Coefficient (ADC), is used to refer to the mean diffusivity in a voxel.

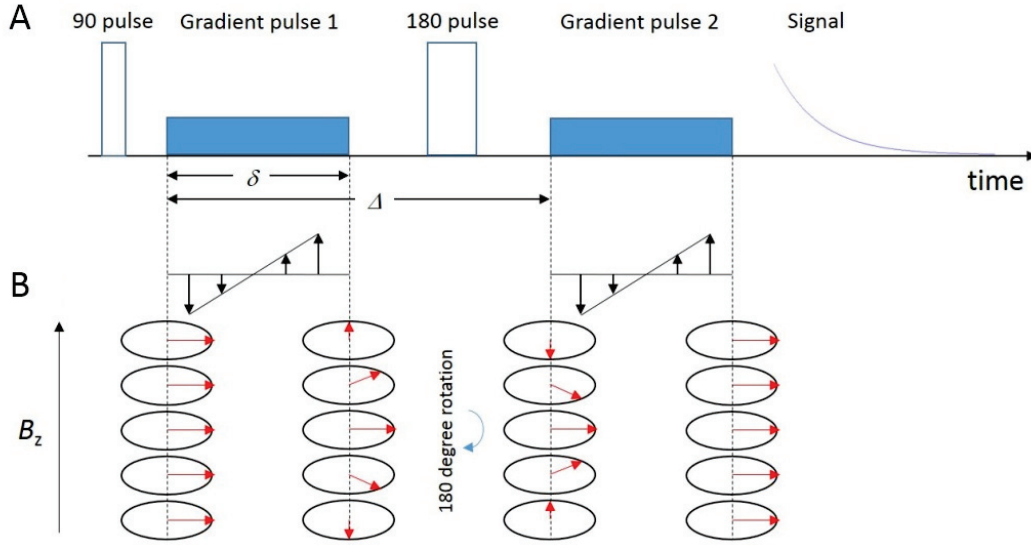


Figure 1.15: (A) Spin-echo imaging sequence diagram and (B) phase evolution of the spins at different locations along the gradient direction.  $\delta$  is the gradient diffusion duration and the  $\Delta$  is the diffusion time. The  $180^\circ$  pulse inverts the phase wrap produced by the first gradient pulse and the second gradient pulse, which is now identical to the first one in amplitude and length, completely refocuses this phase wrap.

### 4.3 Diffusion Tensor Imaging (DTI)

White matter is made of fiber tracts with different orientations, so water molecules are constrained by axonal membranes in the brain. Within these conditions, the diffusion is anisotropic and cannot be exhaustively described with a scalar diffusion coefficient ADC, but by a diffusion tensor  $D_{ij}$ . Introduced by Bassar in 1994, Diffusion tensor imaging (DTI) is a technique based on the hypothesis that diffusion in each voxel does not have a single direction, but follows a gaussian distribution [Basser *et al.* (1994)]. The equation 1.13 written with a diffusion tensor is the following:

$$J_i = -D_{ij} \frac{\partial C}{\partial_i} \quad (1.16)$$

and 1.14 becomes:

$$S(b) = S_0 e^{-\sum_{i=1}^3 \sum_{j=1}^3 b_{ij} D_{ij}} \quad (1.17)$$



where the tensors  $D_{ij}$  and  $b_{ij}$  are:

$$D_{ij} = \begin{pmatrix} D_{xx} & D_{xy} & D_{xz} \\ D_{yx} & D_{yy} & D_{yz} \\ D_{zx} & D_{zy} & D_{zz} \end{pmatrix}; b_{ij} = \begin{pmatrix} b_{xx} & b_{xy} & b_{xz} \\ b_{yx} & b_{yy} & b_{yz} \\ b_{zx} & b_{zy} & b_{zz} \end{pmatrix}. \quad (1.18)$$

From the equation 1.17 using the tensors we obtain:

$$\begin{aligned} \ln \left( \frac{S(b)}{S(b=0)} \right) &= -(b_{xx}D_{xx} + 2b_{xy}D_{xy} + 2b_{xz}D_{xz} + b_{yy}D_{yy} + 2b_{yz}D_{yz} + b_{zz}D_{zz}) \\ &= -\text{Trace}(bD) \end{aligned} \quad (1.19)$$

Since the diffusion tensor is symmetric, its diagonalization provides three eigenvectors ( $\epsilon$ ) and three eigenvalues ( $\lambda$ ):

$$D_{ij} = \begin{pmatrix} D_{xx} & D_{xy} & D_{xz} \\ D_{xy} & D_{yy} & D_{yz} \\ D_{xz} & D_{yz} & D_{zz} \end{pmatrix} = \begin{pmatrix} \lambda_1 & 0 & 0 \\ 0 & \lambda_2 & 0 \\ 0 & 0 & \lambda_3 \end{pmatrix} \begin{pmatrix} \vec{\epsilon}_1 \\ \vec{\epsilon}_2 \\ \vec{\epsilon}_3 \end{pmatrix} \quad (1.20)$$

The three eigenvectors define one major and two minor diffusion axes and the eigenvalues are proportional to the diffusion in the corresponding direction. So the optimal representation for the diffusion tensor is an ellipsoid with the main axis parallel to the principal diffusion direction and two other axes parallel to the two minor diffusion directions.

Diffusion eigenvalues allow to understand diffusion motion:

- $\lambda_1 \gg \lambda_2 > \lambda_3$ : anisotropic diffusion along  $\epsilon_1$  axis;
- $\lambda_1 \sim \lambda_2 \neq \lambda_3$ : anisotropic diffusion in the  $\epsilon_1 - \epsilon_2$  plane;
- $\lambda_1 \sim \lambda_2 \sim \lambda_3$ : isotropic diffusion.

From diffusion eigenvalues and eigenvectors combinations, different brain images can be created. The bigger eigenvalue ( $\lambda_1$ ) is the Axial diffusivity (AD) that shows the amount of water molecules diffusing along the main diffusivity axis. Radial diffusion (RD) is the average between the two small eigenvalues:

$$RD = \frac{\lambda_2 + \lambda_3}{2} \quad (1.21)$$

RD shows the diffusion in the  $\epsilon_2 - \epsilon_3$  plane perpendicular to the principal direction.



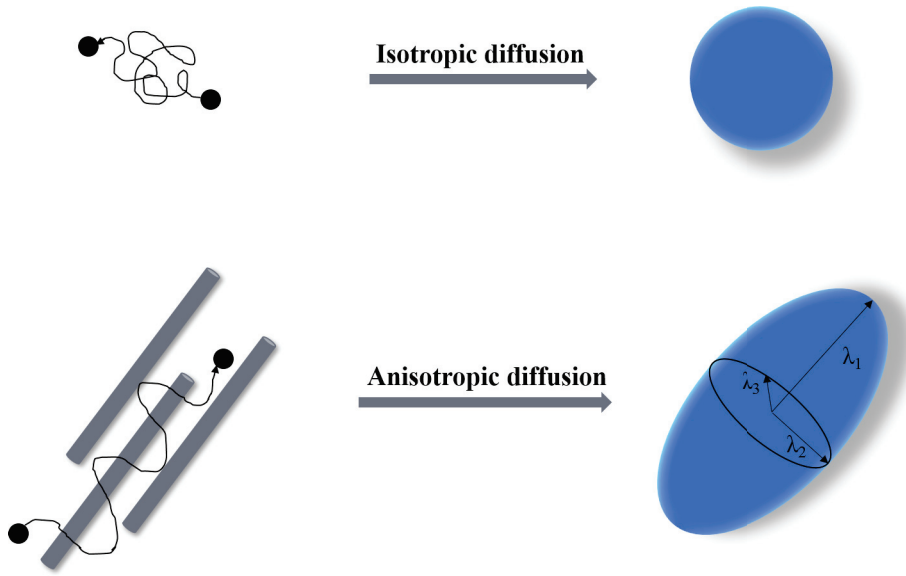


Figure 1.16: Isotropic diffusion versus anisotropic diffusion. The anisotropic diffusion is represented by an ellipsoid with three eigenvalues  $\lambda_1 \gg \lambda_2 > \lambda_3$ , while for isotropic diffusion the ellipsoid becomes a sphere with  $\lambda_1 \sim \lambda_2 \sim \lambda_3$ .

Mean diffusivity (MD), proportional to ADC, is the average of the three eigenvalues:

$$MD = \frac{\lambda_1 + \lambda_2 + \lambda_3}{3} \quad (1.22)$$

Fractional anisotropy (FA) measures the diffusion asymmetry within a voxel and is defined as:

$$FA = \sqrt{\frac{(\lambda_1 - \lambda_2)^2 + (\lambda_2 - \lambda_3)^2 + (\lambda_1 - \lambda_3)^2}{2(\lambda_1^2 + \lambda_2^2 + \lambda_3^2)}} \quad (1.23)$$

FA value varies between 0 and 1. In the case of isotropic diffusion ( $\lambda_1 \sim \lambda_2 \sim \lambda_3$ ), FA is 0. On the contrary, for anisotropic diffusion ( $\lambda_1 \gg \lambda_2 > \lambda_3$ ) FA tends to 1.

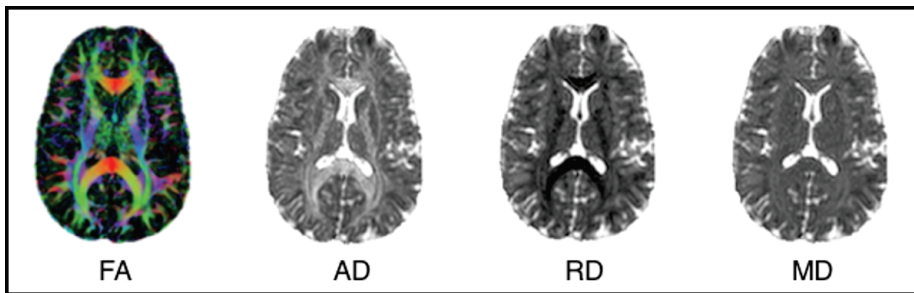


Figure 1.17: Examples of images acquired with DTI. From left to right FA, AD, RD, and MD weighted images. Data acquired at CERMEP.

## 4.4 Tractography technique

White matter axons are wrapped inside a membrane sheet composed of a lipid-rich substance, called myelin, which increases the signal transmission speed along the axon (Figure 1.18). The arrangement of nerve fibers into bundles promotes water diffusion along the direction parallel to the fibers due to the restriction of water diffusion caused by myelin and the cell walls of the axons. This ability to estimate fiber-bundle orientation within a voxel allows *in-vivo* estimation of white matter fiber tracts that have been validated with *postmortem* dissections [Pierpaoli *et al.* (1996)].

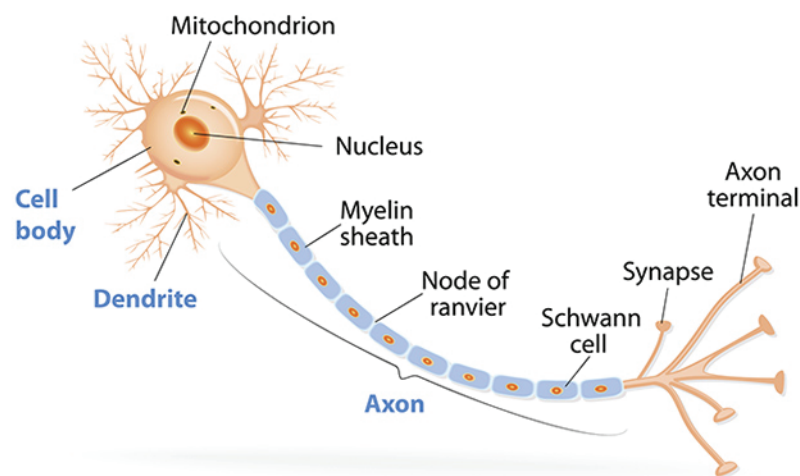


Figure 1.18: Diagram of a neuron with a myelinated axon (adapted from wikipedia).

Once the principal direction of water diffusion is estimated in each voxel, the direction of white matter fibers can be estimated by tractography technique. Tractography is a modeling technique used to reconstruct white matter tract in 3D from voxelwise data by estimating curvature of streamlines extracted from the principle eigenvector of adjacent voxels [Catani *et al.* (2002)]. It can be obtained, either applying deterministic or probabilistic techniques. On one hand, deterministic tracking reconstructs a fiber from a seed voxel to the next until stopping criteria are verified [Mori *et al.* (1999)]. On the other hand, probabilistic tractography reconstructs several paths from a seed voxel to the next through random direction and iterating this process until the probabilistic maps of streamlines is obtained [Parker and Alexander (2003)]. While, the first method is very fast, the second one allows the reconstruction of the full tractogram.

In spite of DTI is the most used reconstruction technique for diffusion MRI, it is limited by the gaussian model used for the description of water diffusion probability. Since the voxel resolution is much higher than the axon resolution, in each voxel there

are several axons with different direction. Allowing to estimate only one diffusion direction for each voxel, gaussian distribution can not reproduce the tractography in voxel with crossing fibers. Thus, more general mathematical models are needed (Figure 1.19).

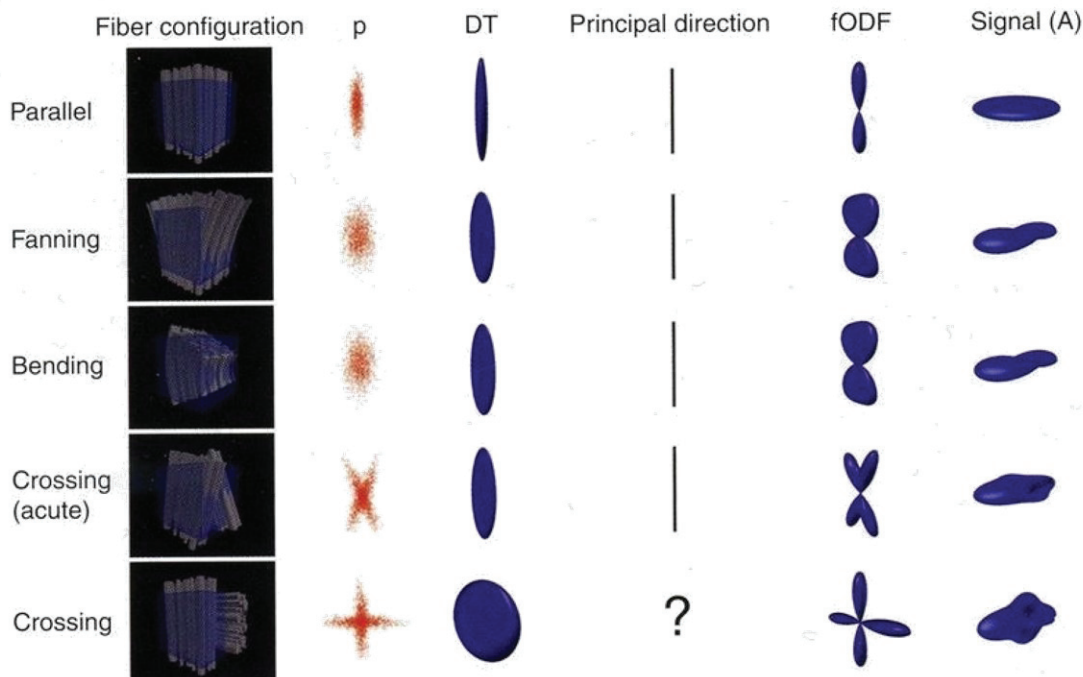


Figure 1.19: Examples of different possible fiber configurations in white matter and for each configuration the following information are showed: diffusion probability ( $p$ ) along the three directions, diffusion tensor (DT), principal direction obtained from DT, fODF, and diffusion signal (adapted from [Johansen-Berg and Behrens (2009)])

In order to overcome this limitation, several models, parametric and non-parametric have been proposed. For the purpose of this thesis, only non-parametric models were used and will be introduced in the following sections. These methods permit the computation of water molecule displacement probabilities over a sphere and these probabilities are called the fiber orientation distribution functions (fODF). fODF can be estimated applying different methods: some of them use DTI signal for fODF estimation such as the spherical deconvolution [Tournier *et al.* (2004), Tournier *et al.* (2007)], while DSI [Tuch *et al.* (2002)] and Q-Ball [Tuch (2004)] use an other spherical function that measures diffusion probability along different directions. These last two techniques provide only diffusion ODF (dODF) and not fODF that is obtained instead with spherical deconvolution methods [Tournier *et al.* (2004)]. This technique is based on the hypothesis that diffusion MRI signal in a voxel is the convolution of its fiber population signal and the fiber ODF.

The most used method [Tournier *et al.* (2004)] estimates a response function from the average signal of voxels presenting the highest anisotropy in the whole brain. Finally, a simple diffusion signal deconvolution from the response function allows to obtain fODF (Figure 1.20).

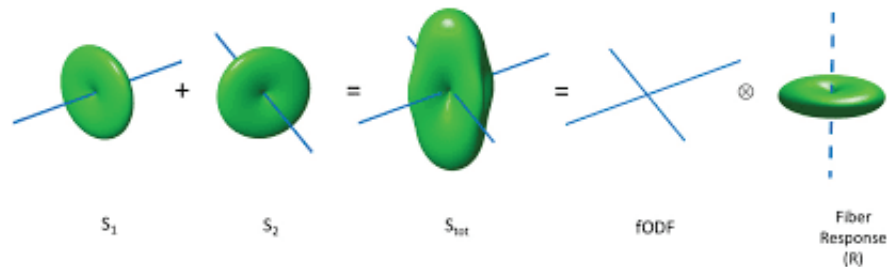


Figure 1.20: Spherical convolution illustration: voxel diffusion signal ( $S_{tot}$  is composed by signals of multiple fibre populations ( $S_1$  and  $S_2$ ) within it. Under the assumption of a common fibre signal profile (fODF), it is also the convolution of fODF with the fiber response function (R) (adapted from wikipedia).



# Chapter 2

---

## Brain connectivity

---

### Contents

---

<b>1</b>	<b>Introduction . . . . .</b>	<b>34</b>
<b>2</b>	<b>Graph theory . . . . .</b>	<b>35</b>
2.1	Graph definition . . . . .	36
2.2	Graph properties . . . . .	36
<b>3</b>	<b>Graph metrics . . . . .</b>	<b>38</b>
3.1	Nodal metrics . . . . .	38
3.2	Global metrics . . . . .	40
3.3	Hub disruption index . . . . .	41
<b>4</b>	<b>Matrix notation . . . . .</b>	<b>42</b>
<b>5</b>	<b>Brain graph topology . . . . .</b>	<b>43</b>
<b>6</b>	<b>Brain connectivity with MRI . . . . .</b>	<b>45</b>
6.1	Brain parcellation . . . . .	45
6.2	Connectivity matrix . . . . .	45

---

# 1 Introduction

As presented in section 4.3, a recent approach for exploring brain is the connectionism theory. The major idea is that brain regions are specialized for particular tasks, but the higher level functions require the coordination among the brain areas that are connected through the long fiber-bundles of the brain.

The history of brain connectivity research starts with the description of the structure of the nervous system and especially of the brain by Santiago Ramón y Cajal [Ramon y Cajal and Azoulay (1911)]. He illustrated the cellular connections in the brain proving that each brain unit interacts with others through their connections in order to perform some tasks. These units can be at three different levels [Sporns *et al.* (2005)]:

- at micro-scale brain: brain units are represented by single neurons;
- at meso-scale: neuronal populations are studied;
- at macro-scale: brain units are the connections between different brain regions.

In this work, we are interested in describing the brain connectivity at the macro-scale. The connections between different regions can be studied using modern imaging techniques like MRI, electroencephalography [EEG], or positron emission tomography [PET].

Considering the brain subdivision into brain areas, it could be studied as a network with brain areas as "nodes" and the communication between the regions as "edges". We will then focus on brain connectivity networks obtained with MRI and the brain connectivity will be studied using the graph theory. Starting from mathematical problems solving, graph theory has become a common tool to model biological and physical, as well as real life problems. The most common examples of graph theory application in social life are: airline networks, banking networks, social networks, physician networks, supply chain networks, as well as protein networks. Details of nodes and edges for each of these networks are explained in Table 2.1. The application in cerebral connectivity started when it has been demonstrated that the neural networks presents a graph organization [Eguíluz *et al.* (2005)], with small-world topological properties [Achard *et al.* (2006)].

NETWORK	NODES	EDGES
Airlines Network	Airports	Airplanes / Routes
Banking Network	Account Holders	Transactions
Social Network	Users	Interactions
Physician Network	Doctors	Patients
Supply Chain Network	Warehouses	Trucks
Protein Network	Protein	Protein-Protein Interactions

Table 2.1: Example of six common networks in real life. For each of them, nodes and edges for the application of graph theory are specified.

## 2 Graph theory

Graph theory is a mathematical branch that describes how objects are connected between them, representing these relationships with a graph.

It was applied for the first time in the 18th century by the mathematician Leonhard Euler. He tried to solve the "konigsberg bridge problem" answering to the question "*was it possible to take a walk through the town in such a way as to cross over every bridge once, and only once?*".

Euler represented this problem with a graph in which the nodes were the four bodies of land (A, B, C, and D in Figure 2.1), and the edges, the seven bridges (a, b, c, d, e, and f in Figure 2.1). He concluded that for the bridge physical arrangement there was no solution to the problem.

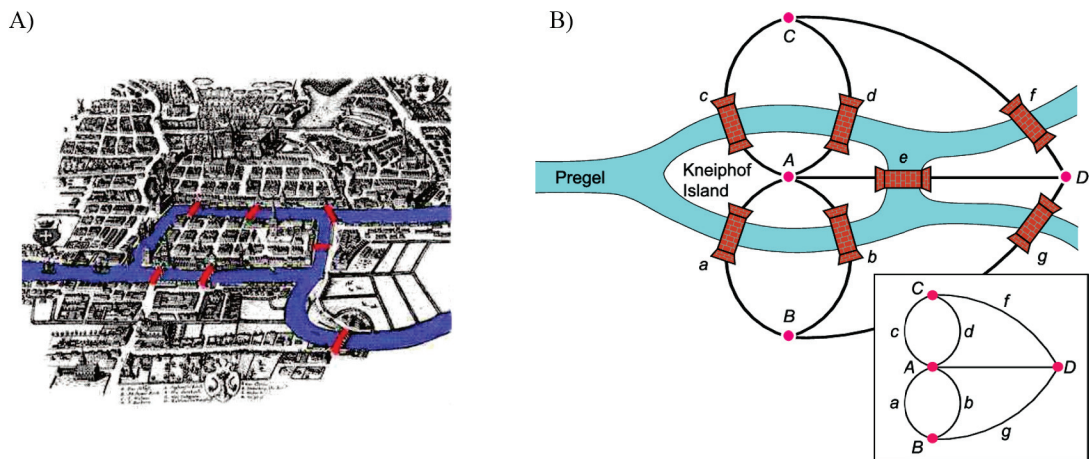


Figure 2.1: Representation of the Euler's problem. (A) The map of the ancient Prussian city of Königsberg with its seven bridges across the river Pregel. (B) Euler's representation of the problem by a graph that helps to realize that it is not possible to visit all the nodes passing on each edge only once. Figure adapted from [Toroczkai (2005)].

Indeed, he observed that, since a bridge connected two land masses, if you have to



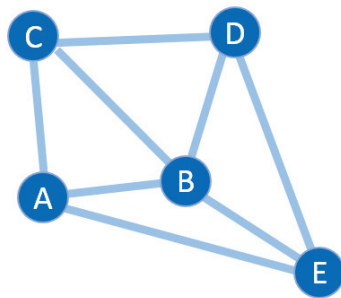
reach and then live one of them without crossing a bridge twice, then the number of bridges connecting each land should be even. In the "konigsberg bridge problem" the four vertices had odd number of edges, therefore he concluded that it was impossible to have a walk crossing every bridge only once.

From this observation, a graph in which each node has even edges is defined the "Euler path".

## 2.1 Graph definition

A graph is defined as *an ordered pair*,  $G=(V,E)$  (Figure 2.2), where:

- $V$  is a set of vertices or nodes;
- $E$  is a set of edges or links.



**$V: \{A, B, C, D, E\}$**   
 **$E: \{AB, AC, BC, BD, BE, CD, DE, EA\}$**

Figure 2.2: Example of a simple graph  $G=(V,E)$ , with five nodes  $V=A, B, C, D, E$  and eight edges that link the nodes  $E=AB, AC, BC, BD, BE, CD, DE, EA$ .

## 2.2 Graph properties

Based on its properties, different types of graph can be identified:

- undirected graph, when there is no preferential direction in the connections (Figure 2.3 on the left);
- directed graph, when there is a preferential direction in the connections (Figure 2.3 on the right);
- an unweighted graph, when the nodes or the edges do not have an assigned weight (Figure 2.4 on the left);

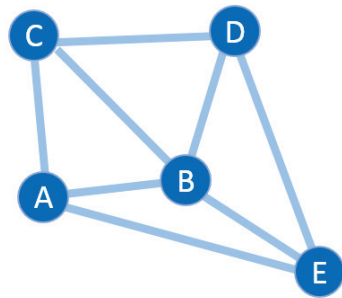
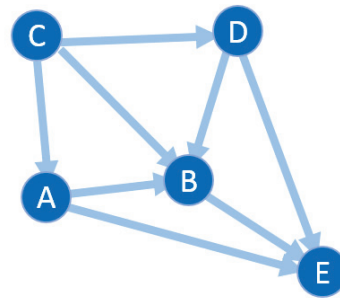
**Undirected Graph****Directed Graph**

Figure 2.3: Example of undirected graph (on the left), and directed graph (on the right).

- a weighted graph, when the nodes or the edges have an assigned weight (Figure 2.4 on the right);

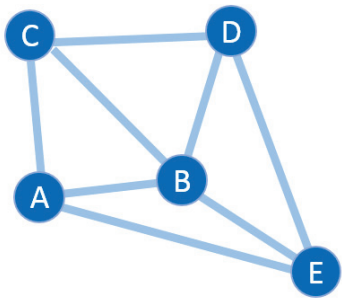
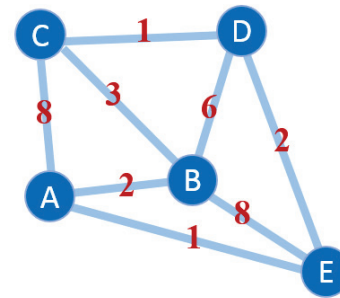
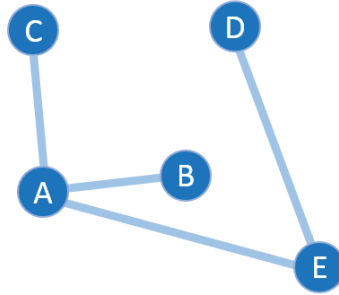
**Unweighted Graph****Weighted Graph**

Figure 2.4: Example of unweighted graph (on the left), and weighted graph with a different weight for each connection (on the right).

- a fully connected graph, when all nodes are connected at least to an other node (Figure 2.5).



**V:** {A, B, C, D, E}  
**E:** {AB, AC, DE, EA}

Figure 2.5: Example of fully connected graph, with all nodes having at least one connection.

### 3 Graph metrics

The graph topology can be described measuring metrics at different scales: at the scale of the entire graph, the so-called **global metrics** or at the scale of the node, the **nodal metrics**. The graph metrics allow to characterize three main graph properties:

- **integration properties** relate to the way that the information propagate in the graph, is based on the measure of the distance (Figure 2.6)
- **segregation properties** reflect how a graph is divided into different modules (Figure 2.7)
- **centrality properties** or hubness measure the importance of a node for the communication in the graph (Figure 2.7)

These three properties can be described by global or nodal metrics.

#### 3.1 Nodal metrics

Nodal metrics are computed for a single node and measure the properties of each node. The main nodal metrics are showed in this section.

The **degree** of a node  $i$  ( $k_i$ ) is defined as the number of connections of the node  $i$  with the other nodes of the graph:

$$k_i = \sum_{j \in N} A_{ij} \quad (2.1)$$

where  $N$  is the set of all nodes in the network and  $A_{ij}$  is the connection between nodes  $i$  and  $j$ .

The **minimum path length** is the minimum number of edges that must be traversed to go from one node to another. In Figure 2.6, the shortest path to go from the extreme node on the left to the extreme node on the right is 4.

The **efficiency** is the average of the inverse of the distance

$$E_i = \frac{1}{n} \sum_{j \in N, j \neq i} \frac{d_{ij}^{-1}}{n-1}. \quad (2.2)$$

These three nodal metrics reflect the integration properties (Figure 2.6).

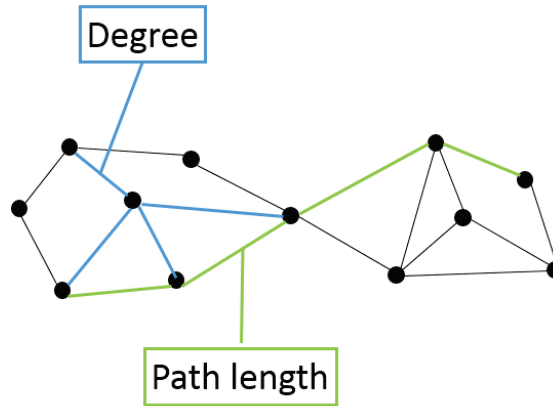


Figure 2.6: Graphical representation of two integration metrics: the degree (blue), and the minimum path length (green). Adapted from [Sporns].

The **clustering coefficient** measures the density of connections between the node's neighbors given from the number of triangles ( $t$ ) around a node. It reflects thus local segregation property.

$$C_i = \frac{2t_i}{k_i(k_i - 1)} \quad (2.3)$$

The **betweenness centrality** is the main nodal metric that reflects the centrality of a node and it is defined as:

$$b_i = \frac{1}{(n-1)(n-2)} \sum_{\substack{j, h \in N, \\ h \neq j, h \neq i, j \neq i}} \frac{\rho_{hj}(i)}{\rho_{hj}}, \quad (2.4)$$

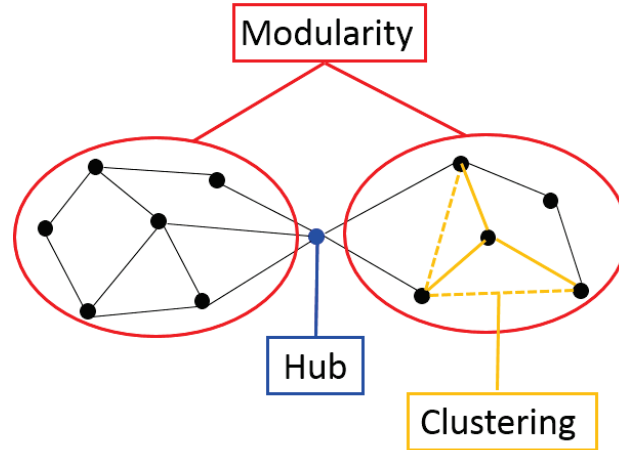


Figure 2.7: Graphical representation of segregation and hubs metrics. Two modules, that are limited by red lines, communicate between them thanks to a hub node that is highlighted in blue. In the second module, the clustering coefficient is coloured in orange. Adapted from [Sporns].

where  $\rho_{hj}$  is the shortest path length between the nodes  $h$  and  $j$  and  $\rho_{hj}(i)$  is the shortest path length between the nodes  $h$  et  $j$  passing throughout  $i$ .

## 3.2 Global metrics

Global metrics characterize the whole network with a single value. We present in this paragraph the main global metrics used in this thesis.

The **modularity** is a global metric that reflects segregation properties and defined as

$$Q = \sum_{u \in M} [e_{uu} - (\sum_{v \in M} e_{uv})^2] \quad (2.5)$$

where  $M$  is the number of modules of the network,  $e_{uv}$  is the edges connecting the nodes of the module  $u$  with that of the module  $v$ .

The **transitivity** is a variant of the global clustering coefficient:

$$T = \frac{\sum_{i \in N} 2t_i}{\sum_{i \in N} k_i(k_i - 1)} \quad (2.6)$$

A graph with a strong transitivity is composed by modules within which the nodes are very connected between them, but only a few connection allow the communication between different modules.

The **assortativity** is the Pearson correlation between the degree of the nodes:

$$r = \frac{l^{-1} \sum_{(i,j) \in L} k_i k_j - [l^{-1} \sum_{(i,j) \in L} \frac{1}{2}(k_i + k_j)]^2}{l^{-1} \sum_{(i,j) \in L} \frac{1}{2}(k_i^2 + k_j^2) - [l^{-1} \sum_{(i,j) \in L} \frac{1}{2}(k_i + k_j)]^2}. \quad (2.7)$$

where  $L$  is the set of all links in the network.

The **characteristic path length** is the average of the distance matrix of the graph:

$$CPL = \frac{1}{n} \sum_{i \in N} L_i = \frac{1}{n} \sum_{i \in N} \frac{\sum_{j \in N, j \neq i} d_{ij}}{n-1} \quad (2.8)$$

where  $n$  is the number of nodes,  $L_i$  is the minimum path length between the node  $i$  and all the others and  $d_{ij}$  is the shortest distance between the node  $i$  and the node  $j$ .

### 3.3 Hub disruption index

Introduced by Achard et al. [Achard *et al.* (2012)], the "Hub Disruption Index" ( $\kappa$ ) describes the topological changes of an individual subject brain networks with respect to a referential networks topology from a group of reference subjects. In this work, this index is measured in two groups with different intelligence quotient: Standard intelligence quotient group represents the referential group, and High intelligence quotient (HIQ) group is the population to study. To understand how this index is defined, consider a nodal metric, for example the degree, and plot the degree value of each node for a SIQ subject against the average degree of the corresponding nodes in the SIQ group (Figure 2.8.A). We can observe that the distribution of the points falls approximately on a positive slope line ( $y = x$ ). This happens because for a SIQ subject, the nodal metric values are close to the average value for the same node computed in the SIQ group. Constructing the same plot for a HIQ subject, we can observe that the points have a different distribution (Figure 2.8.B), so they are not well predicted by the SIQ average degree.

$\kappa$  is defined following the following steps. First, the SIQ group mean metric of each node is subtracted from the metric of the corresponding node in an individual subject. Second, this difference is plotted against the SIQ group mean for all the nodes. Finally, the gradient of the linear regression that models this points is defined as  $\kappa$ . According to this definition, data of a SIQ subject will scatter around a horizontal line ( $\kappa \sim 0$ ) (Figure 2.8.C), while for a HIQ subject data will follow a negative slope ( $\kappa < 0$ ) (Figure 2.8.D).

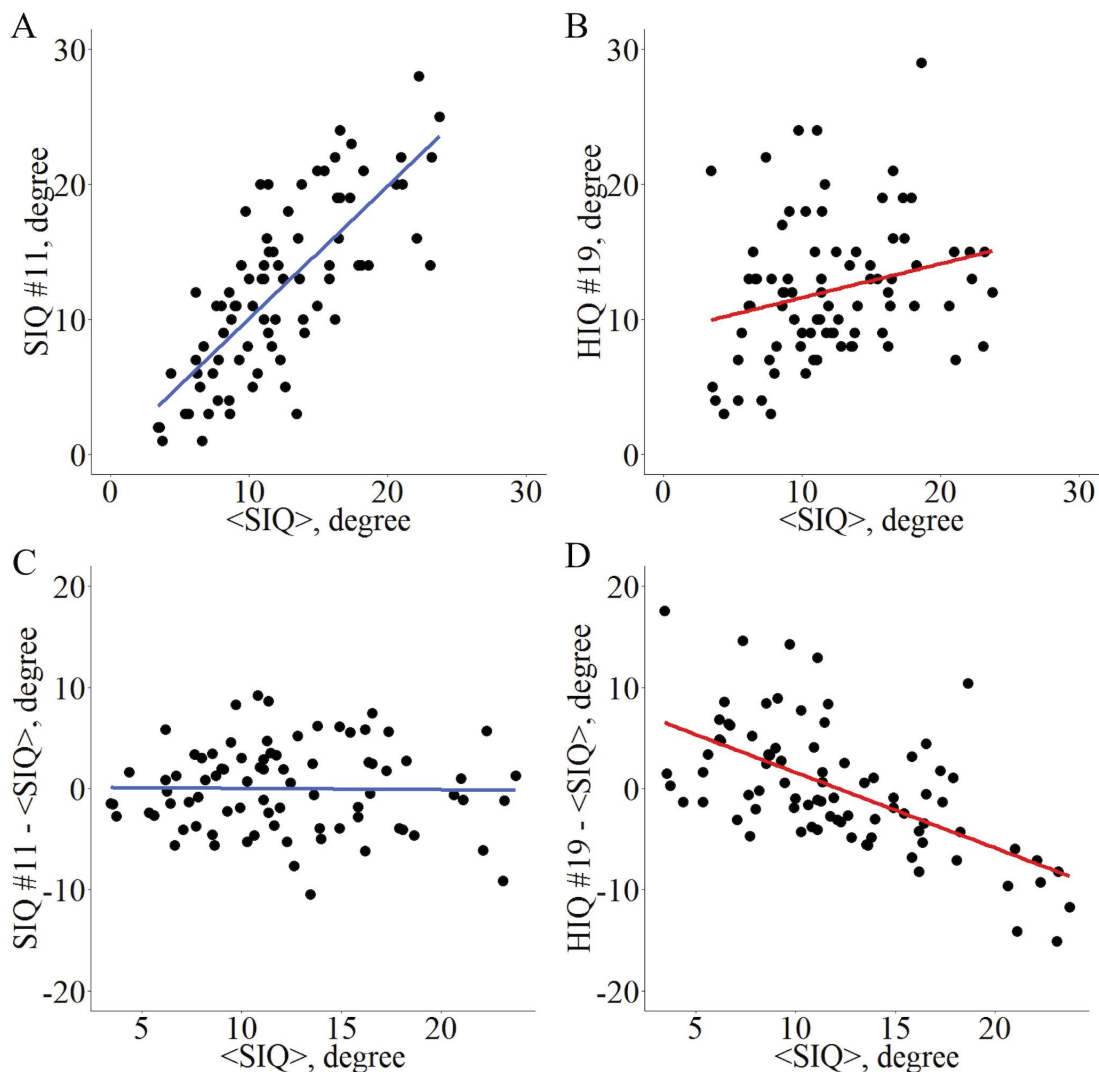


Figure 2.8: Hub disruption index  $\kappa$  computation for nodal degree metric: nodal degree of an individual subject in relation to the degree average of the standard intelligence quotient (SIQ) group (A) for one standard intelligence quotient (SIQ) child and (B) for one high intelligence quotient (HIQ) child. The mean nodal degree of the SIQ group is subtracted from the degree of the corresponding node in an individual subject and then this individual difference is plotted against the SIQ group mean.  $\kappa$  is the slope of the regression line computed on this scatter plot. Based on this definition, the data for a SIQ child (C) will be scattered around a horizontal line ( $\kappa \sim 0$ ), whereas the data for a HIQ child (D) will be scattered around a negatively sloping line ( $\kappa < 0$ ).

## 4 Matrix notation

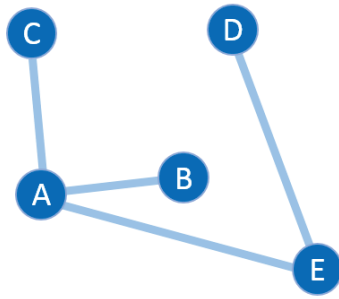
The mathematical representation of a graph is a square matrix in which rows and columns are both labelled as the set of vertices. Inside the matrix, the connection between each pair of nodes is showed at the intersection between the row and the

column corresponding to the two nodes.

A particular type of matrix is the **adjacency matrix**. In an adjacency matrix, the intersection between two nodes shows 1 if they are adjacent, and 0 if they are not.

In a mathematical description, an unweighted graph  $G=(V,E)$  is represented by a  $|V| \times |V|$  matrix  $M$  with:

- $M_{i,j} = 1$  if the nodes  $i$  and  $j$  are connected;
- $M_{i,j} = 0$  if the nodes  $i$  and  $j$  are not connected.



**V:** {A, B, C, D, E}  
**E:** {AB, AC, DE, EA}

	A	B	C	D	E
A	0	1	1	0	1
B	1	0	0	0	0
C	1	0	0	0	0
D	0	0	0	0	1
E	1	0	0	1	0

Figure 2.9: Example of a graph  $G=(V,E)$  on the left of the image and its adjacency matrix on the right.

## 5 Brain graph topology

Depending on its connections distribution, a network may present a specific structure that is characterized by peculiar properties. Two graph metrics that highlight the structure differences are the clustering coefficient and the path length.

At one extreme of the topology there are regular graphs. Since the number of connections of each node with the others is the same, these graphs are characterized by a very low heterogeneity and randomness. The dense connections between the nodes tend to divide the graph into groups and it is reflected by a high clustering coefficient and long average path. Figure 2.10 shows on the left a typical diagram of a regular graph, well ordered with homogeneous connections. On the opposite, there are random graphs. They are constructed by choosing a number of nodes  $n$  and joining pairs of them together until a number of  $m$  connections is reached. The



resulting diagram is a snarl of criss-crossed lines as shown on the right of Figure 2.10. An example of random graph is the computer network and they are characterized by a low clustering coefficient and short average paths in this structure.

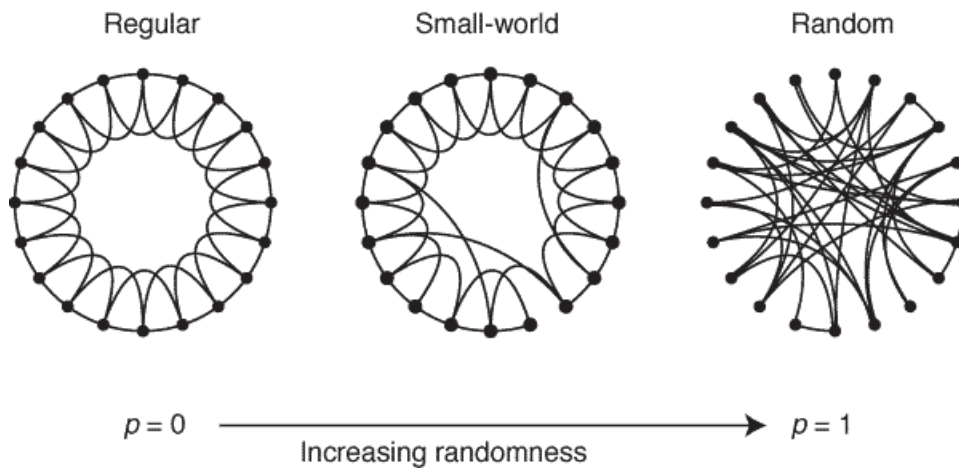


Figure 2.10: Graphical representation of three different graph topologies. A regular graph (on the left), a random graph (on the right), and a small-world graph (in the middle). Image taken from [Watts and Strogatz (1998)].

Obviously, real-world networks cannot be neither regular nor random. On one hand, the regular graphs do not favor the information change between distant nodes. On the other hand, the numerous long distance connections of the random networks lead to a high graph cost. The model that can describe the networks present in nature is an intermediary model named "small-world" network [Watts and Strogatz (1998)]. The idea of the small-world network is simple to explain in the social interaction context. Each person has a group of close friends that are friends with each other as well. If we will know other people in a distant city, we may discover that some of them are socially connected with the previous group of friends. This relationship network represents a small world model and it was quantitatively translated by Watts and Strogatz in 1998 as a network in which the connections between the nodes in a regular graph were rewired with a certain probability. In this way, they have a higher cluster number than the random networks, but they are directly connected also with distant networks. Several biological networks present these properties, and in particular it has been demonstrated that the brain network is a small-world network [Bassett and Bullmore (2006), Eguíluz *et al.* (2005)].

## 6 Brain connectivity with MRI

The characterization of the brain network topology is an important issue in neuroscience. It can reveal structural and functional organization that can explain the information transfer throughout the human brain [Sporns and Zwi (2004)].

As it has been described in the previous sections of this chapter, the brain network is represented by a graph that is a set of nodes linked between them with some connections. The study of the brain connectivity is based on the choice of nodes and their connections.

### 6.1 Brain parcellation

In brain networks, different choices can be made for the definition of the nodes. We can consider each voxel as a node, or we can define the nodes as the brain regions obtained from the segmentation of the cortical and sub-cortical gray matter. Indeed, the number of nodes and their size depend on the atlas that has been chosen for the parcellation. In this work, the nodes are labeled only using atlas segmentation. The most used atlas in literature are:

- AAL anatomical scheme of [Tzourio-Mazoyer *et al.* (2002)], composed of 89 regions plus cerebellum;
- Desikan Killiany parcellation [Desikan *et al.* (2006)], composed of 84 regions obtained from probabilistic information estimated from a manually labeled training set;
- Destrieux atlas [Destrieux *et al.* (2010)], composed of 74 regions for each hemisphere;
- Harvard-Oxford probabilistic atlas [Makris *et al.* (2006)], covering 48 cortical and 21 subcortical structural areas for each hemisphere, derived from structural data.
- Glasser atlas derived from Human Connectome Project (HCP) data [Glasser *et al.* (2016)], composed of 180 areas in each hemisphere.

### 6.2 Connectivity matrix

The edges that link the nodes, instead, derive from the MRI sequence used. According to them, they can provide three different brain connectivity: morphological, structural and functional brain connectivity (Figure 2.11).

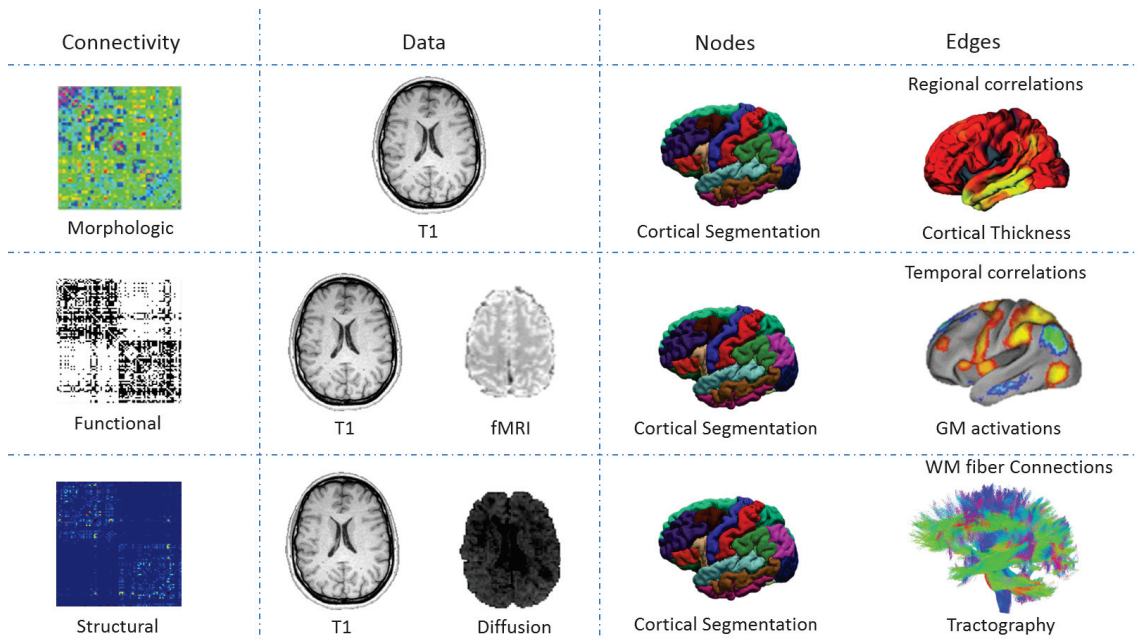


Figure 2.11: Three brain connectivity measures. First, in morphological connectivity, the connections between the nodes are obtained from cortical GM thickness correlations. Second, functional connectivity is estimated from temporal correlations of BOLD signals between regions. Third, structural connectivity is calculated from WM fibers obtained from tractography.

**Morphological connectivity** Morphological connectivity derives from anatomical measurements of *in-vivo* MRI. The characterization of the anatomical network reveals intrinsically structural organizational principles in the human brain. Morphometric based correlation networks have been commonly constructed using divergent structural measurements such as cortical thickness, cortical surface area, and gray matter (GM) volume. In this section, cortical thickness was chosen to explore brain connectivity. Some studies demonstrated that association in cortical thickness between different regions provides information about human brain connectivity [Lerch *et al.* (2006), He *et al.* (2007)]. Indeed, this morphometric feature reflects the size, density, and arrangement of cells in the brain [Narr *et al.* (2005)]. It has been demonstrated that correlation between thickness values are characterized by high clustering coefficient and short path length reflecting a small-world topology [He *et al.* (2007)].

In order to explore morphological brain connectivity first, the cortical thickness of each region can be measured applying different computation algorithm. Second, the Pearson's correlation between the cortical thickness of each pair of region is computed. Two regions are considered connected if the correlation between their cortical thickness measurement is significant across all the population studied. Once

obtained the matrix of the significant correlations, an undirected graph can be constructed from the thresholded correlation matrix. This procedure is shown in Figure 2.12.

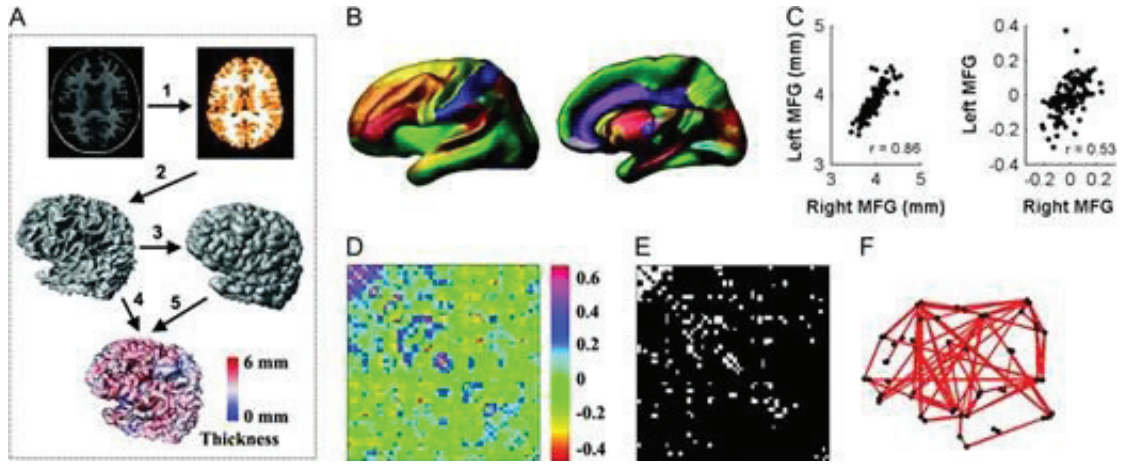


Figure 2.12: Example of a pipeline for obtaining morphological connectivity matrix from [He *et al.* (2007)]. (A) Cortical thickness estimation from the anatomical MRI: the inner and outer surfaces were extracted and finally cortical thickness was measured at each vertex; (B) cerebral cortex segmentation; (C) Significant correlations between cortical thickness measurement of two brain regions; (D) Correlation matrix across all the population; (E) Anatomical correlation matrix obtained from the thresholded correlation matrix; (F) Graph representation of morphological correlation matrix. Adapted from [He *et al.* (2007)].

**Functional connectivity** Functional connectivity refers to synchronization level of neuronal activity of different brain regions [Friston *et al.* (1993)] that can be captured in BOLD signal during resting-state fMRI acquisitions. It is defined as the statistical correlations between time-series recorded in two brain regions. The first work that explored functional correlations was conducted by Biswal and colleagues [Biswal *et al.* (1995)] using resting-state fMRI. Measuring the correlation between time course of a seed region of interest (ROI) in the motor area and time course of all other voxels, they demonstrated the functional connectivity between left and right regions of primary motor network. In the past few years, several studies examined the whole-brain functional connectivity demonstrated that at rest the brain is organized into different Resting-State Networks (RSNs) [Damoiseaux *et al.* (2006), Salvador *et al.* (2005)].

Functional connectivity is measured using different methods as like as seed-based, model-free and network analysis method, but in this work, only the third method is used. Many studies using graph methods have demonstrated that whole-brain functional networks exhibit effective small-world properties [Stam (2004), Salvador

*et al.* (2005), Achard *et al.* (2006), Van den Heuvel *et al.* (2008)]. In this thesis, we used wavelets transformation to decompose fMRI time-series obtained for cortical and subcortical brain regions. This technique realizes a time-scale decomposition that partitions the total energy of a signal over a set of compactly supported basis functions, or little waves, each of which is uniquely scaled in frequency and located in time [Akansu and Haddad (2001), Bullmore *et al.* (2004)]. Then, the maximal overlap discrete wavelet transform (MODWT) was applied to each regional mean time-series and Pearson's correlations between wavelet coefficients were estimated at each decomposition scale (Figure 2.13).

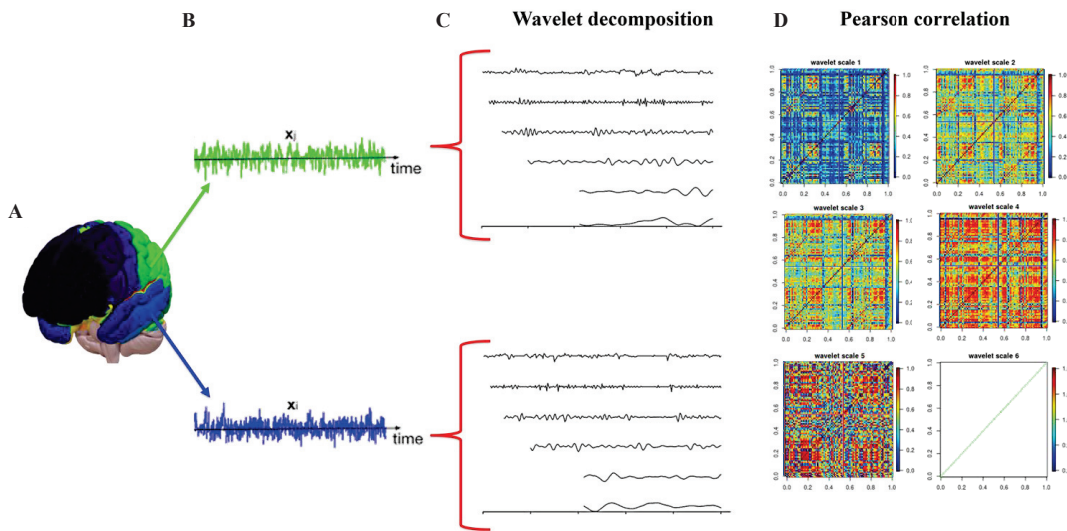


Figure 2.13: Representation of graph generation from functional connectivity. After brain parcellation (A), time-series of brain regions are extracted (B), each time-series is decomposed using wavelet transformation (C), and finally, the Pearson correlation between each pair of nodes is computed for all the wavelets scales (D).

**Structural connectivity** The structural connectivity is based on modern MRI technique, namely DTI, that allows to reconstruct white matter tracts and to estimate the integrity and efficacy of the connections. Indeed, connection between regions is given from the number of WM fibers that link these regions. Once the brain regions are defined and DTI data are preprocessed, the direct fiber connections between two brain regions can be quantified in different ways, including mean FA [Beaulieu (2002)], mean diffusivity, and fiber count [Damoiseaux and Greicius (2009)]. This information is extracted applying tractography technique on DTI data. Connectivity matrices are generated by summing the number of streamlines connecting each pair of nodes (Figure 2.14). Several studies explored structural con-



nectivity topology using this technique and they found that the network exhibited small-world topology with high clustering and short path length [Iturria-Medina *et al.* (2007), Iturria-Medina *et al.* (2008), Hagmann *et al.* (2007)].

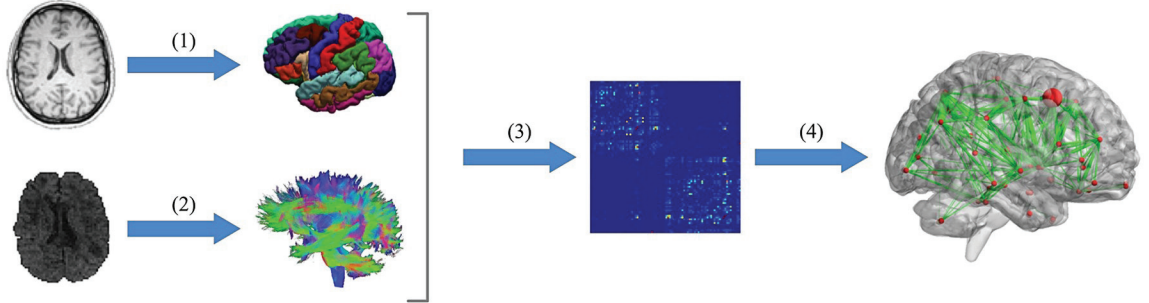


Figure 2.14: Representation of graph generation from structural connectivity. First, (1) the nodes are defined from an anatomical parcellation of the anatomical image. Second, (2) diffusion images are preprocessed and the tractography is generated. Third, (3) the connectivity matrix is created using the number of fibers that connect each pairs of nodes. From this matrix, structural connectivity graph of the brain is generated (4).

Since the structural connectivity matrix refers on the number of streamline, the graph properties depends on the total number of fibers that have been reconstructed in the brain. Indeed, a graph generated with a low fiber numbers will have a lower density than a graph generated with high fiber numbers. Graph measure, consequently, are not absolute measures and they can be compared only if the total fiber number of tractography is the same.



# Chapter 3

## Intelligence

---

### Contents

<b>1</b>	<b>Introduction . . . . .</b>	<b>52</b>
<b>2</b>	<b>g-Factor Model . . . . .</b>	<b>52</b>
<b>3</b>	<b>Other Models . . . . .</b>	<b>53</b>
<b>4</b>	<b>Intelligence Quotient (IQ) measure . . . . .</b>	<b>54</b>
<b>5</b>	<b>Wechsler Intelligence Scales . . . . .</b>	<b>55</b>
5.1	WISC-IV . . . . .	55
5.2	WAIS-IV . . . . .	56
<b>6</b>	<b>MRI application to intelligence . . . . .</b>	<b>57</b>
6.1	Early MRI studies . . . . .	57
6.2	The Parieto-Frontal Integration Theory (P-FIT) . . . . .	61
6.3	The role of brain connectivity in intelligence . . . . .	62

---



# 1 Introduction

Interest in human intelligence began thousands years ago, when the Greek philosopher Aristotle introduced the concept of reason. During the later centuries, lots of different definitions of intelligence have been proposed. They all share a single idea: intelligence is a general mental ability and it must have something to do with the brain [Haier (2016)]. Researchers developed measure of intelligence for empirical investigations using sophisticated statistical methods.

*"Intelligence is what intelligence tests measure." E. G. Boring*

Boring's 1923 definition is not really accepted from psychology community. Indeed, test scores do not measure intelligence but they estimate the general mental ability. Being influenced by many things, they are not perfect predictors. Nonetheless, they are necessary tools for research about intelligence.

## 2 g-Factor Model

Intelligence is actually the result of many abilities, each one estimated by a test. All these abilities are not independent, indeed they are all related to each other. This relationship is named structure of mental abilities and it is reported in figure 3.1. In this structure, there are 15 different tests that measure 5 mental abilities: reasoning, spatial ability, memory, processing speed and vocabulary. However, all the mental abilities, being related each other, have in common a factor, namely the factor of intelligence  $g$ .

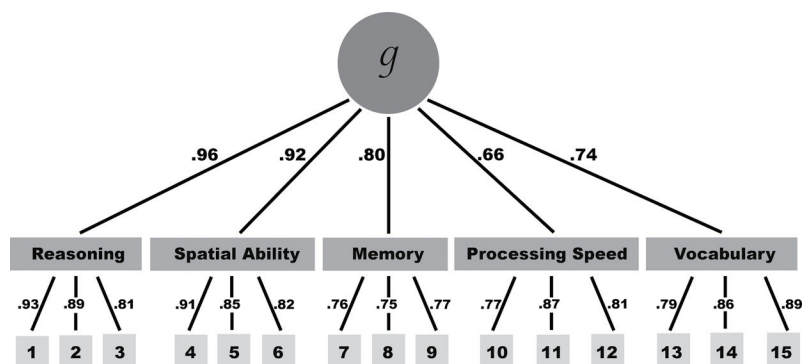


Figure 3.1: Structure of mental abilities. On the bottom, from 1 to 15, the different tests. In the middle, 5 mental abilities from the tests. On the top,  $g$  that is common to all abilities. Numbers represent the correlations between tests, mental abilities and  $g$ . [Haier (2016)]

$g$  factor was described for the first time by Charles Spearman in 1904 [Spearman (1904)] who realized that all mental processes were inter-correlated and he used a statistical analysis, called factor analysis, to identify these correlations.

### 3 Other Models

Other models were introduced to describe intelligence structure. In 1971, Raymond Cattell described intelligence as composed of two factors: crystallized intelligence (Gc) and fluid intelligence (Gf) [Cattell (1971)]. Crystallized intelligence refers to capacities to use skills that a person has acquired through knowledge and expertise. The fluid intelligence is the innate learning capacity of all individuals to solve new problems. The two factors have a different evolution during the lifespan (Figure 3.3). While Gc continues to improve until late adulthood because it is fed by each new think learned, Gf has a peak during adolescence and then it decreases slowly with age because of age-related brain degeneration.

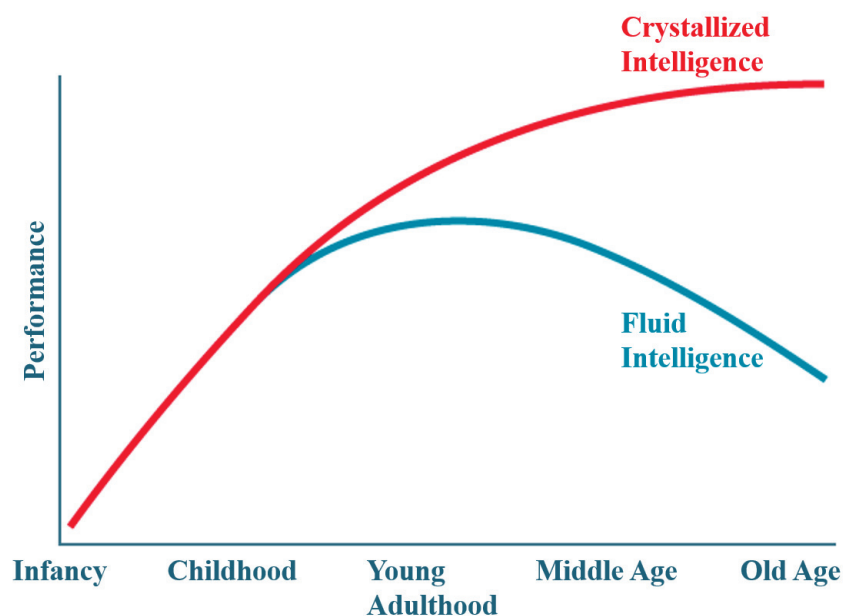


Figure 3.2: Schematic representation of changes in crystallized and fluid intelligence during the life span. Adapted from [Horn (1982)].

Other models that have been proposed are based on three factors [Johnson and Bouchard (2005)] or they have less empirical evidences [Sternberg (2000), Gardner (1987)].

## 4 Intelligence Quotient (IQ) measure

Intelligence quotient (IQ) is not the same as  $g$  factor, but IQ scores can estimate  $g$  because both of them are measured by tests that measure different mental abilities. The first IQ test was developed in 1904 by a French psychologist Alfred Binet and his colleague Theodore Simon. The French government wanted to identify children who needed specialized assistance in order to help them in school achievement. The test was composed of questions to test mental abilities such as attention, memory, and problem solving. Once many children underwent these questions, Binet measured averaged score for each age and sex. He then introduced the concept of mental age that was a measure of the intelligence compared to abilities of children of a certain age group.



Figure 3.3: Page from the Binet-Simon Intelligence Scale: children were asked which face, of each pair, was prettier. Adapted from [Binet and Simon (1916)].

Successively, the Binet-Simon Scale was standardized using a sample of American participants by a Stanford University psychologist. This test, published in 1916 as the Stanford-Binet Scale, calculated a single number named intelligence quotient by multiplying for 100 the ratio between mental age and chronological age. The focal point of these tests is that a child score is a measure relative to their peers. Even today, IQ is not an absolute measure, but it is a relative measure that has a meaning only if compared with other people.

## 5 Wechsler Intelligence Scales

Based on the Stanford-Binet test, in 1939 David Wechsler combined several sub-tests to develop a new IQ test. Wechsler believed that intelligence was

*"the global capacity of a person to act purposefully, to think rationally, and to deal effectively with his environment" .*

For this reason, its IQ test was composed of questions that tapped many verbal and non-verbal abilities. This test has undergone to many revisions and it is today the most used in psychology. Three intelligence tests developed by Wechsler for different populations are used in United States: the Wechsler Adult Intelligence Scale-fourth edition (WAIS), the Wechsler Intelligence Scale for Children (WISC), and the Wechsler Preschool and Primary Scale of Intelligence (WPPSI). All the Wechsler scales rely on the idea that IQ scores is normally distributed throughout the population (Figure 3.4) with an average score fixed at 100.

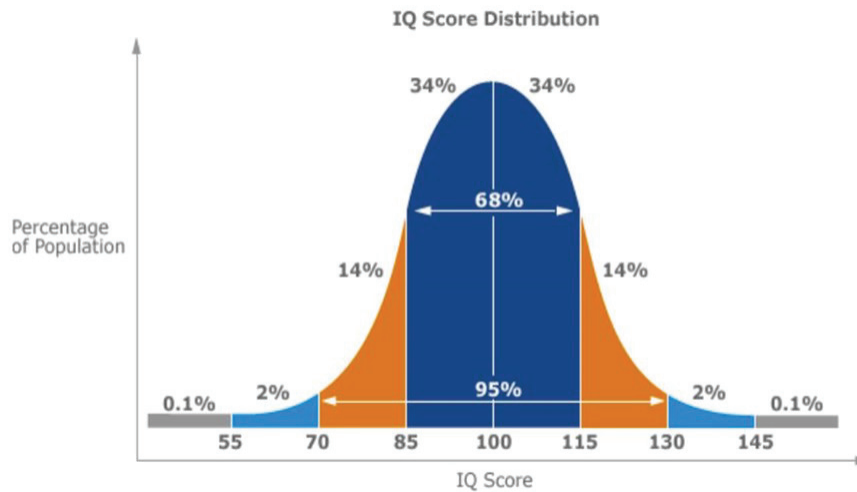


Figure 3.4: Normal distribution of IQ scores. The average IQ is 100 and 68% of the population has a normal IQ in the range between 85 and 115. Only the 2.5% of the population has a very high IQ (IQ > 130). Adapted from <https://www.iqtestforfree.net>.

### 5.1 WISC-IV

The Wechsler Intelligence Scale for Children (WISC) has been developed around 1949 to measure different aspects of intelligence in children between the ages of 6 to 16 [Wechsler (2003)]. The test has undergone several updates and the current version of the test is the fifth edition WISC-V. However, in this work we used the fourth

edition WISC-IV. It contains 10 principal and 5 additional sub-tests to measure child's abilities in four cognitive domains represented by 4 primary index scores: Verbal Comprehension Index (VCI), Perceptual Reasoning Index (PRI), Working Memory Index (WMI), and Processing Speed Index (PSI) as shown in figure 3.5. The VCI measures the child's ability to verbally reason and it is influenced by semantic knowledge. The PRI estimates non-verbal and fluid reasoning, WMI is a measure of working memory abilities, and PSI measures the processing speed. Finally, child's general intellectual ability namely Full Scale IQ (FSIQ) is obtained from the 4 indices. Like Binet's tests, sub-tests of the WISC-IV are compared to a sample of children with the same age.

## 5.2 WAIS-IV

The Wechsler Adult Intelligence Scale (WAIS) is the most used intelligence test today. The last version, namely WAIS-IV, was released in 2008 and it contains 10 sub-tests along with five supplemental tests. As well as the WISC-IV, the WAIS-IV provides scores on four major areas of intelligence namely VCI, PRI, WMI and PSI and their combination provides the Full Scale IQ (FSIQ) that summarizes the general intellectual ability. The details of the 10 sub-tests are shown in the following image:

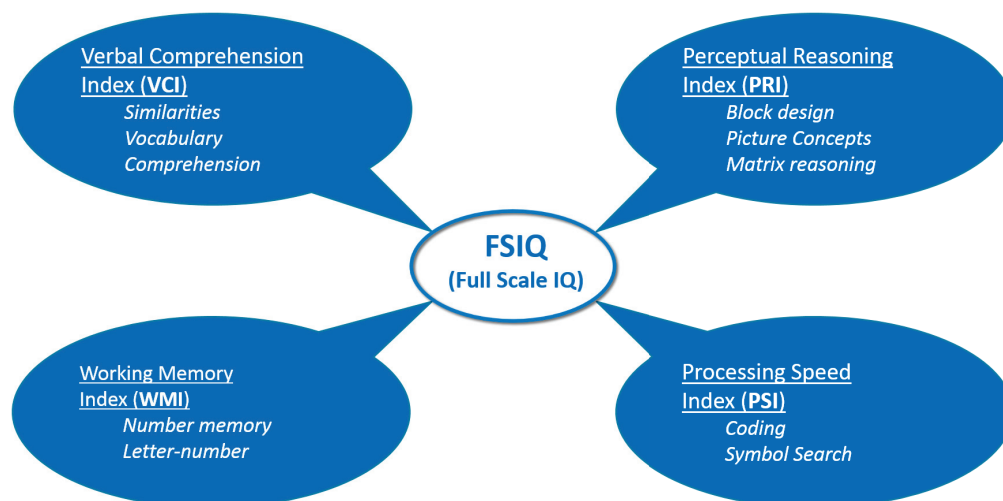


Figure 3.5: Structure of Wechsler Intelligence Scale for Children (WISC-IV) and Wechsler Adult Intelligence Scale (WAIS-IV). The 10 principal sub-tests are distributed in four groups, each for a different intelligence score.

The WAIS results are scored comparing the obtained score to the scores of an adults population of the same age.

## 6 MRI application to intelligence

Since XIX century, the relationship between brain volume and intelligence has been a topic of a scientific debate. Numerous studies demonstrated this relationship [Galton *et al.* (1869)], but they have been severely hindered by difficulties in obtaining direct measures of brain size measure [Van Valen (1989)], that was achieved indirectly with head circumferences, or "number of metal pellets" required to fill a skull. Over the past three decades, the extraordinary development of brain imaging technology techniques, like PET and MRI, have allowed to investigate the neural substrate of intelligence. Because it provides images of all the body without radiation exposure, with a great contrast and allowing the detection of pathology with a great sensitivity, MRI has become the pillar of cognitive neuroscience research.

In this section, we review the literature of MRI application to human intelligence. First, we introduce some studies that showed important relationship between intelligence and simple MRI measures obtained from anatomical, diffusion weighted, and functional MRI study. Second, the most important intelligence theory based on 37 neuroimaging studies is presented. Finally, we detail literature studies that explored the relationship between brain connectivity and intelligence differences and we focus our attention on those that analyzed brain connectivity throughout graph theory.

### 6.1 Early MRI studies

**Structural MRI studies** The first MRI study demonstrated in 1991 that differences in human brain size are relevant for explaining differences in intelligence test performance [Willerman *et al.* (1991)]. Until today, this result was confirmed many times [Wickett *et al.* (2000), Haier *et al.* (2004)] and in 2005 McDaniel wrote a complete review on this subject comparing 37 studies for a total of 1530 subjects [McDaniel (2005)]. The main result was a mean correlation over all subjects of 0.33, that was higher for females (0.40), between intelligence test score and brain size. He concluded that the debate was resolved and intelligence and brain volume are meaningfully related.

In order to have more detailed results, relationship between single region of interest (ROI) and intelligence was explored. These studies reported that volume of frontal, temporal, parietal lobes, along with hippocampus and cerebellum are the most related to intelligence [Andreasen *et al.* (1993), Flashman *et al.* (1997)]. Using more sophisticated methods that allow to distinguish gray and white matter volume, higher resolution results have been reached. With voxel-based morphometry (VBM) technique, Haier and colleagues demonstrated that several areas in overall the brain

are correlated with IQ [Haier *et al.* (2004)], and with  $g$  factor [Colom *et al.* (2006)] and that these relationships depend on sex [Haier *et al.* (2005)].

A more recent method to investigate the brain structure, uses Euclidean geometry to calculate thickness of the cortex in many points. Applying this measure to a large population of children, significant correlation between cortical thickness and IQ were measured (Figure 3.6) and the strongest correlation was observed in late childhood [Shaw *et al.* (2006)].

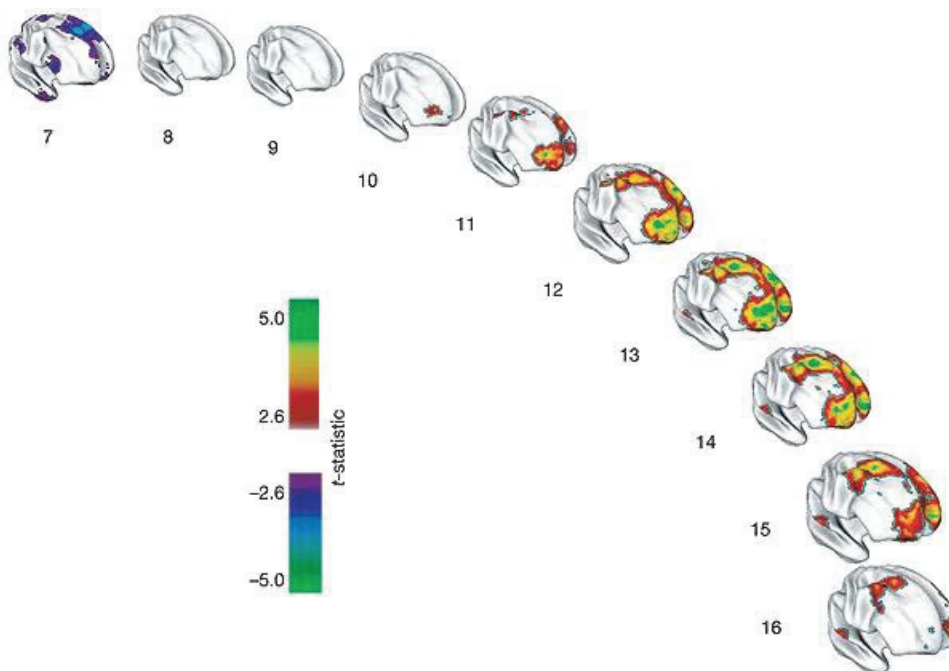


Figure 3.6: Evolution of cortex thickness difference between high and standard intelligence group from 7 to 16 years old. In early childhood, high intelligence group presents a thinner cortex that increases. The most significant result is obtained at age 13 when an elevated increase in cortical thickness is measured in high intelligence group. Adapted from [Shaw *et al.* (2006)].

**White matter measure with DTI** Diffusion tensor imaging (DTI) also constitutes a very sensitive MRI technique for the characterization of WM microstructural organization and the identification of neural pathways. The high sensitivity of this technique demonstrates the association between WM microstructure and IQ during lifespan. The first DTI study, performed by Schmithorst and colleagues, showed positive associations in a children population between IQ and fractional anisotropy (FA) in frontal and parietal areas [Schmithorst *et al.* (2005)]. Another study in children, demonstrated a correlation between visuospatial abilities and FA in the right uncinate fascicle [Muetzel *et al.* (2015)]. The relationship between FA and IQ was also demonstrated to exist also in adolescents [Navas-Sánchez *et al.* (2014)]. In 2017, our



group demonstrated that not only FA, but also axial diffusivity (AD) is correlated with IQ, and that DTI measures present a significant difference of the hemispheric lateralization in two IQ children profiles namely Homogeneous HIQ (Hom-HIQ) and Heterogeneous HIQ (Het-HIQ) [Nusbaum *et al.* (2017)]. These results are shown in Figure 3.7, where the significant AD differences, compared to a standard IQ group, are represented in Hom-HIQ group (Top), and in Het-HIQ group (Bottom). Significant voxels were found mainly (60%) in the right hemisphere for Hom-HIQ, and in the left hemisphere for Het-HIQ.

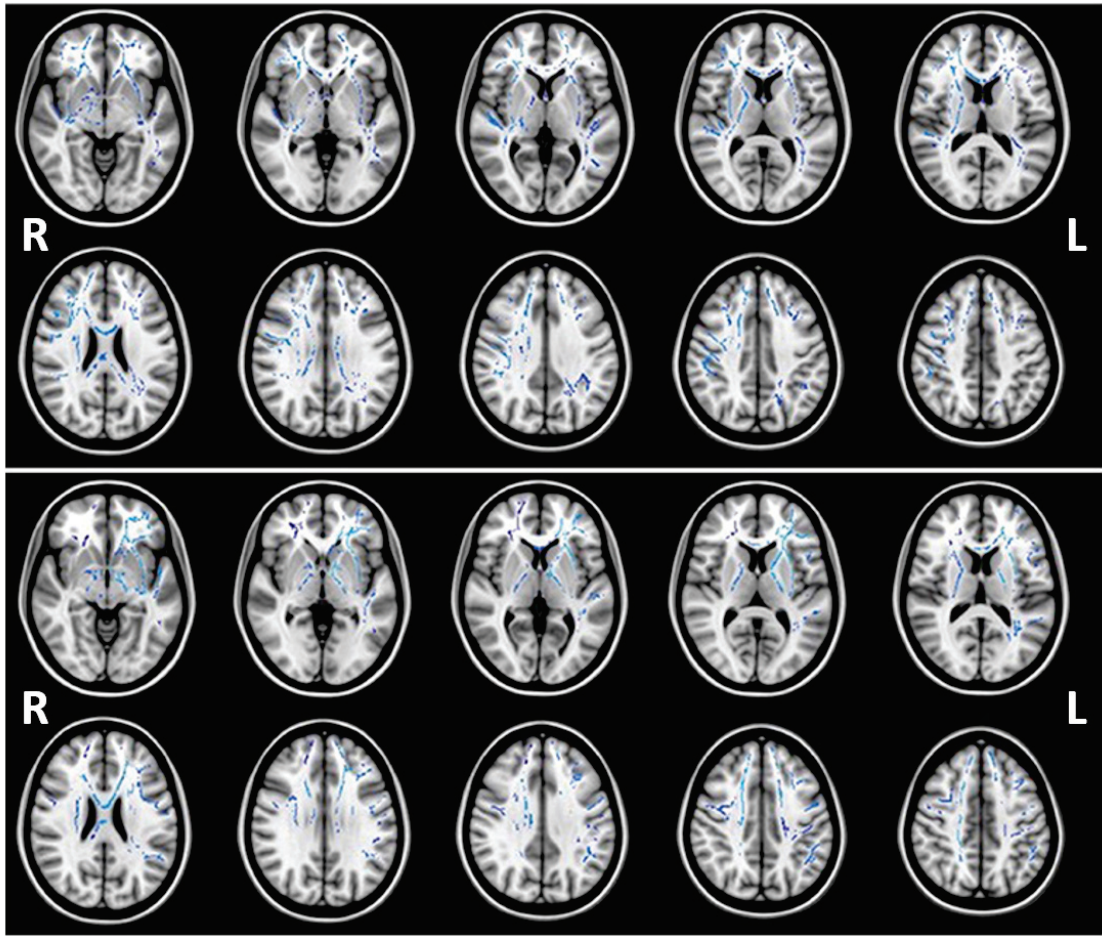


Figure 3.7: Regions with significant greater AD when comparing the homogeneous HIQ group (Top) and heterogeneous HIQ group (Bottom) with the standard IQ group. Adapted from [Nusbaum *et al.* (2017)].

Several studies demonstrated that high intelligence is also positively associated in adults to WM microstructure [Clayden *et al.* (2012), Dunst *et al.* (2014)]. More in detail, Tamnes and colleagues showed that cognitive abilities are related to FA, mainly in the left hemisphere [Tamnes *et al.* (2010)]. The authors explained this left hemisphere dominance as a verbal mediation during reasoning, since other studies



proved that performance on matrix reasoning is associated with measures of verbal abstract reasoning and verbal fluency.

**Functional MRI studies** Since the end of XX century, several studies explored brain functions related to intellectual abilities throughout task fMRI. The first study that explored the neural substrates of fluid reasoning was conducted by Prabhakaran's group that measured blood flow increase in frontal and parietal lobes during reasoning tasks from Raven's test [Prabhakaran *et al.* (1997)].

Despite the use of different tests that measure various intelligence components, more recent studies also highlighted a relationship between fronto-parietal regions activation and intelligence. A large-sample of imaging studies probed individual differences in general fluid intelligence, using verbal and nonverbal working memory tasks [Gray *et al.* (2003)]. They found that greater activity in prefrontal cortex is associated with higher fluid intelligence. Intellectual giftedness in adolescents has been investigated in [Lee *et al.* (2006)a]. As shown in Figure 3.8, when performing visual reasoning tasks, the superior intelligence group presents higher activation than the average intelligence group in fronto-parietal network particularly driven by the posterior parietal activation.

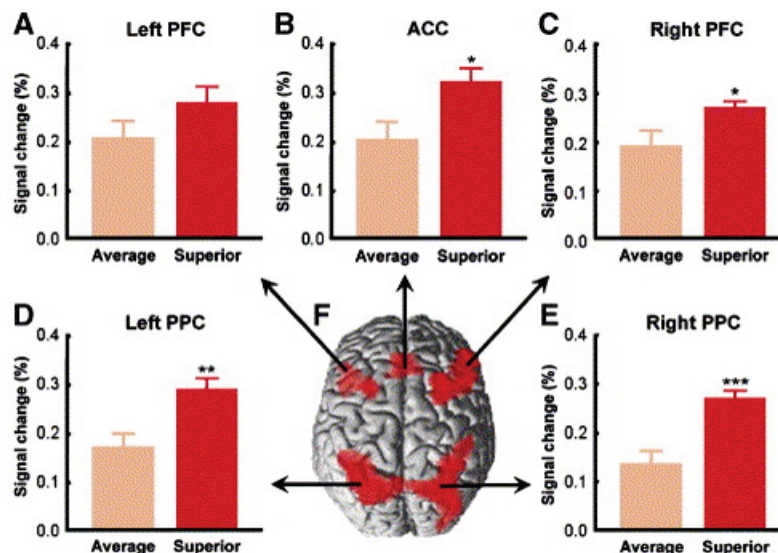


Figure 3.8: Example of frontal and parietal regions ((A) and (C) PFC, prefrontal cortex; (B) ACC, anterior cingulate cortex; (D) and (E) PPC, posterior parietal cortex) with their activation level in two different intelligence group: Average intelligence and Superior intelligence groups. Activation levels are represented by changes in BOLD signal during reasoning task. Adapted from [Lee *et al.* (2006)b].

Noveck's group explored brain activation during employed propositional syllo-

gisms involving conditional reasoning [Noveck *et al.* (2004)]. The main finding of this study was a lateralization of parieto-frontal network, that was more activated in the left hemisphere, when reasoning becomes more challenging. Another study on a large cohort of over 300 children performing the semantic processing task of silent verb, observed activation differences between brain hemispheres [Schmithorst and Holland (2006)]. Regions of the left hemisphere (namely the middle temporal gyrus, prefrontal cortex, medial frontal gyrus, precuneus, and cingulate gyrus) exhibited positive correlations with IQ, while the superior temporal gyrus in the right hemisphere showed negative correlations.

## 6.2 The Parieto-Frontal Integration Theory (P-FIT)

The most important review of neuroimaging studies of intelligence was written in 2007 by the two major researchers of intelligence: Rex Jung and Richard Haier. They collected the results of 37 imaging studies that used PET, functional, and structural MRI. Results in common to more than half studies were grouped in order to build their theory, named Parieto-Frontal Integration Theory (P-FIT). This name comes from the spatial position of the brain regions mainly associated with intelligence that were distributed in parietal and frontal lobes.

The majority of the activation was observed in the left hemisphere while a few in the right hemisphere. Furthermore, from structural studies results, Jung and Haier concluded that frontal and parietal lobes communicate between them thanks to white matter fibers (Figure 3.9).

They proposed a very detailed information processing among these regions composed of 4 steps. First, the information arrives and it is raveled from the sensory perception regions in occipital and temporal brain areas (BA 18-19, BA 37 and 22). During the second step, the information are integrated thanks to association brain areas (BA 39, 40, and 7) that are also relied to memory. This integration processing ends during the third step, when parietal regions interact with frontal areas (BA 6, 9, 10, 45, 46, and 47) allowing problem solving and evaluation. Finally, in the decision making the frontal region BA32 is involved.

This model is still used today, but in 2015, Basten and colleagues meta-analysis showed that also posterior cingulate cortex and subcortical structures are associated with intelligence [Basten *et al.* (2015)].

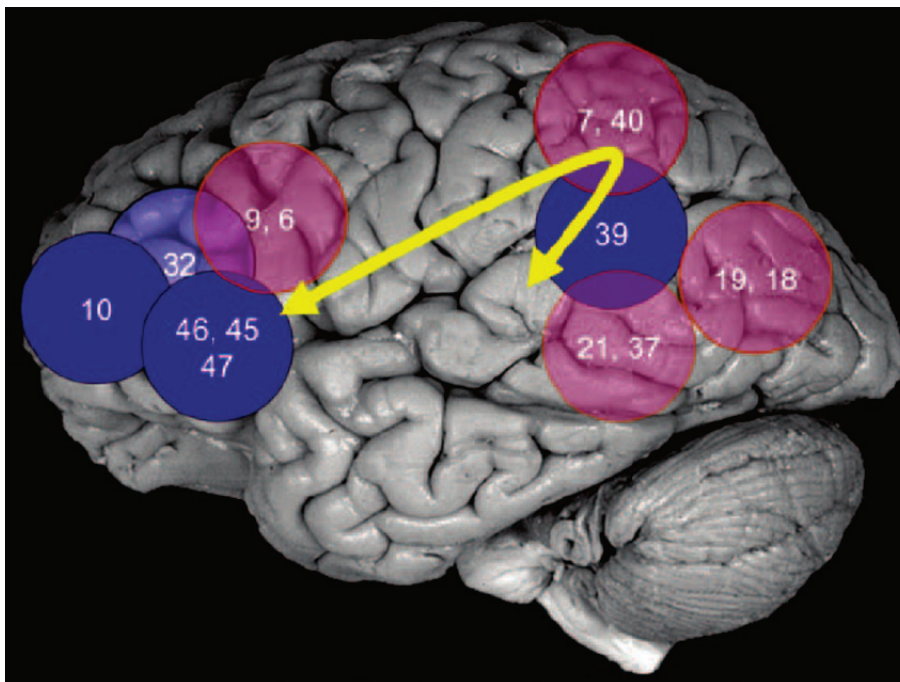


Figure 3.9: The Parieto-Frontal Integration Theory (PFIT) network: blue circles indicate PFIT regions located in the left hemisphere, while pink regions are located in both hemispheres. The yellow arrow represents the transfer of information through the major white matter tracts of fiber-bundles that connects the regions. The regions numbers refer to the Brodmann area (BA) nomenclature. Adapted from [Eggermont (2012)].

### 6.3 The role of brain connectivity in intelligence

**Resting-state functional connectivity** The turning point in neuroimaging research was the development of connectivity methods with resting-state fMRI. Indeed, this technique allows to measure the functional connectivity between two regions without any cognitive task, but during resting conditions [Fox *et al.* (2005), Shirer *et al.* (2012)]. The first study to apply functional connectivity in intelligence was performed by Song’s lab. Since dorsolateral prefrontal (BA 46-9) cortex has been found to be one of the most important brain region supporting intelligent behavior [Gray and Thompson (2004)], in this work the bilateral BA 46-9 were chosen as seed regions. First, the authors identified brain voxels with a significant functional connectivity with seed regions. Second, they correlated the connectivity strength with intelligence scores. The main results supported the PFIT model as they showed that differences in intelligence can be predicted from functional connectivity between frontal regions and between frontal and posterior brain regions [Song *et al.* (2008)]. Association between the local connectivity within a specific brain region and intelligence during rest was explored measuring local synchronization of voxels within the

regions [Wang *et al.* (2011)]. Consistent with PFIT theory, these results measured significant correlations between FSIQ and local connectivity in bilateral inferior parietal lobules, middle frontal, parahippocampal and inferior temporal gyri, the right thalamus, superior frontal and fusiform gyri, and the left superior parietal lobule. These results remain valid during childhood, in spite of the frontal pole is the last region area to be finalized and its connectivity with the distant strengthens during this life period [Langeslag *et al.* (2013)].

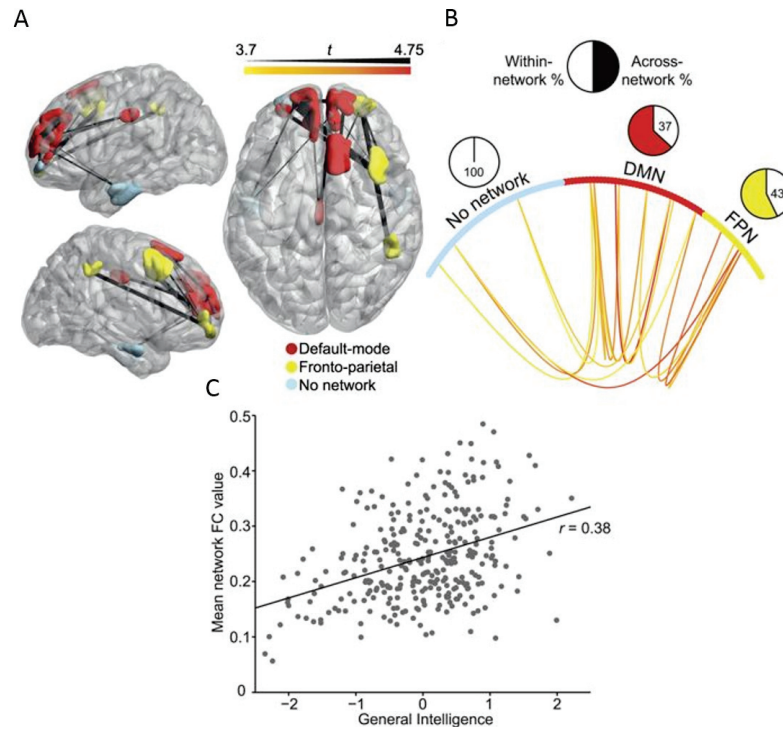


Figure 3.10: Results obtained from functional connectivity analysis on HCP population that are located mainly in default mode network (DMN) and fronto-parietal network (FPN). Functional connections significantly associated with intelligence scores are represented (A) in anatomical space, and (B) outside the anatomical space. Correlations between the average functional connectivity values in the whole implicated network showed in panel (C) and general intelligence scores. Adapted from [Hearne *et al.* (2016)].

Since resting-state brain activity is organized into distinct neural networks, some neuroimaging researchers analyzed the association of the connectivity in these networks and intelligence. A positive association has been demonstrated to exist between the functional connectivity of the default mode network (DMN) and the fronto-parietal network (FPN) with intelligence scores [Hearne *et al.* (2016)]. This result was obtained with two different analysis: a meta-analysis from studies present in literature, and an exploration of the functional brain network based on the Hu-

man Connectome Project (HCP) (Figure 3.10). Another study that explored brain networks on early adolescents, showed a significant relationship between intelligence performance and the functional connectivity of DMN and central executive networks (CEN) [Sherman *et al.* (2016)].

**Graph theory** The brain connectivity horizons have been broaden with the use of graph theory, an advanced mathematical approach [Watts and Strogatz (1998)]. Indeed, as explained in the previous chapter, graph theory is particularly suitable to explore without *a priori* hypothesis brain networks that present a "small-world" topology [Achard and Bullmore (2007)]. Such networks can be described at two different scales using global and local graph metrics. A few studies have applied graph theory to structural and functional MRI to explore brain connectivity changes with intelligence.

The first application of graph theory on structural connectivity for the study of intelligence hypothesized that higher intelligence scores correspond to more efficient information transfer in the brain [Li *et al.* (2009)]. Since white matter tracts assure flow information in the brain, they measured the global efficiency metric of the structural network. Their main finding was a higher IQ in brain networks characterized by higher global efficiency, and consequently, shorter characteristic path length. Moreover, this is the only work that observed the normal aging population with graph theory. No significant correlation was measured between network properties and WAIS sub-tests scores in elderly population. However, in a subgroup of individuals aged 75 and above, high local clustering and global efficiency as well as overall short path lengths between brain areas were correlated with higher intelligence scores [Fischer *et al.* (2014)]. On one hand, these results highlighted that intelligence is not associated with brain structure in elderly. On the other hand, in advanced elderly, intelligence may be affected by network deterioration only if the brain structural damage goes beyond a threshold. Two graph network analysis to structural neuroimaging extended the previous results obtained for adults [Li *et al.* (2009)] to a children population [Koenis *et al.* (2015), Kim *et al.* (2016)]. In the first study, children showing an increased global efficiency where the ones with the highest IQ and, at local scale, frontal and temporal areas showed the strongest associations between their efficiency changes and intelligence (Figure 3.11) [Koenis *et al.* (2015)]. In the second study, perceptual reasoning measurements (PRI) revealed a significant positive association with global efficiency of structural brain networks [Kim *et al.* (2016)].

The firsts to explore brain functional substrate of intelligence with graph theory



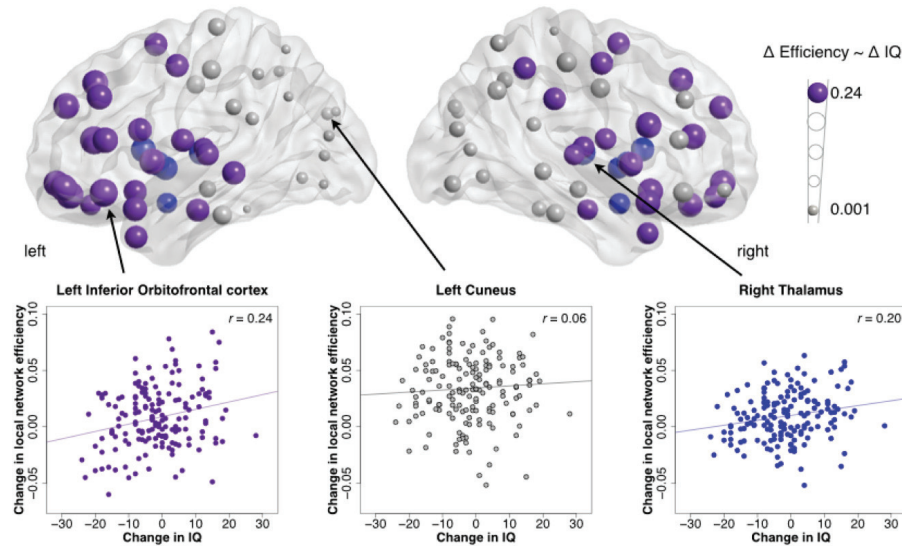


Figure 3.11: Correlations between local efficiency and IQ changes in adolescents: purple and blue nodes present a significant correlation in cortical and subcortical regions respectively. On the bottom, example of correlation scatterplots in left inferior orbitofrontal cortex, left cuneus, and right thalamus. Adapted from [Koenis *et al.* (2015)].

were Van den Heuvel and colleagues. They extended the idea of the relationship between intelligence and brain efficiency to functional networks, that has previously demonstrated in structural connectivity studies. Indeed, they found that IQ correlates negatively with shortest path length measured on the whole resting-state brain networks [Van Den Heuvel *et al.* (2009)a], suggesting that it depends on efficiency of functional connections between brain regions. The DMN being the most important resting-state network, its activity in two groups with different cognitive capacities has also been subject of study [Song *et al.* (2009)]. In this network, the hub, represented by the node with the greatest degree, was found to be the posterior cingulate cortex and the regions with the weaker connectivity with the major DMN nodes were the parahippocampal gyrus and cerebellar tonsils. While these results were in common in both intelligence groups, the network global efficiency and the strength of some functional connectivity were significantly different between them. The exploration of network efficiency not only at global scale but also at local scale as function of intelligence, was the goal of Hilger's group. They identified anterior insula (AI) and dorsal anterior cingulate cortex (dACC) as hub functional nodes of brain network associated with intelligence since they showed a nodal efficiency positively associated with it [Hilger *et al.* (2017)a]. Since these regions are part of the Salience network, this result suggests that intelligence performance is associated with functional connectivity of the salience network. On the contrary, a negative

association was measured for the efficiency of the left temporo-parietal junction (TPJ) (Figure 3.12). However, no significant results have been found at a global scale neither in network efficiency nor in modularity that this group explored in another study [Hilger *et al.* (2017)b]. In this last report, the node measures of within- and between-module connectivity showed a significant relationship with intelligence. This result was mainly measured in frontal and parietal regions and highlighted the importance of topological reorganization in higher cognitive abilities.

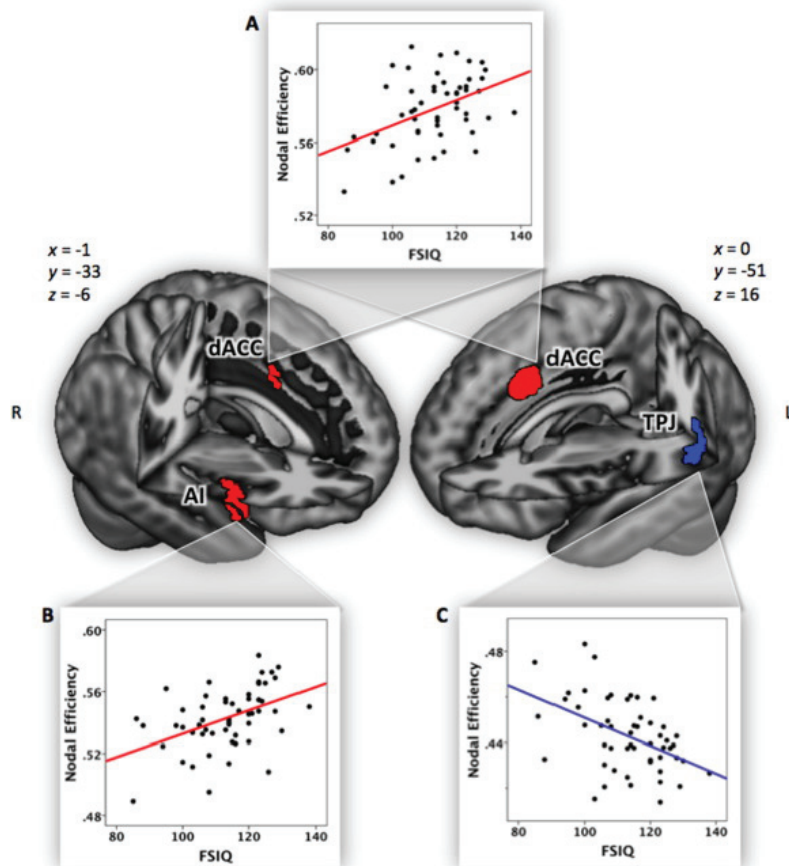


Figure 3.12: Nodes showing significant associations between intelligence and nodal efficiency. In red, (A) dorsal anterior cingulate cortex (dACC), and (B) insula (AI) present a positive association while, in blue (C) temporo-parietal junction (TPJ) presents a negative association. Adapted from [Hilger *et al.* (2017)a].

A surprising finding from Santerrecchi's team, demonstrated that weaker long-distant connections are more important than the strong short one in IQ differences [Santarrecchi *et al.* (2014)]. These researchers also performed other studies that allowed to know other details of the neuronal substrate of different intelligence performance. For instance, they applied randomly a technique to simulate a damage of a brain area demonstrating that people with higher intellectual capacities showed

a more resilient brain in that the flow of information continues also if the most important regions are damaged [Santarnecci *et al.* (2015)a]. Analyzing functional connectivity between the same brain region in the right and the left hemisphere, namely homotopic connectivity, the same group reported a decreased functional connectivity in the principal sensory areas in association with high IQ [Santarnecci *et al.* (2015)b]. Not only this result was unexpected, but also it was the unique study to investigate homotopic connectivity in intelligence. Finally, they investigated the connectivity in the network related to fluid intelligence (Gf) and they compared it with the most important resting-state networks [Santarnecci *et al.* (2017)]. Gf networks showed the strongest positive correlation with regions of the dorsal attention and executive control networks, and negative correlation with DMN regions. These results suggested a link between fluid intelligence and resting-state networks and, particularly, the DMN which may be a marker of intelligence.





## Chapter 4

---

### Aim of the thesis

---

High Intelligence Quotient (HIQ) people are characterized by different neurological, cognitive, relational and emotional functioning. Based on scientific studies, 2-3% of the population is concerned by this mental specificity that represents an average of one child per class in school. The prevalent thought of the society is that HIQ people know everything. They are considered as geniuses, gifted child or talented people. They are usually characterized by better cognitive abilities such as faster processing speed based on a rich vocabulary range, greater attention, and visuo-spatial abilities, fast and large memory, superior problem solving capacities, mental flexibility, and reasoning strategies [[Vaivre-Douret \(2011\)](#)]. These particular skills are reflected in a High Intelligence Quotient quantified by a high Full Scale Intelligence Quotient (FSIQ>130) as measured by the Wechsler Intelligence Scales.

However, HIQ people do not always feel to be lucky persons or to be better than other people. On the contrary, their capabilities may lead to social or learning difficulties. Their thinking is different, faster, and their interests are usually broader. Furthermore, they present an increased sensibility that may lead some of them to present different disabilities in managing their attention, emotions, and relationships. Indeed, they are characterized by hypersensitivity, perfectionism, low self-esteem. As they understand everything very quickly at school, they could be bored in class. For all these aspects, HIQ person feel himself different from the others, and his hypersensitivity makes him suffering from this difference. The coexistence of two opposite aspects in the same person that on one hand, have better

cognitive capabilities and on the other have relationship difficulties, has been called a "dyssynchrony syndrome" based on a dyssynchrony between cognitive and emotional abilities [Terrassier (2009), Guénolé *et al.* (2015)]. These clinical observations have led Fanny Nusbaum, the psychologist and neuroscientist of our group, to define two profiles based on her clinical experience and measured by their Wechsler Intelligence scores, namely the Homogeneous-HIQ profile (Hom-HIQ) and the Heterogeneous-HIQ profile (Het-HIQ) also named "laminar philocognitive" and "complex philocognitive", respectively. The first ones usually present a well-controlled behaviour and a successful curriculum that is reflected in homogeneous results to the Wechsler's scores. On the contrary, Het-HIQ show social maladjustment and learning troubles that can be detected by a significant difference between verbal comprehension index (VCI) and perceptual reasoning index (PRI) as well as standard memory and speed processing index [Sweetland *et al.* (2006), Guénolé *et al.* (2013)].

In the third chapter of this thesis, we reviewed the literature of MRI studies investigating the intelligence neuronal substrate. Because we support the idea that intelligence does not depend only on some specific brain regions, but mostly on the dynamic organization of brain networks [Barbey (2018)], we studied the role of brain connectivity in intelligence, using graph analysis. Graph theory with its metrics, providing information on both local and global connectivity of brain networks, is a powerful technique to explore the intelligence neuronal substrate. Furthermore, the interest into the global reorganization of brain networks has led us to apply a graph measure that detects changes in brain reorganization compared to a reference group, namely the hub disruption index. In this work, we measured the brain structural and functional connectivity in order to characterize the brain topology of a general HIQ population.

The major part of this thesis concerns our research in children with High Intelligence Quotient (HIQ). First, we focused our attention on brain network connectivity in HIQ children with two different MRI techniques: resting-state fMRI and DTI. After an optimization of rs-fMRI processing for the application of graph theory methods, we measured functional connectivity in two HIQ profiles compared to a reference group (SIQ). We explored then the changes in the functional topology of the brain networks depending on the cognitive abilities. We also studied differences in structural connectivity obtained by diffusion MRI. Finally, we performed a task-fMRI study in order to detect differences in functional activation to a semantic memory task in two HIQ profiles.

In order to have an overall view of brain connectivity along lifespan, we studied in the second part of this work, a population of HIQ adults.

---

The final purpose of this work, is to characterize the neural substrate of intelligence. Once the functioning of HIQ people brain is understood, this could be a scientific explication for their difference and it could help them to be more integrated in everyday life, from the education age to work age.



## II Research project on HIQ children

---



# Introduction

Already before the introduction of the “general model” described by Spearman in 1904 [Spearman (1904)], and the first standardized psychological tests developed by Binet [Binet (1905)], people were interested in knowing where the intelligence could be localized in the brain. On one hand, there was the notion that higher cognitive functions were related to a harmonic work of the brain as a single entity [Flourens (1824)]. On the other, the idea that intelligence was related to specific regions was disclosed [Gall (1825)]. Only in 1949, these two ideas were synthesized providing the new concept that high intelligence performances are related to the interactions of single brain regions [Pavlov (1949)].

This idea still persists to day and the concept of intelligence remained a challenge in cognitive research [Haier (2016)]. Nowadays, neuropsychological tests, such as the Wechsler Intelligent scale for Children (WISC) [Wechsler (2003)], can provide a reliable estimation of the intelligence quotient (IQ), and help the clinical problem of children with high intelligence quotient (HIQ).

Understanding HIQ children has always been a question that is dear to psychologists and clinicians of our research team. A HIQ child has often an atypical development from several points of view. On the psycho-motor level, they start to walk very early [Vaivre-Douret (2004)]. This fact allows them to explore the environment and to acquire skills earlier than other children. On the cognitive level, they start to say the first words at 9 months [Vaivre-Douret (2004), Revol and Bléandonu (2012)], and they have a great capacity of concentration and memorization. On psycho-social level, they prefer the company of older children and they show hypersensitivity and empathy [Robert *et al.* (2010)].

Two profiles of HIQ children have been identified by [Liratni and Pry (2011)]. They hypothesised that there would be a "clinical" group with psychopathological difficulties and a "non-consultant" group with no psychopathological disorders. Although the Full Scale of Intelligence Quotient (FSIQ) is not significantly different, it has been noticed that the cognitive profile of the "clinical" group was more heterogeneous than in the other group. This heterogeneity is significant between the Verbal



---

Comprehension Index (VCI) and the Perceptual Reasoning Index (PRI). Through the research of different authors and our personal observations, two groups of HIQ children have been distinguished, who differ in their cognitive profile, but also in their education and sociability. Then, Fanny Nusbaum proposed to distinguish these two groups: the Homogeneous HIQ (Hom-HIQ) and Heterogeneous HIQ (Het-HIQ).

Hom-HIQ is characterized by harmonious indices on Wechsler scales and the FSIQ reflects the general cognitive profile of these children. They are generally well integrated socially and academically. Despite they exhibit emotional hypersensitivity, they have the capacity to hide it. At school, they will succeed easily in all the subjects but these learning facilities may lead them to get bored.

Het-HIQ is commonly encountered in clinic, showing associative learning troubles, attention deficits, emotional, and social maladjustments. These aspects are described as the “dys-synchrony syndrome” [Silverman (1997), Terrassier (2009)] and most often detected as a VCI higher than the other indices. In particular, Terrassier identified three types of dyssynchrony: internal, cognitive-affective, and social. The internal dyssynchrony is reflected by an elaborate oral language but also a difficulty in learning. This dyssynchrony is evident at school, where the child appears gifted for certain subjects, but he has serious problem to succeed in other. The cognitive-affective dyssynchrony may be revealed as a discrepancy between the intellectual and the emotional development. They are hypersensitive as Hom-HIQ, but they are completely overwhelmed by their emotions. Finally, the social dyssynchrony is characterized by a gap between the child and the social relations with his parents, his teachers or his classmates. Het-HIQ child is thirsty for knowledge and wants to know everything, in a very detailed way. This behavior may cause attention disorders at school where they are bored and feel to be rejected from their classmates. All these dyssynchronies can lead to anxiety, depression, attentional and behavioral disorders, as well as academic failure [Terrassier (2009), Revol and Bléandonu (2012), Robert *et al.* (2010)]. It is also important to note that the HIQ is recognized by the French national education but only on the basis of the FSIQ. However, Het-HIQ children, as previously explained, have particularly heterogeneous Wechsler index scores, which prevents a correct interpretation of the FSIQ that may be quite standard when at least one of the indices is above the average. For this reason, Het-HIQ child may be not recognized as a HIQ child and thus may not benefit from an academic program adapted to his .

In order to better understand the behavior of both HIQ profiles in everyday life, a few years ago, our group designed a research project that links psychological and behavioral observations with neuroimaging explorations. Furthermore, the distinc-

---

tion between Hom-HIQ and Het-HIQ groups remains nowadays only at a theoretical stage while no scientific study allow to confirm it. For this reason, the goal of our project was to explore the brain function and structure using MRI investigations.

Indeed, the development of advanced MRI techniques allowed to investigate the neural bases of intelligence and to accept the assumption that human intelligence has biological basis [Duncan *et al.* (2000), Gray *et al.* (2003), Colom *et al.* (2010)]. For this reason, both structural and functional correlates of cognitive abilities were explored by MRI.

Neural substrate exploration of intelligence in children was performed with three different techniques in order to cover the entire spectrum of information that can be obtained from MRI. First, brain network connectivity networks was explored: functional connectivity was measured by resting-state fMRI to investigate the differences in topology of brain network for HIQ children compared to children with a standard QI. Then, we studied with DTI the microstructure organization and structural connectivity in HIQ children. Finally, a task fMRI experiment was set up in order to investigate how HIQ children respond to semantic tasks, and which regions they active during these tasks.



## Chapter 5

---

# Functional connectivity: a resting-state fMRI study

---

### Contents

---

<b>1</b>	<b>Introduction . . . . .</b>	<b>82</b>
<b>2</b>	<b>Development of the pre-processing of rs-fMRI . . . . .</b>	<b>84</b>
2.1	Signal to noise ratio . . . . .	84
2.2	Subjects' motion . . . . .	84
2.3	fMRI signal processing . . . . .	87
2.4	Anatomical atlas . . . . .	90
2.5	Wavelet decomposition scale . . . . .	91
2.6	Graph's cost . . . . .	93
<b>3</b>	<b>Materials and Methods . . . . .</b>	<b>93</b>
3.1	Participants . . . . .	93
3.2	MRI acquisition . . . . .	94
3.3	Data preprocessing . . . . .	94
3.4	Wavelets decomposition . . . . .	95
3.5	Graph construction . . . . .	96
3.6	Hub Disruption Index ( $\kappa$ ) estimation . . . . .	96

3.7	Statistical analysis . . . . .	98
<b>4</b>	<b>Results . . . . .</b>	<b>99</b>
4.1	Modifications of FC organization with intelligence . . . .	99
4.2	Correlations between FC organization and intelligence . .	103
<b>5</b>	<b>Discussion . . . . .</b>	<b>104</b>
5.1	Brain networks changes with high intelligence . . . . .	104
5.2	Correlation between brain networks changes and IQ sub- scales . . . . .	109
<b>6</b>	<b>Conclusion . . . . .</b>	<b>110</b>

---

---

This chapter is dedicated to the exploration of functional neuronal substrate of intelligence. As it has been presented in Chapter 2, from resting-state fMRI data, we can extract BOLD time-series from different brain areas. Exploiting this information, the temporal correlation between the time-series can be calculated to estimate the functional connectivity between brain regions. A graph of networks is obtained from anatomical parcellation of the cortical regions considered as nodes and from correlation between time-series considered as edges that link the nodes between them. With these assumptions, the brain connectivity networks can be analyzed applying graph theory. In Chapter 3, we have illustrated the great potentiality of this technique that allows to explore networks at two main scales. From local metrics, properties of each node are obtained, while global metrics provide information about the total graph. In literature, few studies investigated both topology of graph metrics and their association with intellectual abilities. The majority of these studies focused on finding a relationship between brain network efficiency and intelligence, as it is expected from the efficiency theory. However at global scale, a previously work [Van Den Heuvel *et al.* (2009)b] that demonstrated the existence of this relationship were not confirmed by a more recent study [Kruschwitz *et al.* (2018)] on a large cohort of the Human Connectome Project. Indeed, the authors tried to confirm the efficiency theory but, the correlations measured between global efficiency and IQ did not show any significant results.

Based on these controversial results, and on the idea that intellectual abilities are supported by brain network reorganization [Barbey (2018)], we investigated the brain topology using the "Hub disruption index" ( $\kappa$ ). This graph parameter is a measure of network reorganization and it has been demonstrated to be more sensitive than global graph metrics to detect group differences [Termenon *et al.* (2016)b]. We measured the reorganization of segregation, integration, and hub properties defining a  $\kappa$  for four local graph metrics, namely the degree, the local efficiency, the clustering coefficient, and the betweenness centrality. The four  $\kappa$  were estimated using a reference group with standard IQ, for a group of High IQ children that was furthermore splitted in two different profiles, namely Homogeneous and Heterogeneous HIQ groups. Comparing differences in brain organization among these groups, significant changes in brain topology have been detected in children with High Intelligence Quotient.

This chapter is based on the article published in the journal "Frontiers in Human Neuroscience" titled **Topological modification of brain networks organization in children with high intelligence quotient: a resting-state fMRI study**. Ilaria Suprano, Chantal Delon-Martin, Gabriel Kocevar, Claudio Stamile, Salem Hannoun, Sophie Achard, Amanpreet Badhwar, Pierre Fourneret, Olivier Revol, Fanny Nusbaum and Dominique Sappey-Marinier .

## 1 Introduction

Resting-state fMRI (rs-fMRI) allows the measurement of functional connectivity (FC) in large-scale brain networks dedicated either to specific cognitive processing demands [Shirer *et al.* (2012)] or to intrinsic brain activity [Fox *et al.* (2005)]. These properties led several neuro-scientists to apply this technique to characterize functional intelligence networks.

Based on these approaches, Sherman *et al.* reported a correlation with intelligence in the default mode network (DMN) and the central executive network (CEN) of early adolescents [Sherman *et al.* (2016)]. In a cohort of young children, Langeslag *et al.* [Langeslag *et al.* (2013)] reported associations between high nonverbal intelligence and increased FC between parietal and frontal, and parietal and anterior cingulate regions. Based on an exploratory mapping of the literature, and a network analysis of the Human Connectome Project (HCP) data, Hearne *et al.* [Hearne *et al.* (2016)] showed that both the DMN and the FPN were strongly correlated with high intelligence scores in young adults. Moreover, the cognitive functions related to adult intelligence (measured using IQ) seemed to correlate with the FC of homotopic regions, which was reported to be reduced in the primary sensorimotor cortex [Santarnecchi *et al.* (2015)b]. Exploration of homotopic connectivity is currently gaining interest, as it has been demonstrated to robustly increase with advancing gestational age in the fetus [Thomason *et al.* (2013)], and be highly consistent within and across subjects [Finn *et al.* (2015)].

The concept of intelligence being embedded not only in a single brain network, but rather in a complex organization of communicating brain networks, has recently emerged [Ponsoda *et al.*]. Graph theory [Watts and Strogatz (1998)], is in particular relevant for modeling brain FC as a global efficient network, supporting both segregated and distributed information processing [Sporns and Zwi (2004)] that is modeled by a “small-world” topology [Achard and Bullmore (2007)]. This approach was recently applied to characterize the neuronal substrate of intelligence attributable to both structural and functional connectivity, using diffusion tensor

imaging (DTI) [Kim *et al.* (2016), Kocevar *et al.* (2019)] and rs-fMRI [Hilger *et al.* (2017)a, Kruschwitz *et al.* (2018), Van Den Heuvel *et al.* (2009)b]. These studies investigated specific metrics reflecting network integration properties (global efficiency (GE) and degree (D)), segregation properties (local efficiency (LE) and clustering coefficient (CC)), and hubness properties (betweenness centrality (BC)). Van den Heuvel *et al.* [Van Den Heuvel *et al.* (2009)b] reported a significant correlation between GE and intelligence, though this finding was not reproduced in the larger HCP cohort [Kruschwitz *et al.* (2018)]. Furthermore, LE was demonstrated to be positively correlated with FSIQ in regions of the salience network and negatively in the temporo-parietal junction [Hilger *et al.* (2017)a].

Taken together, these results suggest that HIQ brain could be related to global modification of network topology. This was recently conceptualized by Barbey [Barbey (2018)] who suggested that “intelligence depends on the dynamic organization of brain networks, modifying their topology and community structure in the service of system-wide flexibility and adaptation”. Therefore, we propose to investigate the relationship between intelligence and brain network FC using a graph organization measure, the “hub disruption index  $\kappa$ ”. This approach has been applied to several brain pathologies demonstrating significant brain network reorganizations, such as coma [Achard *et al.* (2012)], epilepsy [Gendon *et al.* (2015)], and stroke [Termenon *et al.* (2016)a]. Moreover, the hub disruption index has been shown to be more reliable and sensitive than global graph metrics to detect group differences between patients and healthy controls [Termenon *et al.* (2016)b].

In this work, we first focused on the development of a processing pipeline used to obtain functional brain connectivity. Second, the methods were optimized in several steps of rs-fMRI preprocessing and graph analysis. Graph analyses were then performed on different brain networks scales: the whole brain, both cerebral hemispheres (given the asymmetry of brain functions), and between homotopic regions. From graph metric measures, we finally assessed the topological modification of brain networks organization in HIQ children using the  $\kappa$  index to characterize the neural substrate of intelligence. Whether FC changes relate to FSIQ and/or to its subscales was also investigated by correlational analysis. This approach will allow for better understanding of the differences in FC substrate between high and standard IQ children, as well as between the two HIQ profiles.



## 2 Development of the pre-processing of rs-fMRI

As we have anticipated, the principal goal of this work was to investigate human functional connectivity measured from resting-state fMRI in a children population. The precision of this measure depends on each step of preprocessing pipeline. However, there is no consensus about which is the better pipeline to use and it is still a topic of interest. Furthermore, the connectivity measure depends on the choice of the graph technique parameters used to built the graph and measure the metrics.

In this study, we tested several steps of data analysis focusing on: signal to noise ratio, subject motion, fMRI signal processing regressors, anatomical atlases for the parcellation, wavelet decomposition scales, and graph costs.

Our goal was to choose a robust graph theory methodology, in order to obtain the best significant temporal correlations, and the best precision to compare different HIQ groups.

### 2.1 Signal to noise ratio

Because there are regions of the brain where signal is reduced due to inhomogeneities of the magnetic field, the first step of our processing pipelines concerns the measure of the signal to noise ratio (SNR) in functional images.

Since we measured various nodal graph metrics, it is important to measure the SNR of each parcellated region. This SNR verification is essential to avoid statistical variations due to insufficient SNR.

For each region of the brain atlas, we measured the signal and verified the following property:

$$SNR_{region} > \frac{SNR_{max}}{10} \quad (5.1)$$

Since this property was satisfied in all the brain regions defined by the atlas, we considered as graph nodes all the areas of the brain atlas.

### 2.2 Subjects' motion

Since the beginning of fMRI, the subject motion has been a hot methodological topic [Friston *et al.* (1996)]. In resting-state fMRI, the correlations between time-series represent the basis of the functional connectivity analysis. For this reason, the suppression of motion artefacts is critical. A great obstacle in resting-state fMRI data analysis is contamination of the BOLD signal by head motion and fluctuations. Small movements of the head between volumes acquired during a scan will cause

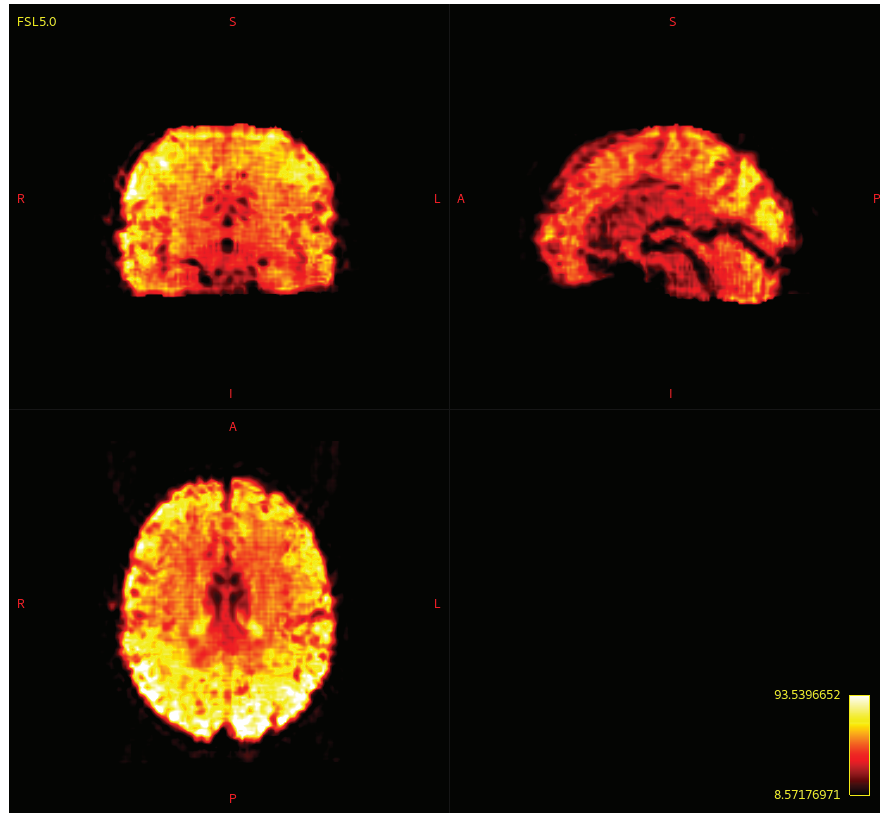


Figure 5.1: Example of distribution of signal to noise ratio for a subject of our population.

erroneous intensity changes in BOLD data influencing measurement of localized haemodynamics. Time-series denoising is, thus, an important field in development. In 2012, three different studies recognized the influence of motion artifact in previously connectivity studies [Power *et al.* (2012), Satterthwaite *et al.* (2012), Van Dijk *et al.* (2012)]. They demonstrated that correlations are not uniformly modified by motion which increases the signal variance signal between nearby voxels, and decreases it in distant voxels.

Since our population is composed of children between 8 and 12 years old, the evaluation of head motion is extremely important for connectivity analysis.

Subject movement is estimated during the realignment step when each volume of data is realigned using a rigid body transformation. This process locate the head position throughout six parameters: 3 translational that measure the displacement along X, Y, and Z axis, and 3 rotational measures of pitch, yaw, and roll. In addition to this step, we added to the preprocessing pipeline the artifact detection using the Art Toolbox of Matlab. It measures for each TR the variation of head position, derived from translation and rotation parameters, and the variation of the signal. It indicates all the scans affected by scan-to-scan head motion. The following figures

show two example of Art Toolbox applications. In Figure 5.2, a high movement was detected only in 4 scans, while in Figure 5.3, 62 scans present high signal variation caused by head movement that represents more than 24 % of noised scans.

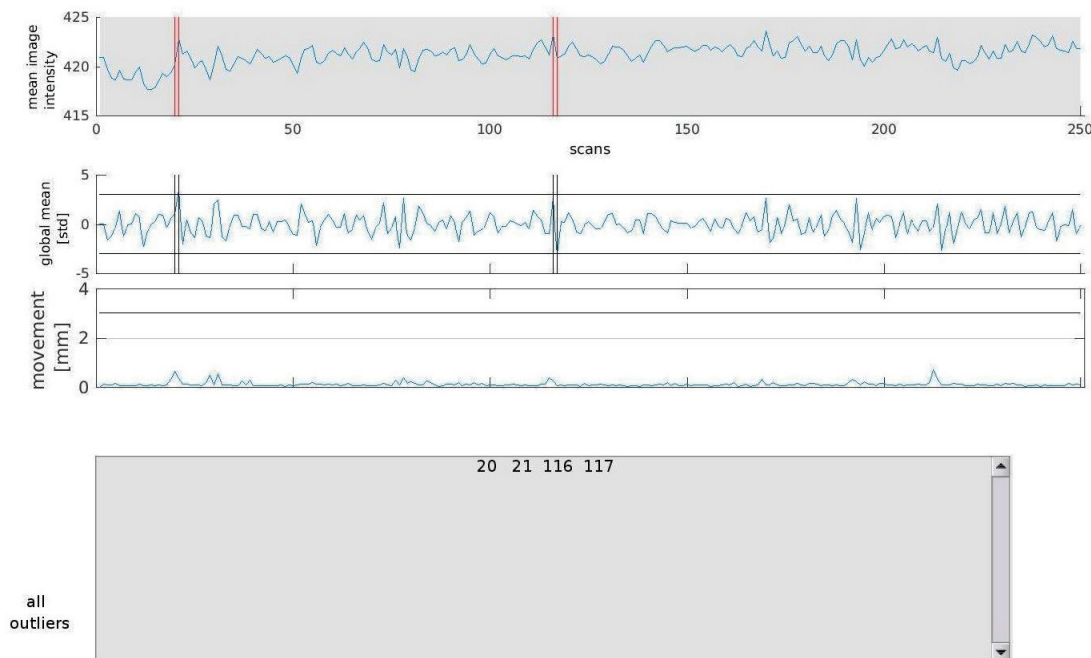


Figure 5.2: Example of a child presenting only 4 scans with a high head motion. Data from our children population.

In the first part of this analysis, subject movement was analyzed with Art Toolbox and the number of the artefacted scans (Art parameters:  $z$ -threshold = 4 and movement-threshold = 3 mm) were computed. In order to study the influence of the movements on the percentage of significant correlations, the correlation matrices were calculated. Exploring these data, we observed that the subjects without any artefacted scans were not the subjects with the highest amount of significant correlations. Thus, no direct relationship were observed between movement and temporal correlations.

However, we chose to exclude from the following analysis the subjects with a number of artefacted scans higher than 20 % of total scans (250). For all the other subjects, a corresponding artifact regressor was constructed for all the scans detected from Art Toolbox. This regressor information together with the movement parameters of each scan were inserted in the time-series extraction in order to regress the contribution of the movement from BOLD time-series.

In the second part of the movement analysis, motion parameters were measured for each subject and compared between the three groups. Indeed, when multiple cohorts are compared, the differences in functional correlations may be affected by

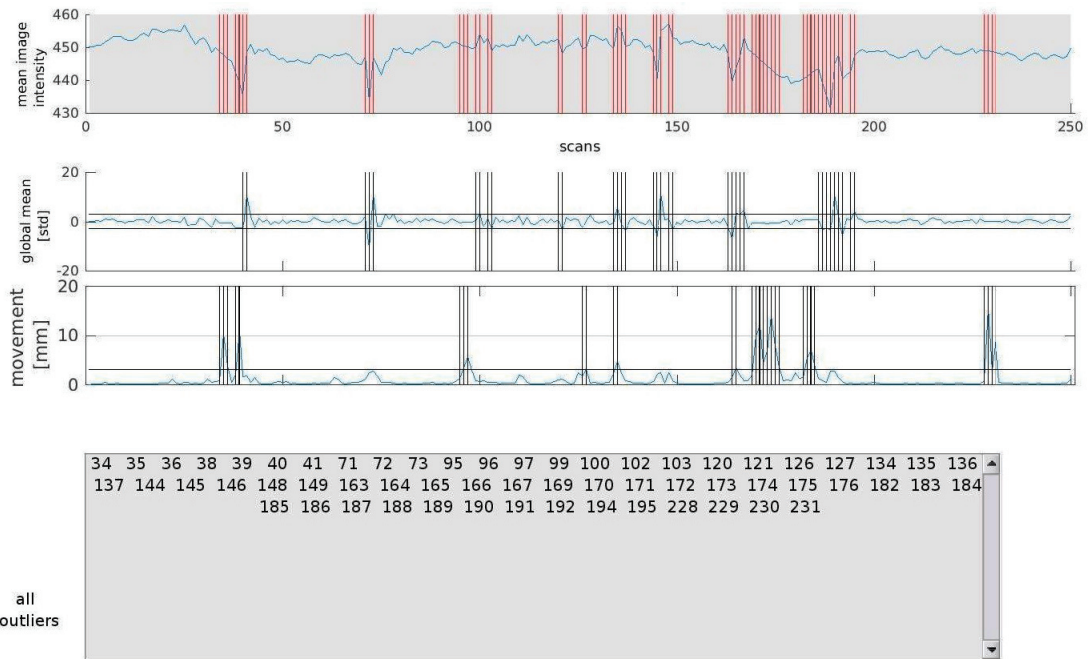


Figure 5.3: Example of a child presenting more than 24% of scans suffering by high head motion that affects resting-state fMRI signal.

the movement in each group [Power *et al.* (2012)]. In order to compare the effect of motion between groups, the six parameters of the rigid body transformation have been condensed into a single parameter: the root mean squared head position change (RMS). The statistical analysis showed that the movement parameters were not statistically different among the three groups. This result confirms that our findings were not influenced by inter-group motion differences.

### 2.3 fMRI signal processing

One of the most controversial procedure in the analysis of resting-state fMRI imaging data is the regression of nuisance signal derived from non-neuronal sources. A common method for correcting for this source of noise is a global signal regression that corrects the covariance of the BOLD signals between voxels, and the mean across all the voxels. On one hand, this technique has been demonstrated to reduce non-neuronal signal [Birn (2012)]. On the other hand, some studies demonstrated that global signal regression may remove also neuronal signal [Chen *et al.* (2012)], and it may introduce artefactual correlations [Murphy *et al.* (2009), Saad *et al.* (2012)]. For these reason, we decided to not apply a global signal regression.

Physiological signals, mainly heart beat and respiration, may introduce confounding factors. As some regions in CSF and WM correlates with these sig-

nals [Perlberg *et al.* (2007)], it was proposed to regress signals from CSF and WM to eliminate contribution from physiological source of noise [Behzadi *et al.* (2007)]. Several studies regress WM and CSF signals from BOLD time-series [Fox and Raichle (2007)]. Power and colleagues demonstrated in a recent study that WM and CSF signals can be correlated to gray matter (GM) signal [Power *et al.* (2017)]. Thus, regressing WM and CSF signals may cause the same consequences than general signal regression.

These findings have led us to investigate the influence of WM and CSF signal regression on the correlation matrices obtained from BOLD time-series. In order to be sure to have only the signal due to BOLD variation and not to other contributions such as subject motion, we applied four different procedures for nuisance signal regression, only on subjects with no movement as revealed by Art Toolbox:

- Method 1: time-series extraction regressing both WM and CSF signals;
- Method 2: time-series extraction regressing only WM signal;
- Method 3: time-series extraction regressing only CSF signal;
- Method 4: time-series extraction without any nuisance signal regression.

Once the correlation matrices were computed from time-series, we counted the number of correlations significantly different from 0 (using R function *const.adj.mat* of brain waver toolbox) given a p-value, FDR corrected, of 0.05.

We reported the resulting percentage obtained using Harvard-Oxford template for each methods for the 6 subjects who did not present any significant head movement in Table 2.3 and a graphical representation in Figure 5.4.

	SIGNAL REGRESSION			
	Method 1	Method 2	Method 3	Method 4
SUBJ #1	19.65	20.51	28.456	39.09
SUBJ #2	4.53	5.25	22.81	50.72
SUBJ #3	6.05	7.06	7.60	11.24
SUBJ #4	3.24	3.18	6.99	24.38
SUBJ #5	5.02	5.85	17.04	21.67
SUBJ #6	9.44	11.45	19.45	23.47

Table 5.1: Percentage of significant correlations in correlation matrix for 6 subjects with no movement artefact for the presented methods from 1 to 4.

Table and Figure 5.4 showed that almost all subjects present a small percentage of significant correlations ( $< 10\%$ ) when regressing both WM and CSF signals. These

results were not improved using the second method. For two subjects, a percentage of significant correlations higher than 10% of the total correlation number was reached. Regressing only CSF signal instead, allowed to considerably increase the number of significant correlations. All but two subjects showed a percentage higher than 15%. Finally, the results obtained using the last method showed a number of significant correlations higher than 10% for all the subjects analyzed without any nuisance signal regression.

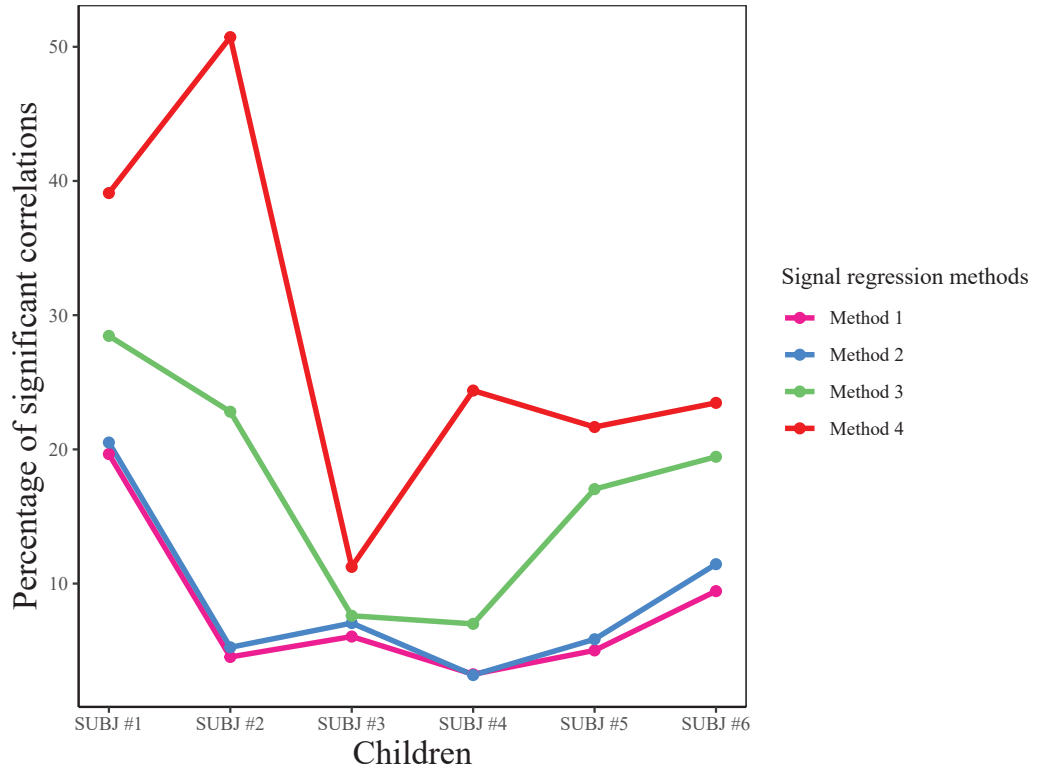


Figure 5.4: Percentage of significant correlation in the correlation matrix derived from the subjects who did not present any significant head motion, obtained using four procedures to extract time-series. Method 1: time-series extraction regressing both WM and CSF signals; Method 2: time-series extraction regressing only WM signal; Method 3: time-series extraction regressing only CSF signal; Method 4: time-series extraction without any nuisance signal regression.

This analysis allowed us to conclude that without any signal regression, we were able to compute the graph analysis. The high loss of significant correlations with WM or/and CSF signal regression could be explained by the contamination of mixed GM and WM voxels or GM and CSF in WM and CSF masks respectively.

In order to limit the contamination from physiological contributions, we weighted fMRI data by the GM probability maps.



## 2.4 Anatomical atlas

Since the nodes of the brain connectivity graphs are defined from the anatomical atlas, the choice of its parcellation is fundamental for the connectivity measurements. Several studies compared connectivity measures obtained with different parcellations, but there was no consensus on the better choice.

In this work, we chose to use two different parcellation schemes to define the graph nodes, and to measure the percentage of significant correlations in the two cases. First, we used Harvard-Oxford atlas that is based on the structural images of 37 healthy adults [Makris *et al.* (2006)]. Second, the nodes have been defined using the Desikan Killiany parcellation obtained from probabilistic information [Desikan *et al.* (2006)]. Both atlases are based on anatomical features, but they are composed of regions that have really different anatomical boundaries.

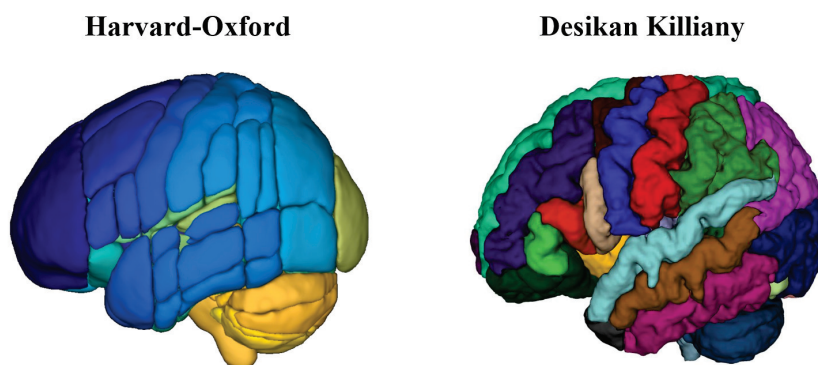


Figure 5.5: Representation of parcellation schemes: on the left, the Harvard-Oxford parcellation and on the right, the Desikan Killiany parcellation.

More in details, Harvard-Oxford parcellation covers 138 regions composed of 48 cortical and 21 subcortical areas for each hemisphere. Desikan Killiany parcellation consists of 84 brain regions. For each subject, we measured the percentage of significant correlations with the two parcellation schemes. An example for the reference group of children with standard intelligence quotient is shown in Figure 5.6

As shown in the previous figure, for each child of the reference group, the Desikan Killiany parcellation allowed to reach a percentage of significant correlations higher than that obtained with the other parcellation. The difference between the percentages values is probably due to the total number of brain areas that compose the parcellation. Indeed consisting of 138 regions, Harvard-Oxford atlas causes a dispersion of significant correlations.

This investigation of two different parcellations have led us to choose Desikan Killiany parcellation scheme for the definition of nodes in the graph analysis. In

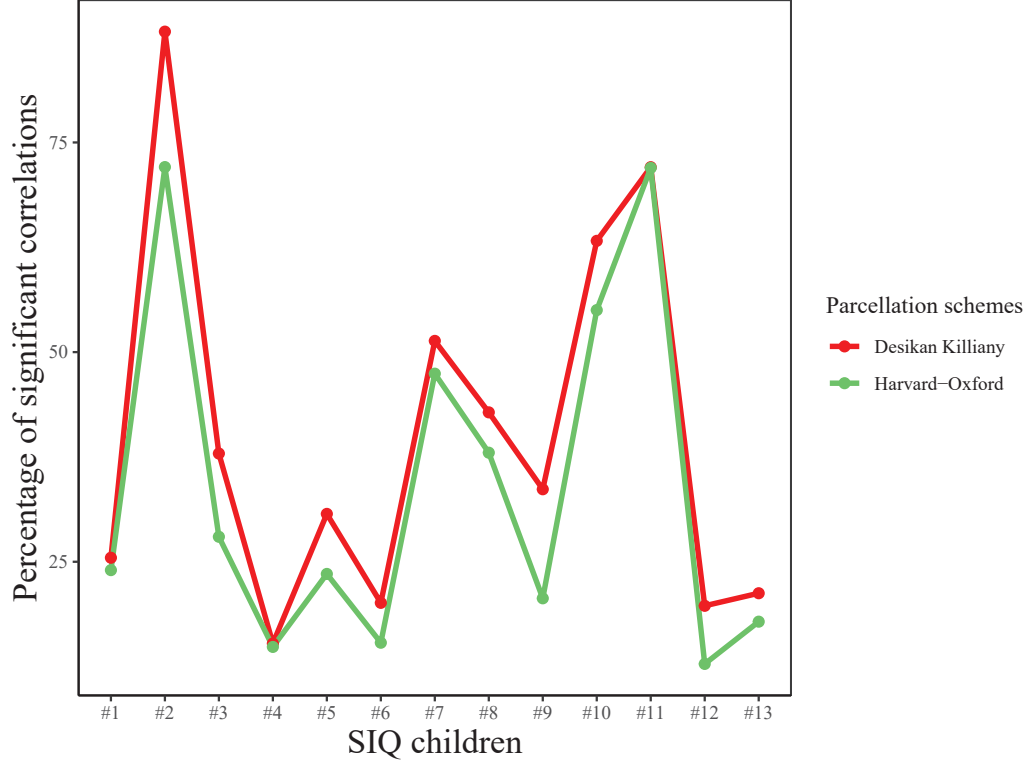


Figure 5.6: Percentage of significant correlation in each subject of the reference group (SIQ) for the two anatomical atlases: in red, Desikan Killiany parcellation and in green, Harvard-Oxford parcellation.

addition, this atlas follows the gyral configuration of the brain.

## 2.5 Wavelet decomposition scale

Once the parcellation scheme has been chosen, time-series were extracted for each cortical and subcortical nodes. At this stage, we decided to apply dyadic wavelet transforms that decomposes time-series, partitioning the total energy, over a set of basis function uniquely scaled in frequency and located in time [Achard *et al.* (2006)]. Time-series were thus decomposed into four scales of dyadic wavelets whose limits are dependent from repetition time (TR):

- scale 1 ranges from  $1/(4 \cdot \text{TR})$  to  $1/(2 \cdot \text{TR})$  (here 0.1 to 0.2 Hz);
- scale 2 from  $1/(8 \cdot \text{TR})$  to  $1/(4 \cdot \text{TR})$  (here 0.05 to 0.1 Hz);
- scale 3 from  $1/(16 \cdot \text{TR})$  to  $1/(8 \cdot \text{TR})$  (here 0.025 to 0.05 Hz);
- scale 4 from  $1/(32 \cdot \text{TR})$  to  $1/(16 \cdot \text{TR})$  (here from 0.0125 to 0.025 Hz).



Based on the fMRI studies literature, it is established that resting-state activity is characterized by slow intrinsic fluctuations of the BOLD signal between 0.01 Hz and 0.1 Hz [Biswal *et al.* (1995)]. Among our four wavelets scales, only two of them respect this range. For this reason, we restricted our analysis to the second and the third wavelet scales representing the frequency ranges [0.05 to 0.1 Hz], and [0.025 to 0.05 Hz], respectively. For each subject, the correlation between wavelet coefficients of all the possible pairs ( $N=84$ ) of the time-series extracted, was calculated for both wavelets scales.

Also in this case, the choice between the two wavelet scales has been driven by the percentage of significant correlations obtained with each of them.

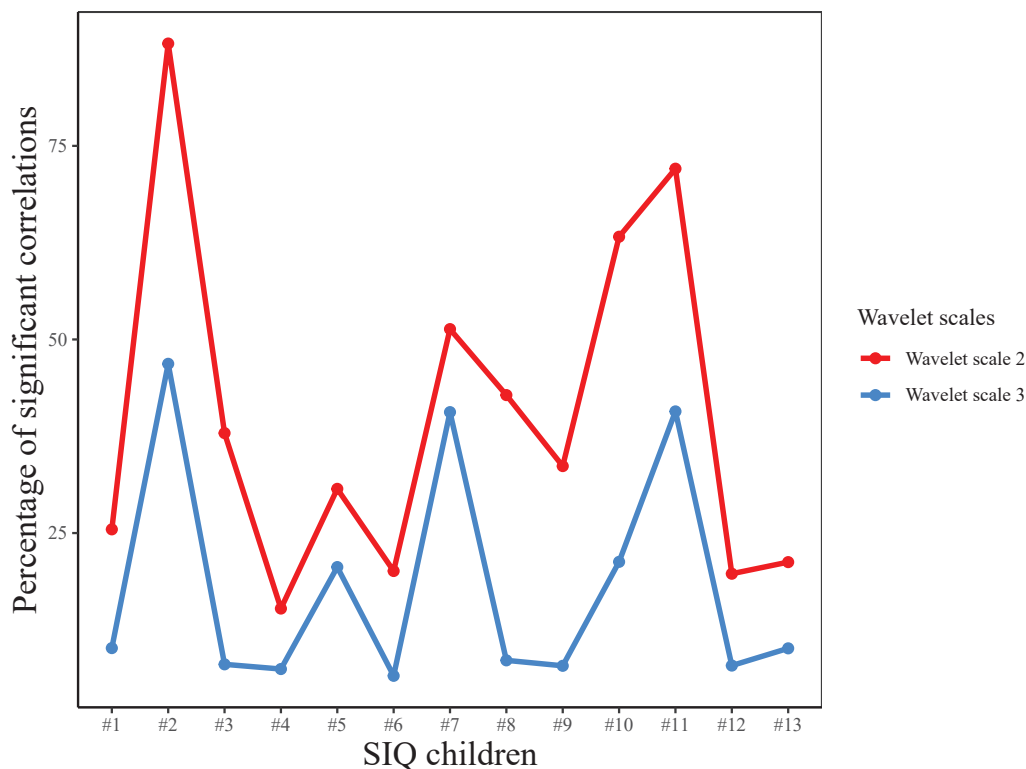


Figure 5.7: Percentage of significant correlations in the correlation matrices derived for each subject of the reference group (SIQ) for the two wavelet scales: in red, wavelet scale 2 and in blue, wavelet scale 3.

Figure 5.7 shows the percentage of significant correlations for each child in the reference group with a standard Intelligence Quotient (SIQ). As shown in the graphic, the second wavelet scale of dyadic decomposition allowed to obtain a percentage of significant correlation that is consistently higher than the other wavelet scale for all the children studied. Indeed, being characterized by a wider frequency range [0.05 Hz - 0.1 Hz], this wavelet scale provides more robust correlations. These findings allowed us to choose this wavelet scale for the following composition of the correlation

matrices.

## 2.6 Graph's cost

In order to conclude the optimization of the processing pipelines, graph analysis was computed on binarized matrix using two graph costs: 0.15 and 0.20. The choice of this values is driven by the study of Termenon et al. who demonstrated that a cost a of 0.20 provides a good reliability of graph metrics [Termenon *et al.* (2016)b]. In fact, our results obtained with the two costs are concordant as reported in Annex. In order to obtain a stronger robustness driven by larger population, a threshold of 0.15 was applied for the graph analysis.

The pipeline obtained from this preprocessing methodological analysis (Figure 5.8) has been applied in the following resting-state fMRI study.

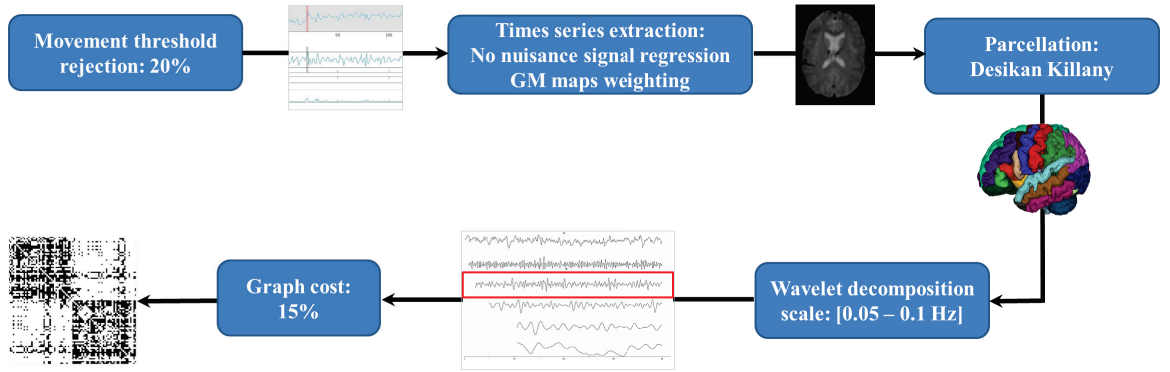


Figure 5.8: Pipeline used in rs-fMRI study detailing all the steps from subject movement to graph cost.

## 3 Materials and Methods

### 3.1 Participants

Fifty-eight children (44 males and 14 females) aged from 8 to 12 years (mean age  $10.1 \pm 1.2$  y.o.) were recruited from the children psychiatry department of Lyon's Neurological Hospital, the PSYRENE Center, a psychological center for High IQ children and adults, and via advertisement in schools for controls. Children with neurological diseases, learning disabilities and psychotropic treatments were excluded from this study. Children underwent the fourth edition of WISC (WISC-IV) test and their FSIQ was established from the results of its four subscales (VCI, PRI, WMI and PSI). Children with a high Intelligence Quotient ( $IQ > 130$ ) were labeled

as HIQ children and two HIQ profiles were defined based on the score difference between VCI and PRI (Table 5.2). This prospective study was approved by the local ethics committee (CPP Sud-Est IV) and the French national agency for medicine and health products safety (ANSM). Written informed consent was obtained from the two parents of all participants.

	SIQ	HIQ	Hom-HIQ	Het-HIQ
	(n=12)	(n=37)	(n=15)	(n=22)
Age	10.0 $\pm$ 1.1	10.0 $\pm$ 1.1	9.8 $\pm$ 0.8	10.1 $\pm$ 1.3
FSIQ	104.1 $\pm$ 8.5	134.1 $\pm$ 12.3 ***	141.6 $\pm$ 11.8	129.3 $\pm$ 10.2 #
VCI	108.1 $\pm$ 6.8	143.0 $\pm$ 9.8 ***	141.6 $\pm$ 12.5	143.9 $\pm$ 8.0
PRI	97.7 $\pm$ 6.9	124.1 $\pm$ 13.8 ***	136.4 $\pm$ 9.2	116.8 $\pm$ 10.5 ##
WMI	95.6 $\pm$ 10.3	117.2 $\pm$ 15.3 ***	125.3 $\pm$ 15.5	112.0 $\pm$ 13.0 #
PSI	102.3 $\pm$ 15.1	107.8 $\pm$ 16.8	114.3 $\pm$ 18.4	103.8 $\pm$ 14.9

Table 5.2: Population characteristics (Mean  $\pm$  SD): age, full scale IQ (FSIQ), Verbal Comprehension Index (VCI), Perceptual Reasoning Index (PRI), Processing Speed Index (PSI), and Working Memory Index (WMI) for Standard Intelligence Quotient (SIQ), High Intelligence Quotient (HIQ) groups and HIQ subgroups: Homogeneous (Hom-HIQ) and Heterogeneous (Het-HIQ). \*\*\*  $p < 0.001$  when comparing HIQ and SIQ using a Wilcoxon test;  $p < 0.01$ ;  $p < 0.001$  when comparing Hom-HIQ and Het-HIQ using Dunn’s post-hoc test after the comparison of SIQ, Hom-HIQ and Het-HIQ using Kruskal-Wallis test.

### 3.2 MRI acquisition

MRI examinations were performed on a 1.5T Siemens Sonata MRI system (Erlangen, Germany) with an 8-channel head-coil at the MRI department of CERMEP-Imagerie du Vivant. A structural 3D T1-weighted MPRAGE sequence was first acquired in the sagittal plane with a 1mm isotropic spatial resolution (TI/TE/TR = 1100/3.93/1970 ms, FOV: 256 x 256 x 176 mm, 8 min acquisition duration). Then a full examination with task fMRI, DTI and rs-fMRI was conducted. rs-fMRI data were recorded using an EPI BOLD sequence (250 scans, TR = 2500 ms, TE = 50 ms, voxel size = 3.4 x 3.4 x 3 mm) while subjects lay quietly at rest with eyes open and fixating on a projected cross for 10.3 min. For this study, only the rs-fMRI (at the end of the exam) is reported.

### 3.3 Data preprocessing

The rs-fMRI data were preprocessed using SPM12 software (<https://www.fil.ion.ucl.ac.uk/spm/software/spm12>). For each subject, functional images were corrected

for delay between slice acquisitions, motion, and co-registered to the anatomical image. Time-series data were not spatially smoothed because the smoothing step introduces spurious spatial correlations between adjacent regions [Fornito *et al.* (2010)]. Using Art toolbox that evaluates the scans affected by scan-to-scan motion, we scrubbed the data carefully. When scans with movements greater than 3 mm or with an exceptionally high variation (signal higher than 4 standard deviations from mean) were found, a corresponding artifact regressor was constructed. Subject's data was excluded if more than 20% of the available scans were affected by head motion. Motion parameters for each group were measured and compared among the groups to verify that the correlation results were not influenced by inter-group motion differences [Power *et al.* (2012)]. The anatomical MRI from each participant was segmented into six different brain and non-brain tissues according to prior tissue probability maps. This step generates gray-matter (GM), white-matter (WM) and cerebrospinal fluid (CSF) probability maps that will be eventually be used to extract time-series to compute the graph. These maps were further normalized to the MNI152 template using DARTEL, a diffeomorphic registration method that accurately align brains within the MNI space [Ashburner (2007)]. This registration provides a deformation field that was then applied to functional and anatomical images to be later used to extract the time-series to compute the graphs. The structural images were parcellated into 84 cortical, subcortical and cerebellar areas according to the Desikan Atlas [Desikan *et al.* (2006)]. Regional mean time-series were estimated by averaging the fMRI time-series over all voxels in each parcel weighted by GM probability map using the Conn Toolbox (<https://www.nitrc.org/projects/conn>). Finally, time-series were regressed by the residual contamination from motion parameters and outliers detected using the ART toolbox and band-pass filtering was applied using wavelets transforms.

### 3.4 Wavelets decomposition

Following the approach proposed by Achard *et al.*, time-series were decomposed using dyadic wavelet transforms that subdivides the total energy of a signal over a set of compactly supported basis functions, each of which is uniquely scaled in frequency and located in time [Achard *et al.* (2006)]. The pairwise interregional correlations between wavelets coefficients of fMRI time-series extracted from each individual data set were estimated for 4 wavelet scales. Because frequencies below 0.1 Hz contain relevant information in resting-state fMRI, we restricted our analysis to two wavelet scales: the scale 2 from  $f = 1/(8 \text{ TR})$  to  $f = 1/(4 \text{ TR})$ , that represents the frequency interval 0.05 - 0.1 Hz, and the scale 3 from  $f = 1/(16 \text{ TR})$  to  $f = 1/(8 \text{ TR})$ , that

represents the frequency interval 0.025 - 0.05 Hz. At this stage, we measured the percentage of significant correlations obtained for the two scales. Since the wavelet scale 2 presents a higher percentage of significant correlations, we chose to proceed with the graph computation using only the correlation matrices of this scale.

### 3.5 Graph construction

To construct the binarized graph, two steps are necessary. Following Alexander-Bloch, we kept the graph fully connected, using the minimum spanning tree based on the absolute correlation matrix [Alexander-Bloch *et al.* (2012)]. This creates a preliminary graph that contains a number of edges equal to the number of nodes minus one. In the second step, the remaining absolute values of the correlation matrices were thresholded to create an adjacency matrix that defines, for each subject, an unweighted and undirected graph using two graph costs: 15% and 20%. The choice of these values was guided by the results of a test-retest study of graph metrics derived from graph analysis of rs-fMRI dataset, where the cost of about 20% provides a good reliability of all graph metrics [Termenon *et al.* (2016)a]. Since our results obtained with the two costs were concordant, we reported in this study those related to 15%, allowing a larger inclusion of subjects and a greater robustness of the correlations. After having verified that the small-world property was satisfied for each subject and that the topology of the three groups were the same, four topological metrics were estimated for each node using Brain Connectivity Toolbox (<http://www.brain-connectivity-toolbox.net/>): degree, betweenness centrality, local efficiency, and clustering. When the graph was computed with the 84 regions from the Desikan atlas, we referred to it as the “whole brain networks” in the manuscript. When the graph was computed with the 42 regions of the right (or left) hemisphere, we referred to it as the “right hemispheric networks” (or the “left hemispheric networks”). Finally, we considered the connectivity related to the homotopic regions: 42 nodes in each hemisphere as the “homotopic connectivity”.

### 3.6 Hub Disruption Index ( $\kappa$ ) estimation

Introduced by Achard *et al.* [Achard *et al.* (2012)], the "Hub Disruption Index" describes the topological changes of an individual subject brain networks with respect to a referential networks topology from a group of reference subjects. To understand how this index is defined, consider a nodal metric, for example the degree, and plot the degree value of each node for a SIQ subject against the average degrees of the corresponding nodes in the SIQ group (Figure 5.9.A). Since for a SIQ

subject, the nodal metric values are close to the average value for the same node computed in the SIQ group, the distribution of the points falls approximately on a positive slope line ( $y = x$ ). Constructing the same plot for a HIQ subject, we can observe that the point cloud does not scatter around the same slope (Figure 5.9.B), so they are not well predicted by the SIQ average degree. For each nodal metric,  $\kappa$  is defined following several steps. The SIQ group mean metric of each node was first subtracted from the metric of the corresponding node in an individual subject. This difference was further plotted against the SIQ group mean for all the nodes and the gradient of the linear regression that models this points cloud represents  $\kappa$ . According to this definition, data of a SIQ subject will scatter around a horizontal line ( $\kappa \sim 0$ ) (Figure 5.9.C), while for a HIQ subject data will follow a negative slope ( $\kappa < 0$ ) (Figure 5.9.D).  $\kappa$  index was calculated for the degree, the betweenness centrality, the local efficiency and the clustering coefficient in whole brain networks ( $\kappa_D$ ,  $\kappa_{BC}$ ,  $\kappa_{LE}$  and  $\kappa_{CC}$ ) and in both left ( $\kappa_D^L$ ,  $\kappa_{BC}^L$ ,  $\kappa_{LE}^L$  and  $\kappa_{CC}^L$ ) and right ( $\kappa_D^R$ ,  $\kappa_{BC}^R$ ,  $\kappa_{LE}^R$  and  $\kappa_{CC}^R$ ) networks, and for functional homotopic connectivity ( $\kappa^{HC}$ ).

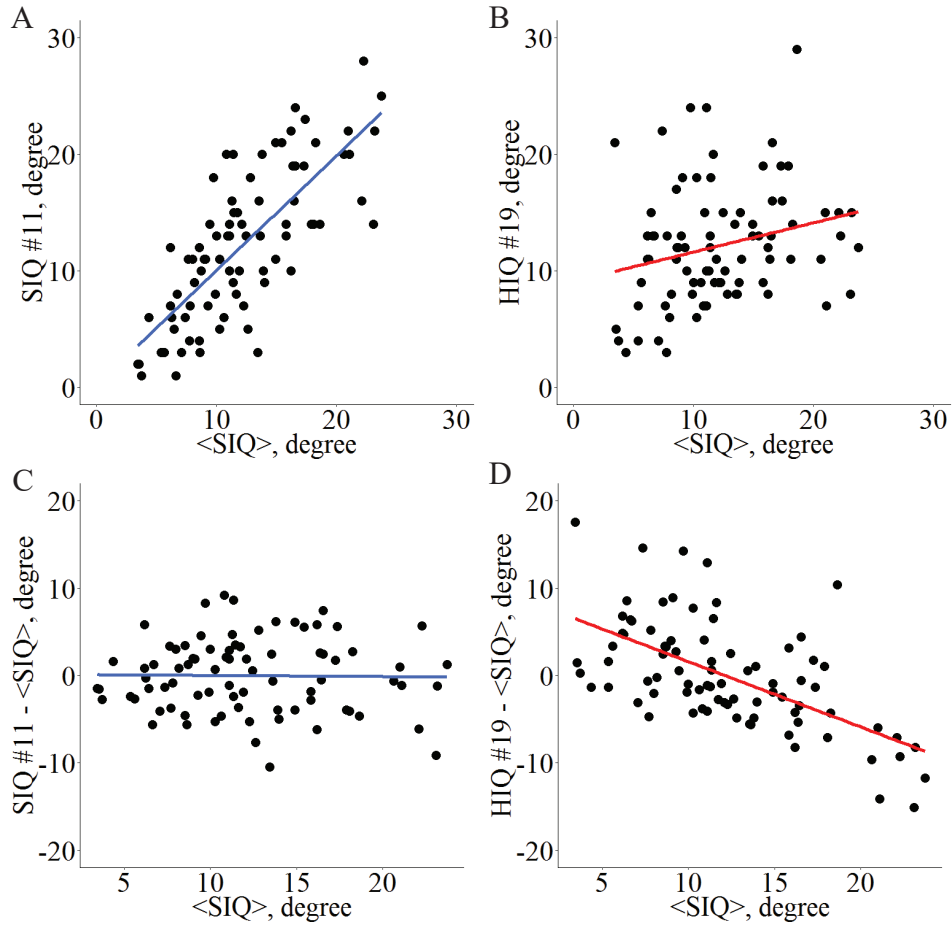


Figure 5.9: Hub disruption index  $\kappa$  computation for nodal degree metric. Given a set of nodes from an atlas  $N_i, i \in [1, n]$ , and a nodal metric  $M$ , each node  $i$  presents a value  $M_i, i \in [1, n]$  for a given subject. Across a set of reference subjects  $R_j, j \in [1, m]$ , the averaged nodal metric can be computed  $\langle M_i \rangle_R$ . For each individual  $I_k, k \in [1, \rho]$ , whatever its status (patient, HIQ child, or healthy subject), its metric in each node is  $M_{i,I_k}$  and the difference in nodal metric with the reference group is  $M_{i,I_k} - \langle M_i \rangle_R$ . The scatterplot with all nodes is computed with  $\langle M_i \rangle_R$  in abscissa and  $M_{i,I_k} - \langle M_i \rangle_R$  in ordinates. For each node  $i$ , if the nodal metric is close to the reference's nodal metric, then the linear trend of this plot is about 0. Conversely, if the nodal metrics are reduced in some nodes and increased in others, then the linear trend will differ from 0.  $\kappa$  is the slope of the regression line computed on this scatter plot. Example for the nodal degree (D) as metric of interest.  $D_{i,I}$  vs.  $\langle D_i \rangle_R$  for a standard intelligence quotient (SIQ) child (A) and for a high intelligence quotient (HIQ) child (B),  $D_{i,I} - \langle D_i \rangle_R$  vs.  $\langle D_i \rangle_R$  for a SIQ child (C) is scattered around a horizontal line ( $\kappa \sim 0$ ), whereas for a HIQ child (D) is scattered around a negatively sloping line ( $\kappa < 0$ ).

### 3.7 Statistical analysis

First, statistical differences between  $\kappa$  indices of each group were computed using permutation tests, by randomly reassigning subjects to three groups: 12 children played the role of the SIQ group, 15 of Hom-HIQ group and 22 of Het-HIQ group. For each subject,  $\kappa$  was computed following its definition. This process was repeated for 1000 permutations of the data to sample the null distribution of  $\kappa$ . The p-value was computed counting how many times the  $\kappa$ -values were higher than the one obtained using the true SIQ and HIQ groups. As the  $\kappa$  definition is based on the reference group (SIQ), its homogeneity was controlled using the Grubbs' test. One outlier was identified and excluded from the SIQ group. Furthermore, as nodes could play different roles in brain networks organization, we tested for metric differences in graph's nodes between each HIQ group and SIQ. A statistical analysis was performed at each node using a non-parametric Wilcoxon test and a Benjamini-Hochberg correction for multiple comparisons. Second, the correlations between intelligence scores (FSIQ, VCI, PRI) and hub disruption index ( $\kappa$ ) were analyzed using a non-parametric Spearman correlation coefficient ( $\rho$ ) controlling for sex. Correlation significance level was evaluated replicating a permutation test, by randomly reassigning WISC-IV scores to the subjects, for 1000 iterations. The p-value was computed counting how many times the  $\rho$ -values were higher than the one obtained with our true intelligence scores and corrected for multiple comparisons using the Benjamini-Hochberg correction. All statistical analyses were computed on R (<http://www.R-project.org/>) and since the groups were matched in age, with



small standard deviation values. No regression of age effect was applied.

## 4 Results

### 4.1 Modifications of FC organization with intelligence

In the whole brain networks, HIQ children showed significant differences in hub disruption indices of several graph metrics, namely  $\kappa_D$  ( $p < 0.01$ ),  $\kappa_{CC}$  ( $p < 0.05$ ) and  $\kappa_{LE}$  ( $p < 0.05$ ), compared to SIQ children (Table 5.3.A and Figure 5.10). These results suggest significant topological modifications in the graph's integration and segregation properties. Locally, D was significantly decreased in the left dorsolateral prefrontal cortex (BA 9-10-46) ( $p < 0.01$ ), indicating decreased prefrontal functional connectivity in HIQ children (Figure 5.11.A). These networks changes were further assessed in the two HIQ subgroups separately, relative to the SIQ group. The Hom-HIQ group didn't show any significant changes, whereas the Het-HIQ group showed significant changes in integration and segregation properties related to all graph metrics (Table 5.3.A and Figure 5.10).

Networks	$\kappa$	HIQ (n=37)	Hom-HIQ (n=15)	Het-HIQ (n=22)
A. Whole brain	$\kappa_{BC}$	-0.472	-0.475	-0.470
	$\kappa_D$	-0.317 (**)	-0.228	-0.378 (**)
	$\kappa_{LE}$	-0.291 (*)	-0.201	-0.352 (*)
	$\kappa_{CC}$	-0.350 (*)	-0.259	-0.413 (*)
B. Left hemisphere	$\kappa_{BC}^L$	-0.399	-0.396	-0.402
	$\kappa_D^L$	-0.299 (**)	-0.306 (*)	-0.294 (**)
	$\kappa_{LE}^L$	-0.340	-0.299	-0.369
	$\kappa_{CC}^L$	-0.399	-0.342	-0.438
C. Right hemisphere	$\kappa_{BC}^R$	-0.311	-0.292	-0.324
	$\kappa_D^R$	-0.228	-0.070	-0.336 (*)
	$\kappa_{LE}^R$	-0.364	-0.209	-0.471 (*)
	$\kappa_{CC}^R$	-0.406	-0.264	-0.502
D. Homotopic	$\kappa^{HC}$	-0.198 (*)	-0.214 (*)	-0.187 (*)

Table 5.3: Reorganization indices ( $\kappa$ ) in High Intelligence Quotient (HIQ), Homogeneous HIQ (Hom-HIQ) and Heterogeneous HIQ (Het-HIQ) groups measured in whole brain networks (A), left and right hemispheres networks (B, C) and between homotopic regions (D).

\*  $p < 0.05$ ; \*\*  $p < 0.01$ ; when testing significance of values in HIQ, Hom-HIQ or Het-HIQ groups compared to SIQ group using permutation test (number of permutations = 1000).



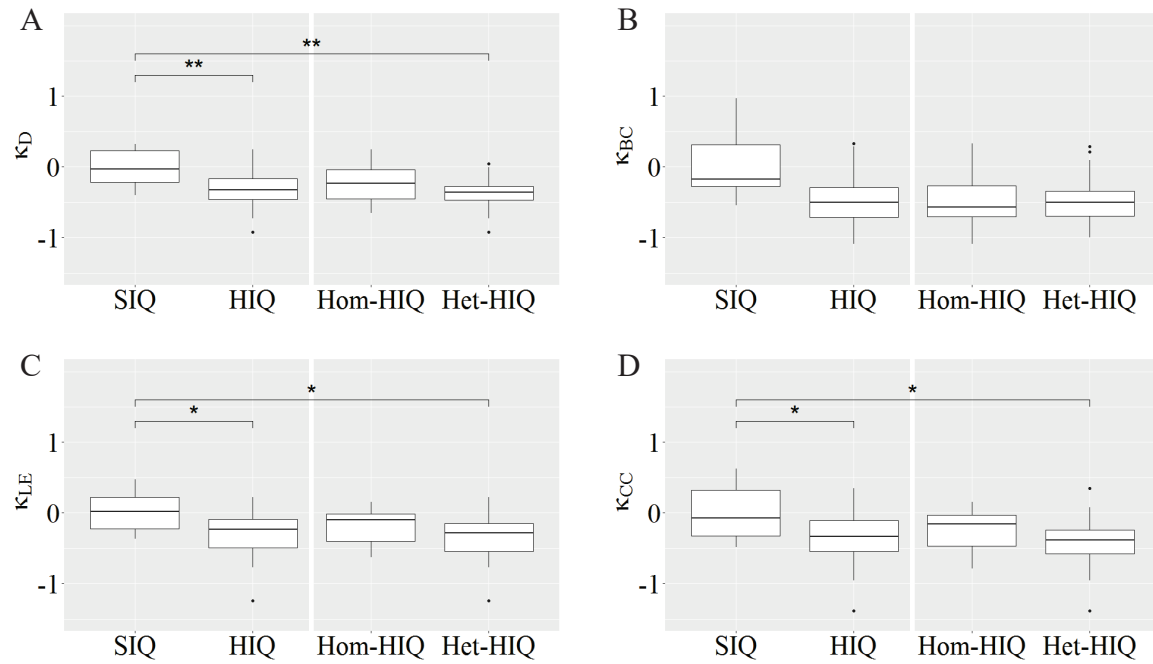


Figure 5.10: Boxplot (first quartile, median and third quartile) of  $\kappa$  values in Standard Intelligence Quotient (SIQ), High Intelligence Quotient (HIQ) groups, and its Homogeneous HIQ (Hom-HIQ), and Heterogeneous HIQ (Het-HIQ) subgroups for each graph metrics in the whole brain networks: A) Degree (D), B) Betweenness Centrality (BC), C) Local Efficiency (LE), and D) Clustering Coefficient (CC). \*  $p < 0.05$ ; \*\*  $p < 0.01$ ; when testing significance of  $\kappa$  values in HIQ, Hom-HIQ or Het-HIQ groups compared to SIQ group using permutation test (number of permutations = 1000).

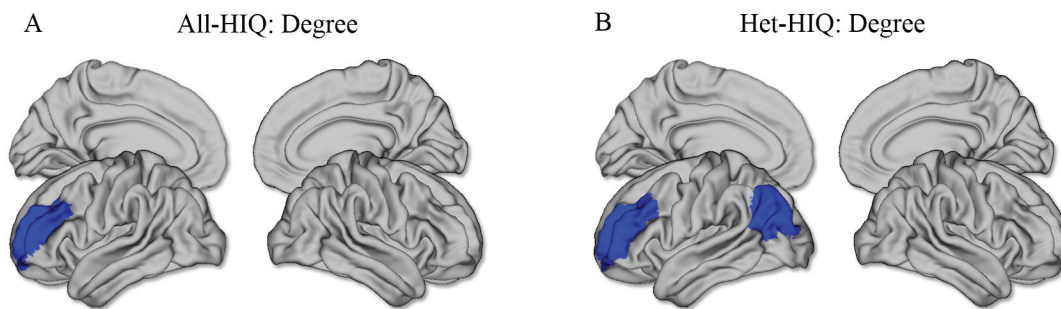


Figure 5.11: Local results: (A) significant decreased nodal degree metric in left dorsolateral prefrontal nodes when comparing all High Intelligence Quotient (All-HIQ) and Heterogeneous High Intelligence Quotient (Het-HIQ) to Standard Intelligence Quotient (SIQ) groups in whole brain networks analysis; (B) trend for decreased nodal degree metric in left inferior parietal cortex when comparing Het-HIQ to SIQ.

A significant degree reduction was also locally observed in the left dorsolateral prefrontal node ( $p < 0.01$ ) of the Het-HIQ group, while a trend towards a de-

creased degree was measured in the left inferior parietal cortex ( $p < 0.1$ ) (Figure 5.11.B). Since the neural substrate of high intelligence may be related to hemispheric characteristics [Hearne *et al.* (2016), Nusbaum *et al.* (2017)], we additionally explored the topological changes of brain FC organization by computing the  $\kappa$  values of intra-hemispheric networks connectivity (ignoring inter-hemispheric connectivity). In the left hemisphere, only integration properties measured by  $\kappa_D$  ( $p < 0.01$ ) were significantly reorganized in the HIQ group, compared to the SIQ group (Table 5.3.B). Specifically, nodal analysis showed a significant degree reduction ( $p < 0.01$ ) in the left dorsolateral prefrontal node (BA 9-10-46) (Figure 5.12.A). No significant changes were found in the right hemisphere (Table 5.3.C). When exploring the intra-hemisphere graph networks of each HIQ subgroup, significant modifications of integration properties were found in the left hemisphere of both Hom-HIQ ( $p < 0.05$ ) and Het-HIQ groups ( $p < 0.01$ ), relative to SIQ (Table 5.3.B). This difference was locally highlighted by a D reduction in the left dorsolateral prefrontal cortex of the Het-HIQ group (Figure 5.12.A).

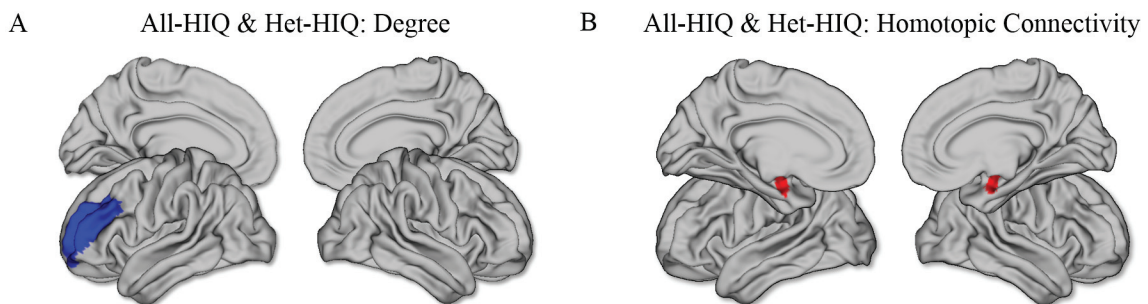


Figure 5.12: Local results: (A) significant decreased nodal degree metric in left dorsolateral prefrontal nodes when comparing all High Intelligence Quotient (All-HIQ) and Heterogeneous High Intelligence Quotient (Het-HIQ) to Standard Intelligence Quotient (SIQ) groups in hemispherical network analysis; (B) trend for increased functional connectivity in amygdala nodes when comparing All-HIQ, and Het-HIQ to SIQ.

While right hemisphere networks were not significantly modified in the Hom-HIQ group, integration and segregation properties, measured by D ( $p < 0.05$ ) and LE ( $p < 0.05$ ), were significantly changed in the Het-HIQ group (Table 5.3.C and Figure 5.13). In sum, both HIQ groups showed modifications of integration properties in the left hemisphere, while only the Het-HIQ profile showed changes of integration and segregation properties in the right hemisphere.

Since homotopic FC has been shown to correlate with IQ [Santarnecchi *et al.* (2015)b], we analyzed the FC between homotopic regions in each HIQ group by measuring their  $\kappa$  indices. Significant changes ( $p < 0.05$ ) in homotopic connectivity

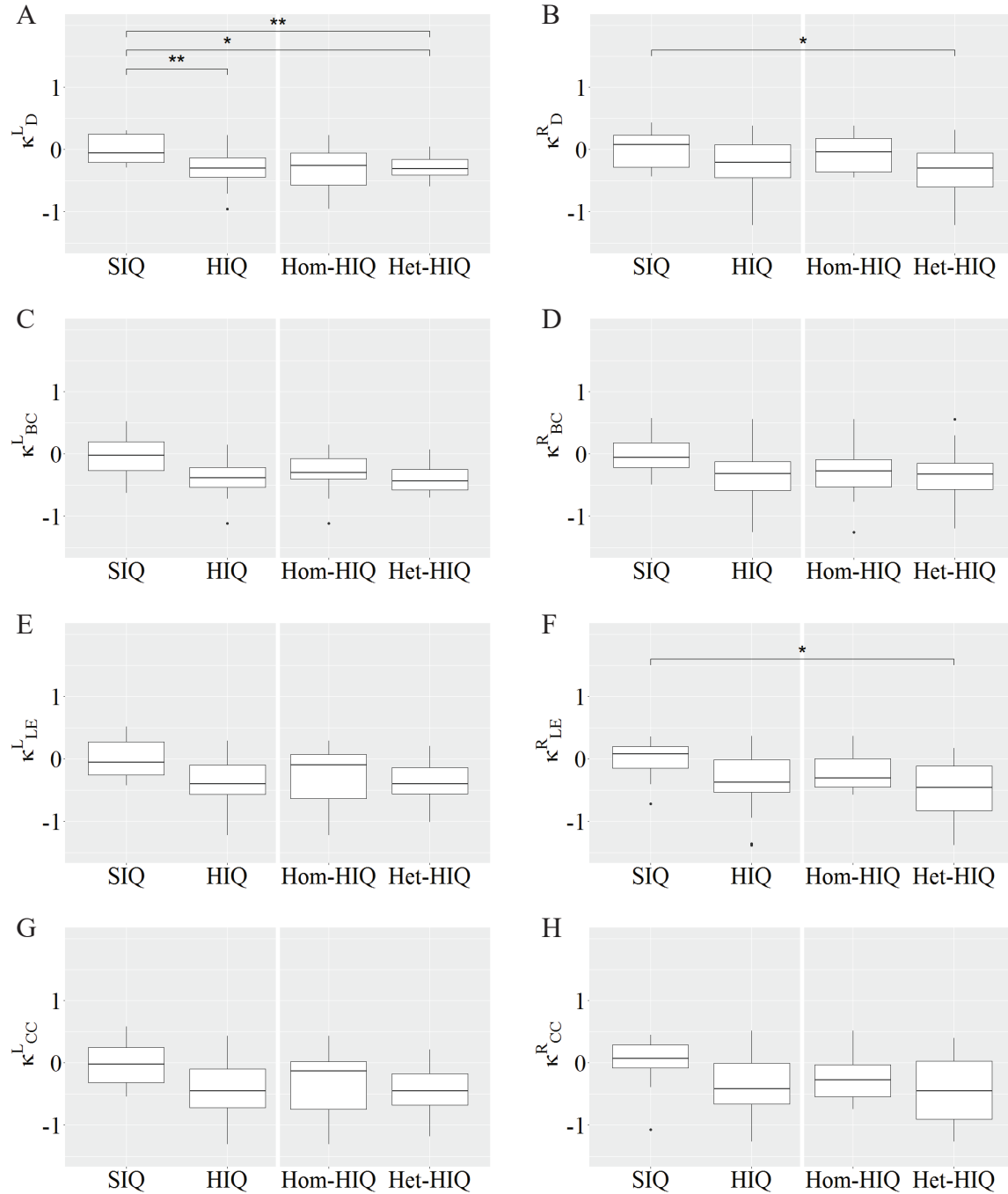


Figure 5.13: Boxplot of  $\kappa$  values of the left (A, C, E, G) and the right (B, D, F, H) hemispheres networks in SIQ, HIQ groups, and its Hom-HIQ, and Het-HIQ subgroups for each graph metrics: A-B) Degree (D); C-D) Betweenness Centrality (BC); E-F) Local Efficiency (LE), and G-H) Clustering Coefficient (CC). \* $p < 0.05$ ; \*\* $p < 0.01$ ; when testing significance of  $\kappa$  values in HIQ, Hom-HIQ or Het-HIQ compared to SIQ group using permutation test (number of permutations = 1000).

were found in the HIQ group compared to the SIQ group (Table 5.3.D). Exploring the two HIQ subgroups separately, significant changes ( $p < 0.05$ ) of the homotopic

FC were found in both Hom-HIQ and Het-HIQ groups (Table 5.3.D and Figure 5.14). At a regional level, a trend towards increased homotopic FC was found in the amygdala nodes of the Het-HIQ group ( $p < 0.1$ ) (Figure 5.12.B).

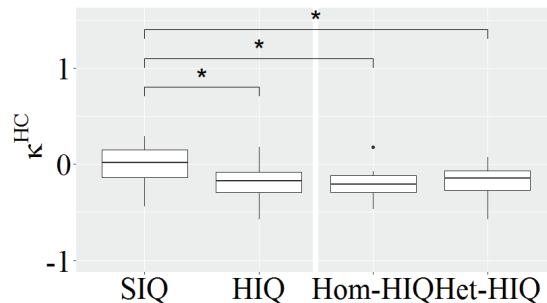


Figure 5.14: Boxplot of  $\kappa$  values of functional connectivity between homotopic regions network in SIQ, HIQ groups, and its Hom-HIQ, and Het-HIQ subgroups. \*  $p < 0.05$  when testing significance of  $\kappa$  values in HIQ, Hom-HIQ or Het-HIQ groups compared to SIQ group using permutation test (number of permutations = 1000).

## 4.2 Correlations between FC organization and intelligence

We further investigated how these topological organization changes could be related to the high abilities of HIQ children. A correlation analysis between the previously measured  $\kappa$  indices and the different IQ scales was performed in different brain networks.

In the whole brain networks, significant negative correlations were found between the hub disruption indexes, related to integration ( $\kappa_D$ ) or hubness ( $\kappa_{BC}$ ) properties, and the FSIQ and VCI (Table 5.4.A). As shown in Figure 5.15, the higher the FSIQ, the greater the hub disruption index, thereby reflecting a high sensitivity of  $\kappa_{BC}$  to highlight the differences in FSIQ.  $\kappa_{BC}$  was also correlated ( $p < 0.05$ ) with PRI and WMI (Figure 5.17-5.18).

In addition, VCI significantly ( $p < 0.05$ ) correlated with all the hub disruption indices ( $\kappa_{BC}$ ,  $\kappa_D$ ,  $\kappa_{LE}$  and  $\kappa_{CC}$ ) (Table 5.4.A and Figure 5.16). When separately exploring the networks in the left hemisphere, FSIQ and PRI were negatively correlated with modifications of integration and segregation metrics ( $\kappa_D^L$ , and  $\kappa_{LE}^L$ ) ( $p < 0.05$ ), while VCI was correlated only with the modifications of segregation metrics ( $\kappa_{CC}^L$  and  $\kappa_{LE}^L$ ) ( $p < 0.05$ ). In the right hemisphere, only the segregation metrics changes ( $\kappa_{CC}^R$  and  $\kappa_{LE}^R$ ) were significantly correlated ( $p < 0.05$ ) with VCI (Figure 5.16). Finally, the strongest correlations ( $p < 0.01$ ) were observed between the hub disruption index in homotopic regions ( $\kappa^{\text{HC}}$ ) and the three major intelligence subscales, namely FSIQ, VCI and PRI (Figure 5.15-5.17).

Networks	$\kappa$	FSIQ	VCI	PRI
A. Whole brain	$\kappa_{BC}$	-0.344 (*)	-0.316 (*)	-0.306 (*)
	$\kappa_D$	-0.277 (*)	-0.310 (*)	-0.218
	$\kappa_{LE}$	-0.153	-0.250 (*)	-0.138
	$\kappa_{CC}$	-0.133	-0.253 (*)	-0.131
B. Left hemisphere	$\kappa_{BC}^L$	-0.250	-0.138	-0.107
	$\kappa_D^L$	-0.267 (*)	-0.213	-0.295 (*)
	$\kappa_{LE}^L$	-0.290 (*)	-0.305 (*)	-0.255 (*)
	$\kappa_{CC}^L$	-0.250	-0.279 (*)	-0.228
C. Right hemisphere	$\kappa_{BC}^R$	-0.143	-0.171	-0.100
	$\kappa_D^R$	-0.172	-0.223	-0.028
	$\kappa_{LE}^R$	-0.209	-0.261 (*)	-0.115
	$\kappa_{CC}^R$	-0.226	-0.260 (*)	-0.135
D. Homotopic	$\kappa^{HC}$	-0.396 (**)	-0.431 (**)	-0.379 (**)

Table 5.4: Coefficients of non-parametric correlations ( $\rho$ ) between the topological reorganization coefficient ( $\kappa$ ) of different nodal metrics (Betweenness Centrality (BC), Degree (D), Local Efficiency (LE), and Clustering (CC), and Homotopic Connectivity (HC)) with intelligence scores (Full Scale IQ (FSIQ), Verbal Comprehension Index (VCI) and Perceptual Reasoning Index (PRI)) at different network levels: whole brain (A), left and right hemispheres (B and C) and homotopic regions (D). \*  $p < 0.05$ ; \*\*  $p < 0.01$ ; when testing significance of values in HIQ, Hom-HIQ or Het-HIQ groups compared to SIQ group using permutation test (number of permutations = 1000).

## 5 Discussion

The hub disruption index  $\kappa$  was used in this study, on one hand, to uncover the topological organization modification of brain networks in children with high intelligence, and on the other hand, to investigate whether these changes could be related to their specific cognitive profiles.

### 5.1 Brain networks changes with high intelligence

Our study provided evidence that FC networks in HIQ children undergo modifications of integration and segregation properties, in comparison to SIQ children. Indeed,  $\kappa_D$  (related to integration properties) as well as  $\kappa_{LE}$  and  $\kappa_{CC}$  (related to networks segregation properties) were modified in the whole brain networks, while only  $\kappa_D$  was changed in the left hemisphere of HIQ children. This last result was observed in both subgroups of HIQ children, showing a common integration properties changes in the left hemisphere. Conversely, in the right hemisphere, modifications of integration and segregation properties were only highlighted in the Het-HIQ subgroup. These changes in integration properties support the hypothesis that intelligence is

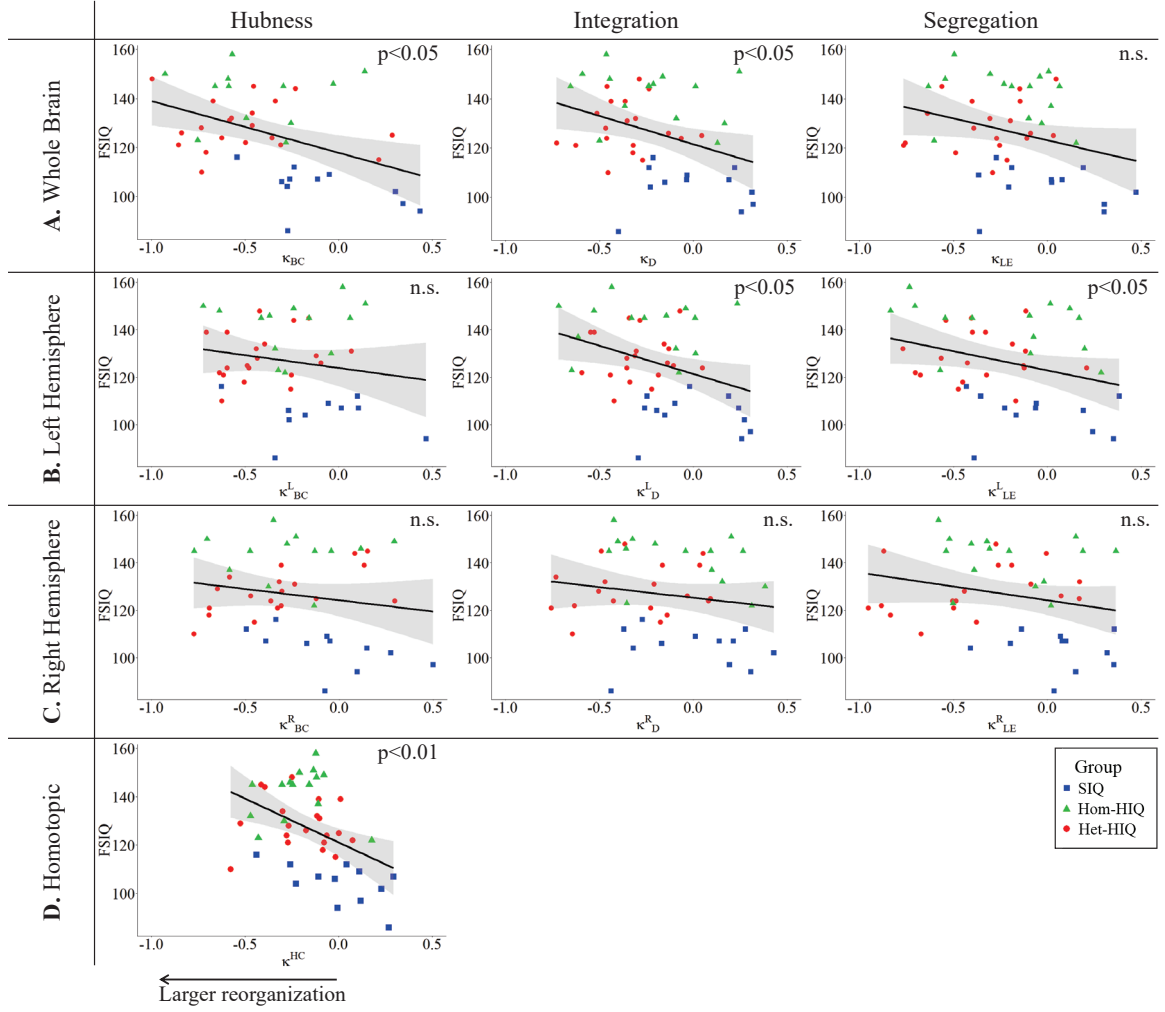


Figure 5.15: Correlations between Full Scale Intelligence Quotient (FSIQ) and reorganization indices ( $\kappa$ ) of graph metrics measured in: (A) the whole brain networks, (B) the left hemisphere networks, (C) the right hemisphere networks and (D) the homotopic nodes. Significant correlations were measured for  $\kappa$  describing hubs ( $\kappa_{BC}$ ) and integration properties ( $\kappa_D$ ) in the whole brain network, for integration and segregation properties in the left hemisphere network ( $\kappa_D^L$  and  $\kappa_{LE}^L$ ) and for homotopic connectivity ( $\kappa_{HC}$ ). No significant correlations were found in the right hemisphere network.

based on better neural efficiency, which promotes better information transmission. Our results are in concordance with previous observations of greater FC associated with high intelligence in certain regions of the fronto-parietal and default mode networks [Basten *et al.* (2015), Hearne *et al.* (2016), Jung and Haier (2007)], two nodes of the salience network, and one node of the DMN [Hilger *et al.* (2017)a].

The WISC-IV test provides a global index (FSIQ), as well as four subscales including verbal (VCI) and non-verbal (PRI) indices, that are sensitive to different cognitive capabilities. Based on a significant difference between these two subscales,

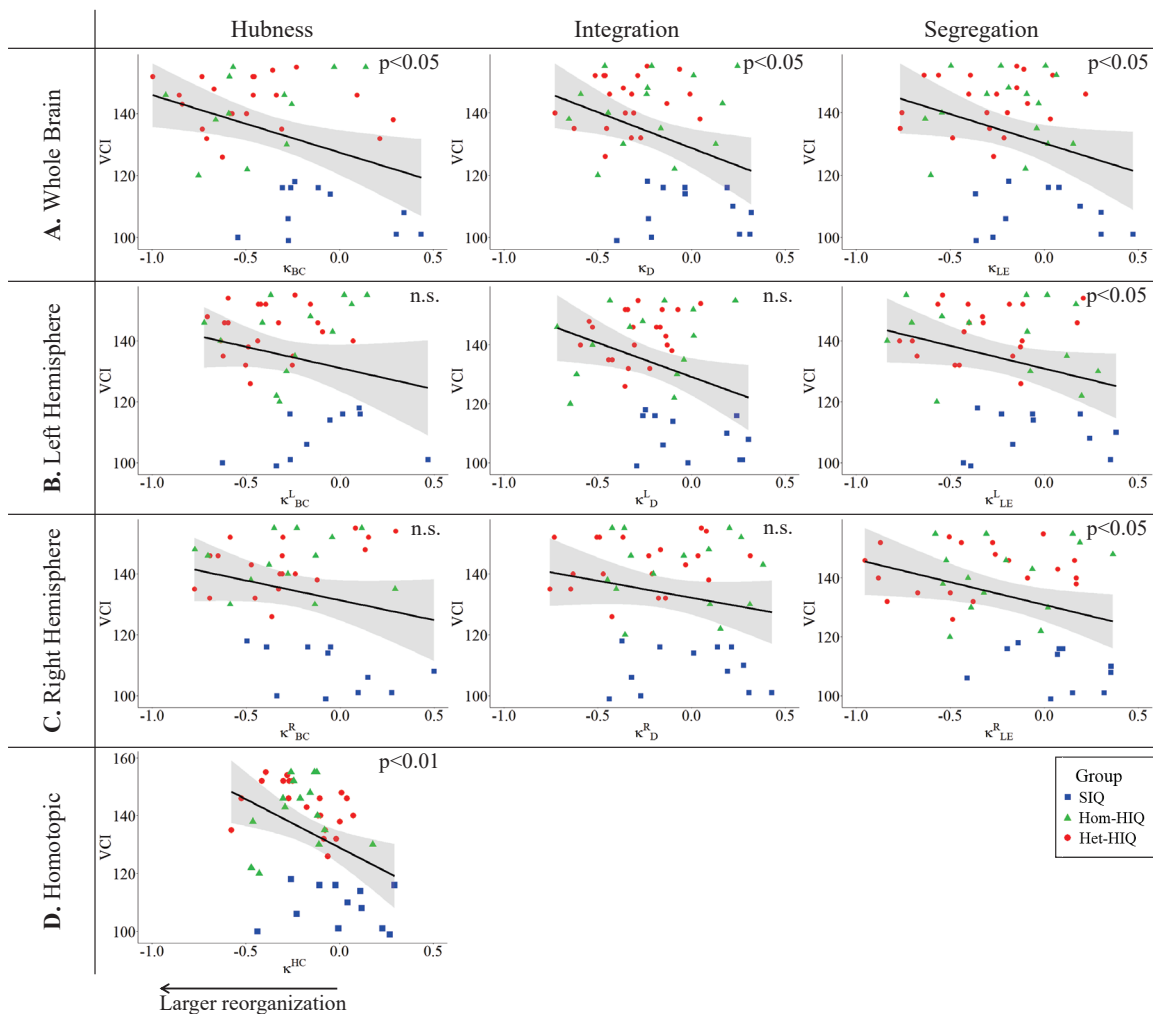


Figure 5.16: Correlations between Verbal Comprehension Index (VCI) and reorganization indices ( $\kappa$ ) of graph metrics measured in: (A) the whole brain networks, (B) the left hemisphere networks, (C) the right hemisphere networks and (D) the homotopic nodes. Significant correlations were measured for  $\kappa$  describing hubs properties in the whole brain networks ( $\kappa_{BC}$ ), for integration properties in the whole brain network ( $\kappa_D$ ) and for segregation properties in the whole brain networks ( $\kappa_{CC}$  and  $\kappa_{LE}$ ), in the left ( $\kappa_{CC}^L$  and  $\kappa_{LE}^L$ ) and right hemisphere networks ( $\kappa_{CC}^R$ ,  $\kappa_{LE}^R$ ) and for homotopic connectivity ( $\kappa_{HC}$ ).

two profiles of HIQ children were identified, namely the Hom-HIQ and the Het-HIQ (Table 5.2). It is interesting to underline that we found a significant modification of brain networks organization common to both Hom-HIQ and Het-HIQ subgroups. Additionally, we also observed specific changes in the Het-HIQ subgroup. These results support the existence of different intelligence profiles that should be taken into account during investigations on intelligence. Moreover, our results showed that high intelligence associated functional neural changes occur differently in the left and right hemispheres. Surprisingly, the neuroimaging literature does not report



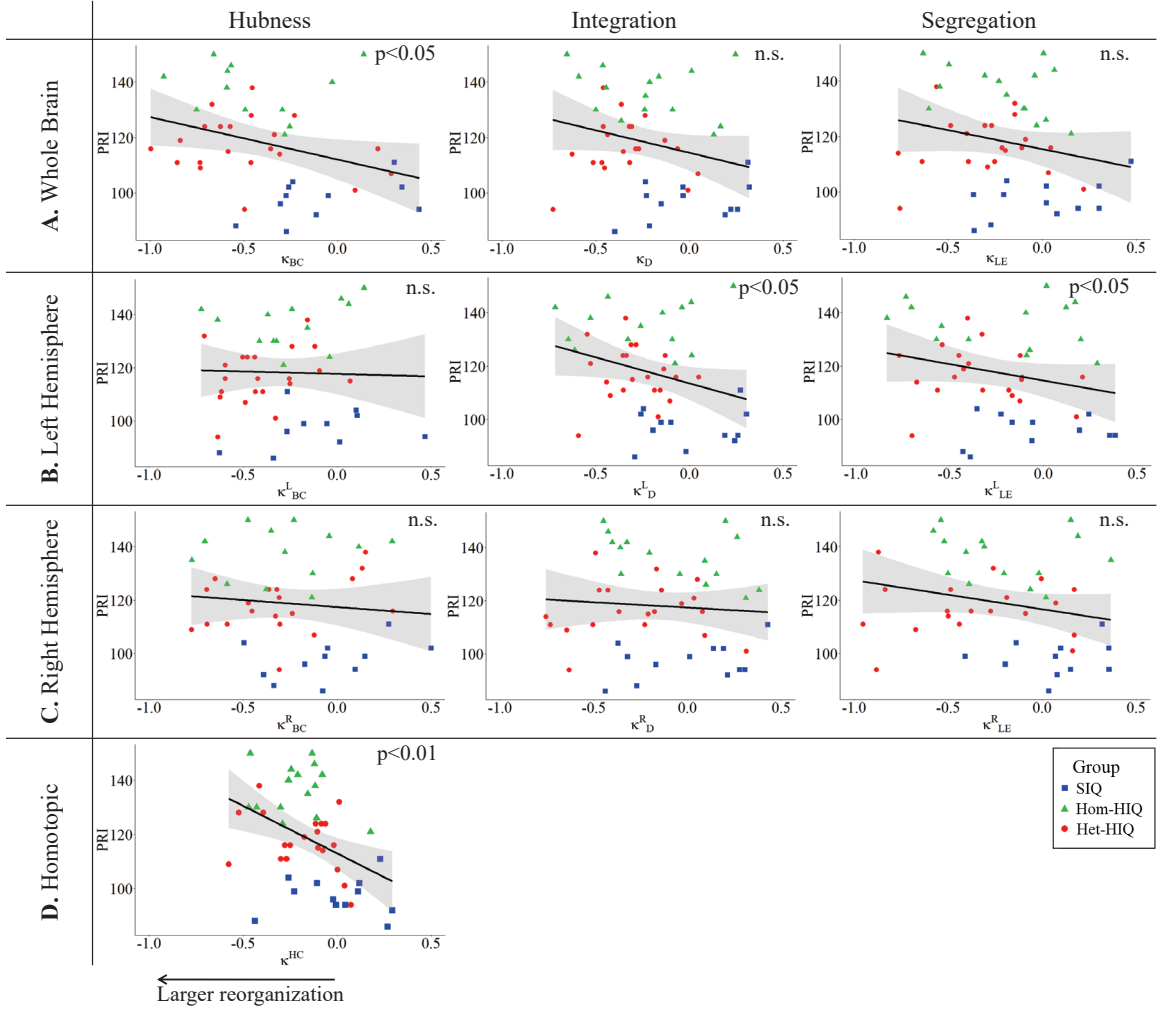


Figure 5.17: Correlations between Perceptual Reasoning Index (PRI) and reorganization indices ( $\kappa$ ) of graph metrics measured in: (A) the whole brain networks, (B) the left hemisphere networks, (C) the right hemisphere networks and (D) the homotopic nodes. Significant correlations were measured for  $\kappa$  describing hubs properties in the whole brain networks ( $\kappa_{BC}$ ), for integration ( $\kappa_D^L$ ) and segregation properties in the left hemisphere networks ( $\kappa_{LE}^L$ ) and for homotopic connectivity ( $\kappa_{HC}$ ).

such lateralization, except for a rs-fMRI study by Santarnecchi et al. [Santarnecchi et al. (2015)b], a DTI study by Tamnes et al. [Tamnes et al. (2010)], and our previous DTI study of Hom-HIQ and Het-HIQ children that included subjects described in the present study [Nusbaum et al. (2017)]. This last study found increased structural connectivity (measured using axial diffusivity) in both Hom- and Het-HIQ groups, with the Het-HIQ group being more lateralized in the left hemisphere and the Hom-HIQ group in the right. These findings demonstrated that brain lateralization of both structural and functional connectivity play a significant role in intelligence. This observation led us to further investigate the role of ho-



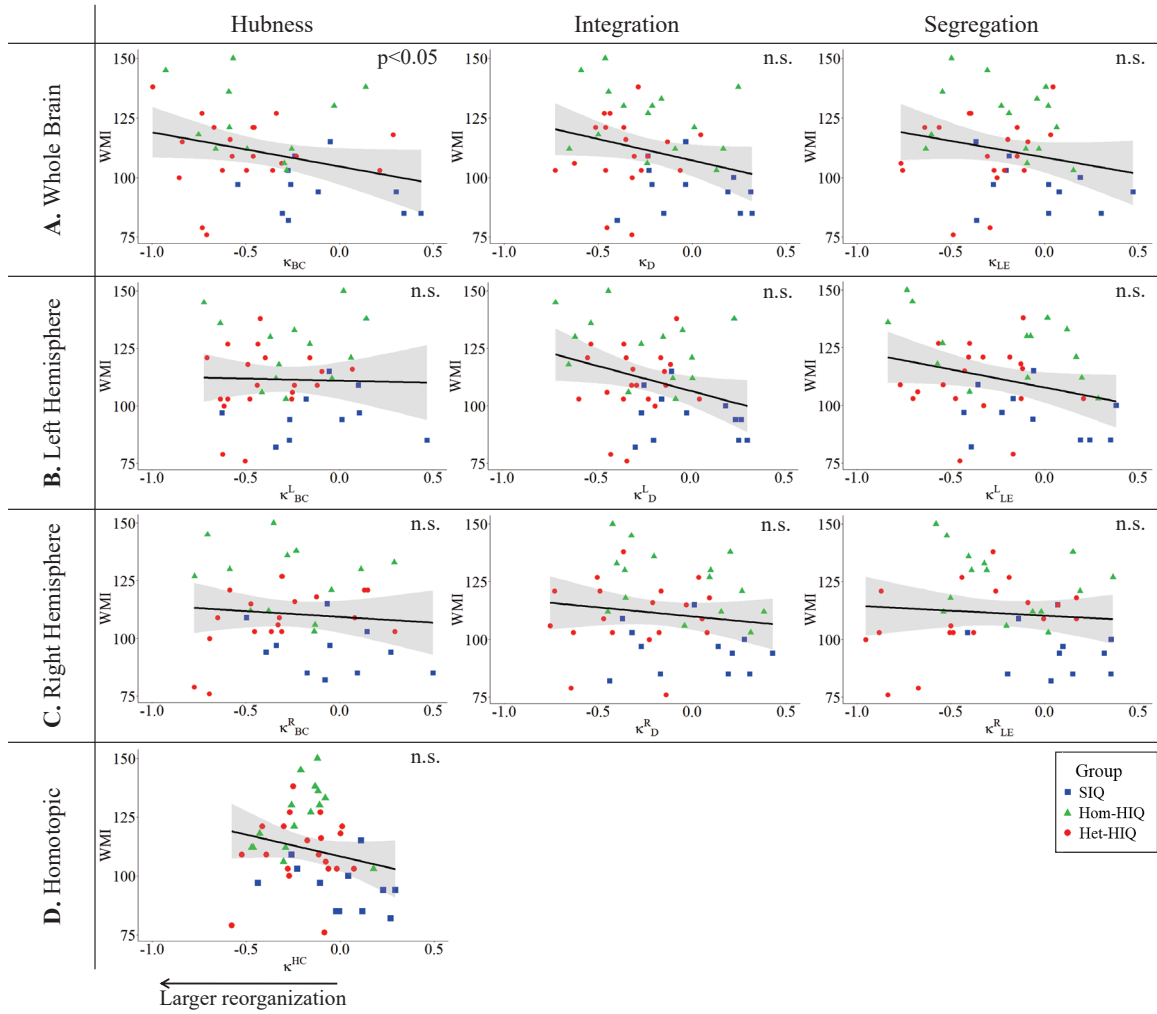


Figure 5.18: Correlations between Working Memory Index (WMI) and reorganization indices ( $\kappa$ ) of graph metrics measured in: (A) the whole brain networks, (B) the left hemisphere networks, (C) the right hemisphere networks and (D) the homotopic nodes. Significant correlations were measured for  $\kappa$  describing hubs properties in the whole brain networks ( $\kappa_{BC}$ ), for integration properties in the left hemisphere networks ( $\kappa_D$ ).

motopic regions in intelligence. During brain development, homotopic functional connectivity was shown to increase with advancing gestational age [Thomason *et al.* (2013)]. Along the lifespan, sensorimotor regions tend to show increasing homotopic functional connectivity, whereas prefrontal higher-order processing regions show decreasing connectivity [Zuo *et al.* (2010)]. Santarnecchi *et al.* [Santarnecchi *et al.* (2015)b] addressed the relation between homotopic connectivity and intelligence in adults. Reduced homotopic connectivity was reported in above average-IQ versus average-IQ subjects in the primary sensory regions, suggesting that a downgrading of inter-hemispheric transmission at rest could be associated with higher intelligence

for efficiency purpose. In our study, significant changes of the homotopic connectivity were found in HIQ children and in both HIQ subgroups, reflecting decreased connectivity in some node pairs and an increase in others.

## 5.2 Correlation between brain networks changes and IQ subscales

We additionally demonstrated that the reported topological organization changes were correlated with cognitive abilities, thus supporting the hypothesis that intelligence relates to the brain network functional organization (Table 5.4). As illustrated in Figure 5.15, FSIQ significantly correlated with the hub's changes, as measured by  $\kappa_{BC}$  in the whole brain networks. Hubs' modifications, therefore, occur in children with high cognitive abilities, as demonstrated by the significant correlations with VCI, PRI and WMI subscales (Figure 5.16-5.18). In parallel, integration properties changes were correlated with FSIQ and VCI in the whole brain networks, and with FSIQ and PRI in the left hemisphere networks. These findings support the association of high intelligence with greater network efficiency throughout the brain, and especially in the left hemisphere. Our results are in agreement with the study of Santarnecchi et al. [Santarnecchi *et al.* (2014)], that highlighted an association between IQ scores and the global efficiency measures of both strong and weak connections. Moreover, a recent study introduced the idea that differences in intelligence are related to different ways of information processing, with some networks being more efficient in integration and propagation of information across the modules, and others in segregation, i.e. ensuring communication within the module [Hilger *et al.* (2017)b]. In line with this hypothesis, our study showed that modifications occurred not only in integration but also in segregation properties, which were correlated with intelligence scores in both whole brain and hemispheres networks. Finally, the correlation found between FC changes of homotopic pairs of regions and FSIQ, as well as VCI and PRI, confirmed that homotopic FC is modified in high intelligence, in agreement with the report of Santarnecchi et al. [Santarnecchi *et al.* (2015)b]. Among all the brain networks differences found in our study, several regions presented decrease or increase in their nodal metrics. It is the case for the dorsolateral prefrontal cortex that showed a significant reduction in degree, suggesting less FC. This observation was found both in the whole brain and in the left hemisphere networks of HIQ and Het-HIQ groups. These findings support the hypothesis that this prefrontal region constitutes a weaker node in HIQ children, which might result from a late gray matter maturation, as previously observed in

high intelligence children [Shaw *et al.* (2006)]. As the rationale of the hub disruption index  $\kappa$  is to highlight simultaneous decreases in some nodes metrics and increases in others (see Figure 5.9 for a scheme-based explanation), the degree decrease observed in the prefrontal cortex may suggest potential increases of integration properties in other brain areas. Overall, our study demonstrated the sensitivity of rs-fMRI graph metrics to characterize the specificities in functional brain networks changes of HIQ children, and particularly of Het-HIQ children. As Het-HIQ children could be associated with specific social behavioral and learning difficulties, these findings support our initial hypothesis that FC measurements may constitute a promising approach for a better characterization of HIQ brain function and neural characteristics. Future studies may extend these findings on a larger cohort of children.

## 6 Conclusion

In this chapter, we have addressed the issue of the functional neural substrate of intelligence. Based on the idea that intelligence is related to network capacity to adapt and reorganize its topology [Barbey (2018)], we measured the "hub disruption index". This graph measurement was introduced by [Achard *et al.* (2012)] and provides information about brain organization change respect to a reference group. In our case, brain changes were measured in HIQ in general, and two HIQ different profiles were compared to the SIQ group.

While different global metrics have been used in several rs-fMRI studies, Hub disruption index was never used to investigate the neuronal substrate of intelligence.

In this work, we have demonstrated that there is a strong relationship between cognitive abilities and brain functional topology. Indeed, all the HIQ children present a reorganization of brain networks. Some regions that are very important in brain network of SIQ, become less important in HIQ brain networks. More specifically, Het-HIQ children showed the strongest topological changes. As presented in chapter 4, this group benefits from a higher IQ than the standard population, particularly in the Verbal Comprehension Index test which is significantly higher than the Perceptual Reasoning Index. This dyssynchrony is also related to clinical observations. Indeed, they present several disabilities that include managing their emotions, learning difficulties and social relationships. We believe that these differences in respect to other children, may be reflected with a reorganization of functional connectivity between brain regions. Thanks to the high sensitivity of fMRI graph metrics, we have been able to reveal this topological reorganization.

## Chapter 6

---

# Structural connectivity: a DTI study

---

### Contents

---

<b>1</b>	<b>Introduction . . . . .</b>	<b>113</b>
<b>2</b>	<b>Materials and Methods . . . . .</b>	<b>114</b>
2.1	Participants . . . . .	114
2.2	Intelligence scores . . . . .	115
2.3	MRI acquisition and processing . . . . .	115
2.4	Fiber-Bundle Analysis . . . . .	116
2.5	Graph analysis . . . . .	116
2.6	Statistical analysis . . . . .	119
<b>3</b>	<b>Results . . . . .</b>	<b>120</b>
3.1	Correlation with WISC scores and graph metrics . . . . .	120
3.2	Correlation with intelligence domains using factor analysis . . . . .	123
<b>4</b>	<b>Discussion . . . . .</b>	<b>129</b>
<b>5</b>	<b>Conclusion . . . . .</b>	<b>132</b>

---

In this chapter, we will present our second study on the children population. Indeed, after the exploration of functional connectivity, we would like to complete the connectivity analysis by exploring the structural connectivity obtained from DTI.

As explained in the next section, several neuroimaging groups studied how the structural brain connectivity is related to intelligence level. However, only few studies focused their attention on a children population. Furthermore, carrying out a meticulous study of the literature, we noticed that no work performed a complete graph analysis of structural brain networks and showed results at both local and brain scales.

This literature gap strengthened our interest and motivation in exploring the structural substrate of intelligence through several graph metrics. We started performing a simple correlation between the intelligence scores of WISC test and the graph metrics. Once we obtained significant results, we pushed our analysis by using factor analysis to extract a single common factor ( $g$  factor) of all the intelligence sub-tests. From this information, we can then extract "pure" intelligence domains that are not biased by the  $g$  factor. So, in the second part, of this chapter we present the correlation between three intelligence domains, obtained by a statistical analysis, and the graph metrics.

Finally, to complete this work, we decided to explore the relationship between WM microstructure and intelligence. From diffusivity metrics, we grouped WM fiber-bundles in diffusivity components, using a principal component analysis (PCA). These diffusivity components were then correlated with intelligence domains.

This chapter contains the article published in the journal "Intelligence" titled **Brain Structural Connectivity Correlates with Fluid Intelligence in Children: a DTI Graph Analysis**.

Gabriel Kocevar\*, Ilaria Suprano\*, Claudio Stamile, Salem Hannoun, Pierre Fourneret, Olivier Revol, Fanny Nusbaum and Dominique Sappey-Marinier. (\* co-first authors)

## 1 Introduction

Diffusion tensor imaging (DTI) constitutes a very sensitive imaging tool for the characterization of WM microstructural organization and the identification of neural pathways [Basser *et al.* (1994), Basser *et al.* (2002), Beaulieu (2002)].

Indeed, WM fiber organization and integrity in brain tissue can be measured through the estimation of diffusivity metrics such as the fractional anisotropy (FA), and the axial (AD) and radial (RD) diffusivities, estimating the amount of diffusion along and perpendicular to the main fiber direction. During the last decade, the high sensitivity of DTI to WM changes allowed to explore relationship between WM microstructure and IQ from childhood to adulthood. Initially, Schmithorst *et al.* reported a positive association between IQ and FA in numerous cerebral regions of children [Schmithorst *et al.* (2005)]. More recently, a positive correlation between FA values and intelligence scores, was observed in several large WM fiber-bundles, namely the splenium of the corpus callosum, the left inferior longitudinal, and the arcuate fasciculi [Clayden *et al.* (2012)]. Muetzel *et al.* also reported a positive association between FA and both IQ and visuospatial abilities in children, mainly in the right uncinate fasciculus [Muetzel *et al.* (2015)]. In a study of 168 subjects, aged between eight and 30 years, both verbal and performance abilities were positively associated to FA, particularly in the left hemisphere, independently of age and sex [Tamnes *et al.* (2010)]. During adolescence, Navas-Sanchez *et al.* confirmed the correlation between IQ and FA, mainly in the corpus callosum [Navas-Sánchez *et al.* (2014)], while Dunst *et al.* showed that adults' WM microstructure differs between individuals as a function of intelligence and gender [Dunst *et al.* (2014)]. Along with the FA, AD may also be well correlated with IQ. Indeed, Nusbaum *et al.* showed increased AD in children with high IQ compared to standard IQ. This study also showed, that diffusivity measures could discriminate two groups of high IQ children profiles, namely homogeneous and heterogeneous [Nusbaum *et al.* (2017)].

Based on a geometrical graph representation, a simple description of structural brain connectivity was recently proposed [Shuman *et al.* (2013)]. Indeed, connections between GM regions, represented as graph nodes, can be derived from DTI

tractography. Using such formalism, the brain could be considered as a small-world network, whose organization can be explored at both local and global scales using graph theory [Hagmann *et al.* (2007)]. The relationship between graphs structural connectivity and IQ was first evaluated in adults by Li *et al.*, showing higher global efficiency (Eg) and shorter characteristic path length (L) in subjects with higher IQ scores [Li *et al.* (2009)]. A recent study, performed in a population of 99 children (six to eleven years old), showed that Eg was correlated to the perceptual reasoning index (PRI) and its subtests [Kim *et al.* (2016)]. Furthermore, this study highlighted several associations between local network organization and intelligence. Indeed, PRI sub-scores were positively correlated to local efficiency in the pre- and post-central gyrus, the precuneus, the superior and inferior frontal gyri, and in the inferior temporal cortex. However, this unique study in children was limited to the analysis of only PRI and its subtests.

In the present study, we propose to explore the neural substrate of intelligence in a cohort of children. We tested the hypothesis that intelligence is associated with a better structural connectivity and a specific network organization at different anatomical levels: whole brain, intra- and inter-hemispheres, and lobes. To this end, first, the relationships between all IQ indices and topological properties of brain structural networks as well as diffusivity metrics of the main WM fiber-bundles were investigated. Second, the relationship between diffusion metrics and the major intelligence domains, based on the Wechsler intelligence scale for children (WISC-IV) subtests inter-correlations, was assessed in the main WM fiber-bundles. Finally, the association between intelligence domain and the brain structural networks properties were investigated using a graph theory approach at both global and local scales.

## 2 Materials and Methods

### 2.1 Participants

This prospective MRI study included 43 children (11 girls and 32 boys, age (mean  $\pm$  SD):  $9.82 \pm 1.06$  years). Subjects were recruited from the private psychological center (PSYRENE) and the children's psychiatry unit of Lyon's Neurological Hospital, both specialized in high IQ children evaluation and follow-up, as well as through advertisement in medical practices and public institutions. All children with any neurological diseases, medical psychiatric comorbidities, learning disabilities, psychotropic treatments, or contra-indications for MRI were excluded. Prior to enrollment, children received a medical examination and were fully informed along

with their parents of the study details. Ethical committee approval (“CPP Sud-Est IV”) and written informed consent from the children and their parents were obtained.

## 2.2 Intelligence scores

All children underwent comprehensive neuropsychological testing using the Wechsler intelligence scale for children (WISC-IV) which provided a reliable estimation of the full-scale IQ (FSIQ) based on four subscales, namely, the verbal comprehension index (VCI), the perceptual reasoning index (PRI), the working memory index (WMI), and the processing speed index (PSI).

These WISC subscales have been calculated from ten subtests, namely the vocabulary, comprehension, and similarities subtests (estimating the verbal comprehension abilities), the picture concept, matrix reasoning, and block design (reflecting the perceptual reasoning abilities), the letter-number sequencing and digit span subtests (estimating the working memory), and the coding and symbol search subtests (estimating the processing speed).

## 2.3 MRI acquisition and processing

MRI examinations were performed without any sedation or contrast agent at the MRI department of the CERMEP-Imagerie du Vivant, on a 1.5T Siemens Sonata system (Erlangen, Germany) with an 8-channels head-coil and 40mT/m gradients. The MRI protocol included a 3D T1-weighted magnetization prepared rapid gradient echo (MPRAGE) sequence (time of repetition / time of echo / time for inversion [TR/TE/TI] = 1970/3.93/1100 ms; flip angle = 15°; matrix size = 256x256; field of view = 256x256 mm; slice thickness = 1 mm; voxel size = 1x1x1 mm; acquisition time = 8 min). DTI protocol was based on a 2D multi-slice spin-echo echo-planar imaging (EPI) sequence (TR/TE = 6900/86 ms, resolution 2.5x2.5x2.5 mm, FOV = 240x240 mm, acquisition time = 7 min). Fifty-one contiguous axial slices were acquired in the anterior commissure - posterior commissure (AC-PC) plane. Twenty-four diffusion gradient directions ( $b = 1000 \text{ s/mm}^2$ ) were applied. The  $b_0$  image was acquired four times to increase signal to noise ratio while other directions were acquired twice. Diffusion data were corrected for subjects’ motion and Eddy currents using the FMRIB Software Library (FSL) [Jenkinson *et al.* (2012)]. Non-brain voxels were removed using FSL-BET. Transformation matrices generated during the Eddy current correction were also used to compute the Root Mean Square deviation. As a result, we obtained a mean patient displacement value of  $1.26 \pm 0.52 \text{ mm}$  (mean



$\pm$  SD), which is half of a voxel size (2.5 mm). For each subject, the tensor model was then fitted on diffusion data using FSL-FDT and four diffusion maps (FA, AD, RD, and mean diffusivity (MD)) were extracted [Reuter *et al.* (2012)].

## 2.4 Fiber-Bundle Analysis

Large WM fiber-bundles were defined using the Illinois Institute of Technology (IIT) atlas, which included the forceps major (Fmajor), the forceps minor (Fminor), the superior and inferior longitudinal fasciculus (SLF and ILF respectively), the inferior fronto-occipital fasciculus (IFOF), the uncinate fasciculus (Unc), the cingulum (Cing), and the cortico-spinal tract (CST) [Varentsova *et al.* (2014)]. The IIT atlas FA map was co-registered to each subject's FA image using a non-rigid transformation performed using NiftyReg [Ourselin *et al.* (2001)]. The resulting deformation field was then applied to co-register the IIT atlas large WM fiber-bundles to each patient's space. Since fiber-bundles masks contained the probability of each voxel to belong to a specific fiber-bundle, a threshold was used to discard all voxels having a probability lower than 35%. The resulting masks were then binarized. Finally, the mean value of FA, MD, AD, and RD, were extracted from each subject's fiber-bundles. This pipeline for fiber-bundles analysis is illustrated in Figure 6.1.

## 2.5 Graph analysis

The previously generated deformation field was used to transform the Desikan cortical and subcortical GM parcellation to each subject space, to define the 84 nodes of the structural brain networks [Desikan *et al.* (2006)]. Whole brain tractography was performed for every subject using MRtrix software [Tournier *et al.* (2012)]. First, the main diffusion directions were estimated in each voxel using diffusion orientation distribution function (dODF). The maximum spherical harmonics ( $h=4$ ) order was selected to match with the acquisition protocol. Then, based on the four-tissue-class classification (WM, cortical GM, sub-cortical GM and cerebro-spinal fluid (CSF)) of the IIT atlas and dODF, anatomically constrained probabilistic streamline tractography was performed to generate 1'000'000 streamlines. Finally, adjacency matrices were generated for each subject by summing the number of streamlines connecting each pair of nodes. In order to remove the weakest connections generated by tractography, a proportional threshold ( $\tau$ ) must be applied to obtain binary connectivity matrices. As this threshold strongly affects the network topology and density, it has to be carefully chosen [Simpson *et al.* (2013), Bullmore and Sporns (2009)]. Two methods are commonly used in brain network studies,

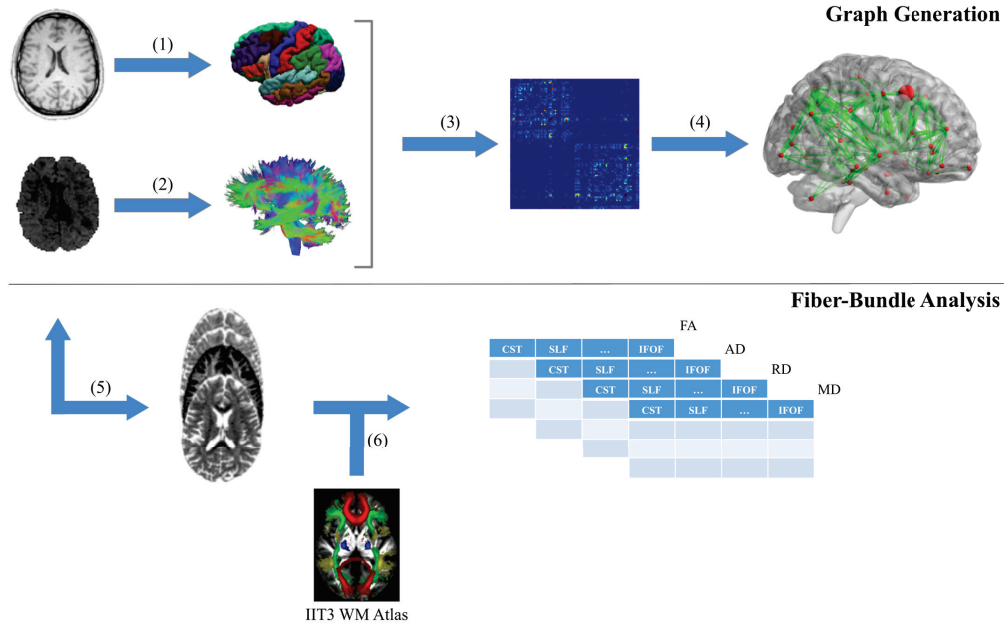


Figure 6.1: Overview of the pipeline used for data processing. On top, the pipeline for graph generation: graph nodes are generated through anatomical parcellation on T1 image (1) and probabilistic anatomically constrained streamline tractography is generated from diffusion images (2). Then, the numbers of streamlines connecting each pair of nodes are used to define edges in the weighted graph and generate the connectivity matrices. (3) Finally, a proportional threshold ( $\tau=0.25$ ) was applied to remove the weakest connections before generating adjacency matrices (4). On bottom, the pipeline for fiber-bundles extraction. Computation of FA, MD, AD, and RD (5) from diffusion images. Registration of the atlas on the subject space (6) and extraction of the mean value inside WM masks.

namely absolute and proportional thresholding. In this work, proportional threshold  $\tau = 0.25$  was selected according to the method described elsewhere [Kocevar *et al.* (2016)]. The pipeline for graph generation is illustrated in Figure 6.1. Brain structural connectivity was analyzed globally as well as locally by dividing the connectivity matrices in different sub-graphs: the left and right hemispheres, and the inter-hemisphere connections graph. The connectivity matrices were also divided into subnetworks of lobes (frontal, occipital, parietal and temporal), and sub-cortical nuclei. Details of the cortical regions composing each lobe and a schematic representation of this subdivision on the connectivity matrix is shown in Figure 6.2.

The topological properties of brain networks were analyzed using global and nodal metrics from graph theory [Rubinov and Sporns (2010)]. Six global graph metrics were estimated to analyze the networks properties. First, the graph density

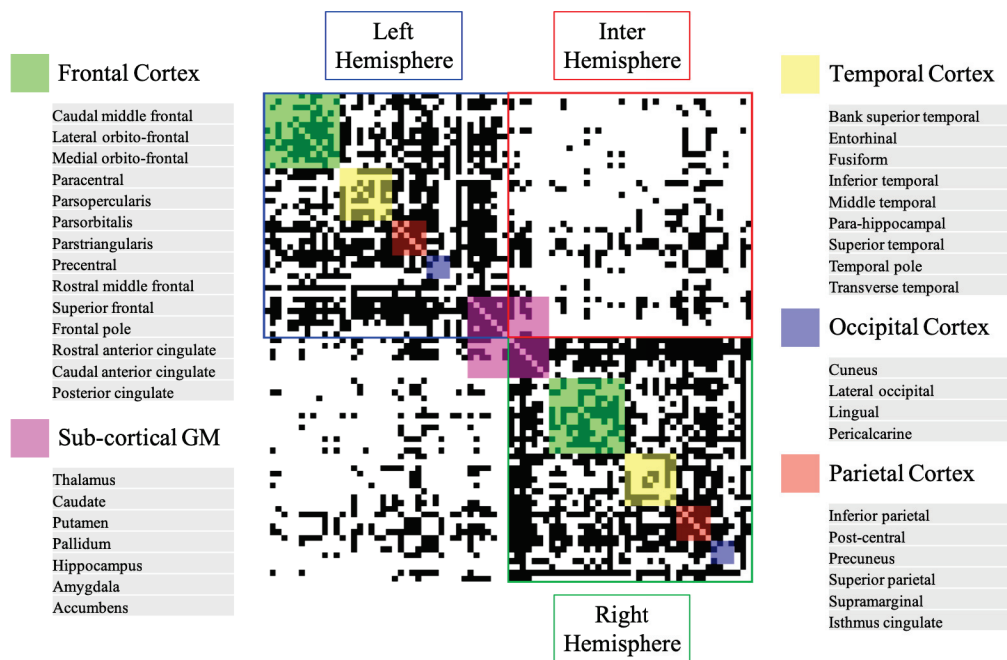


Figure 6.2: Schematic representation of the connectivity matrix subdivision in different networks, including left-, right-, and inter- hemispheres networks and lobes networks. The cortical regions in each lobe are also reported.

(D) is measured as the ratio between the numbers of effective connections in the graph (l) to the number of possible connections. Second, the integration property of the graph was evaluated using the following two metrics: the characteristic path length (L), which is the mean of the shortest paths in the graph, and the global efficiency (Eg), which is the mean of the inverse of the distance matrix of the graph. Third, the segregation property of the graph was analyzed using the following three metrics: the transitivity (T) which is the ratio between the number of triangles and the number of triplets in the graph, the assortativity (r) which is the Pearson coefficient between the degrees of two nodes at the extremities of an edge, and the modularity (Q) which is the difference between the number of intra-modules connections and the number of inter-modules connections. Four nodal graph metrics were also computed. The degree ( $k_i$ ) represents the number of connections of each node. The clustering coefficient ( $C_i$ ) defined as the ratio between the number of triangles and the number of triplets around each node, measures the network's tendency to form dense local clusters. The betweenness centrality ( $B_i$ ), defined as the ratio of the number of the shortest paths comprising the node to the total number of shortest paths in the graph, measures the hub property of the node. The nodal efficiency ( $E_i$ ) defined as the mean of the inverse of the distance vector, measures the signal transmission efficiency. Small-world properties of each subject's graph were

estimated. First, a random graph with preserved degree distribution was generated. Then the characteristic path length (L) and the mean clustering coefficient (C) were estimated for both the subject and the random graph. Finally,  $\lambda$ ,  $\gamma$ , and  $\sigma$  were estimated as follows:

$$\lambda = \frac{L_{subject}}{L_{random}}; \gamma = \frac{C_{subject}}{C_{random}}; \sigma = \frac{\gamma}{\lambda} \quad (6.1)$$

Compared with a random network, small-world networks are known to have similar L and higher C, resulting in  $\lambda \approx 1$ ,  $\gamma > 1$ , and  $\sigma > 1$  [Uehara *et al.* (2014)]. All the metrics, except graph density, were computed based on the binarized connectivity matrices using the brain connectivity toolbox on Matlab [Rubinov and Sporns (2010)].

## 2.6 Statistical analysis

The statistical analysis is mainly composed of two parts.

First, partial correlations between intelligence scores and network measures were calculated in the total sample using age and gender as covariates. A linear model (LM) was used to investigate the relationship between each WISC ( $W_i$ ) index and the global and nodal graph metrics as well as the diffusion metrics of the WM fiber-bundles. The general expression of this model was as follows:

$$W_i \sim (diffusion/graph)metric + Age + Gender \quad (6.2)$$

Statistical significance of all predictor was tested for each fit by applying analysis-of-variance and analysis-of-deviance with a 5% significance level corrected for multiple comparisons, applying FDR correction to p values.

As previously described in Karama’s work [Karama *et al.* (2011)], a factor analysis was performed on the correlation matrix of the ten WISC subtests in order to explore their inter-correlations and to extract intelligence domains not biased by the factor “g”. First, a factor analysis using the oblique “promax” rotation was applied to the subtests, defining the principal intelligence domains. Second, an unrotated factor analysis was performed to extract the g-score, defined as the scores of the first factor component. Finally, the correlations between each intelligence domains and the g-score were processed to extract their residuals, considered as g-unbiased intelligence domains. As previously described by Privado *et al.* [Privado *et al.* (2017)], a principal component analysis (PCA) was performed to explore potential groups of inter-correlated WM fiber-bundles, based on their diffusivity metrics (FA, AD, RD, MD). The resulting components were rotated to the simple structure using a “pro-

max” rotation. Partial correlations between g-unbiased intelligence domains and graph network metrics or diffusivity components were calculated in the total subject sample. A linear model (LM) was used to investigate the relationship between each intelligence domain and the diffusion metrics of the WM fiber-bundles, as well as the global and nodal graph metrics. Age and sex were added to the linear model as cofactors in order to account for any imbalance effect. The general expression of this model was as follows:

$$Intelligence_{domain} \sim (diffusion/graph)metric + Age + Gender \quad (6.3)$$

Significance of all predictors for each fit was tested by applying analysis-of-variance and analysis-of-deviance with a 5% significance level. All statistical analysis were computed using R and the “psych” library [R Development Core Team (2015)]. In order to correct for multiple comparisons between the local graph metrics, Sidak correction was applied to the p-values.

## 3 Results

### 3.1 Correlation with WISC scores and graph metrics

In the first analysis of this study, the five WISC scores (FSIQ, VCI, PRI, WMI, and PSI) have been correlated with both local and global graph metrics derived from structural connectivity.

#### Global graph metrics

When measured in whole brain, significant correlations were found between graph metrics and FSIQ as well as WISC-IV subscales. More in details, FSIQ, VCI, PRI, and WMI showed positive correlations with the density D (Figure 6.3). In contrast, negative correlations were found between FSIQ, PRI, and WMI and the modularity Q, as well as between VCI and WMI and the transitivity T. When measured in both hemispheres, FSIQ, VCI, PRI, and WMI values were positively correlated with D. In the right hemisphere, a negative correlation was observed between PRI and Q. Finally, positive correlations were observed between FSIQ, VCI, and WMI and D, and between PSI and T, in the inter-hemispheric connections.

The same graph metrics were also measured in other networks such as brain lobes (frontal, parietal, occipital, and temporal) as well as sub-cortical nuclei. In

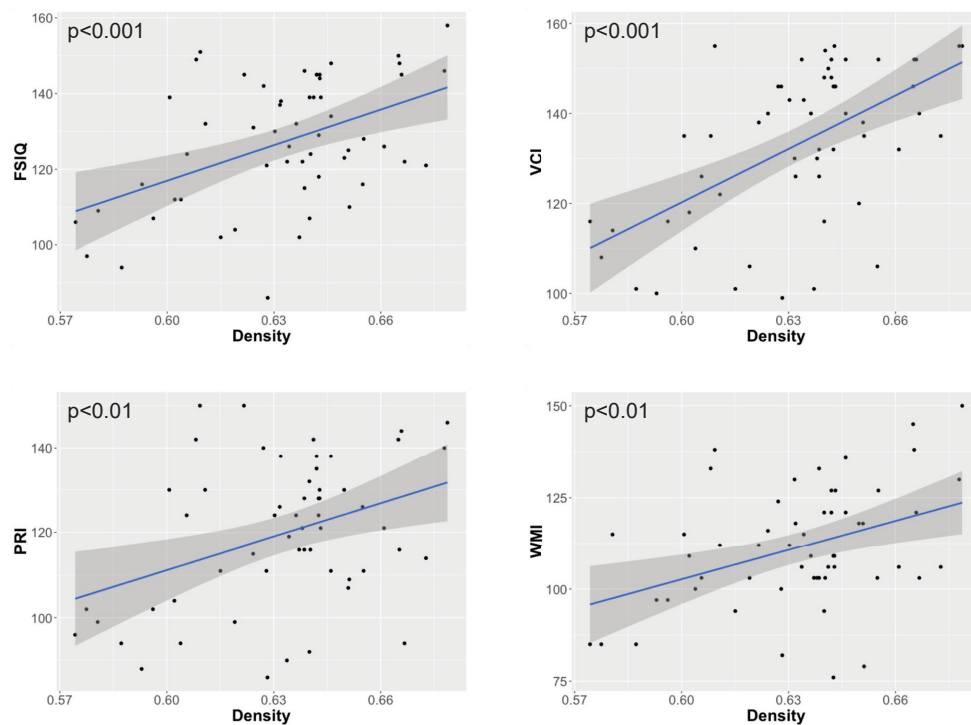


Figure 6.3: Significant positive correlations obtained between the graph density of the whole brain networks and the full-scale intelligence quotient (FSIQ), the verbal comprehension index (VCI), the perceptual reasoning index (PRI), and the working memory index (WMI).

the left parietal lobe FSIQ and WMI were negatively correlated with  $Q$ . In the right occipital lobe, WMI was negatively correlated with  $T$ , and positively with CPL. In the left temporal lobe, FSIQ and WMI were positively correlated with  $r$  and  $T$ . FSIQ, PRI, and PSI were negatively correlated with  $Q$ . VCI, and PRI were negatively correlated with  $Eg$ . FSIQ, and VCI were positively correlated with CPL. Finally, in the left subcortical GM networks, PRI was negatively correlated with  $r$ , while PSI was positively correlated with  $T$ . All the correlations between global graph metrics and intelligence scores are reported in Table 8.2.

Networks		Metric	FSIQ	VCI	PRI	WMI	PSI
Whole brain	-	D	304.17***	399.66***	243.49**	278.01**	-
		Q	-420.93*	-	-377.73*	-466.40*	-
		T	-	-926.32*	-	-813.38*	-
Inter-Hemisphere	-	D	165.23**	227.24***	-	170.64**	-
		T	-	-	-	-	136.55*
Hemisphere	L	D	342.05**	413.26***	331.26**	309.88**	-
	R	D	233.15**	291.27**	237.35*	183.05*	-
		Q	-	-	-381.91*	-	-
Parietal	L	Q	-259.65*	-	-	-288.69*	-
Occipital	R	CPL	-	-	-	85.58*	-
		T	-	-	-	-42.79*	-
Temporal	L	r	55.21*	-	-	68.88*	-
		Q	-182.99*	-	-192.70*	-	-180.22*
		T	147.48*	-	-	203.72**	-
	R	Eg	-	-365.17*	-344.62*	-	-
		CPL	139.88*	164.08*	-	-	-
Sub-Cortical	L	r	-	-	-215.61*	-	-
		T	-	-	-	-	62.34*

Table 6.1: Correlation slopes and statistical significances obtained with a LM model between global graph metrics, namely density (D), assortativity (r), transitivity (T), modularity (Q), characteristic path length (CPL), and efficiency (Eg) measured in different brain networks (whole brain, inter-hemisphere, left and right hemispheres, different lobes, and subcortical regions), and the IQ scores (full scale intelligence quotient (FSIQ), verbal comprehension index (VCI), perceptual reasoning index (PRI), working memory index (WMI), and processing speed index (PSI)). \*  $p < 0.05$ ; \*\*  $p < 0.01$ .

### Nodal graph metrics

Several significant correlations were observed between the nodal graph metrics and the intelligence scores, including mainly FSIQ and VCI, and to a lesser extent PRI. These correlations were observed in numerous networks, mainly located in the left hemisphere, as reported in Table 6.2. As shown in Figure 6.4, FSIQ was positively correlated with the degree  $k_i$  and negatively with the local efficiency  $E_i$  in the left precuneus networks and in the left middle temporal networks. In the middle and superior temporal networks, VCI was positively correlated with  $k_i$  and only in the middle temporal networks negatively with  $E_i$  (Figure 6.5). In the right caudate nuclei networks, PRI was positively correlated with  $k_i$  (Figure 6.6).



Networks		GM nodes	Metric	FSIQ	VCI	PRI	WMI	PSI
Frontal	L	Paracentral	$k_i$	-	3.0*	-	-	-
		Frontalpole	$k_i$	-3.9*	-3.9*	-	-	-
			$B_i$	-2.9*	-	-	-	-
Parietal	L	Precuneus	$k_i$	2.1*	1.9*	2.1*	-	-
			$C_i$	-279.0*	-	-294.2*	-	-
			$E_i$	-463.6*	-	-	-	-
	R	Supramarginal	$B_i$	-	0.4*	-	-	-
Occipital	R	Lateraloccipital	$B_i$	1.1*	-	-	-	-
Temporal	L	Fusiform	$k_i$	-	-2.7*	-	-	-
			$k_i$	2.3*	2.4*	-	-	-
		Middletemporal	$C_i$	-106.9*	-	-	-	-
			$E_i$	-212.2*	-	-	-	-
		Superiortemporal	$k_i$	-	3.0*	-	-	-
			$B_i$	-	0.2*	-	-	-
			$C_i$	-	-176.6*	-	-	-
			$E_i$	-	-340.6*	-	-	-
		Transversetemporal	$k_i$	-3.8*	-3.2*	-3.8*	-	-
	R	Bankssts	$k_i$	-	-3.6*	-	-	-
			$B_i$	-	-4.5*	-	-	-
		Transversetemporal	$k_i$	-4.6*	-3.8*	-4.2*	-	-
			$k_i$	-	-	-	-	-
Sub-Cortical	R	Caudate	$k_i$	2.8*	2.6*	3.5**	-	-
Cerebellum	R	Cerebellum	$k_i$	-	-	2.2*	-	-

Table 6.2: Correlation slopes and statistical significances obtained with a LM model between the local graph metrics, namely degree ( $k_i$ ), betweenness centrality ( $B_i$ ), clustering coefficient ( $C_i$ ), and efficiency ( $E_i$ ), measured from gray matter (GM) nodes of brain lobes of each hemispheres (left (L) and right (R)), and the IQ scores (full scale intelligence quotient (FSIQ), verbal comprehension index (VCI), perceptual reasoning index (PRI), working memory index (WMI), and processing speed index (PSI)). \*  $p < 0.05$ , \*\*  $p < 0.01$ , \*\*\*  $p < 0.001$

### 3.2 Correlation with intelligence domains using factor analysis

In the second part of this study, the correlations between intelligence domains and brain microstructure were explored.

Based on the ten WISC-IV subtests data, three broad g-score domains were defined by the factor analysis as shown in Figure 6.7. Table 6.3 shows the descriptive statistics for the ten intelligence measures and the correlations among them. The first domain (PA1) including the matrix reasoning, block design, digit span, and similarities subtests, is named “fluid intelligence”. The second domain (PA2) including the symbol search, coding, and letter-number sequencing subtests, is named “Classification ability”; and the third domain including the comprehension, vocabulary, and picture concept subtests, is named “crystalized intelligence”. A second



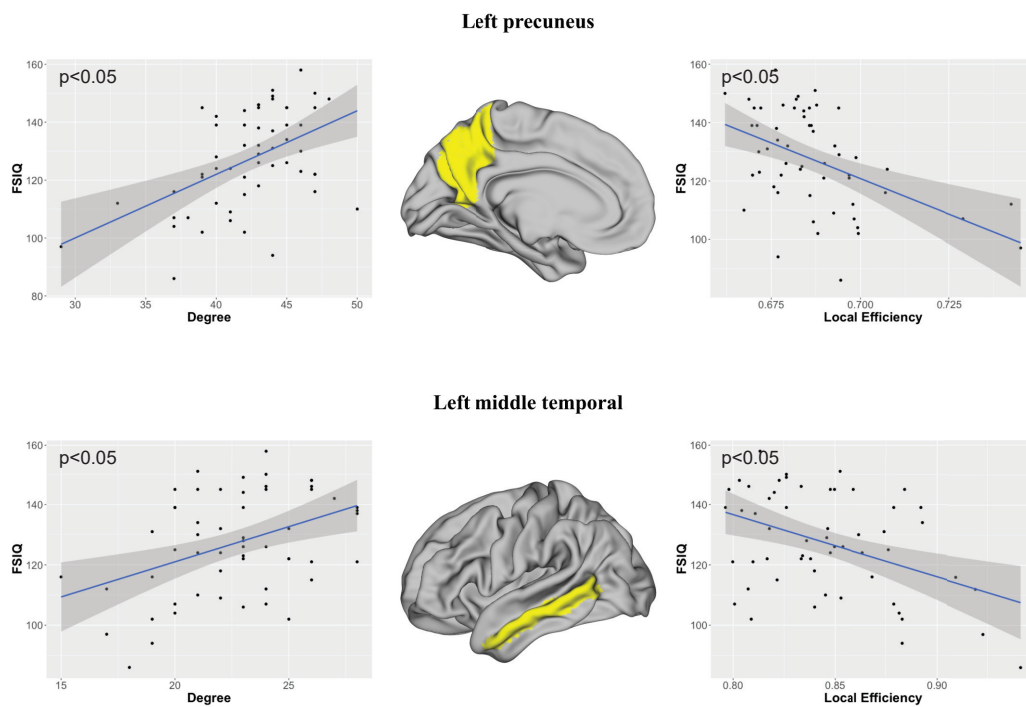


Figure 6.4: Significant correlations obtained between the full-scale intelligence quotient (FSIQ) and the local graph metrics in the left precuneus and the left middle temporal networks.

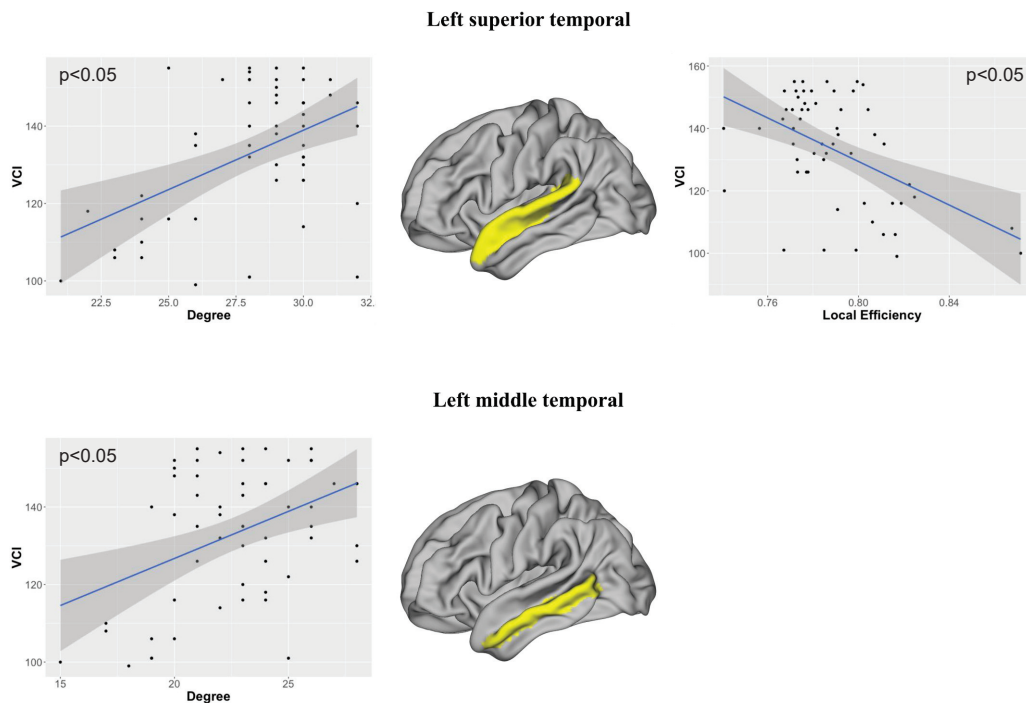


Figure 6.5: Significant correlations obtained between the verbal comprehension index (VCI) and the local graph metrics in the left superior and middle temporal networks.

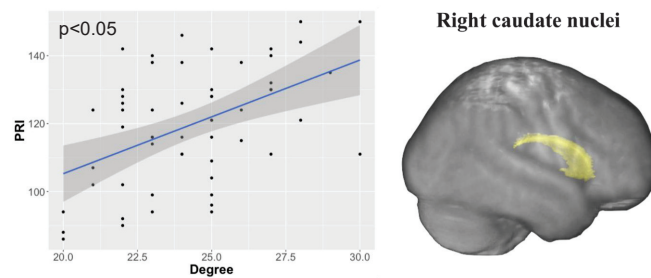


Figure 6.6: A significant positive correlation obtained between the perceptual reasoning index (PRI) and degree metric in the right caudate.

factor analysis, based on the three major intelligence domains, was then applied on the correlation matrix to define the g-score and the g-unbiased intelligence domains (PA1-g, PA2-g, and PA3-g; Table S2 in the supplementary data).

	1	2	3	4	5	6	7	8	9	10
1		0.42**	0.43**	0.19	0.17	0.27	0.42**	0.56***	0.23	0.20
2			0.57***	0.52***	0.12	0.43**	0.51***	0.46**	0.41**	0.33*
3				0.43**	0.19	0.30	0.54***	0.49***	0.44**	0.03
4					0.32*	0.30	0.52***	0.21	0.34*	0.16
5						0.30	0.42**	0.21	0.09	0.41**
6							0.43**	0.13	0.56***	0.19
7								0.53***	0.35*	0.36*
8									0.23	0.30
9										-0.06
10										
Mean	13.19	15.86	12.28	12.6	10.86	15.93	11.44	13.37	14.47	11.14
sd	3.86	3.11	3.13	3.25	3.19	3.06	3.11	3.02	3.38	2.62

Table 6.3: Correlation matrix and descriptive statistics of the ten WISC-IV subtests (1: Block Design, 2: Similarities, 3: Digit span, 4: Picture concept, 5: Coding, 6: Vocabulary, 7: Letter-Number, 8: Matrix reasoning, 9: Comprehension, 10: Symbol search). \*  $p < 0.05$ , \*\*  $p < 0.01$ , \*\*\*  $p < 0.001$

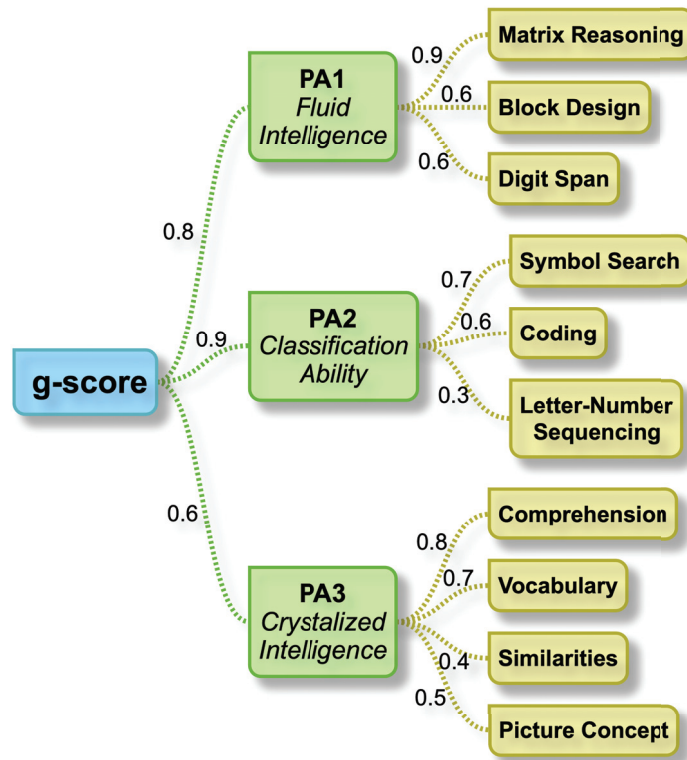


Figure 6.7: The g-score, obtained using a factor analysis of the ten WISC subtests, was composed of three major broad domains, named “fluid intelligence” (PA1), “classification ability” (PA2), and “crystallized intelligence” (PA3).

### 3.2.1 Fiber-bundles analysis

Based on the diffusion data of the seventeen WM fiber-bundles, broad components of fiber-bundles were defined by a factor analysis. First performed on FA values of the WM fiber-bundles (Table S2 in supplementary materials), the factor analysis extracted five broad components with eigenvalues of 6.93, 1.78, 1.40, 1.30, and 1.17, explaining 74% of the total variance (41%, 10%, 8%, 8%, and 7%). The first component (FA-Comp1) showed high loadings for the Fmajor, Fminor, left and right ILF and left hippocampal part of the Cing and left IFOF. The second component (FA-Comp2) comprised the left and right Unc, the right hippocampal part of the Cing and the right IFOF, whereas the third component (FA-Comp3) showed high loadings for the left and right cingular parts of the Cing and the right SLF. The fourth component (FA-Comp4) comprised the left and right CST, whereas the fifth component (FA-Comp5) showed high loadings for the fornix and the left SLF. When performed on AD values of the WM fiber-bundles (Table S3 in supplementary data), four broad components were obtained with eigenvalues of 7.22, 2.60,

1.56, and 1.12, explaining 74% of the total variance (42%, 15%, 9%, and 7%). The first component (AD-Comp1) showed high loadings for the Fmajor and Fminor, and for the right hippocampal part of the Cing, CST, IFOF, ILF, SLF, and Unc. The second component (AD-Comp2) comprised the left IFOF, ILF, SLF, and Unc. The third component (AD-Comp3) showed high loadings for the fornix and the left and right cingular part of the Cing. Finally, the fourth (AD-Comp4) component comprised the left hippocampal part of the Cing and CST. As reported in Table 6.4, the broad components based on AD and FA values of the WM fiber-bundles were further correlated to the intelligence domains. First, significant positive correlations were observed between AD-Comp1 and PA1, PA2, PA3, and g-score. Also, significant positive correlations were observed between AD-Comp2 and PA1, g-score and PA1-g, and between AD-Comp4 and PA3-g. Finally, a significant negative correlation was observed between AD-Comp2 and PA2-g. Second, significant positive correlations were observed between FA-Comp1 and PA1 and between FA-Comp5 and PA2 and g-score. A significant negative correlation between FA-Comp1 and PA2-g was observed. The factor analysis was also performed on the radial and mean diffusivities of WM fiber-bundles and showed no significant correlations with intelligence (Loadings matrices are reported in Tables S4 and S5 of supplementary data).

		PA1	PA2	PA3	g-score	PA1-g	PA2-g	PA3-g
AD	Comp-1	0.397**	0.402**	0.259*	0.433**			
	Comp-2	0.496**			0.353*	0.197*	-0.116*	
	Comp-4							0.257**#
FA	Comp-1	0.323*					-0.112*	
	Comp-5		0.320*		0.327*			

Table 6.4: Correlations between WM fiber-bundles diffusivity components of fractional anisotropy (FA) and axial diffusivity (AD), and intelligence domains (PA1, PA2, and PA3), g-score, and g-unbiased intelligence domains (PA1-g, PA2-g, and PA3-g). \*  $p < 0.05$ ; \*\*  $p < 0.01$ ; #  $p < 0.05$  for effect of age.

### 3.2.2 Graph analysis

#### Global graph metrics

Structural brain networks were successfully reconstructed using a threshold of 0.25 and 1'000'000 fibers. The resulting networks showed overall small world characteristics for all subjects with a mean of 1.62, a mean of 1.74, and a mean of 1.08. Global Graph metrics Correlations between graph metrics and the three intelligence domains, the g-score, and the g-unbiased intelligence domains are reported in Table

6.5. PA1, PA2, and g-score showed significant correlations with the density in the whole brain (Figure 6.8). In the inter-hemispheric network, PA1 and g-score were positively correlated with density, PA1-g was positively correlated with efficiency, characteristic path length, and modularity, and PA2-g was negatively correlated with transitivity. PA1, PA2, and g-score were positively correlated with density in both left and right hemispheres, whereas PA1-g showed negative correlations with transitivity in the right hemisphere and PA3-g with modularity in the left hemisphere.

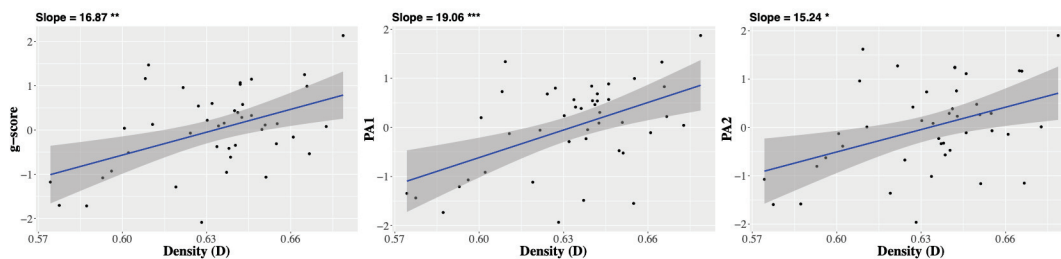


Figure 6.8: Significant positive correlations measured between graph density in the whole brain networks and the g-score ( $p < 0.01$ ), the fluid intelligence domain (PA1;  $p < 0.001$ ), and the classification ability domain (PA2;  $p < 0.05$ ).

Global graph metrics were also measured in brain networks of lobes, namely the frontal, parietal, occipital, and temporal lobes, as well as in the sub-cortical nuclei. In the frontal lobe, PA3-g was positively correlated with modularity, whereas PA2 and g-score were negatively correlated with transitivity. In the parietal lobe, PA1, PA2, and g-score were positively correlated with density, while PA1 and PA1-g were negatively correlated with modularity. Also, PA1, PA2, and g-score were negatively correlated with assortativity. In the occipital lobe, PA1 was positively correlated with density. PA3-g was positively correlated with efficiency and transitivity, but negatively correlated with characteristic path length. In the temporal lobe, PA1 and g-score were positively correlated with characteristic path length and assortativity and negatively with efficiency. PA2 was positively correlated with assortativity and negatively with modularity. Also, g-score was negatively correlated with modularity. Finally, in the sub-cortical network, PA3 was positively correlated with efficiency and assortativity, while PA3-g was negatively correlated with characteristic path length and positively correlated with assortativity.

### Nodal graph metrics

Significant correlations were observed between intelligence domains and g-score and local graph metrics in all the brain lobes. However, after correcting p-values for

		g-score	PA1	PA2	PA3	PA1-g	PA2-g	PA3-g
Whole brain	D	16.87**	19.06***	15.24*	-	-	-	-
	D	9.20*	11.58**	-	-	-	-	-
Inter-hemisphere	E	-	-	-	-	4.82*	-	-
	L	-	-	-	-	0.30*	-	-
	Q	-	-	-	-	1.68*	-	-
	T	-	-	-	-	-	-3.25*	-
Left Hemisphere	D	19.52**	19.48**	19.53*	-	-	-	-
	Q	-	-	-	-	-	-	-16.59*
Right Hemisphere	D	13.17*	12.76*	12.68*	-	-	-	-
	T	-	-	-	-	-20.26*	-	-
Frontal	Q	-	-	-	-	-	-	11.46*
	T	-14.26*	-	-14.37*	-	-	-	-
Parietal	D	18.24***	20.16***	15.86***	-	-	-	-
	Q	-	-10.85**	-	-	-4.87*	-	-
	r	-7.27**	-8.12**	-6.24*	-	-	-	-
Temporal	E	-45.01*	-52.19*	-	-	-	-	-
	L	10.22*	12.12**	-	-	-	-	-
	Q	-225.66*	-	-218.25*	-	-	-	-
	r	6.13**	5.82*	5.81*	-	-	-	-
Occipital	D	-	2.67*	-	-	-	-	-
	E	-	-	-	-	-	-	18.84**
	L	-	-	-	-	-	-	-5.38**
	T	-	-	-	-	-	-	2.68*#
Subcortical	E	-	-	-	4.43*	-	-	-
	L	-	-	-	-	-	-	-1.13**
	r	-	-	-	2.86*	-	-	2.01*

Table 6.5: Correlation slopes between global graph metrics, namely the density (D), assortativity (r), transitivity (T), modularity (Q), characteristic path length (L), and efficiency (E) in different brain networks (whole brain, inter-hemispheres, left and right hemispheres, lobes, and subcortical nuclei) and intelligence domains (PA1, PA2, PA3, g-score, and g-unbiased PA1-g, PA2-g, PA3-g). \*  $p < 0.05$ , \*\*  $p < 0.01$ , \*\*\*  $p < 0.001$ . #  $p < 0.05$  for the effect of age

multiple comparisons (84 graph nodes), only few correlations remained significant. More in details, PA1-g was positively correlated with the degree and betweenness centrality, and negatively with clustering coefficient and local efficiency in the right precuneus node (Figure 6.9). Also, PA1-g was negatively correlated with the degree in the right isthmus cingulate node.

## 4 Discussion

In this work, WM structural connectivity was measured using fiber-bundle analysis as well as graph theory method. To our knowledge, this study is the first to

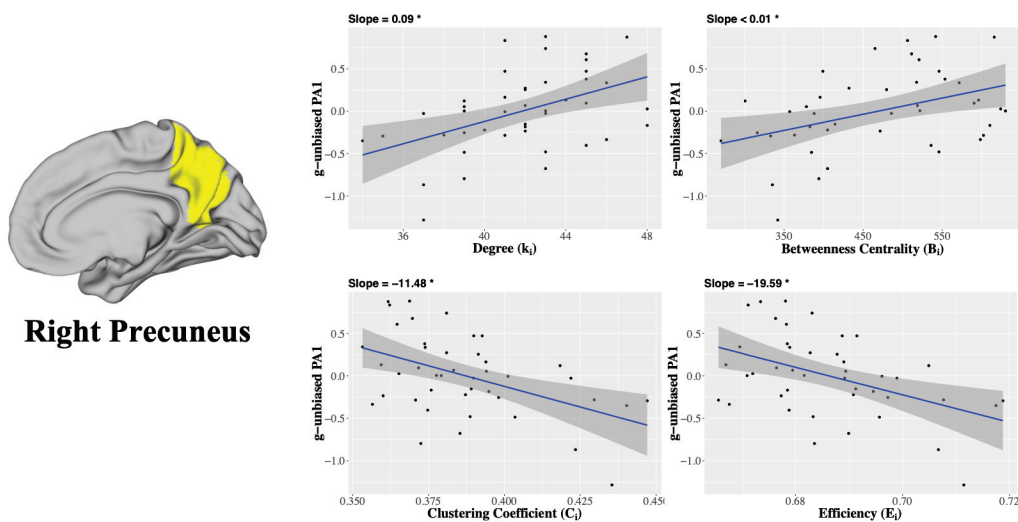


Figure 6.9: Correlations between PA1-g intelligence domain and local graph metrics in the right precuneus node.

correlate children intelligence with both global and local graph metrics of brain networks.

The exploration of structural connectivity using graph metrics provided evidence of a strong relationship between brain networks connectivity and intelligence. More specifically, we showed that higher intelligence is related to a dense and homogeneous brain networks. Indeed, most of the IQ indices (VCI, PRI and WMI) correlated positively with graph density and negatively with modularity and transitivity, two metrics describing segregation properties. These results are in accordance with the idea that intelligence depends on the brain networks capacity to enhance their structural connectivity [Barbey (2018)]. On one hand, the strong correlations observed between both VCI and WMI scores and graph metrics in the temporal lobe confirmed that high integration and density levels of the temporal connectivity are related to high verbal and memory abilities, as previously reported [Squire and Zola-Morgan (1991)]. On the other hand, the high levels of structural connectivity observed in the parietal lobe in relation with high FSIQ confirmed the important role of parietal functions in children intelligence, such as visuospatial and memory abilities (mirror neurons), as well as mathematical operations processing [Desco *et al.* (2011)]. Moreover, as shown by [Sowell *et al.* (1999)], the parietal lobe presents the most important changes during adolescence, a period of rapid cerebral development.

These results have been confirmed when three intelligence domains were extracted from WISC scores by PCA, and finer results have been obtained. First, the increase of density with the general intelligence domains (g-score, PA1, and PA2) in the whole brain, the left and right hemispheres, and the inter-hemisphere net-



works demonstrated that a high level of intelligence is associated with increased WM connectivity. More specifically, the graph density in whole brain and hemisphere networks was correlated with PA1 and PA2 but not with PA3 intelligence domains, showing the predominance of fluid intelligence and classification abilities. Second, the decreased segregation properties (modularity and transitivity) with the general intelligence domains (g-score, PA1, and PA2) in the frontal (PA2), parietal (PA1), and temporal (g-score and PA2) lobes networks showed that the main intelligence domains are related to homogenous brain organization. These correlations observed between frontal and temporo-parietal regions and intelligence are in agreement with the meta-analysis of Jung and Haier [Jung and Haier (2007)], and Basten et al. [Basten et al. (2015)]. Nevertheless, as concluded by Basten et al. [Basten et al. (2015)], one should carefully distinguish structural and functional brain correlates of intelligence. In contrast, the third broad intelligence domain, named crystallized intelligence (PA3 and PA3-g), was mainly associated to increased integration properties in the occipital lobe and sub-cortical nuclei networks. This finding is in agreement with the previous report of Colom et al., showing that crystallized intelligence correlates mainly with occipital regions [Colom et al. (2008)]. These findings on global network organization support the model proposed by Barbey [Barbey (2018)], in which high intelligence is related to a balance between high integration (high density) and mean segregation (modularity and transitivity) levels in the network, which correspond to the definition of a small-world network as observed in this study.

To further explore the relationship between intelligence and brain organization at a lower scale, local graph metrics were computed. Associations were mainly found in the parietal, temporal, and frontal lobes, which correspond to the P-FIT regions [Jung and Haier (2007)]. In particular, metrics measured a better network integration in the left and right precuneus in relation with FSIQ, mostly driven by the PRI, and the g-unbiased fluid intelligence (PA1-g), respectively. This result is in agreement with previous studies, highlighting the importance of the precuneus in visuospatial abilities and self-consciousness [Oshio et al. (2010)]. Local metrics, measured in the left middle and superior temporal networks, were associated to VCI. These findings are concordant with the report of [Crinion et al. (2003)], showing that speech comprehension employs both temporal lobes, with a left predominance. Moreover, in agreement with the report of Basten et al., we observed a relation between PRI and local graph metrics in the subcortical networks [Basten et al. (2015)]. High PRI was associated to high network integration of the right caudate nucleus, region also involved in reasoning [Melrose et al. (2007)].



These results on structural brain network organization were confirmed by the diffusivity measurements obtained from the major WM fiber-bundles. Indeed, positive correlations were observed between AD values and intelligence domains. Based on the hypothesis that AD values reflect myelination and axonal density or diameter [Jones *et al.* (2013), Mori and Zhang (2006)], these findings confirmed the relationship between WM fiber-tracts integrity and intelligence, and suggest the potential interest of AD as a marker of general intelligence. More specifically, the correlation with g-score and g-intelligence domains (PA1, PA2, and PA3) were mainly located in the right fiber-bundles (AD-Comp1), while the correlations with g-unbiased intelligence domains were mainly located in the left fiber-bundles (AD-Comp2). These results may suggest a potential lateralization of the intelligence axonal substrate, with the general intelligence being more weighted by the right WM fiber-bundles, and the g-unbiased intelligence being more weighted by the left WM fiber-bundles.

## 5 Conclusion

In this chapter, we aimed to explore the structural brain substrate of intelligence. For this purpose, we applied graph analysis to the connectivity matrix obtained from DTI. A preliminary study of correlation, between graph measures and five WISC sub-tests, showed significant results. These findings have led us to perform a principal component analysis on the 10 WISC sub-tests in order to obtain more precise results on these correlations with well separated intelligence domains. Three major domains were extracted, namely "fluid intelligence", "classification ability", and "crystallized intelligence" that composed all together the "g-factor".

The graph analysis showed significant correlations between several graph metrics based on diffusion measures and intelligence factors. First, the increase of network density with intelligence scores, confirmed that fiber-bundles density of brain networks plays a significant role in children intelligence. Second, considering that modularity represents a measure of segregation level between graph modules, and that transitivity reflects the redundancy in the network connections, the low modularity and low transitivity observed in high IQ children confirmed that homogeneous brain organization correlates with intelligence. These findings showed that children's high IQ may be related to a high fiber density and optimally distributed brain networks, thanks to the global sensitivity of such graph-based methods for the investigation of brain topological organization. Furthermore, diffusion metrics measured in WM fiber-bundles confirmed that children intellectual abilities are cor-

related with enhanced WM myelination and integrity. Our findings showed that both inter- and intra-hemispheric WM integrity are enhanced in children with high intellectual abilities. In agreement with the literature, these results confirmed that diffusion metrics measured in WM fiber-bundles constitute accurate and quantitative markers of intelligence. In summary, this study demonstrated that intelligence quotient is correlated with the microstructure as well as the topological organization of the WM brain networks.



## Chapter 7

---

# Brain activation during semantic tasks

---

### Contents

---

<b>1</b>	<b>Introduction . . . . .</b>	<b>136</b>
<b>2</b>	<b>Materials and Methods . . . . .</b>	<b>137</b>
2.1	Subjects . . . . .	137
2.2	MRI acquisition . . . . .	138
2.3	Verbal semantic memory task . . . . .	138
2.4	MRI processing . . . . .	139
2.5	First level analysis . . . . .	140
2.6	Second level analysis . . . . .	140
2.7	Task paradigm . . . . .	140
<b>3</b>	<b>Results . . . . .</b>	<b>141</b>
3.1	Task performance . . . . .	141
3.2	fMRI activation . . . . .	143
<b>4</b>	<b>Discussion . . . . .</b>	<b>145</b>
<b>5</b>	<b>Conclusion . . . . .</b>	<b>148</b>

---

Our research on children intelligence, has been concluded with a task-fMRI study which is presented in this chapter. We were interested in knowing if their brain reacts differently to task stimulation compared to children with a standard IQ (SIQ), and if the two HIQ profiles, previously introduced in the chapter 5, present different functional networks. For this purpose, we designed a fMRI experiment with a semantic memory task. As well as in the functional connectivity study, we distinguished a group of children with heterogeneous HIQ and a group with homogeneous HIQ, and a control group composed of children of the same age with a standard IQ. The study consisted of passing an fMRI in which a verbal semantic memory task was presented. During this task, children had to memorize semantically linked pairs of words and then return them using a response box. This task was selected because of its similarity to the WISC IV "Similarities" test, in which children must extract a common concept linking two words presented orally, and for which the two HIQ profiles do not differ. Brain activation, response times, and the number of correct, incorrect, or missed responses were registered.

However, being an ongoing study in this chapter, we present only some preliminary results, and further analysis are needed.

## 1 Introduction

The most simple and natural way to investigate the neural substrate of intelligence is to use task fMRI. Indeed, this technique allows to study functional correlates of intelligence subjecting people to cognitive tasks stimulating reasoning, working memory or other abilities.

In the first MRI study of reasoning, subjects performed three types of tasks: match, figural reasoning, and analytical problems [Prabhakaran *et al.* (1997)]. Activation in several brain regions mostly overlapping working memory networks were registered, highlighting the existence of a link between neural correlates of working memory and those of reasoning. After this first work, several studies of intelligence processes were performed with task fMRI. All of them were then included in a meta-analysis of 37 neuroimaging studies that led Jung and Haier to introduce the Parieto-Frontal Integration Theory (P-FIT) [Jung and Haier (2007)]. This model identified a network of fourteen cortical regions connected with intelligence that belong to the Default Mode Network (DMN) and to the Central Executive Network (CEN) main situated in parietal and frontal lobes. An extension of P-FIT was later suggested, with the addition of some subcortical structures and other cortical areas as relevant regions for intelligence [Basten *et al.* (2015)].

More recently, other aspects of intelligence were explored more thoroughly, thanks to task fMRI studies. Indeed, fluid intelligence has been demonstrated to be linked to specific frontal and parietal regions [Cole *et al.* (2015)] that showed reduced activation in lower fluid intelligence subjects when performing memory tasks [Tschentscher *et al.* (2017)]. Another interesting finding showed that higher cognitive abilities are also associated with a lower deactivation in task negative networks, and a lower activity in task positive network during working memory tasks [Takeuchi *et al.* (2018)]. This finding is in agreement with the efficiency theory suggesting that, when working on the same cognitive tasks, more intelligent individuals show lower brain activation in comparison to individuals with standard intelligence [Neubauer and Fink (2009)].

In the present study, we explored the functional brain activity of two HIQ children groups as compared to standard IQ (SIQ) children. HIQ children were identified by a full scale intelligence quotient (FSIQ) higher than 130, measured with the fourth edition of Wechsler Intelligence scale for Children (WISC). The two HIQ profiles were characterized: homogeneous HIQ (Hom-HIQ) children had homogeneous results to the WISC subscales, while heterogeneous HIQ (Het-HIQ) showed a verbal comprehension index (VCI) or perceptual reasoning index (PRI) higher than 130, and a significant difference ( $>15$ ) between VCI and PRI. We proposed to identify the difference in the functional activation of the three different intelligence groups during the execution of a semantic memorization task. We hypothesized to obtain different brain activation during the semantic task according to the two HIQ profiles and SIQ group.

## 2 Materials and Methods

### 2.1 Subjects

Fifty-seven children (43 males and 14 females) were recruited from the children psychiatry department of Lyon's Neurological Hospital and the PSYRENE Center. Children with neurological diseases, learning disabilities and psychotropic treatments were excluded from this study. Based on the results of the WISC-IV test and its four indices (Verbal comprehension index [VCI], Perceptual reasoning index [PRI], Working memory index [WMI] and Processing speed index [PSI]) three groups were composed. Fourteen children (mean age = 9.91, SD = 1.17), with a full scale intelligence quotient (FSIQ) in the standard of children corresponding to their age, composed the SIQ group. Het-HIQ group was composed of 23 children (mean age = 9.97, SD = 1.24) characterized by a FSIQ higher than 130 and heterogeneous results

in VCI and PRI. More in details, VCI measure was higher than the value of 130 and a minimum difference between VCI and PRI of 15 points was measured. Finally, the Hom-HIQ group was composed of 19 children with a FSIQ higher than 130 with homogeneous values of the VCI and PRI.

## 2.2 MRI acquisition

MRI examinations were performed on a 1.5T Siemens Sonata system with an 8-channels head-coil and 40  $mT/m$  gradients, at the MRI department of CERMEP-Imagerie du Vivant. The MRI protocol included a 3D T1-weighted magnetization prepared rapid gradient echo (MPRAGE) sequence acquired for 8 minutes with temporal parameters  $TR/TE/TI = 1970/3.93/1100\ ms$  and a millimetre spatial resolution (flip angle =  $15^\circ$ , matrix size =  $256 \times 256$ , field of view (FOV) =  $256 \times 256\ mm$ ). Task fMRI protocol was also acquired using a T2\*-weighted BOLD-sensitive gradient-echo EPI sequence with 30 axial slices of 3  $mm$  thickness, 1  $mm$  inter-slice gap, repetition time (TR) 2500  $ms$ , echo time (TE) 50  $ms$  and spatial resolution  $3.4 \times 3.4 \times 3\ mm$  ( flip angle =  $80^\circ$ , matrix size =  $64 \times 64$ , FOV = 192  $mm$  ). Four runs of 440 volumes were acquired.

## 2.3 Verbal semantic memory task

During the verbal semantic memory task, the subject had first to learn a list of 6 word pairs displayed on a screen (Encoding phase) and then should use two answer buttons during the Retrieving phase. In total, each child learned 96 pairs of words, divided into three different categories: words with semantic link (SL), words without any semantic link (WL) and nonsense words (NS). All words were bi-syllabic and consisted of up to eight letters. SL and WL words came from the Ferrand's group works [Ferrand and Alario (1998), Ferrand (2001)] that were focused on concrete and abstract words respectively. The words presented in our study were then either abstract or concrete. NS words were pseudo-words created in such a way that they were easily pronounceable for a young French-speaking reader.

During the encoding phase, six pairs of words (SL, WL or NS) were displayed successively during 2800 ms on a black screen. Each presentation of word pairs was interspersed of 200 ms interval. Following the encoding phase, a fixing cross was presented on the screen for 3000 ms to announce the transition to the retrieving phase. During this phase, three words were displayed on the screen: at the top was shown the word whose couple had to be found, and on the bottom the word of the pair and a distractor of the same category (SL, WL or NS). This was repeated

six times for each previously encoded pair. The child had 3000 ms on each test to answer and over the allotted time, the test was considered "missed".

The succession between encoding phase and restitution phase constitutes a first block (Figure 7.1). Sixteen blocks were presented alternatively during the two runs. An interval of a few minutes between the two runs allowed the child to rest and make sure everything was fine. Answers and response times were recorded. Each response to a trial was counted as either "correct" or "incorrect" or as "missed".

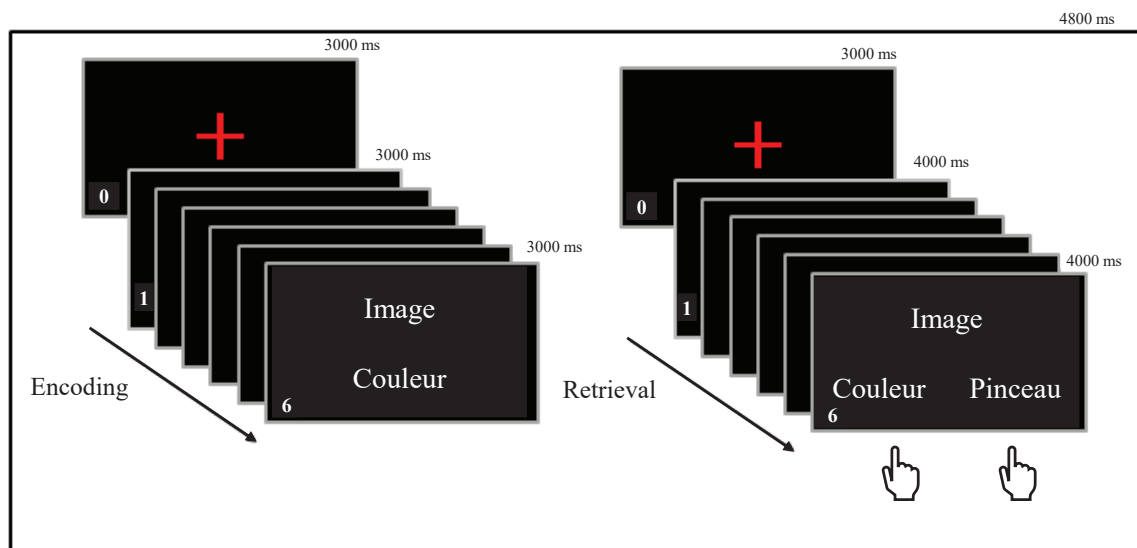


Figure 7.1: Illustration of the task. The Encoding and the Retrieval phases constitute a block

## 2.4 MRI processing

All MRI data analyses were computed using the Statistical Parametric Mapping software package (SPM12)(<https://www.fil.ion.ucl.ac.uk/spm/software/spm12>). The first five functional volumes were eliminated in order to be sure to have a stable signal. For each subject, data were corrected for slice timing, and motion, and were coregistered to the anatomical image. Data artifacts for head motion were detected using Art toolbox. For the scans affected by scan-to-scan motion including rotational movements higher than 3 mm or with an exceptionally high variation (signal higher than 4 standard deviations from mean), a corresponding artifact regressor was constructed. Runs with a number of corrected images higher than 10% of the total volumes, were excluded at this stage for excessive head motion and subjects without an exploitable image were not included in the analysis. After this screening, the analysis of the semantic memory task was conducted on 54 subjects. The anatom-



ical MRI images were segmented according to prior tissue probability maps and grey-matter, white-matter and CSF probability maps were generated. A template was generated using DARTEL, a diffeomorphic registration method that accurately align brains within the MNI space [Ashburner (2007)], from the segmentation of all the subjects. Finally, the deformation field created during the previous step was applied to both anatomical and functional images that were normalized in a standard space applying a Gaussian kernel of  $(3 \times 3 \times 3 \text{ mm}^3)$ .

## 2.5 First level analysis

The statistical analysis was performed for individual subject using the general linear model (GLM) [Friston *et al.* (1995)]. For the cognitive task, the two steps were separately analyzed: the Encoding (E) and Retrieving (R) phases. In the GLM model, three encoding and three retrieving conditions, each one for a single word category (SL, WL and NS), were considered as predictors of interest. Furthermore, the information about the type of response (miss, hit or incorrect) was entered in the model in order to take into account this information in the creation of the design matrix. In order to compare the different task conditions, several contrasts were defined and statistically analyzed with t-Student test using SPM12.

## 2.6 Second level analysis

In order to search for activated areas that were consistent for each group, the GLM parameters estimated in the previous analysis were entered in a second level analysis. For each contrast previously defined, the activated areas for each group (SIQ, Hom-HIQ, and Het-HIQ) were extracted. Furthermore, the activation of the two HIQ groups were compared between them and to those in SIQ group. A two-sample t-test was applied thresholding the results at  $P < 0.05$ .

## 2.7 Task paradigm

The response time and answers obtained for each task were statistically analyzed using R library (<http://www.R-project.org/>). Differences among responses time were evaluated applying an ANOVA test with three factors and the interactions between them: intelligence group (SIQ, Hom-HIQ, and Het-HIQ), task (SL, WL, and NS), and response factor (incorrect, missed, correct).

$$time \sim Intelligence * task * response \quad (7.1)$$

Differences in the percentage of incorrect, missed, or correct answers ( $r_i$  where  $i \in : \{ incorrect, miss, correct \}$ ) were explored with an ANOVA test with two factors and the interactions between them: intelligence group (SIQ, Hom-HIQ, and Het-HIQ), task (SL, WL, and NS).

$$r_i \sim Intelligence * task \quad (7.2)$$

Furthermore, Tukey's post-hoc test was applied to explore the multicomparisons within each factor for both statistical analyses.

### 3 Results

#### 3.1 Task performance

##### Response time

Statistical analysis on response time showed that the ANOVA test was significantly different for all the three factors: intelligence group, task, and response. The interactions between the three factors were not significant, but a trend resulted for the interaction between the intelligence group factor and the response factor. Furthermore, Tukey's post-hoc test showed for all the factors significant difference in response time in all the multi-comparisons (Table 7.1).

Factors	Comparisons	Difference
Intelligence	Het-HIQ - SIQ	-0.148 ***
	Hom-HIQ - SIQ	-0.216 ***
	Hom-HIQ - Het-HIQ	-0.068 ***
Task	NS-SL	0.231 ***
	WL-SL	0.151 ***
	WL-NS	-0.079 ***
Response	Miss-incorrect	1.076 ***
	Correct-incorrect	-0.166 ***
	Correct-miss	-1.243 ***

Table 7.1: Results obtained with Tukey's post hoc test comparing the time response for all the combinations in each factor. \*\*\*  $p < 0.001$ .

More in detail, Hom-HIQ children answered the questions faster than the two other groups, while the response time of Het-HIQ group was shorter than that of SIQ group. Concerning the different tasks, the time of answer was increased in WL

task compared to SL task, and NS resulted to have the longest response time (Figure 7.2).

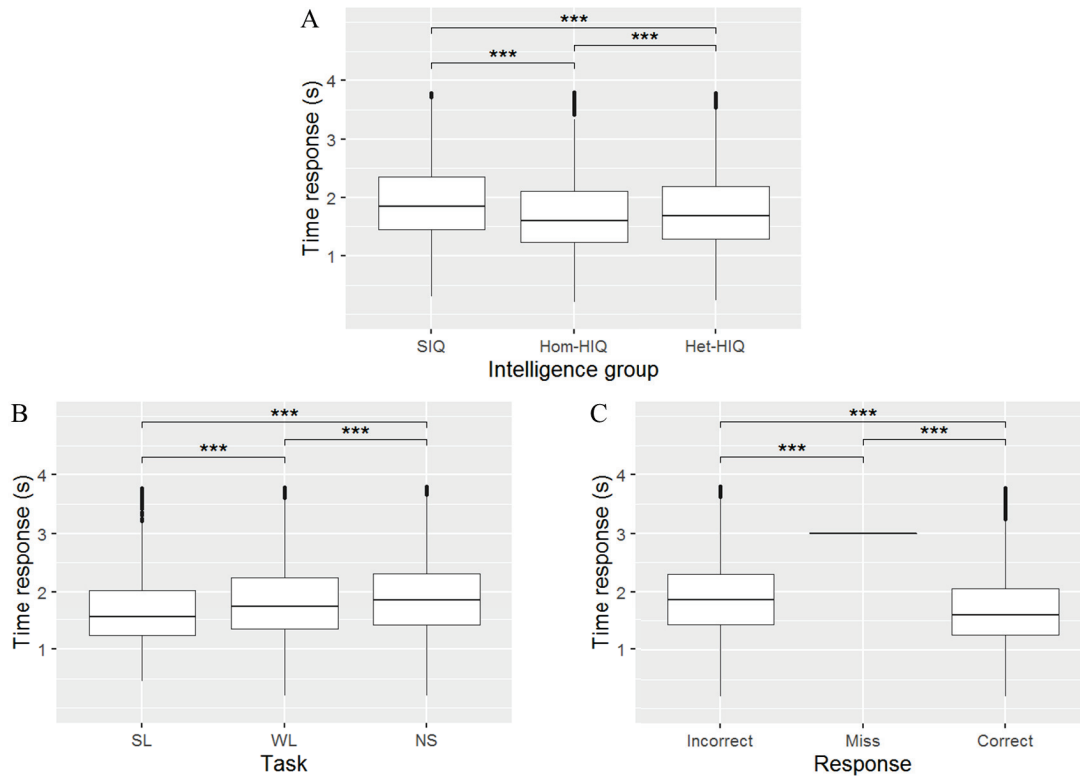


Figure 7.2: Boxplots of response time measured in seconds for three different factors. (A) for Intelligence group: Standard Intelligence Quotient (SIQ), Homogeneous High Intelligence Quotient (Hom-HIQ), and Heterogeneous High Intelligence Quotient (Het-HIQ); (B) for task factor: words with semantic link (SL), words without semantic link (WL), and non-sense words (NS); (C) for response factor: incorrect, miss, and correct. \*\*\*  $p < 0.001$ .

Finally for the time of response, the corrected answers were shorter than the uncorrect ones. Obviously, the missed answers present the slowest response time.

## Response type

The difference in the percentage of answers was explored for each response type (correct, incorrect or missed). No significant difference among intelligence groups was found. Indeed, as we can see in Table 7.2, the values among the three groups are similar for each response type.

However, for incorrect and correct responses a significant difference was measured among the tasks (SL, WL, NS). More in details (Table 7.3), Tukey's post hoc test showed a high significance level ( $p < 0.001$ ) for all the comparisons of the correct

	SIQ	Het-HIQ	Hom-HIQ	SL	WL	NS
Incorrect	30.85	30.64	28.25	18.88	31.33	44.44
Missed	3.44	3.30	1.96	2.01	3.19	3.86
Correct	65.71	66.06	69.79	79.11	65.48	51.70

Table 7.2: Percentage of total incorrect, missed, and correct answers for each intelligence group (SIQ, Het-HIQ, and Hom-HIQ) without differentiating for task typology, and for each task typology (SL, WL, and NS) without differentiating for intelligence group.

answers and for (NS-SL) and (WL-SL) comparisons in incorrect answers, while (WL-NS) was modestly significant. Finally, the percentage of missed answers resulted in no significant changes among the three intelligence groups and among the three tasks.

Comparisons	Incorrect	Miss	Correct
NS-SL	25.56 ***	-	-27.41 ***
WL-SL	12.45 ***	-	-13.63 ***
WL-NS	-13.11 *	-	13.78 ***

Table 7.3: Percentage difference of incorrect, missed, and correct answers for each pair of task (SL, WL, NS). \*  $p < 0.05$ , \*\*\*  $p < 0.001$

## 3.2 fMRI activation

Several brain regions were activated for each contrast defined in the first level statistical analysis in standard IQ group and both high IQ profiles. We reported in this work the activation resulting to be significantly different between each pair of intelligence group.

### Encoding phase

During the encoding phase of words without a semantic link (WL), standard IQ showed a higher activation than heterogeneous HIQ profile in the left inferior occipital gyrus (BA 19) (Figure 7.3.A).

A significant activation difference between homogeneous and heterogeneous HIQ profiles was observed during the encoding phase for the words without a semantic link (WL). For this task, the homogeneous group showed a stronger activation in the left prefrontal cortex (BA10) (Figure 7.3.B).

No significant activation difference was found between homogeneous HIQ group and standard IQ group during encoding phase of the task.

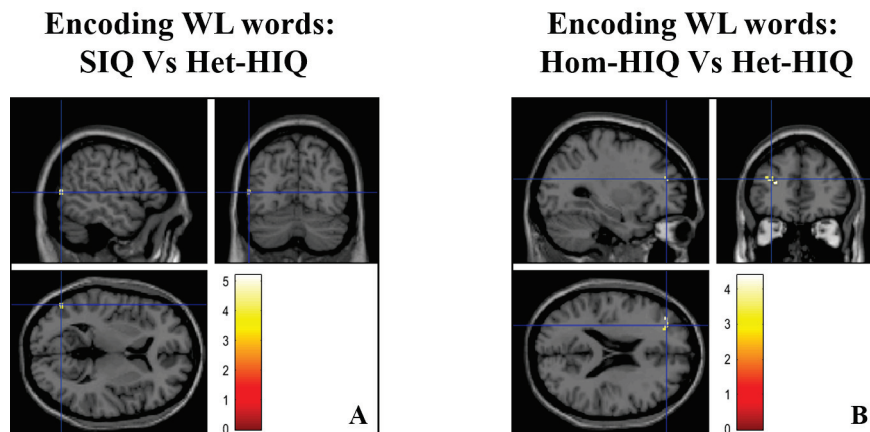


Figure 7.3: Illustration of regions that showed significant higher activation during encoding phase of words without semantic link (WL): (A) left inferior occipital cortex in standard intelligence group compared to the heterogeneous HIQ profile, (B) left prefrontal cortex in homogeneous HIQ profile compared to heterogeneous profile.

### Retrieving phase

Significant results were observed during the retrieval phase when the heterogeneous HIQ group was compared to the reference group with a standard IQ. The heterogeneous profile showed a stronger functional activation in left thalamus for words without semantic link (WL) compared to words with semantic link (Figure 7.4.A). A trend was also measured in the left occipital cortex (BA17-18) where the activation of heterogeneous HIQ profile was stronger than SIQ (Figure 7.4.B 7.4.C) comparing the retrieval of NS to SL pair of words.

Two significant results were also observed comparing the two High Intelligence Quotient profiles. A stronger ( $p < 0.01$ ) activation was observed in left posterior cingular gyrus (BA 23) (Figure 7.5.B) in the Heterogeneous group when the difference between the retrieving of NS to SL words is compared. For the same contrast, heterogeneous profile showed also higher activation in the right pre-central gyrus (BA4) ( $p < 0.05$ ) and in the right supplementary motor area ( $p < 0.01$ ) (Figure 7.5.C and 7.5.D).

Comparing the retrieval phase of NS words to SL+WL pair of words taken together, the heterogeneous HIQ profile showed higher ( $p < 0.01$ ) activation of the left middle frontal gyrus (BA6) (Figure 7.5.A) than the homogeneous HIQ profile.

Finally, no significant result was found when comparing Hom-HIQ group with SIQ group.

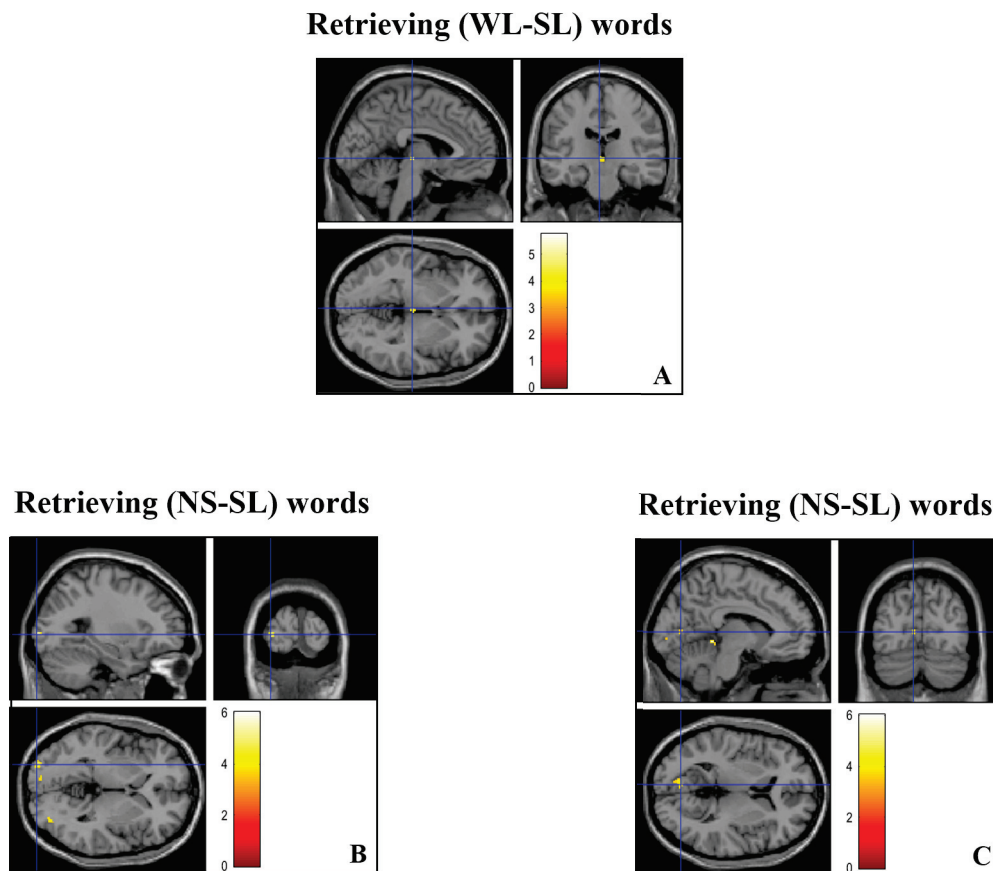


Figure 7.4: Illustration of the regions that showed higher activation in Het-HIQ profile compared to reference group (SIQ), (A) in the left thalamus in the difference between the retrieving of words without link (WL) and word with semantic link (SL), and (B) & (C) in the left occipital cortex for the difference between the retrieving of non-sense words (NS) and all sense words (SL+WL).

## 4 Discussion

### Task performance

In this study, we aimed to explore the performances of two HIQ profiles. Our first hypothesis was that Het-HIQ and Hom-HIQ may present higher scores in the different tasks compared to the reference group. This hypothesis has been confirmed by the behavioural results. Indeed, we measured significant different response times among the three groups. In particular, Hom-HIQ resulted to be the fastest group to respond. Next, very close to homogeneous profile, we found heterogeneous profile that showed intermediate response time. Finally, we found that SIQ was the slowest group in the retrieving phase. This first analysis confirms that both HIQ groups have effectively higher performances during cognitive tasks. We may also affirm that a significant difference in performance exists between the two HIQ profiles.

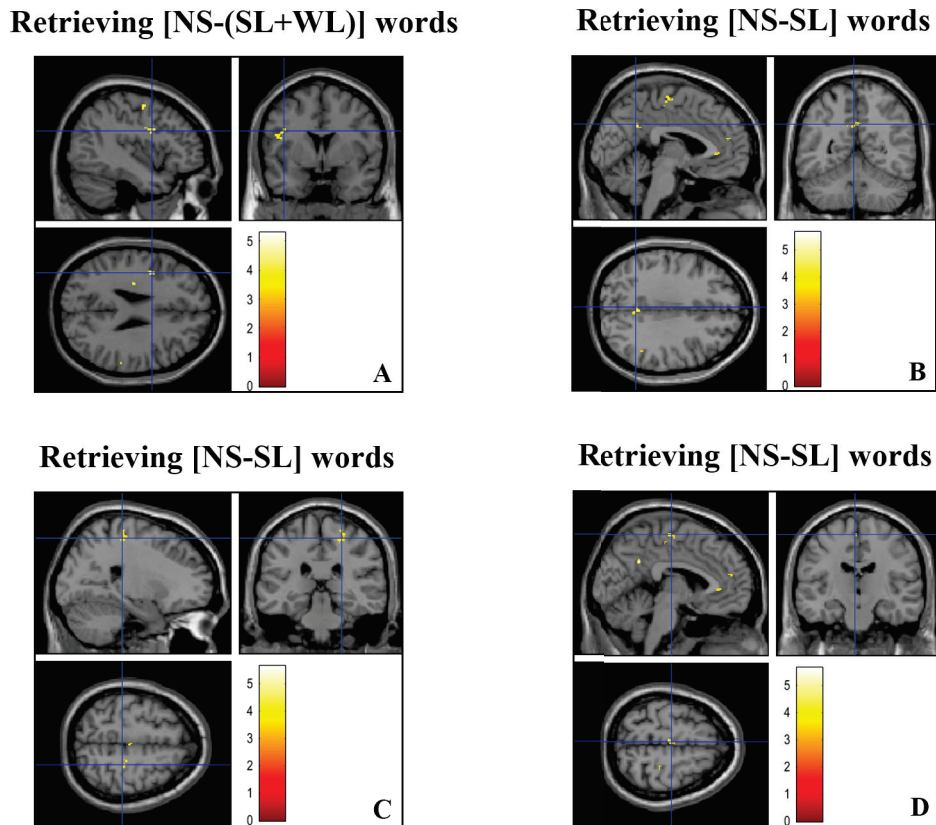


Figure 7.5: Illustration of the regions that showed higher activation in the Het-HIQ profile compared to the Hom-HIQ profile, (A) in the left middle frontal gyrus for the difference between the retrieving of non-sense words (NS) and both sense words (SL+WL). During the retrieving of non sense (NS) and words with semantic link (SL), (B) in the left posterior cingulate gyrus, (C) in the right posterior central gyrus, and (D) in the right pre-central gyrus.

However, the three groups could not be differentiated based on percentage of response type (incorrect, miss, correct). Indeed, no significant difference was observed for this analysis among the Intelligence groups. This result was supported by the scores obtained during the "Similarities" test of the WISC, where no significant difference was observed between the two HIQ profiles.

### fMRI activation

Concerning fMRI activation, we hypothesized that both HIQ profiles would have significantly different brain activation, compared to the SIQ group as it has been previously found in the literature [O'Boyle *et al.* (2005), Lee *et al.* (2006)b]. However, our results allowed to conclude that our hypothesis was confirmed only for the heterogeneous HIQ profile. Indeed, for both encoding and retrieving phases, this group showed significant different activations as compared to standard IQ group.



The neural substrate of depth encoding is not fully understood and several brain regions have been associated with this task. For instance, left inferior occipital cortex has been identified to be part of the semantic system. On one hand, it is involved in reading [Taylor *et al.* (2019)] task, during which the brain maps visual information onto language information. On the other hand, it is possible that it may also serve a semantic function [Binder *et al.* (2009)]. In our study, this region is more activated in the SIQ group than in the Het-HIQ group during the reading of words without any semantic link.

Our results highlight also a strong activation during encoding of words without semantic links in left (BA 10). This finding is in agreement with the literature that demonstrated an engagement of the prefrontal cortex (BA 10, 45, 46, 47) in tasks demanding high semantic elaboration [Nyberg (2002)]. We found that this region has a higher activity in homogeneous than in heterogeneous HIQ groups. Increased activity in these regions has been demonstrated to be responsible for deeper encoding and leads to better retrievable memory traces [Nyberg (2002)]. According to this study, Hom-HIQ performed a deeper encoding for words without semantic link in order to then better remember the association between the words.

During the retrieving phase, the left thalamus was more activated in Het-HIQ group than in the SIQ group. This region is involved in a variety of high cognitive functions, including cognition, motor, speech and prosody, semantic processing, and verbal memory [Hebb and Ojemann (2013)]. Although the bulk of the evidence refers to episodic memory, it was recently proposed that this region supports memory performance also in semantic retrieval tasks [Pergola *et al.* (2013)]. Indeed, it seems to be important during semantic retrieval, possibly because of their role in the activation of phonological representations. Our result is then consistent with the literature and shows that the heterogeneous group activated more the left thalamus for the semantic retrieval of more complex words, such as the words without semantic link.

Even if it was only a trend, the primary and the secondary visual cortex (SVC) were more activated in Het-HIQ group than in the SIQ group. While the classical model of the neurobiology of language proposed a left-lateralized linguistic network of the fronto-temporal regions, more recent studies included also several regions all around the brain. Since SVC is one of this region [Binder *et al.* (2009)], our finding suggest a higher activation of the semantic reading region in the heterogeneous HIQ profile.

Left pre-motor cortex was also found to be involved in the comparison between the retrieval of non-sense (NS) words and the sense (SL+WL) words. The association



of the pre-motor cortex with memory formation has been found in numerous studies grouped in a meta-analysis [Kim (2011)]. This result showed that heterogeneous profile activated more the memory region than homogeneous group, probably due to the difficulty of the task with non-sense words.

The heterogeneous HIQ profile, showed also significant activation in precentral and postcentral frontal gyri and in the posterior cingulate gyrus. These results are supported by a meta-analysis of 120 functional neuroimaging studies exploring the brain semantic system [Binder *et al.* (2009)]. While this region has generally been linked with episodic and visuospatial memory, this meta-analysis highlighted its function in semantic task as an interface between the semantic retrieval and episodic encoding systems, thanks to its strong connections with the hippocampus. Finally, somatosensory cortex has been demonstrated to be linked to language, in particular in some aspects of phonological processing [Bouchard *et al.* (2013)].

## 5 Conclusion

The purpose of this study was to characterize the functional differences between the two groups of HIQ children during a semantic memory task. From these results, it seems difficult to reject this hypothesis. Indeed, we have highlighted differences in both performances and brain activation during the task.

First, our results showed that the two HIQ profiles and the SIQ group can be differentiated from their response time during the retrieving phase of the task. More precisely, homogeneous profile presented the shortest response time, while SIQ resulted to be the slowest group. Since time response of heterogeneous group were really very close to those of Hom-HIQ, we could conclude that both HIQ groups are more rapid in answering than SIQ group.

Second, we compared brain activations between intelligence groups. Exploring different contrasts in both encoding and retrieving phases, different activations were observed in the heterogeneous HIQ profile compared to the reference group, and to the homogeneous HIQ profile. This higher activity was observed in several regions that are recognized to belong to the semantic reasoning and memory networks. We aimed to focus our attention to the contrasts that showed significant results implying the encoding or retrieving of the words without any signification (NS), and the words without any semantic link (WL). We can conclude that, during harder tasks, like as NS and WL retrieving, heterogeneous profile needs to activate more the regions related to semantic reasoning or memory in order to obtain the same performance of Hom-HIQ and SIQ groups.

From all these findings, we may confirm our hypothesis that both HIQ profiles are characterized by a different brain activity, with stronger evidences in Het-HIQ children.



### III Research project on HIQ Adults

---



---

# Functional and structural connectivity

---

### Contents

---

<b>1</b>	<b>Introduction . . . . .</b>	<b>154</b>
<b>2</b>	<b>Materials and Methods . . . . .</b>	<b>155</b>
2.1	Population . . . . .	155
2.2	MRI acquisition . . . . .	155
2.3	Intelligence scores . . . . .	156
2.4	Data preprocessing . . . . .	156
2.5	Connectivity measurement . . . . .	158
2.6	Graph metrics . . . . .	159
2.7	Statistical analysis . . . . .	159
<b>3</b>	<b>Results . . . . .</b>	<b>159</b>
3.1	Behavioral observations . . . . .	159
3.2	Functional connectivity . . . . .	160
3.3	Structural connectivity . . . . .	161
<b>4</b>	<b>Discussion . . . . .</b>	<b>163</b>
<b>5</b>	<b>Conclusion . . . . .</b>	<b>164</b>

---

# 1 Introduction

The last part of this thesis is completely dedicated to the study of brain connectivity in adults. Indeed, after the investigation of the neural substrate of intelligence in children, we wondered whether the adult neural substrate of intelligence remains along lifespan.

However, on this population, we did not perform the same functional and structural analysis that were previously performed in children. In particular, concerning the functional connectivity analysis, we did not measure the "hub disruption index" as the control SIQ group was not complete. This fact has led us to explore only the relationship between intelligence scores, as measured by the Wechsler Adult Intelligence Scale (WAIS), and both functional and structural network topology, as described by several graph metrics.

As it has been presented in detail in the previous chapters, several works explored functional (FC) or structural (SC) brain connectivity in adults with graph analysis. Concerning the whole brain networks, these studies showed a correlation between intelligence and brain network efficiency in both connectivity typologies [Li *et al.* (2009), Van Den Heuvel *et al.* (2009)a]. However, this result was not confirmed by a study of structural connectivity on a larger population of HCP [Kruschwitz *et al.* (2018)]. Local graph metrics have been also demonstrated to be associated with intelligence in several brain regions [Jung and Haier (2007), Fischer *et al.* (2014), Hilger *et al.* (2017)b].

In this ongoing work, we explored brain networks in adults by analyzing the activity of GM regions, and WM structure that connects these regions (Section 3). To this end, we measured several metrics of graph from the functional and the structural networks. The association between intelligence subscores, as measured by the WAIS, and the brain functional and structural networks properties, as measured by both global and local graph metrics, have been investigated (Section 3).

## 2 Materials and Methods

### 2.1 Population

Fifty male adults were recruited by advertisement in public and medical environment. Participants have to fulfill the following prerogatives: being right-handed, aged between 20 and 60 years old, male, and without any neurological or psychiatric diseases, nor any MRI contraindication. All these investigations were verified during a medical examination and the participants were informed of the study details and before signing a consent form. This study was approved by the local ethics committee (CPP Sud-Est III).

### 2.2 MRI acquisition

MRI examinations were performed on a 3T Siemens Prisma MRI system (Erlangen, Germany) at the MRI department of CERMEP-Imagerie du Vivant. Subjects brain was scanned using a full MRI protocol, composed of both morphological and advanced sequences. First, the conventional protocol lasts for 11 minutes and consisted on the acquisition of 3D T1-weighted MPRAGE along the sagittal plane (voxel size =  $1 \times 1 \times 1 \text{ mm}$ , TR = 1900 ms, TE = 2.21 ms, FOV = 256 x 176 x 256 mm, 4 min acquisition duration), and a T2-weighted FLAIR (voxel size =  $1 \times 1 \times 1 \text{ mm}$ , TR = 5000 ms, TE = 400 ms). Resting-state fMRI data were recorded along the posterior-anterior direction using an EPI BOLD sequence with a multi-band factor of 6 (700 scans, TR = 750 ms, TE = 30 ms, voxel size =  $2.2 \times 2.2 \times 2.2 \text{ mm}$ , FOV = 211 x 211 mm). This acquisition lasts for 9 minutes during which the subject let its mind wandering while fixing a cross on the screen. A single-band reference image (“SBRef”) was acquired at the beginning of each functional acquisition to improve image registrations. Furthermore, two single-band spin-echo with different phase-encoding (TR = 5000 ms, TE = 45 ms, voxel size =  $2.2 \times 2.2 \times 2.2 \text{ mm}$ ) were recorded. Finally, along the posterior-anterior direction diffusion MRI with multiband factor 3 was acquired. Diffusion imaging protocol was based on a 2D multi-slice spin-echo EPI sequence (TR = 5048 ms, TE = 90 ms, resolution  $1.5 \times 1.5 \times 1.5 \text{ mm}$ , FOV = 160 x 136 mm, acquisition time = 20 min), and 128 diffusion gradient directions were acquired for two b-values ( $b = 1000 \text{ s/mm}^2$ ,  $b = 3000 \text{ s/mm}^2$ ).



## 2.3 Intelligence scores

Intelligence was assessed with the fourth version of the Wechsler Adult Intelligence Scale (WAIS). It allows the computation of a Verbal Comprehension Index (VCI), Perceptual Reasoning Index (PRI), Working Memory Index (WMI), Processing Speed Index (PSI), and a Full Scale Intelligence Quotient (FSIQ). These IQ sub-scores were obtained from ten sub-tests divided in: verbal tests (similitude, vocabulary, and information), reasoning (cubes, matrices, and puzzle), memory (arithmetic and memory of numbers), and speed processing (symbols and codes).

## 2.4 Data preprocessing

Structural and functional data were preprocessed following the pipeline of the Human Connectome Project (HCP) [Glasser *et al.* (2013)]. Indeed, starting from the collaboration between Washington University, University of Minnesota and Oxford University, the aim of this teamwork was to optimize the fMRI data analysis methods, in order to generate the most complete and accurate description of the connections among gray matter locations in the human brain at the millimeter scale [Uğurbil *et al.* (2013)]. HCP protocol contains two structural MRI acquisitions ( $T_{1w}$ -MPRAGE and  $T_{2w}$ -SPACE), slice-accelerated multiband functional scans, and two single-band spin-echo EPI with different phase-encoding direction. These latest sequences allowed to obtain a better distortion correction. Indeed, the most important characteristic of HCP is the refinements made in the preprocessing pipelines concerning correction of spatial distortions, data alignment and registration into standard space [Van Essen *et al.* (2012)]. Since our functional protocol is similar to HCP one, structural and functional pipelines of HCP were implemented to obtain high quality data.

### Structural MRI preprocessing

Anatomical images were analyzed using two steps of the Structural HCP Preprocessing: PreFreeSurfer, and FreeSurfer. During the first step, a bias field and distortion corrections were applied to both T1w and T2w. Through linear and non-linear registrations, the anatomical images have been coregistered together and then registered to MNI space using linear FLIRT and non linear FNIRT FSL's functions. The FreeSurfer step, applied a segmentation of white matter, gray matter, cerebrospinal fluid and subcortical structures using T1w images. Finally, a parcellation in 84 regions of the Desikan atlas was computed.

## Functional MRI preprocessing

After the "Structural Preprocessing", the functional data were preprocessed using fMRIVolume HCP Pipelines (Figure 8.1). This step of functional preprocessing is similar to the PreFreeSurfer step, which is based on two spin-echo images designed to compute field maps (each one in one direction AP or PA), and on a reference image acquired with single-band sequence (SBRef Image). Functional data were corrected for gradient distortions and for motion using FLIRT. Phase encoding distortions were then corrected applying the fieldmap derived from the pair of spin-echo EPI with an opposite phase encoding. Finally, the functional images were re-sampled to the MNI atlas space and normalized to a global mean. No spatial smoothing was applied.

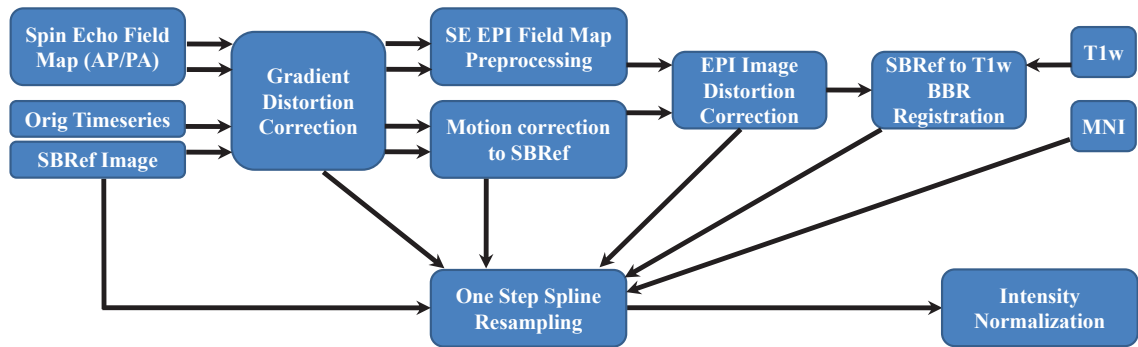


Figure 8.1: Steps of the fMRIVolume HCP Pipeline. Starting from gradient distortion correction to the intensity normalization [Glasser *et al.* (2013)].

## Diffusion MRI preprocessing

Diffusion preprocessing starts with data denoising, eddy current-induced distortion correction, and motion correction by the FMRIB Software Library (FSL) using the b0 volume as reference [Jenkinson *et al.* (2012)]. Non-brain voxels were then removed using FSL-BET. The diffusion tensor has also been reconstructed to estimate the FA. T1 image was then coregistered on the diffusion image space using the affine non-rigid transformation of NiftyReg Tool [Ourselin *et al.* (2001)]. The resulting transformation has been applied to the previously generated segmentation of the cortical and subcortical gray matter in 84 regions that was obtained by FreeSurfer.

## 2.5 Connectivity measurement

### Functional Connectivity

After the preprocessing of rs-fMRI data, the functional brain connectivity matrices were computed. First, in each region time series were estimated, using the Conn Toolbox (<https://www.nitrc.org/projects/conn>), by averaging the fMRI time series over all voxels weighted by the GM probability map. With this process, the partial volume effect was reduced and the contamination by WM and cerebrospinal fluid signal was limited. Furthermore, head motion was removed by regressing out motion parameters, their first derivative's time series and outliers detected by Art Toolbox.

On the resulting signals, the maximal overlap discrete wavelet transform (MODWT) was applied [Achard *et al.* (2006)], decomposing the signal in 5 frequency bands. Among them, we kept the fourth wavelet scale which represent the frequency band from 0.042 Hz to 0.08 Hz that belongs to the resting-state range frequencies. We then estimated the pairwise inter-regional correlations between wavelet coefficients to construct an  $84 \times 84$  correlation matrix.

Finally, the binarized graphs were constructed using the minimum spanning tree that keeps the graphs fully connected [Alexander-Bloch *et al.* (2012)], and applying a threshold of 20% to create an adjacency matrix.

### Structural Connectivity

Structural brain connectivity was obtained from DTI data. 84 cortical and sub-cortical regions of GM obtained with Freesurfer segmentation, were used as graph nodes. The fiber orientation distribution (FOD) function was estimated using MRtrix software [Tournier *et al.* (2012)] using the spherical deconvolution method. This FOD together with the segmentation in 4 tissues of the IIT atlas (cortical GM, subcortical GM, WM and CSF) were used to obtain an anatomically constrained probabilistic streamline tractography generating 1 000 000 streamline [Smith *et al.* (2012), Tournier *et al.* (2012)]. Finally, adjacency matrices were generated for each subject by summing the number of streamlines connecting each pair of nodes.

The matrices have been binarized applying a threshold of 0.20. This threshold has been chosen following the criteria of inter-subject variability:  $\tau$  is the threshold for which all the estimated global metrics present an inter-subject variability as low as possible [Kocevar *et al.* (2016)].

## 2.6 Graph metrics

Networks properties were explored using graph metrics that were estimated under MATLAB with the toolbox "Brain Connectivity Toolbox (BCT)" [Rubinov and Sporns (2010)] for both functional and structural connectivities. On one hand, connectivity network topology was investigated through the measure of six global graph metrics: density (D), transitivity (T), assortativity (r), modularity (Q), mean path length (CPL) and mean global efficiency (Eg)). On the other hand, four local metrics (degree ( $k_i$ ), coefficient of clustering ( $C_i$ ), betweenness centrality ( $B_i$ ) and efficiency ( $El_i$ )) described properties of each node  $i$ .

## 2.7 Statistical analysis

The statistical analyses have been performed with R [R Development Core Team (2015)]. Correlations between intelligence scores ( $W_i$ ) and graph metrics have been evaluated applying a linear model (LM) (Equation 2.7). This model allowed to evaluate the existence of a relationship between topology of functional or structural brain networks and level of intelligence, taking into account the effect of the age. All the results have been corrected for multiple comparisons using the Sidak correction.

$$W_i \sim \text{Graph metric}(FC \text{ or } SC) + \text{Age} \quad (8.1)$$

# 3 Results

## 3.1 Behavioral observations

Before to apply graph analysis, we explored the composition of our population.

As presented in the section 2.1, our population was aged in the range between 20 and 60 years old. More in details, the age distribution was centred around the average of 40.91 years old with a standard deviation of 9.14 years.

Studying the distribution of intelligence scores, we observed that the Full Scale Intelligence Quotient was distributed around an average of 120.04 with a standard deviation of 10.05. The details of others scores obtained from Wechsler Scale are reported in Table 8.1.

	Population
Age	$40.91 \pm 9.14$
FSIQ	$120.04 \pm 10.05$
VCI	$125.76 \pm 12.34$
PRI	$114.16 \pm 10.78$
PSI	$106.36 \pm 10.84$
WMI	$112.56 \pm 11.41$

Table 8.1: Population characteristics (Mean  $\pm$  Standard Deviation): age, Full Scale Intelligence Quotient (FSIQ), Verbal Comprehension Index (VCI), Perceptual Reasoning Index (PRI), Processing Speed Index (PSI), and Working Memory Index (WMI).

### 3.2 Functional connectivity

The functional connectivity analysis showed a significant result when global metrics were estimated in the whole brain networks. A negative correlation was observed between Transitivity of the brain networks and the PRI intelligence score (Table 8.2 and Figure 8.2).

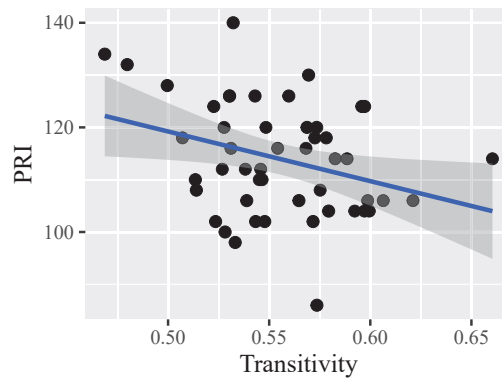


Figure 8.2: Significant correlation obtained between graph transitivity and the perceptual reasoning index (PRI) of the functional connectivity.

Trying to localize more specifically the intelligence correlates, FSIQ showed several correlations with different nodal metrics. The betweenness centrality increased together with a higher FSIQ in the right putamen. Furthermore, FSIQ correlated negatively with both segregation metrics, clustering coefficient and local efficiency, in bilateral anterior cingulate cortices. However, after multicomparison corrections all these local results remain only trends (Table 8.3).

Connectivity	Metric	FSIQ	VCI	PRI	WMI	PSI
Functional	T	-	-	-92.1 *	-	-
Structural	r	-92.58 *	-	-145.1 **	-111.41 *	-

Table 8.2: Correlation Slopes and statistical significances obtained with a LM model between IQ scores (full scale intelligence quotient (FSIQ), verbal comprehension index (VCI), perceptual reasoning index (PRI), working memory index (WMI), and processing speed index (PSI)) and global graph metrics measured for functional connectivity (FC), and structural connectivity (SC). The only significant correlation were found for transitivity metric (T) for FC, and assortativity metric (r) for SC.

\*  $p < 0.05$ , \*\*  $p < 0.01$  after multicomparison correction.

### 3.3 Structural connectivity

Several significant correlations have been observed between intelligence scores and both global and local graph metrics estimated from structural connectivity. When measured in whole brain, a relationship between brain networks assortativity and intelligence scores was highlighted. More in details, assortativity measure decreases in brain networks of high PRI ( $p < 0.01$ ) and FSIQ, and WMI ( $p < 0.05$ ) (Table 8.2 and Figure 8.3).

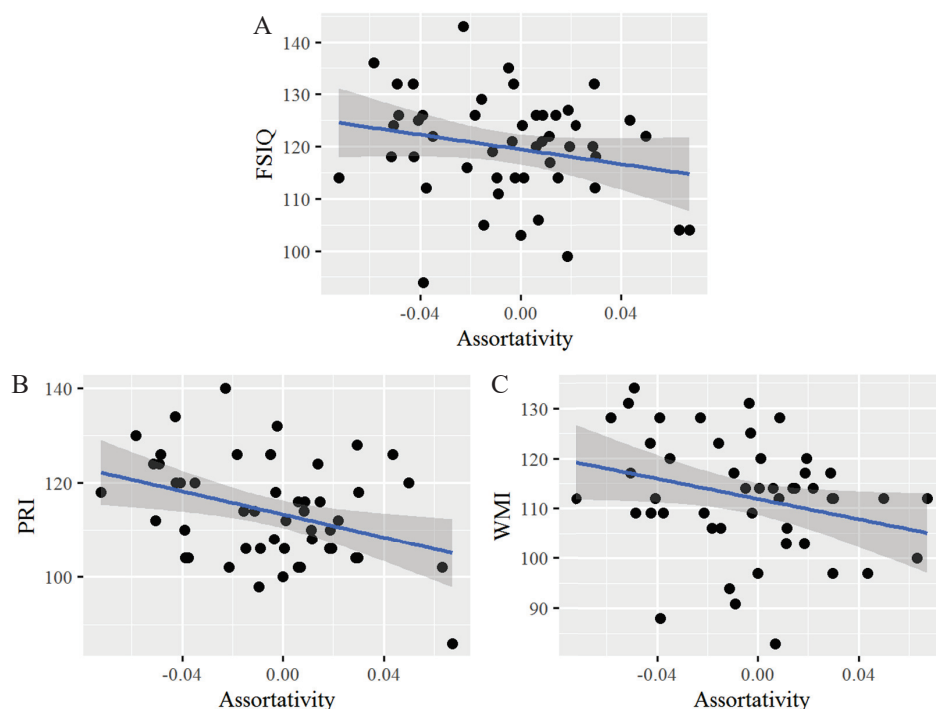


Figure 8.3: Significant correlations obtained between graph assortativity and full scale intelligence quotient (FSIQ), perceptual reasoning index (PRI), and working memory index (WMI) for structural connectivity.

At a nodal scale, after multiple comparison correction, only three significant

results survived ( $p < 0.05$ ) (Table 8.3). A clustering coefficient increase was observed in right inferior temporal cortex in higher PRI scores (Figure 8.4).

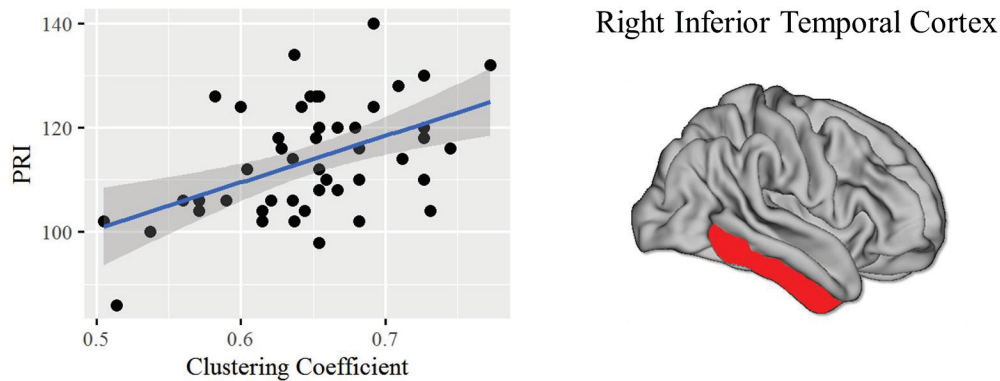


Figure 8.4: Significant correlations obtained between graph clustering coefficient (CC) and perceptual reasoning index (PRI) in the right inferior temporal cortex. Clustering Coefficient increases in high PRI values.

Two nodal metrics showed significant negative association with FSIQ in the right anterior cingulate cortex, meaning that the less ACC is a strong hub, the higher the FSIQ. Both degree and betweenness centrality decreases were observed in this region (Figure 8.5). This hub metric showed also a reduction in inferior temporal cortex that is just a trend ( $p < 0.1$ ) after multicomparison correction.

Connectivity	GM Nodes	Metric	FSIQ	VCI	PRI	WMI	PSI
Functional	Putamen R.	Bi	0.09 ·	-	-	-	-
	Anterior Cingulate L.	Ci	-30.55 ·	-	-	-	-
		Ei	-40.47 ·	-	-	-	-
	Anterior Cingulate R.	Ci	-53.02 ·	-	-	-	-
		Ei	-77.72	-	-	-	-
Structural	Anterior Cingulate R.	ki	-1.98 *	-	-	-	-
		Bi	-0.13 *	-	-	-	-
	Inferior Temporal R.	Ci	-	-	88.02 *	-	-

Table 8.3: Correlation slopes and statistical significances obtained with a LM model between IQ scores (full scale intelligence quotient (FSIQ), verbal comprehension index (VCI), perceptual reasoning index (PRI), working memory index (WMI), and processing speed index (PSI)) and local graph (degree (ki), betweenness centrality (Bi), clustering coefficient (Ci), and local efficiency (Ei)) metrics measured for functional connectivity (FC), and structural connectivity (SC).

·  $p < 0.1$ , \*  $p < 0.05$  after multicomparison correction.



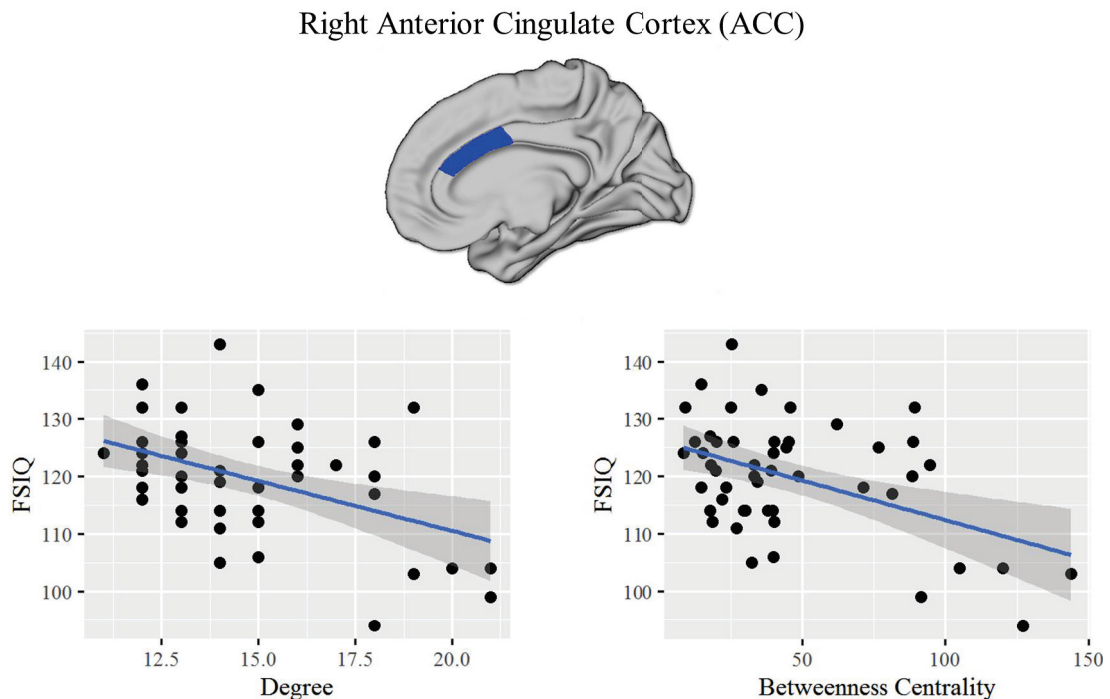


Figure 8.5: Significant correlations obtained between both degree and betweenness centrality (BC) graph metrics and full scale intelligence quotient (FSIQ) in the right anterior cingulate cortex. Both graph metric decrease in high FSIQ.

## 4 Discussion

In this ongoing work, we combined brain connectivity and graph analysis. Our goal was to investigate functional and structural neural substrate of intelligence in adults. To our knowledge, this is the first work that explores in the same study both functional and structural connectivity and that correlates them with cognitive capacities applying graph techniques.

Exploring brain networks with both rs-fMRI and DTI, we demonstrated the existence of a relationship between intelligence level and a less clustered topology of brain networks. Indeed, in functional and structural connectivity analysis different intelligence sub-scores correlated negatively with transitivity and assortativity metric, respectively. From the definitions of these metrics explained in Chapter 3.1, lower assortativity indicates a higher similarity in the degree of all the nodes of the network, while transitivity decreases when the strength that links the nodes within a module is the same of the strength that connects them with the nodes of other modules. We can thus conclude on one hand, that the less the brain is clustered, the higher is the PRI. On the other hand, the less nodes of the same degree are connected, the higher is FSIQ score. These results are in agreement with the idea



that higher intelligence performance are based on the capacity of the brain networks to reorganize the connections in order to facilitate the communication between the brain regions all over the brain [Barbey (2018)].

When we searched intelligence correlates locally in the brain, we found specific regions whose structure changes according to intelligence level. In particular, right anterior cingulate cortex (ACC) seems to be less connected with other regions (lower degree) and less important (lower hubness) in the communication within brain structural networks in adults with high FSIQ. This region is implicated in several complex cognitive functions, such as empathy, impulse control, emotion, and decision-making. Moreover, being part of the limbic system, ACC contributes to affect-regulation and control and management of uncomfortable emotions [Etkin *et al.* (2011), Tolomeo *et al.* (2016)]. A decreased degree in ACC may thus reflect the weakness of this region in HIQ adults for which the control of the emotion is known to be a behavioral difficulty. The importance of this region in brain networks of HIQ is confirmed also by the results obtained with functional connectivity that involve ACC bilaterally. Furthermore, ACC is recognized as a brain region connected with intelligence since the introduction of PFIT by [Jung and Haier (2007)] and it resulted to be an important functional node also in more recent works [Hilger *et al.* (2017)b].

Finally, the last result obtained analyzing structural connectivity showed a higher segregation in the temporal lobe since higher clustering coefficient was found in right inferior temporal cortex, a region involved in visual perception and memory [Ranganath (2006)].

## 5 Conclusion

In this chapter, we explored both functional and structural connectivity with graph analysis in order to found some correlates between networks topology and intelligence.

Our findings showed the existence of a relationship between intelligence performances and brain network homogeneity. The strength of this result is in the coexistence of this correlation in both functional and structural connectivity. To our knowledge, this is the first work to show that brain network homogeneity could relate to intelligence in both functional and structural networks.

Furthermore, the graph analysis at regional level allowed to highlight the importance of some particular regions for the intelligence. Anterior cingulate cortex resulted to be a fundamental region for the description of intelligence performances in both functional and structural brain networks. In adults, the communication

between ACC and the other regions of the brain networks seems to be reduced as FSIQ increases. The implication of this region in the regulation of emotion let us conclude that HIQ people may still present difficulties in managing their emotion and decision.

In conclusion, this work demonstrated that intelligence is related to the plasticity of both functional and structural connectivity of the brain networks that become less modular, and in particular to some specific node of the networks.



# Conclusions

In this thesis, we were interested in characterizing the neural substrate of intelligence. To this end, two main research projects have been performed using advanced MRI techniques, namely functional and diffusion MRI. First, the study of the neural correlates with intelligence was performed in children, and second, functional and structural connectivities were explored in adults. In both projects, intelligence was estimated with Wechsler tests, the WISC for children, and the WAIS for adults, respectively.

Clinical observations and the neurophysiological tests, have led to the definition of two High Intelligence Quotient (HIQ) profiles, namely homogeneous (Hom-HIQ) and heterogeneous HIQ (Het-HIQ).

A first MRI study was conducted in the children population. Brain activity was evaluated at rest when the children were asked to let their mind wandering while fixing a cross on the screen. In a first part, the preprocessing pipeline used for functional connectivity was optimized in order to measure the graph of brain networks, their global and regional metrics as well as a reorganization index, the "Hub disruption index" ( $\kappa$ ), in the entire HIQ group and also in both HIQ profiles separately. This analysis was computed for three different networks: the whole brain networks, the hemispherical networks (left and right), and the homotopic connectivity. The measures showed, first, significant topological modifications of the graph's properties for the HIQ group and, in particular, for the Het-HIQ profile. The left hemisphere networks seems to be reorganized in both HIQ profiles, while the right hemisphere showed significant change only in the Het-HIQ. Finally, the homotopic connectivity was modified in all HIQ population and separately in both HIQ profiles. Furthermore, we observed that these brain networks reorganization measured by graph theory were correlated with higher cognitive abilities measured by the FSIQ, and some intelligence subscales.

In the second study of the children population, we focused on the characterization of the structural connectivity applying the graph theory using diffusion MRI. We were able to demonstrate that graph global metrics, describing the networks proper-

ties, are related to cognitive capacities. Our main result was that higher intelligence is associated to denser and more uniform brain networks. Indeed, preliminary findings showed significant correlations between network density and modularity with almost all WISC-IV sub-tests. This result is found also for each hemispheric network, and for inter-hemispheric connections. In the second part of this study, we refined our analysis extracting from WISC scores three main intelligence domains applying a principal component analysis. In this way, we demonstrated that our previously findings can be enlarged also to specific intelligence domains and particularly to fluid intelligence. We completed this work measuring diffusion metrics in white matter (WM) fiber-bundles showing significant correlation between axial diffusivity (AD) and intelligence domains. Since AD reflects axonal density, we were able to confirm the relationship between WM fiber-tracts integrity and intelligence. Finally, the correlations with intelligence domains suggested that general intelligence domains (g-score, fluid intelligence and classification ability) are more related to the right WM fiber-bundles, while g-unbiased intelligence domains are more related to the left WM fiber-bundles.

In order to finalize the study of intelligence in children, we explored brain activations with task-fMRI aiming at investigating encoding and retrieving of words. With this technique, we were able to better define homogeneous and heterogeneous HIQ profiles. We have, indeed, highlighted differences both at the behavioral level and at the level of brain functions. Concerning the task performance, both HIQ profiles resulted to be faster in answering to different tasks than SIQ group. Also, the three intelligence groups did not differ from each other in response performance measured by the percentage of incorrect, miss, and correct answers. Furthermore, fMRI activations involved different brain regions depending on the intelligence group. Homogeneous profile did not differ from SIQ group while the heterogeneous group presented, instead, a significant different activity of the brain. During the encoding of words, the inferior occipital cortex was more activated in SIQ than in Het-HIQ group, while, during retrieving phase, left thalamus and occipital cortex were more activated in heterogeneous profile than in SIQ. Finally, comparing the two HIQ profiles, in encoding phase homogeneous one activated more left prefrontal cortex, while heterogeneous group showed higher activations during the retrieval in post- and pre-central gyri, cingulate gyrus and premotor cortex.

These results together with those obtained with resting-state fMRI, confirmed the hypothesis that there are many differences in brain connectivity between the two HIQ children profiles. In particular, heterogeneous profile presents several differences with respect to SIQ children, although they are not always characterized by a higher

FSIQ. These results invite us to detect children as soon as possible, but also to take into account not only FSIQ values but all the clinical and behavioral aspect of the psychological assessments.

In order to investigate if the brain neural correlates remains the same or not along lifespan, a second research project was realized to characterize brain connectivity in an adult population with high intelligence quotient. In a first part, we were interested in the measure of functional connectivity through graph analysis. We estimated global and local graph metrics of connectivity matrices to characterize the topology of functional brain networks at different scales. We were able to show that the transitivity of the networks is lower in HIQ. However, graph metrics measuring network properties at nodal level did not show any significant variations based on cognitive abilities. In the second part, the graph analysis was applied on structural connectivity matrices. In this case, assortativity measures of the networks resulted changes according to the intellectual abilities. Lower assortativity was detected when higher full scale IQ was measured, but also in correlation with other subscales of intelligence. At a nodal level, we were able to identify a couple of regions that presented changes in their structural connectivity in HIQ, and in particular, the right anterior cingulate cortex (ACC). The graph analysis showed that ACC was less connected in HIQ. Since the role of this region is to control emotion and decision, we may conclude that this region communicates less with the rest of the graph in people with high IQ. Our clinical observations have led us to identify the difficulty in emotion control as one of the characteristics of HIQ people, and our results may support these observations.

Our global results can be extended to those obtained in the children population. Indeed, since transitivity metric reflect the segregation property of the network, we found that high IQ levels are associated to a less clusterized brain network topology. This involvement of a segregation metric in adulthood high intelligence performances, is in common with our results in childhood. We may, indeed, conclude that brain network of high intelligence quotient people is characterized by a less segregated and thus more uniform topology of brain networks.



# Limitations and perspectives

## Limitations

Through these two research projects of a population that presents a high Intelligence Quotient (HIQ), we were able to characterize the neural substrate of intelligence by developing advanced MRI acquisition techniques. Furthermore, the combination with graph theory allowed to obtain both global and local characteristics of both functional and structural connectivity. These approaches provided a better understanding of the neural substrate of intelligence during two phases of human development, namely childhood and adulthood. However, these two follow-ups suffered from several limitations, both clinical and methodological.

In the resting-state fMRI study, the "Hub disruption index" allowed to evidence differences in topological organization of brain networks of HIQ and also between two HIQ profiles. However, this study is limited by its low sample size, and needs to be replicated in a larger population. From a methodological perspective, this study may have been influenced by the choice of graphs cost. The analysis was thus also computed with a graph cost of 0.20, obtaining concordant results (5). Finally, the population was not equally distributed between girls and boys. This limitation is often encountered in high potential children studies, as girls present the ability to "overadapt" which leads to an under-diagnosis of high IQ girls. Our correlation analysis has, however, been corrected for the effect of gender in order to overcome this problem.

In the DTI study, structural correlations between intelligence and graph metrics were evidenced. Moreover, the principal component analysis allowed to obtain a finer exploration of neural substrates for different intelligence domains. From a methodological perspective, this study may suffer from few limitations. First, the diffusion acquisition was limited to 24 directions, which is relatively low compared to current research standards in diffusion imaging. Nonetheless, potential crossing-fibers errors were minimized by using spherical deconvolution instead of classical diffusion tensor model. Second, as it was already discussed for the resting-state



fMRI study, the unbalanced ratio of girls and boys was overcome by including the gender effect in the statistical analysis.

As well as for the rs-fMRI, the task fMRI study allowed to differentiate the brain activity of HIQ children compared to SIQ and between the two HIQ profiles. However, this is an ongoing study and the findings presented in this work are preliminar. Several more detailed analysis of fMRI data can be carried out further. For instance, the analysis performed on brain activation did not differentiate for the response type (incorrect, miss, correct). Thus, for each intelligence group, we should include the response in the fMRI processing. Furthermore, the common and different activations among the three groups may be studied for each response type.

Finally, for all the three children studies, our subjects' age was limited to the range of eight to twelve years old. At this age, the maturation of the prefrontal cortex is not complete, which may explain the lack of finding in this region. Since brain maturation continues during and after childhood, our results may only hold for this particular age range of 8–12 years old.

In the second research project, functional and structural studies were extended to an adults population. However, this is an ongoing study and thus, in order to be able to really compare the two research projects, further analysis are needed.

## Perspectives

The studies presented in this work are only a starting point for a more general and robust study of human intelligence. Indeed, other questions regarding neural substrate of high intelligence may be addressed by applying graph theory in combination with advanced MRI techniques.

Regarding the research project on children intelligence, we plan to complete this study by another work on the same population studied 10 years after. In this way, we would be able to perform a longitudinal study describing the evolution of the intelligence correlates from childhood to early adult age. Both functional and structural connectivities will be measured on this population in order to compare the results with those obtained during childhood.

Since the research project on the adult population is an ongoing study, further analyses are planned. First of all, the number of SIQ adults has to be incremented in order to measure the "Hub disruption index" in HIQ adults. Furthermore, increasing the number of subjects will improve the statistical power of our findings. As well as for the structural study of children population, a principal component analysis could be performed on the adult population. In this way, both functional and structural measures could be correlated with each intelligence domain in order to obtain a finer characterization of intelligence neural substrate.

Finally, different behavioral tests are provided in this work. All the participants underwent questionnaires evaluating their personality, motivation, success, and executive functions. We would like to explore the relationship between the intelligence brain networks, as measured applying graph analysis and advanced MRI techniques, and the behavioral characteristics. Furthermore, we plan to split our population in two main groups depending on their age. In this way, we aim to investigate neural substrate of intelligence, measured by functional and structural brain connectivity, along aging.



# Bibliography

- [Achard *et al.* (2006)] Achard, S., Salvador, R., Whitcher, B., Suckling, J., and Bullmore, E. (2006). A resilient, low-frequency, small-world human brain functional network with highly connected association cortical hubs. *The Journal of neuroscience : the official journal of the Society for Neuroscience*, 26(1):63–72.
- [Achard *et al.* (2012)] Achard, S., Delon-Martin, C., Vertes, P. E., Renard, F., Schenck, M., Schneider, F., Heinrich, C., Kremer, S., and Bullmore, E. T. (2012). Hubs of brain functional networks are radically reorganized in comatose patients. *Proceedings of the National Academy of Sciences*, 109(50):20608–20613.
- [Achard and Bullmore (2007)] Achard, S. and Bullmore, E. (2007). Efficiency and Cost of Economical Brain Functional Networks. *PLoS Computational Biology*, 3(2):0174–0183.
- [Akansu and Haddad (2001)] Akansu, A. N. and Haddad, R. A. (2001). *Multiresolution Signal Decomposition*. Elsevier.
- [Alexander-Bloch *et al.* (2012)] Alexander-Bloch, A., Lambiotte, R., Roberts, B., Giedd, J., Gogtay, N., and Bullmore, E. (2012). The discovery of population differences in network community structure: New methods and applications to brain functional networks in schizophrenia. *NeuroImage*, 59(4):3889.
- [Andreasen *et al.* (1993)] Andreasen, N. C., Flaum, M., Swayze, V., O’Leary, D. S., Alliger, R., Cohen, G., Ehrhardt, J., and Yuh, W. T. (1993). Intelligence and brain structure in normal individuals. *American Journal of Psychiatry*, 150(1):130–134.
- [Ashburner (2007)] Ashburner, J. (2007). A fast diffeomorphic image registration algorithm. *NeuroImage*, 38(1):95–113.
- [Bandettini *et al.* (1993)] Bandettini, P. A., Jesmanowicz, A., Wong, E. C., and Hyde, J. S. (1993). Processing strategies for time-course data sets in functional mri of the human brain. *Magnetic Resonance in Medicine*, 30(2):161–173.

- [Barbey (2018)] Barbey, A. K. (2018). Network Neuroscience Theory of Human Intelligence.
- [Basser *et al.* (1994)] Basser, P., Mattiello, J., and Lebihan, D. (1994). Estimation of the Effective Self-Diffusion Tensor from the NMR Spin Echo.
- [Basser *et al.* (2002)] Basser, P. J., Basser, P. J., Jones, D. K., and Jones, D. K. (2002). Diffusion-tensor MRI: theory, experimental design and data analysis - a technical review. *NMR in biomedicine*, 15:456–67.
- [Bassett and Bullmore (2006)] Bassett, D. S. and Bullmore, E. (2006). Small-world brain networks. *Neuroscientist*, 12(6):512–523.
- [Basten *et al.* (2015)] Basten, U., Hilger, K., and Fiebach, C. J. (2015). Where smart brains are different: A quantitative meta-analysis of functional and structural brain imaging studies on intelligence. *Intelligence*.
- [Beaulieu (2002)] Beaulieu, C. (2002). The basis of anisotropic water diffusion in the nervous system - A technical review.
- [Behzadi *et al.* (2007)] Behzadi, Y., Restom, K., Liau, J., and Liu, T. T. (2007). A component based noise correction method (CompCor) for BOLD and perfusion based fMRI. *NeuroImage*, 37(1):90–101.
- [Belliveau *et al.* (1991)] Belliveau, J. W., Kennedy, D. N., McKinstry, R., and Al., E. (1991). Functional mapping of the human visual cortex by magnetic resonance imaging. *Science*, 254:716–719.
- [Binder *et al.* (2009)] Binder, J. R., Desai, R. H., Graves, W. W., and Conant, L. L. (2009). Where Is the Semantic System? A Critical Review and Meta-Analysis of 120 Functional Neuroimaging Studies. *Cerebral Cortex*, 19(12):2767–2796.
- [Binet (1905)] Binet, A. (1905). The developement of intelligence in children. *L'Année Psychologique*, 12:191–244.
- [Binet and Simon (1916)] Binet, A. and Simon, T. (1916). *The development of intelligence in children (The Binet-Simon Scale)*. Williams & Wilkins Co, Baltimore.
- [Birn (2012)] Birn, R. M. (2012). The role of physiological noise in resting-state functional connectivity.
- [Biswal *et al.* (1995)] Biswal, B., Zerrin Yetkin, F., Haughton, V. M., and Hyde, J. S. (1995). Functional connectivity in the motor cortex of resting human brain using echo-planar MRI. *Magnetic Resonance in Medicine*, 34(4):537–541.

- [Bouchard *et al.* (2013)] Bouchard, K. E., Mesgarani, N., Johnson, K., and Chang, E. F. (2013). Functional organization of human sensorimotor cortex for speech articulation. *Nature*, 495(7441):327–332.
- [Brown (1828)] Brown, R. (1828). XXVII. A brief account of microscopical observations made in the months of June, July and August 1827, on the particles contained in the pollen of plants; and on the general existence of active molecules in organic and inorganic bodies. *The Philosophical Magazine*, 4(21):161–173.
- [Bullmore *et al.* (2004)] Bullmore, E., Fadili, M. J., Maxim, V., Sendur, L., Whitcher, B., Suckling, J., Brammer, M. J., and Breakspear, M. (2004). Wavelets and functional magnetic resonance imaging of the human brain. *Neuroimage*, 23:S234–S249.
- [Bullmore and Sporns (2009)] Bullmore, E. and Sporns, O. (2009). Complex brain networks: graph theoretical analysis of structural and functional systems. *Nature Reviews Neuroscience*, 10(3):186–198.
- [Buxton (2009)] Buxton, R. B. (2009). *Introduction to Functional Magnetic Resonance Imaging*. Cambridge edition.
- [Catani *et al.* (2002)] Catani, M., Howard, R. J., Pajevic, S., and Jones, D. K. (2002). Virtual in Vivo interactive dissection of white matter fasciculi in the human brain. *NeuroImage*, 17(1):77–94.
- [Cattell (1971)] Cattell, B. R. (1971). Abilities: Their Structure, Growth, and Action. Technical report.
- [Chen *et al.* (2012)] Chen, G., Chen, G., Xie, C., Ward, B. D., Li, W., Antuono, P., and Li, S. J. (2012). A method to determine the necessity for global signal regression in resting-state fMRI studies. *Magnetic Resonance in Medicine*, 68(6):1828–1835.
- [Clayden *et al.* (2012)] Clayden, J. D. D., Jentschke, S., Munõz, M., Cooper, J. M. M., Chadwick, M. J. J., Banks, T., Clark, C. A. A., and Vargha-Khadem, F. (2012). Normative Development of White Matter Tracts: Similarities and Differences in Relation to Age, Gender, and Intelligence. *Cerebral Cortex*, 22(8):1738–1747.
- [Cole *et al.* (2015)] Cole, M. W., Ito, T., and Braver, T. S. (2015). Lateral Prefrontal Cortex Contributes to Fluid Intelligence Through Multinetwork Connectivity. *Brain Connectivity*, 5(8):497–504.

- [Colom *et al.* (2006)] Colom, R., Jung, R. E., and Haier, R. J. (2006). Distributed brain sites for the g-factor of intelligence. *NeuroImage*, 31(3):1359–1365.
- [Colom *et al.* (2008)] Colom, R., Haier, R. J., Head, K., Álvarez-Linera, J., Quiroga, M. Á., Shih, P. C., and Jung, R. E. (2008). Gray matter correlates of fluid, crystallized, and spatial intelligence: Testing the P-FIT model. *Intelligence*, 37:124–135.
- [Colom *et al.* (2010)] Colom, R., Karama, S., Jung, R. E., and Haier, R. J. (2010). Human intelligence and brain networks. *Dialogues in clinical neuroscience*, 12(4):489–501.
- [Crinion *et al.* (2003)] Crinion, J. T., Lambon-Ralph, M. A., Warburton, E. A., Howard, D., and Wise, R. J. (2003). Temporal lobe regions engaged during normal speech comprehension. *Brain*, 126(5):1193–1201.
- [Damoiseaux *et al.* (2006)] Damoiseaux, J. S., Rombouts, S. A., Barkhof, F., Scheltens, P., Stam, C. J., Smith, S. M., and Beckmann, C. F. (2006). Consistent resting-state networks across healthy subjects. *Proceedings of the National Academy of Sciences of the United States of America*, 103(37):13848–13853.
- [Damoiseaux and Greicius (2009)] Damoiseaux, J. S. and Greicius, M. D. (2009). Greater than the sum of its parts: A review of studies combining structural connectivity and resting-state functional connectivity. *Brain Structure and Function*, 213(6):525–533.
- [Desco *et al.* (2011)] Desco, M., Navas-Sanchez, F. J., Sanchez-González, J., Reig, S., Robles, O., Franco, C., Guzmán-De-Villoria, J. A., García-Barreno, P., and Arango, C. (2011). Mathematically gifted adolescents use more extensive and more bilateral areas of the fronto-parietal network than controls during executive functioning and fluid reasoning tasks. *NeuroImage*, 57:281–292.
- [Desikan *et al.* (2006)] Desikan, R. S., Ségonne, F., Fischl, B., Quinn, B. T., Dickerson, B. C., Blacker, D., Buckner, R. L., Dale, A. M., Maguire, R. P., Hyman, B. T., Albert, M. S., and Killiany, R. J. (2006). An automated labeling system for subdividing the human cerebral cortex on MRI scans into gyral based regions of interest. *NeuroImage*, 31(3):968–980.
- [Destrieux *et al.* (2010)] Destrieux, C., Fischl, B., Dale, A., and Halgren, E. (2010). Automatic parcellation of human cortical gyri and sulci using standard anatomical nomenclature. *NeuroImage*, 53(1):1–15.

- [De Graaf (1998)] De Graaf, R. (1998). *In Vivo NMR Spectroscopy: Principles and Techniques*. John Wiley & Sons, 2nd edition.
- [Duncan *et al.* (2000)] Duncan, J., Seitz, R. J., Kolodny, J., Bor, D., Herzog, H., Ahmed, A., Newell, F. N., and Emslie, H. (2000). A neural basis for general intelligence. *Science*, 289(5478):457–460.
- [Dunst *et al.* (2014)] Dunst, B., Benedek, M., Koschutnig, K., Jauk, E., and Neubauer, A. C. (2014). Sex differences in the IQ white matter microstructure relationship: A DTI study. *Brain and Cognition*, 91:71–78.
- [Eggermont (2012)] Eggermont, J. J. (2012). *The Neuroscience of Tinnitus*. Oxford University Press.
- [Eguíluz *et al.* (2005)] Eguíluz, V. M., Chialvo, D. R., Cecchi, G. A., Baliki, M., and Apkarian, A. V. (2005). Scale-free brain functional networks. *Physical Review Letters*, 94(1):018102.
- [Etkin *et al.* (2011)] Etkin, A., Egner, T., and Kalisch, R. (2011). Emotional processing in anterior cingulate and medial prefrontal cortex. *Trends in Cognitive Sciences*, 15(2):85–93.
- [Ferrand (2001)] Ferrand, L. (2001). Normes d’associations verbales pour 260 mots « abstraits ». *L’année Psychologique*, 101(4):683–721.
- [Ferrand and Alario (1998)] Ferrand, L. and Alario, F.-X. (1998). Normes d’associations verbales pour 366 noms d’objets concrets. *L’année psychologique*, 98(4):659–709.
- [Finn *et al.* (2015)] Finn, E. S., Shen, X., Scheinost, D., Rosenberg, M. D., Huang, J., Chun, M. M., Papademetris, X., and Constable, R. T. (2015). Functional connectome fingerprinting: identifying individuals using patterns of brain connectivity. *Nature Neuroscience*, 18(11):1664–1671.
- [Fischer *et al.* (2014)] Fischer, F. U., Wolf, D., Scheurich, A., and Fellgiebel, A. (2014). Association of structural global brain network properties with intelligence in normal aging. *PLoS ONE*, 9(1).
- [Flashman *et al.* (1997)] Flashman, L. A., Andreasen, N. C., Flaum, M., and Swayze, V. W. (1997). Intelligence and regional brain volumes in normal controls. *Intelligence*, 25(3):149–160.



- [Flourens (1824)] Flourens, M. J. P. (1824). *Recherches experimentales sur les proprietes et les fonctions du systeme nerveux dans les animaux vertebres*.
- [Fornito *et al.* (2010)] Fornito, A., Zalesky, A., and Bullmore, E. T. (2010). Network scaling effects in graph analytic studies of human resting-state fMRI data. *Frontiers in Systems Neuroscience*, 4:22.
- [Fox *et al.* (2005)] Fox, M. D., Snyder, A. Z., Vincent, J. L., Corbetta, M., Van Essen, D. C., and Raichle, M. E. (2005). The human brain is intrinsically organized into dynamic, anticorrelated functional networks. *Proceedings of the National Academy of Sciences of the United States of America*, 102(27):9673 – 9678.
- [Fox and Raichle (2007)] Fox, M. D. and Raichle, M. E. (2007). Spontaneous fluctuations in brain activity observed with functional magnetic resonance imaging. *Nature Reviews Neuroscience*, 8(9):700–711.
- [Friston (2011)] Friston, K. J. (2011). Functional and Effective Connectivity: A Review. *Brain Connectivity*, 1(1):13–36.
- [Friston *et al.* (1993)] Friston, K. J., Frith, C. D., Liddle, P. F., and Frackowiak, R. S. (1993). Functional connectivity: The principal-component analysis of large (PET) data sets. *Journal of Cerebral Blood Flow and Metabolism*, 13(1):5–14.
- [Friston *et al.* (1994)] Friston, K. J., Jezzard, P., and Turner, R. (1994). Analysis of Functional MRI Time-Series. Technical report.
- [Friston *et al.* (1995)] Friston, K. J., Holmes, A. P., Worsley, K. J., Poline, J.-P., Frith, C. D., and Frackowiak, R. S. J. (1995). Statistical Parametric Maps in Functional Imaging: A General Linear Approach. *Human Brain Mapping*, 2.
- [Friston *et al.* (1996)] Friston, K. J., Williams, S., Howard, R., Frackowiak, R. S. J., and Turner, R. (1996). Movement-Related effects in fMRI time-series. *Magnetic Resonance in Medicine*, 35(3):346–355.
- [Gall (1825)] Gall, F. J. (1825). *Sur les fonctions du cerveau et sur celles de chacune de ses parties*.
- [Galton *et al.* (1869)] Galton, F., Sydney, S. W., Dudley, J., Warwick, E., Henry, S., Mary, S., Robt, S., and Herbert, W. (1869). Hereditary Genius. *Macmillan*, page 465.
- [Gardner (1987)] Gardner, H. (1987). The Theory of Multiple Intelligences. *Annals of Dyslexia*, 37:19–35.

- [Gendon *et al.* (2015)] Gendon, B., Ridley, Y., Rousseau, C., Wirsich, J., Le Troter, A., Soulier, E., Confort-Gouny, S., Bartolomei, F., Ranjeva, J.-P., Achard, S., and Guye, M. (2015). Nodal approach reveals differential impact of lateralized focal epilepsies on hub reorganization. *NeuroImage*, 118:39–48.
- [Glasser *et al.* (2013)] Glasser, M. F., Sotiropoulos, S. N., Wilson, J. A., Coalson, T. S., Fischl, B., Andersson, J. L., Xu, J., Jbabdi, S., Webster, M., Polimeni, J. R., Van Essen, D. C., and Jenkinson, M. (2013). The minimal preprocessing pipelines for the Human Connectome Project. *NeuroImage*, 80:105–124.
- [Glasser *et al.* (2016)] Glasser, M. F., Coalson, T. S., Robinson, E. C., Hacker, C. D., Harwell, J., Yacoub, E., Ugurbil, K., Andersson, J., Beckmann, C. F., Jenkinson, M., Smith, S. M., and Van Essen, D. C. (2016). A multi-modal parcellation of human cerebral cortex. *Nature*, 536(7615):171–178.
- [Gray *et al.* (2003)] Gray, J. R., Chabris, C. F., and Braver, T. S. (2003). Neural mechanisms of general fluid intelligence. *Nature Neuroscience*, 6(3):316–322.
- [Gray and Thompson (2004)] Gray, J. R. and Thompson, P. M. (2004). Neurobiology of intelligence: science and ethics. *Nature Reviews Neuroscience*, 5(6):471–482.
- [Guénolé *et al.* (2013)] Guénolé, F., Louis, J., Creveuil, C., Baleyte, J.-M., Montlahuc, C., Fournieret, P., and Revol, O. (2013). Behavioral profiles of clinically referred children with intellectual giftedness. *BioMed research international*, 2013:540153.
- [Guénolé *et al.* (2015)] Guénolé, F., Speranza, M., Louis, J., Fournieret, P., Revol, O., and Baleyte, J.-M. (2015). Wechsler profiles in referred children with intellectual giftedness: Associations with trait-anxiety, emotional dysregulation, and heterogeneity of Piaget-like reasoning processes. *European Journal of Paediatric Neurology*, 19(4):402–410.
- [Hagmann *et al.* (2007)] Hagmann, P., Kuran, M., Gigandet, X., Thiran, P., Wedeen, V. J., Meuli, R., and Thiran, J. P. (2007). Mapping human whole-brain structural networks with diffusion MRI. *PLoS ONE*, 2(7).
- [Haier (2016)] Haier, R. J. (2016). *The Neuroscience of Intelligence*. Cambridge Fundamentals of Neuroscience in Psychology. Cambridge University Press.

- [Haier *et al.* (2004)] Haier, R. J., Jung, R. E., Yeo, R. A., Head, K., and Alkire, M. T. (2004). Structural brain variation and general intelligence. *NeuroImage*, 23(1):425–433.
- [Haier *et al.* (2005)] Haier, R. J., Jung, R. E., Yeo, R. A., Head, K., and Alkire, M. T. (2005). The neuroanatomy of general intelligence: Sex matters. *NeuroImage*, 25(1):320–327.
- [He *et al.* (2007)] He, Y., Chen, Z. J., and Evans, A. C. (2007). Small-World Anatomical Networks in the Human Brain Revealed by Cortical Thickness from MRI. *Cerebral Cortex*, 17(10):2407–2419.
- [Hearne *et al.* (2016)] Hearne, L. J., Mattingley, J. B., and Cocchi, L. (2016). Functional brain networks related to individual differences in human intelligence at rest. *Scientific Reports*, 6(1):32328.
- [Hebb and Ojemann (2013)] Hebb, A. O. and Ojemann, G. A. (2013). The thalamus and language revisited. *Brain and language*, 126(1):99–108.
- [Hilger *et al.* (2017)a] Hilger, K., Ekman, M., Fiebach, C. J., and Basten, U. (2017a). Efficient hubs in the intelligent brain: Nodal efficiency of hub regions in the salience network is associated with general intelligence. *Intelligence*, 60:10–25.
- [Hilger *et al.* (2017)b] Hilger, K., Ekman, M., Fiebach, C. J., and Basten, U. (2017b). Intelligence is associated with the modular structure of intrinsic brain networks. *Scientific Reports*, 7(1):16088.
- [Horn (1982)] Horn, J. L. (1982). The Theory of Fluid and Crystallized Intelligence in Relation to Concepts of Cognitive Psychology and Aging in Adulthood. In *Aging and Cognitive Processes*, pages 237–278. Springer US.
- [Iturria-Medina *et al.* (2007)] Iturria-Medina, Y., Canales-Rodríguez, E. J., Melie-García, L., Valdés-Hernández, P. A., Martínez-Montes, E., Alemán-Gómez, Y., and Sánchez-Bornot, J. M. (2007). Characterizing brain anatomical connections using diffusion weighted MRI and graph theory. *NeuroImage*, 36(3):645–660.
- [Iturria-Medina *et al.* (2008)] Iturria-Medina, Y., Sotero, R. C., Canales-Rodríguez, E. J., Alemán-Gómez, Y., and Melie-García, L. (2008). Studying the human brain anatomical network via diffusion-weighted MRI and Graph Theory. *NeuroImage*, 40(3):1064–1076.

- [Jenkinson *et al.* (2012)] Jenkinson, M., Beckmann, C. F., Behrens, T. E., Woolrich, M. W., and Smith, S. M. (2012). FSL. *NeuroImage*, 62:782–790.
- [Jezzard (2001)] Jezzard, P. (2001). *Functional MRI: An introduction to methods*, volume 17. Oxford University.
- [Johansen-Berg and Behrens (2009)] Johansen-Berg, H. and Behrens, T. E. (2009). *Diffusion MRI: from quantitative measurement to in-vivo neuroanatomy*.
- [Johnson and Bouchard (2005)] Johnson, W. and Bouchard, T. J. (2005). The structure of human intelligence: It is verbal, perceptual, and image rotation (VPR), not fluid and crystallized. *Intelligence*, 33(4):393–416.
- [Jones *et al.* (2013)] Jones, D. K., Knösche, T. R., and Turner, R. (2013). White matter integrity, fiber count, and other fallacies: The do’s and don’ts of diffusion MRI. *NeuroImage*, 73:239–254.
- [Jung and Haier (2007)] Jung, R. E. and Haier, R. J. (2007). The Parieto-Frontal Integration Theory (P-FIT) of intelligence: converging neuroimaging evidence. *Behavioral and Brain Sciences*, 30(2):135–54.
- [Karama *et al.* (2011)] Karama, S., Colom, R., Johnson, W., Deary, I. J., Haier, R., Waber, D. P., Lepage, C., Ganjavi, H., Jung, R., and Evans, A. C. (2011). Cortical thickness correlates of specific cognitive performance accounted for by the general factor of intelligence in healthy children aged 6 to 18. *NeuroImage*, 55(4):1443–1453.
- [Kim (2011)] Kim, H. (2011). Neural activity that predicts subsequent memory and forgetting: A meta-analysis of 74 fMRI studies. *NeuroImage*, 54(3):2446–2461.
- [Kim *et al.* (2016)] Kim, D.-J., Davis, E. P., Sandman, C. A., Sporns, O., O’Donnell, B. F., Buss, C., and Hetrick, W. P. (2016). Children’s intellectual ability is associated with structural network integrity. *NeuroImage*, 124:550–556.
- [Kocevar *et al.* (2016)] Kocevar, G., Stamile, C., Hannoun, S., Cotton, F., Vukusic, S., Durand-Dubief, F., and Sappey-Marinier, D. (2016). Graph Theory-Based Brain Connectivity for Automatic Classification of Multiple Sclerosis Clinical Courses. *Frontiers in Neuroscience*, 10:478.
- [Kocevar *et al.* (2019)] Kocevar, G., Suprano, I., Stamile, C., Hannoun, S., Fournieret, P., Revol, O., Nusbaum, F., and Sappey-Marinier, D. (2019). Brain Structural Connectivity Correlates with Fluid Intelligence in Children: a DTI Graph Analysis. *Intelligence*, 72:67–75.

- [Koenis *et al.* (2015)] Koenis, M. M., Brouwer, R. M., van den Heuvel, M. P., Mandl, R. C., van Soelen, I. L., Kahn, R. S., Boomsma, D. I., and Hulshoff Pol, H. E. (2015). Development of the brain’s structural network efficiency in early adolescence: A longitudinal DTI twin study. *Human Brain Mapping*, 36(12):4938–4953.
- [Kruschwitz *et al.* (2018)] Kruschwitz, J., Waller, L., Daedelow, L., Walter, H., and Veer, I. (2018). General, crystallized and fluid intelligence are not associated with functional global network efficiency: A replication study with the human connectome project 1200 data set. *NeuroImage*, 171:323–331.
- [Kwong *et al.* (1992)] Kwong, K. K., Belliveau, J. W., Chesler, D. A., Goldberg, I. E., Weisskoff, R. M., Poncelet, B. P., Kennedy, D. N., Hoppel, B. E., Cohen, M. S., Turner, R., and Al., E. (1992). Dynamic magnetic resonance imaging of human brain activity during primary sensory stimulation. *Proceedings of the National Academy of Sciences of the United States of America*, 89(12):5675–9.
- [Langeslag *et al.* (2013)] Langeslag, S. J., Schmidt, M., Ghassabian, A., Jaddoe, V. W., Hofman, A., van der Lugt, A., Verhulst, F. C., Tiemeier, H., and White, T. J. (2013). Functional connectivity between parietal and frontal brain regions and intelligence in young children: The Generation R study. *Human Brain Mapping*, 34(12):3299–3307.
- [Lee *et al.* (2006)a] Lee, J. K., Lee, J. M., Kim, J. S., Kim, I. Y., Evans, A. C., and Kim, S. I. (2006a). A novel quantitative cross-validation of different cortical surface reconstruction algorithms using MRI phantom. *NeuroImage*, 31(2):572–584.
- [Lee *et al.* (2006)b] Lee, K. H., Choi, Y. Y., Gray, J. R., Cho, S. H., Chae, J.-H., Lee, S., and Kim, K. (2006b). Neural correlates of superior intelligence: Stronger recruitment of posterior parietal cortex. *NeuroImage*, 29(2):578–586.
- [Lerch *et al.* (2006)] Lerch, J. P., Worsley, K., Shaw, W. P., Greenstein, D. K., Lenroot, R. K., Giedd, J., and Evans, A. C. (2006). Mapping anatomical correlations across cerebral cortex (MACACC) using cortical thickness from MRI. *NeuroImage*, 31(3):993–1003.
- [Li *et al.* (2009)] Li, Y., Liu, Y., Li, J., Qin, W., Li, K., Yu, C., and Jiang, T. (2009). Brain anatomical network and intelligence. *PLoS Computational Biology*, 5(5).
- [Liratni and Pry (2011)] Liratni, M. and Pry, R. (2011). Enfants à haut potentiel intellectuel: psychopathologie, socialisation et comportements adaptatifs. *Neuropsychiatrie de l’Enfance et de l’Adolescence*, 59(6):327–335.

- [Makris *et al.* (2006)] Makris, N., Goldstein, J. M., Kennedy, D., Hodge, S. M., Caviness, V. S., Faraone, S. V., Tsuang, M. T., and Seidman, L. J. (2006). Decreased volume of left and total anterior insular lobule in schizophrenia. *Schizophrenia Research*, 83(2-3):155–171.
- [Mandeville *et al.* (1999)] Mandeville, J. B., Marota, J. J., Ayata, C., Moskowitz, M. A., Weisskoff, R. M., and Rosen, B. R. (1999). MRI measurement of the temporal evolution of relative CMRO(2) during rat forepaw stimulation. *Magnetic Resonance in Medicine*, 42(5):944–51.
- [McDaniel (2005)] McDaniel, M. A. (2005). Big-brained people are smarter: A meta-analysis of the relationship between in vivo brain volume and intelligence. *Intelligence*, 33(4):337–346.
- [McRobbie *et al.* (2006)] McRobbie, D. W., Moore, E. A., Graves, M. J., and Prince, M. R. (2006). *MRI from picture to proton*. Cambridge University Press, Cambridge.
- [Melrose *et al.* (2007)] Melrose, R. J., Poulin, R. M., and Stern, C. E. (2007). An fMRI investigation of the role of the basal ganglia in reasoning. *Brain Research*, 1142(1):146–158.
- [Menon *et al.* (1995)] Menon, R. S., Ogawa, S., Hu, X., Strupp, J. P., Anderson, P., and Uğurbil, K. (1995). BOLD based functional MRI at 4 Tesla includes a capillary bed contribution: echo-planar imaging correlates with previous optical imaging using intrinsic signals. *Magnetic Resonance in Medicine*, 33(3):453–9.
- [Mori *et al.* (1999)] Mori, S., Crain, B. J., Chacko, V. P., and Van Zijl, P. C. (1999). Three-dimensional tracking of axonal projections in the brain by magnetic resonance imaging. *Annals of Neurology*, 45(2):265–269.
- [Mori and Zhang (2006)] Mori, S. and Zhang, J. (2006). Principles of Diffusion Tensor Imaging and Its Applications to Basic Neuroscience Research. *Neuron*, 51(5):527–539.
- [Muetzel *et al.* (2015)] Muetzel, R. L. L., Mous, S. E. E., van der Ende, J., Blanken, L. M. M. E., van der Lugt, A., Jaddoe, V. W. W. V., Verhulst, F. C. C., Tiemeier, H., and White, T. (2015). White matter integrity and cognitive performance in school-age children: A population-based neuroimaging study. *NeuroImage*, 119:119–128.

- [Murphy *et al.* (2009)] Murphy, K., Birn, R. M., Handwerker, D. A., Jones, T. B., and Bandettini, P. A. (2009). The impact of global signal regression on resting state correlations: Are anti-correlated networks introduced? *NeuroImage*, 44(3):893–905.
- [Narr *et al.* (2005)] Narr, K. L., Bilder, R. M., Toga, A. W., Woods, R. P., Rex, D. E., Szeszko, P. R., Robinson, D., Sevy, S., Gunduz-Bruce, H., Wang, Y. P., DeLuca, H., and Thompson, P. M. (2005). Mapping cortical thickness and gray matter concentration in first episode schizophrenia. *Cerebral Cortex*, 15(6):708–719.
- [Navas-Sánchez *et al.* (2014)] Navas-Sánchez, F. J., Alemán-Gómez, Y., Sánchez-Gonzalez, J., Guzmán-De-Villoria, J. A., Franco, C., Robles, O., Arango, C., and Desco, M. (2014). White matter microstructure correlates of mathematical giftedness and intelligence quotient. *Human Brain Mapping*, 35(6):2619–2631.
- [Neubauer and Fink (2009)] Neubauer, A. C. and Fink, A. (2009). Intelligence and neural efficiency. *Neuroscience and Biobehavioral Reviews*, 33(7):1004–1023.
- [Noveck *et al.* (2004)] Noveck, I. A., Goel, V., and Smith, K. W. (2004). The neural basis of conditional reasoning with arbitrary content. *Cortex*, 40(4-5):613–22.
- [Nusbaum *et al.* (2017)] Nusbaum, F., Hannoun, S., Kocevar, G., Stamile, C., Fournieret, P., Revol, O., and Sappey-Mariniér, D. (2017). Hemispheric Differences in White Matter Microstructure between Two Profiles of Children with High Intelligence Quotient vs. Controls: A Tract-Based Spatial Statistics Study. *Frontiers in Neuroscience*, 11:1–11.
- [Nyberg (2002)] Nyberg, L. (2002). Levels of processing: a view from functional brain imaging. *Memory (Hove, England)*, 10(5-6):345–8.
- [O’Boyle *et al.* (2005)] O’Boyle, M. W., Cunnington, R., Silk, T. J., Vaughan, D., Jackson, G., Syngeniotis, A., and Egan, G. F. (2005). Mathematically gifted male adolescents activate a unique brain network during mental rotation. *Cognitive Brain Research*, 25(2):583–587.
- [Ogawa *et al.* (1990)] Ogawa, S., Lee, T. M., Kay, A. R., and Tank, D. W. (1990). Brain magnetic resonance imaging with contrast dependent on blood oxygenation. *Proc. Natl. Acad. Sci. USA*, 87:9868–9872.
- [Ogawa *et al.* (1992)] Ogawa, S., Tank, D. W., Menon, R., Ellermann, J. M., Kim, S., Merkle, H., and Ugurbil, K. (1992). Intrinsic signal changes accompanying



- sensory stimulation: Functional brain mapping with magnetic resonance imaging. *Proc Natl Acad Sci USA*, 89:5951–5955.
- [Oshio *et al.* (2010)] Oshio, R., Tanaka, S., Sadato, N., Sokabe, M., Hanakawa, T., and Honda, M. (2010). Differential effect of double-pulse TMS applied to dorsal premotor cortex and precuneus during internal operation of visuospatial information. *NeuroImage*, 49(1):1108–1115.
- [Ourselin *et al.* (2001)] Ourselin, S., Roche, A., Subsol, G., Pennec, X., and Ayache, N. (2001). Reconstructing a 3D structure from serial histological sections. *Image and Vision Computing*, 19(1-2):25–31.
- [Parker and Alexander (2003)] Parker, G. J. and Alexander, D. C. (2003). Probabilistic Monte Carlo based mapping of cerebral connections utilising whole-brain crossing fibre information. In *Lecture Notes in Computer Science (including sub-series Lecture Notes in Artificial Intelligence and Lecture Notes in Bioinformatics)*, volume 2732, pages 684–695. Springer, Berlin, Heidelberg.
- [Pavlov (1949)] Pavlov, I. (1949). *Complete collected works*. Moscow.
- [Pergola *et al.* (2013)] Pergola, G., Bellebaum, C., Gehlhaar, B., Koch, B., Schwarz, M., Daum, I., and Suchan, B. (2013). The involvement of the thalamus in semantic retrieval: A clinical group study. *Journal of Cognitive Neuroscience*, 25(6):872–886.
- [Perlberg *et al.* (2007)] Perlberg, V., Bellec, P., Anton, J. L., Pélégriani-Issac, M., Doyon, J., and Benali, H. (2007). CORSICA: correction of structured noise in fMRI by automatic identification of ICA components. *Magnetic Resonance Imaging*, 25(1):35–46.
- [Pierpaoli *et al.* (1996)] Pierpaoli, C., Jezzard, P., Basser, P. J., Barnett, A., and Di Chiro, G. (1996). Diffusion tensor MR imaging of the human brain. *Radiology*, 201(3):637–648.
- [Ponsoda *et al.*] Ponsoda, V., Martínez, K., Pineda-Pardo, J. A., Abad, F. J., Olea, J., Román, F. J., Barbey, A. K., and Colom, R. Structural Brain Connectivity and Cognitive Ability Differences: A Multivariate Distance Matrix Regression Analysis. *Human Brain Mapping*, 38(2):803–816.
- [Power *et al.* (2012)] Power, J. D., Barnes, K. A., Snyder, A. Z., Schlaggar, B. L., and Petersen, S. E. (2012). Spurious but systematic correlations in functional



- connectivity MRI networks arise from subject motion. *NeuroImage*, 59(3):2142–2154.
- [Power *et al.* (2017)] Power, J. D., Plitt, M., Laumann, T. O., and Martin, A. (2017). Sources and implications of whole-brain fMRI signals in humans. *NeuroImage*, 146:609–625.
- [Prabhakaran *et al.* (1997)] Prabhakaran, V., Smith, J. A., Desmond, J. E., Glover, G. H., and Gabrieli, J. D. (1997). Neural Substrates of Fluid Reasoning: An fMRI Study of Neocortical Activation during Performance of the Raven’s Progressive Matrices Test. *Cognitive Psychology*, 33(1):43–63.
- [Privado *et al.* (2017)] Privado, J., Román, F. J., Saénz-Urturi, C., Burgaleta, M., and Colom, R. (2017). Gray and white matter correlates of the Big Five personality traits. *Neuroscience*, 349:174–184.
- [Raichle (2011)] Raichle, M. E. (2011). The Restless Brain. *Brain Connectivity*, 1(1):3–12.
- [Raichle *et al.* (2001)] Raichle, M. E., Macleod, A. M., Snyder, A. Z., Powers, W. J., Gusnard, D. A., and Shulman, G. L. (2001). A default mode of brain function. *Proceedings of the National Academy of Sciences of the United States of America*, 98:676–682.
- [Raichle and Gusnard (2001)] Raichle, M. E. and Gusnard, D. A. (2001). Appraising the brain’s energy budget. *Proceedings of the National Academy of Sciences*, 98:676–682.
- [Ramon y Cajal and Azoulay (1911)] Ramon y Cajal, S. and Azoulay, L. (1911). *Histologie du système nerveux de l’homme et des vertébrés - II. Cervelet, cerveau moyen, retine, couche optique, corps strie, ecorce cerebrale generale & regionale, grand sympathique*, volume 2.
- [Ranganath (2006)] Ranganath, C. (2006). Working memory for visual objects: Complementary roles of inferior temporal, medial temporal, and prefrontal cortex. *Neuroscience*, 139(1):277–289.
- [Reuter *et al.* (2012)] Reuter, M., Schmansky, N. J., Rosas, H. D., and Fischl, B. (2012). Within-subject template estimation for unbiased longitudinal image analysis. *NeuroImage*, 61(4):1402–1418.

- [Revol and Bléandonu (2012)] Revol, O. and Bléandonu, G. (2012). Enfants intellectuellement précoces: Comment les dépister ? *Archives de Pédiatrie*, 19(3):340–343.
- [Robert *et al.* (2010)] Robert, G., Kermarrec, S., Guignard, J. H., and Tordjman, S. (2010). Signes d’appel et troubles associés chez les enfants à haut potentiel. *Archives de Pédiatrie*, 17(9):1363–1367.
- [Rubinov and Sporns (2010)] Rubinov, M. and Sporns, O. (2010). Complex network measures of brain connectivity: Uses and interpretations. *NeuroImage*, 52(3):1059–1069.
- [Saad *et al.* (2012)] Saad, Z. S., Gotts, S. J., Murphy, K., Chen, G., Jo, H. J., Martin, A., and Cox, R. W. (2012). Trouble at Rest: How Correlation Patterns and Group Differences Become Distorted After Global Signal Regression. *Brain Connectivity*, 2(1):25–32.
- [Salvador *et al.* (2005)] Salvador, R., Suckling, J., Coleman, M. R., Pickard, J. D., Menon, D., and Bullmore, E. (2005). Neurophysiological architecture of functional magnetic resonance images of human brain. *Cerebral Cortex*, 15(9):1332–2342.
- [Santarnecci *et al.* (2014)] Santarnecci, E., Galli, G., Polizzotto, N. R., Rossi, A., and Rossi, S. (2014). Efficiency of weak brain connections support general cognitive functioning. *Human Brain Mapping*, 35(9):4566–4582.
- [Santarnecci *et al.* (2015)a] Santarnecci, E., Rossi, S., and Rossi, A. (2015a). The smarter, the stronger: intelligence level correlates with brain resilience to systematic insults. *Cortex*, 64:293–309.
- [Santarnecci *et al.* (2015)b] Santarnecci, E., Tatti, E., Rossi, S., Serino, V., and Rossi, A. (2015b). Intelligence-related differences in the asymmetry of spontaneous cerebral activity. *Human Brain Mapping*, 36(9):3586–3602.
- [Santarnecci *et al.* (2017)] Santarnecci, E., Emmendorfer, A., Tadayon, S., Rossi, S., Rossi, A., and Pascual-Leone, A. (2017). Network connectivity correlates of variability in fluid intelligence performance. *Intelligence*, 65(October):35–47.
- [Satterthwaite *et al.* (2012)] Satterthwaite, T. D., Wolf, D. H., Loughhead, J., Ruparel, K., Elliott, M. A., Hakon, H., Gur, R. C., and Gur, R. E. (2012). Impact of In-Scanner Head Motion on Multiple Measures of Functional Connectivity: Relevance for Studies of Neurodevelopment in Youth. *NeuroImage*, 60(1):623.

- [Schmithorst *et al.* (2005)] Schmithorst, V. J. J., Wilkes, M., Dardzinski, B. J. J., Holland, S. K. K., Wilke, M., Dardzinski, B. J. J., and Holland, S. K. K. (2005). Cognitive functions correlate with white matter architecture in a normal pediatric population: A diffusion tensor HRI study. *Human Brain Mapping*, 26(2):139–147.
- [Schmithorst and Holland (2006)] Schmithorst, V. J. and Holland, S. K. (2006). Functional MRI evidence for disparate developmental processes underlying intelligence in boys and girls. *NeuroImage*, 31(3):1366–1379.
- [Shaw *et al.* (2006)] Shaw, P., Greenstein, D., Lerch, J., Clasen, L., Lenroot, R., Gogtay, N., Evans, A., Rapoport, J., and Giedd, J. (2006). Intellectual ability and cortical development in children and adolescents. *Nature*, 440(7084):676–679.
- [Sherman *et al.* (2016)] Sherman, L. E., Rudie, J. D., Pfeifer, J. H., Masten, C. L., and Dapretto, M. (2016). Development of the Default Mode and Central Executive Networks Across Early Adolescence: a Longitudinal Study. *Developmental Cognitive Neuroscience*, pages 148–159.
- [Shirer *et al.* (2012)] Shirer, W. R., Ryali, S., Rykhlevskaia, E., Menon, V., and Greicius, M. D. (2012). Decoding subject-driven cognitive states with whole-brain connectivity patterns. *Cerebral Cortex*, 22(1):158–165.
- [Shuman *et al.* (2013)] Shuman, D. I., Narang, S. K., Frossard, P., Ortega, A., and Vandergheynst, P. (2013). The emerging field of signal processing on graphs: Extending high-dimensional data analysis to networks and other irregular domains. *IEEE Signal Processing Magazine*, 30(3):83–98.
- [Silverman (1997)] Silverman, L. K. (1997). The construct of asynchronous development. *Peabody Journal of Education*, 72(3):36–58.
- [Simpson *et al.* (2013)] Simpson, S. L., Bowman, F. D. B., and Laurienti, P. J. (2013). Analyzing complex functional brain networks: Fusing statistics and network science to understand the brain. *Statistics Surveys*, 7.
- [Smith *et al.* (2012)] Smith, R. E., Tournier, J. D., Calamante, F., and Connelly, A. (2012). Anatomically-constrained tractography: Improved diffusion MRI streamlines tractography through effective use of anatomical information. *NeuroImage*, 62(3):1924–1938.
- [Song *et al.* (2008)] Song, M., Zhou, Y., Li, J., Liu, Y., Tian, L., Yu, C., and Jiang, T. (2008). Brain spontaneous functional connectivity and intelligence. *NeuroImage*, 41(3):1168–1176.

- [Song *et al.* (2009)] Song, M., Liu, Y., Zhou, Y., Wang, K., Yu, C., and Jiang, T. (2009). Default network and intelligence difference. In *2009 Annual International Conference of the IEEE Engineering in Medicine and Biology Society*, volume 1, pages 2212–2215. IEEE.
- [Sowell *et al.* (1999)] Sowell, E. R., Thompson, P. M., Holmes, C. J., Batth, R., Jernigan, T. L., and Toga, A. W. (1999). Localizing Age-Related Changes in Brain Structure between Childhood and Adolescence Using Statistical Parametric Mapping. *NeuroImage*, 9(6):587–597.
- [Spearman (1904)] Spearman, C. (1904). "General Intelligence," Objectively Determined and Measured. *The American Journal of Psychology*, 15(2):201.
- [Sporns] Sporns, O. Graph theory methods: applications in brain networks. *Dialogues in Clinical Neuroscience*, 20(2):111–121.
- [Sporns *et al.* (2005)] Sporns, O., Tononi, G., and Kötter, R. (2005). The human connectome: A structural description of the human brain. *PLoS Computational Biology*, 1(4):0245–0251.
- [Sporns and Zwi (2004)] Sporns, O. and Zwi, J. D. (2004). The small world of the cerebral cortex. *Neuroinformatics*, 2(2):145–162.
- [Squire and Zola-Morgan (1991)] Squire, L. R. and Zola-Morgan, S. (1991). The medial temporal lobe memory system.
- [Stam (2004)] Stam, C. J. (2004). Functional connectivity patterns of human magnetoencephalographic recordings: A 'small-world' network? *Neuroscience Letters*, 355(1-2):25–28.
- [Stejskal and Tanner (1965)] Stejskal, E. O. and Tanner, J. E. (1965). Spin diffusion measurements: Spin echoes in the presence of a time-dependent field gradient. *The Journal of Chemical Physics*, 42(1):288–292.
- [Sternberg (2000)] Sternberg, R. J. (2000). The Theory of Successful Intelligence. *Gifted Education International*, 15(1):4–21.
- [Sweetland *et al.* (2006)] Sweetland, J. D., Reina, J. M., and Tatti, A. F. (2006). WISC-III Verbal/Performance Discrepancies Among a Sample of Gifted Children. *Gifted Child Quarterly*, 50(1):7–10.

- [Takeuchi *et al.* (2018)] Takeuchi, H., Taki, Y., Nouchi, R., Yokoyama, R., Kotozaki, Y., Nakagawa, S., Sekiguchi, A., Iizuka, K., Hanawa, S., Araki, T., Miyauchi, C. M., Sakaki, K., Sassa, Y., Nozawa, T., Ikeda, S., Yokota, S., Daniele, M., and Kawashima, R. (2018). General intelligence is associated with working memory-related brain activity: new evidence from a large sample study. *Brain Structure and Function*, 223(9):4243–4258.
- [Tamnes *et al.* (2010)] Tamnes, C. K., Østby, Y., Walhovd, K. B., Westlye, L. T., Due-Tønnessen, P., and Fjell, A. M. (2010). Intellectual abilities and white matter microstructure in development: A diffusion tensor imaging study. *Human Brain Mapping*, 31(10):1609–1625.
- [Taylor *et al.* (2019)] Taylor, J. S. H., Davis, M. H., and Rastle, K. (2019). Mapping visual symbols onto spoken language along the ventral visual stream. *Proceedings of the National Academy of Sciences*, 116(36):17723–17728.
- [Termenon *et al.* (2016)a] Termenon, M., Achard, S., Jaillard, A., and Delon-Martin, C. (2016a). The “Hub Disruption Index,” a Reliable Index Sensitive to the Brain Networks Reorganization. A Study of the Contralesional Hemisphere in Stroke. *Frontiers in Computational Neuroscience*, 10:84.
- [Termenon *et al.* (2016)b] Termenon, M., Jaillard, A., Delon-Martin, C., and Achard, S. (2016b). Reliability of graph analysis of resting state fMRI using test-retest dataset from the Human Connectome Project. *NeuroImage*, 142:172–187.
- [Terrassier (2009)] Terrassier, J.-C. (2009). Les enfants intellectuellement précoces. *Archives de Pédiatrie*, 16(12):1603–1606.
- [Thomason *et al.* (2013)] Thomason, M. E., Dassanayake, M. T., Shen, S., Katkuri, Y., Alexis, M., Anderson, A. L., Yeo, L., Mody, S., Hernandez-Andrade, E., Hassan, S. S., Studholme, C., Jeong, J.-W., and Romero, R. (2013). Cross-Hemispheric Functional Connectivity in the Human Fetal Brain. *Science Translational Medicine*, 5(173):173ra24.
- [Thulborn (1998)] Thulborn, K. R. (1998). A BOLD move for fMRI. *Nature Medicine*, 4(2):155–156.
- [Tolomeo *et al.* (2016)] Tolomeo, S., Christmas, D., Jentsch, I., Johnston, B., Sprengelmeyer, R., Matthews, K., and Steele, J. D. (2016). A causal role for

- the anterior mid-cingulate cortex in negative affect and cognitive control. *Brain*, 139(6):1844–1854.
- [Toroczkai (2005)] Toroczkai, Z. (2005). Complex Networks The Challenge of Interaction Topology. *Los Alamos Science*, 29(29):94–109.
- [Tournier *et al.* (2004)] Tournier, J. D., Calamante, F., Gadian, D. G., and Connelly, A. (2004). Direct estimation of the fiber orientation density function from diffusion-weighted MRI data using spherical deconvolution. *NeuroImage*, 23(3):1176–1185.
- [Tournier *et al.* (2007)] Tournier, J. D., Calamante, F., and Connelly, A. (2007). Robust determination of the fibre orientation distribution in diffusion MRI: Non-negativity constrained super-resolved spherical deconvolution. *NeuroImage*, 35(4):1459–1472.
- [Tournier *et al.* (2012)] Tournier, J. D., Calamante, F., and Connelly, A. (2012). MRtrix: Diffusion tractography in crossing fiber regions. *International Journal of Imaging Systems and Technology*, 22(1):53–66.
- [Tschentscher *et al.* (2017)] Tschentscher, N., Mitchell, D., and Duncan, J. (2017). Fluid Intelligence Predicts Novel Rule Implementation in a Distributed Frontoparietal Control Network. *The Journal of Neuroscience*, 37(18):4841.
- [Tuch (2004)] Tuch, D. S. (2004). Q-ball imaging. *Magnetic Resonance in Medicine*, 52(6):1358–1372.
- [Tuch *et al.* (2002)] Tuch, D. S., Reese, T. G., Wiegell, M. R., Makris, N., Belliveau, J. W., and Van Wedeen, J. (2002). High angular resolution diffusion imaging reveals intravoxel white matter fiber heterogeneity. *Magnetic Resonance in Medicine*, 48(4):577–582.
- [Tzourio-Mazoyer *et al.* (2002)] Tzourio-Mazoyer, N., Landeau, B., Papathanassiou, D., Crivello, F., Etard, O., Delcroix, N., Mazoyer, B., and Joliot, M. (2002). Automated anatomical labeling of activations in SPM using a macroscopic anatomical parcellation of the MNI MRI single-subject brain. *NeuroImage*, 15(1):273–289.
- [Uehara *et al.* (2014)] Uehara, T., Yamasaki, T., Okamoto, T., Koike, T., Kan, S., Miyauchi, S., Kira, J. I., and Tobimatsu, S. (2014). Efficiency of a small-world brain network depends on consciousness level: A resting-state fMRI study. *Cerebral Cortex*, 24(6):1529–1539.

- [Uğurbil *et al.* (2013)] Uğurbil, K., Xu, J., Auerbach, E. J., Moeller, S., Vu, A. T., Duarte-Carvajalino, J. M., Lenglet, C., Wu, X., Schmitter, S., Van de Moortele, P. F., Strupp, J., Sapiro, G., De Martino, F., Wang, D., Harel, N., Garwood, M., Chen, L., Feinberg, D. A., Smith, S. M., Miller, K. L., Sotiropoulos, S. N., Jbabdi, S., Andersson, J. L., Behrens, T. E., Glasser, M. F., Van Essen, D. C., and Yacoub, E. (2013). Pushing spatial and temporal resolution for functional and diffusion MRI in the Human Connectome Project. *NeuroImage*, 80:80–104.
- [Vaivre-Douret (2004)] Vaivre-Douret, L. (2004). Les caractéristiques développementales d'un échantillon d'enfants tout venant « à hautes potentialités » (surdoués): Suivi prophylactique. In *Neuropsychiatrie de l'Enfance et de l'Adolescence*, volume 52, pages 129–141.
- [Vaivre-Douret (2011)] Vaivre-Douret, L. (2011). Developmental and cognitive characteristics of "high-level potentialities" (highly gifted) children. *International journal of pediatrics*, 2011:420297.
- [Van Den Heuvel *et al.* (2009)a] Van Den Heuvel, M. P., Mandl, R. C., Kahn, R. S., and Hulshoff Pol, H. E. (2009a). Functionally linked resting-state networks reflect the underlying structural connectivity architecture of the human brain. *Human Brain Mapping*, 30(10):3127–3141.
- [Van Den Heuvel *et al.* (2009)b] Van Den Heuvel, M. P., Stam, C. J., Kahn, R. S., and Hulshoff Pol, H. E. (2009b). Efficiency of functional brain networks and intellectual performance. *Journal of Neuroscience*, 29(23):7619–7624.
- [Van Dijk *et al.* (2012)] Van Dijk, K. R., Sabuncu, M. R., and Buckner, R. L. (2012). The influence of head motion on intrinsic functional connectivity MRI. *NeuroImage*, 59(1):431–438.
- [Van Essen *et al.* (2012)] Van Essen, D. C., Ugurbil, K., Auerbach, E., Barch, D., Behrens, T. E., Bucholz, R., Chang, A., Chen, L., Corbetta, M., Curtiss, S. W., Della Penna, S., Feinberg, D., Glasser, M. F., Harel, N., Heath, A. C., Larson-Prior, L., Marcus, D., Michalareas, G., Moeller, S., Oostenveld, R., Petersen, S. E., Prior, F., Schlaggar, B. L., Smith, S. M., Snyder, A. Z., Xu, J., and Yacoub, E. (2012). The Human Connectome Project: A data acquisition perspective. *NeuroImage*, 62(4):2222–2231.
- [Van Valen (1989)] Van Valen, L. (1989). Brain Size and Intelligence. *Journal of Child Neurology*, 4(2):146.



- [Van den Heuvel *et al.* (2008)] Van den Heuvel, M. P., Stam, C. J., Boersma, M., and Hulshoff Pol, H. E. (2008). Small-world and scale-free organization of voxel-based resting-state functional connectivity in the human brain. *NeuroImage*, 43(3):528–539.
- [Varentsova *et al.* (2014)] Varentsova, A., Zhang, S., and Arfanakis, K. (2014). Development of a high angular resolution diffusion imaging human brain template. *NeuroImage*, 91:177–186.
- [Wang *et al.* (2011)] Wang, L., Song, M., Jiang, T., Zhang, Y., and Yu, C. (2011). Regional homogeneity of the resting-state brain activity correlates with individual intelligence. *Neuroscience Letters*, 488(3):275–278.
- [Watts and Strogatz (1998)] Watts, D. J. and Strogatz, S. H. (1998). Collective dynamics of 'small-world' networks. *Nature*, 393(6684):440–442.
- [Wechsler (2003)] Wechsler, D. (2003). *Wechsler Intelligence Scale for Children*.
- [Wickett *et al.* (2000)] Wickett, J. C., Vernon, P. A., and Lee, D. H. (2000). Relationships between factors of intelligence and brain volume. *Personality and Individual Differences*, 29(6):1095–1122.
- [Willerman *et al.* (1991)] Willerman, L., Schultz, R., Neal Rutledge, J., and Bigler, E. D. (1991). In vivo brain size and intelligence. *Intelligence*, 15(2):223–228.
- [Zuo *et al.* (2010)] Zuo, X.-N., Kelly, C., Di Martino, A., Mennes, M., Margulies, D. S., Bangaru, S., Grzadzinski, R., Evans, A. C., Zang, Y.-F., Castellanos, F. X., Milham, M. P., and Kline, N. (2010). Growing together and growing apart: regional and sex differences in the lifespan developmental trajectories of functional homotopy. *The Journal of Neuroscience*, 30(45):15034–15043.
- [R Development Core Team (2015)] R Development Core Team (2015). R: A Language and Environment for Statistical Computing.





# Annex



# Reorganization indices in HIQ children: results obtained with a graph threshold of 20%.

Networks	$\kappa$	HIQ (n=32)	Hom-HIQ (n=14)	Het-HIQ (n=18)
A. Whole brain	$\kappa_{BC}$	-0.366	-0.447	-0.324
	$\kappa_D$	-0.280 (**)	-0.285 (*)	-0.278 (***)
	$\kappa_{LE}$	-0.296 (*)	-0.316	-0.286 (*)
	$\kappa_{CC}$	-0.315 (*)	-0.337	-0.304 (*)
B. Left hemisphere	$\kappa_{BC}^L$	-0.429 (**)	-0.473 (*)	-0.407 (**)
	$\kappa_D^L$	-0.256 (**)	-0.304 (*)	-0.231 (**)
	$\kappa_{LE}^L$	-0.221	-0.213	-0.225
	$\kappa_{CC}^L$	-0.285	-0.288	-0.283
C. Right hemisphere	$\kappa_{BC}^R$	-0.232	-0.212	-0.242
	$\kappa_D^R$	-0.211	-0.167	-0.233 (*)
	$\kappa_{LE}^R$	-0.297	-0.257	-0.317 (*)
	$\kappa_{CC}^R$	-0.343	-0.309	-0.361
D. Homotopic	$\kappa^{HC}$	-0.185 (**)	-0.261	-0.145 (*)

Table 1: Results obtained with a graph cost of 20%: reorganization indices ( $\kappa$ ) in Standard Intelligence Quotient (SIQ), High Intelligence Quotient (HIQ), Homogeneous HIQ (Hom-HIQ) and Heterogeneous HIQ (Het-HIQ) groups measured in whole brain networks (A), left and right hemispheres networks (B, C) and between homotopic regions (D).

Networks	$\kappa$	FSIQ	VCI	PRI
A. Whole brain	$\kappa_{BC}$	-0.317 (*)	-0.323 (*)	-0.339 (*)
	$\kappa_D$	-0.278 (*)	-0.277 (*)	-0.278 (*)
	$\kappa_{LE}$	-0.243	-0.303 (*)	-0.248
	$\kappa_{CC}$	-0.272	-0.337 (*)	-0.305 (*)
B. Left hemisphere	$\kappa_{BC}^L$	-0.374 (*)	-0.381 (**)	-0.337 (*)
	$\kappa_D^L$	-0.324 (*)	-0.275 (*)	-0.337 (*)
	$\kappa_{LE}^L$	-0.203	-0.201	-0.247
	$\kappa_{CC}^L$	-0.306 (*)	-0.336 (*)	-0.354 (**)
C. Right hemisphere	$\kappa_{BC}^R$	0.050	0.008	-0.050
	$\kappa_D^R$	-0.215	-0.252	-0.163
	$\kappa_{LE}^R$	-0.092	-0.196	-0.087
	$\kappa_{CC}^R$	-0.166	-0.264 (*)	-0.170
D. Homotopic	$\kappa^{HC}$	-0.515 (**)	-0.589 (***)	-0.523 (***)

Table 2: Results obtained with a graph cost of 0.20: coefficients of non-parametric correlations ( $\rho$ ) between the topological reorganization coefficient ( $\kappa$ ) of different nodal metrics (Betweenness Centrality (BC), Degree (D), Local Efficiency (LE), and Clustering (CC), and Homotopic Connectivity (HC)) with intelligence scores (Full Scale IQ (FSIQ), Verbal Comprehension Index (VCI) and Perceptual Reasoning Index (PRI)) at different network levels: whole brain (A), left and right hemispheres (B and C) and homotopic regions (D).

## Supplementary results of structural connectivity study in HIQ children.

Intelligence domains		PA1	PA2	PA3
Fluid intelligence	PA1	-	0.69***	0.50***
Classification abilities	PA2		-	0.56***
Crystalized intelligence	PA3			-

\*\*\* p<0.001

Table 3: Correlation matrix of the three intelligence domains defined by the factor analysis.

White matter fiber-bundles		Comp-1	Comp-2	Comp-3	Comp-4	Comp-5
Forceps major		<b>0.74</b>	-0.21	0.26	0.04	0.02
Forceps minor		<b>0.48</b>	0.19	0.24	0.23	0.07
Fornix		-0.05	0.08	0.26	0.01	<b>0.78</b>
Cingulate (Hippocampal)	L	<b>0.60</b>	0.18	0.12	-0.30	-0.09
Cingulate (Cingular)	L	0.10	0.19	<b>0.75</b>	-0.17	0.20
Cortico-spinal tract	L	0.26	-0.01	-0.30	<b>0.64</b>	0.42
Inferior Fronto-occipital	L	<b>0.60</b>	0.51	-0.11	-0.05	0.17
Inferior longitudinal	L	<b>0.84</b>	-0.09	0.04	-0.05	0.11
Superior longitudinal	L	0.37	0.27	0.12	0.06	<b>0.56</b>
Uncinate	L	-0.06	<b>0.92</b>	-0.01	-0.11	0.17
Cingulate (Hippocampal)	R	0.28	<b>0.33</b>	0.28	-0.11	-0.26
Cingulate (Cingular)	R	0.06	-0.10	<b>0.88</b>	0.09	0.09
Cortico-spinal tract	R	-0.14	0.00	0.15	<b>0.91</b>	-0.07
Inferior Fronto-occipital	R	0.44	<b>0.52</b>	0.02	0.28	-0.18
Inferior longitudinal	R	<b>0.57</b>	0.17	0.08	0.32	-0.42
Superior longitudinal	R	0.09	0.18	<b>0.61</b>	0.41	-0.11
Uncinate	R	-0.08	<b>0.92</b>	0.09	0.09	-0.07
Explained Variance		41%	10%	8%	8%	7%

Table 4: Loadings matrix of fractional anisotropy in the white matter fiber-bundles obtained by the principal component analysis. Values in bold represent the highest loadings.

White matter fiber-bundles		Comp-1	Comp-2	Comp-3	Comp-4
Forceps major		<b>0.74</b>	0.21	-0.42	0.01
Forceps minor		<b>0.75</b>	0.19	0.11	0.01
Fornix		0.41	0.14	<b>-0.75</b>	0.14
Cingulate (Hippocampal)	L	0.34	0.10	0.34	<b>0.59</b>
Cingulate (Cingular)	L	0.17	0.20	0.75	0.14
Cortico-spinal tract	L	0.20	0.48	0.12	<b>-0.57</b>
Inferior Fronto-occipital	L	0.40	<b>0.64</b>	0.14	-0.05
Inferior longitudinal	L	-0.05	<b>0.92</b>	-0.01	0.19
Superior longitudinal	L	-0.15	<b>0.96</b>	0.06	0.00
Uncinate	L	0.22	<b>0.73</b>	-0.01	-0.31
Cingulate (Hippocampal)	R	<b>0.71</b>	-0.40	0.08	0.03
Cingulate (Cingular)	R	0.40	0.29	<b>0.55</b>	0.12
Cortico-spinal tract	R	<b>0.89</b>	-0.31	0.02	-0.31
Inferior Fronto-occipital	R	<b>0.84</b>	0.15	0.03	0.10
Inferior longitudinal	R	<b>0.64</b>	0.20	-0.16	0.35
Superior longitudinal	R	<b>0.84</b>	0.07	0.04	0.15
Uncinate	R	<b>0.51</b>	0.40	0.10	-0.27
Explained Variance		42%	15%	9%	7%

Table 5: Loadings matrix of axial diffusivity in the white matter fiber-bundles obtained by the principal component analysis. Values in bold represent the highest loadings.

White matter fiber-bundles		Comp-1	Comp-2	Comp-3	Comp-4
Forceps major		0.33	0.06	<b>0.65</b>	-0.17
Forceps minor		<b>0.55</b>	0.19	0.36	0.10
Fornix		-0.11	0.05	<b>0.78</b>	-0.19
Cingulate (Hippocampal)	L	0.01	0.33	-0.02	<b>0.56</b>
Cingulate (Cingular)	L	-0.07	0.09	<b>0.72</b>	0.29
Cortico-spinal tract	L	0.18	<b>0.91</b>	-0.07	-0.26
Inferior Fronto-occipital	L	0.18	<b>0.74</b>	-0.01	0.34
Inferior longitudinal	L	0.06	<b>0.79</b>	0.12	0.19
Superior longitudinal	L	-0.23	<b>0.78</b>	0.29	0.16
Uncinate	L	-0.17	0.43	0.08	<b>0.68</b>
Cingulate (Hippocampal)	R	0.38	-0.43	0.19	<b>0.54</b>
Cingulate (Cingular)	R	0.32	-0.01	<b>0.65</b>	-0.06
Cortico-spinal tract	R	<b>0.91</b>	0.12	-0.08	-0.30
Inferior Fronto-occipital	R	<b>0.75</b>	0.14	0.03	0.38
Inferior longitudinal	R	<b>0.80</b>	-0.03	0.08	0.25
Superior longitudinal	R	<b>0.76</b>	-0.08	0.33	0.05
Uncinate	R	0.33	0.14	0.00	<b>0.70</b>
Explained Variance		42%	17%	8%	8%

Table 6: Loadings matrix of radial diffusivity in the white matter fiber-bundles obtained by the principal component analysis. Values in bold represent the highest loadings.

White matter fiber-bundles		Comp-1	Comp-2	Comp-3	Comp-4
Forceps major		0.07	0.46	<b>0.61</b>	-0.07
Forceps minor		0.23	<b>0.75</b>	0.04	0.09
Fornix		0.12	-0.03	<b>0.90</b>	-0.03
Cingulate (Hippocampal)	L	<b>0.51</b>	0.06	-0.25	0.47
Cingulate (Cingular)	L	<b>0.50</b>	0.49	-0.32	-0.05
Cortico-spinal tract	L	<b>0.82</b>	0.15	-0.05	-0.32
Inferior Fronto-occipital	L	<b>0.82</b>	0.23	0.07	-0.01
Inferior longitudinal	L	<b>0.94</b>	0.01	0.10	0.05
Superior longitudinal	L	<b>0.99</b>	-0.12	0.05	-0.06
Uncinate	L	<b>0.84</b>	-0.12	0.05	0.35
Cingulate (Hippocampal)	R	-0.34	0.43	0.05	<b>0.57</b>
Cingulate (Cingular)	R	0.20	<b>0.83</b>	-0.09	-0.22
Cortico-spinal tract	R	-0.22	<b>0.87</b>	0.06	-0.10
Inferior Fronto-occipital	R	0.12	<b>0.78</b>	0.05	0.28
Inferior longitudinal	R	-0.01	<b>0.66</b>	0.19	0.33
Superior longitudinal	R	-0.08	<b>0.92</b>	0.09	0.06
Uncinate	R	0.42	0.27	0.12	<b>0.53</b>
Explained Variance		44%	21%	7%	6%

Table 7: Loadings matrix of mean diffusivity in the white matter fiber-bundles obtained by principal component analysis. Values in bold represent the highest loadings.





## *Curriculum Vitae*



## SUPRANO Ilaria

04 December 1989, Formia, Italy

Mobile: 06 62 96 00 59

Nationality: Italian

E-Mail: [ilaria.suprano@gmail.com](mailto:ilaria.suprano@gmail.com)

Adresse: 19 Grande rue de la Guillotière - 69007 Lyon

### Formation:

PhD	<b>Biomedical Engineering</b> Université Claude Bernard Lyon 1 Ecole Doctorale Interdisciplinaire Sciences Santé CREATIS UMR 5220 CNRS & U1206 INSERM	<b>2016-2019</b>
Master Degree 2	<b>Physics</b> Specialty in Bio-medical physics University of Rome 'La Sapienza' - Italy	<b>2012-2015</b>
Bachelor Degree	<b>Physics</b> University of Rome 'La Sapienza' - Italy	<b>2009-2012</b>

### Research Experience:

- **PhD Thesis** **2016-2019**  
*Etude de la connectivité cérébrale par IRM fonctionnelle et de diffusion dans l'intelligence*  
Ecole Doctorale Interdisciplinaire Sciences Santé  
Laboratoire CREATIS UMR CNRS 5220 & INSERM 1206  
Université Claude Bernard Lyon 1  
Supervisors : Dr. D. SAPPEY-MARINIER, & Dr. C. Delon-Martin
- **Stage CERMEP:** **04/2016 - 08/2016**  
*Graph Theory study of functional connectivity from resting state fMRI data*  
CERMEP - Imagerie du vivant  
Université Claude Bernard Lyon 1  
Supervisor : Dr. D. SAPPEY-MARINIER.
- **Stage Master Degree:** **12/2014 - 12/2015**  
*Optimization of Multiband Echo Planar Imaging Approaches for Functional MRI in Humans*  
Magnetic Resonance for Brain Investigation Laboratory (MARBILab)  
University of Rome 'La Sapienza' - Italy  
Supervisor : Dr. F. GIOVE.

- **Stage Bachelor Degree:** *06/2012 - 10/2012*  
*Functional magnetic resonance*  
MARBILab  
University of Rome 'La Sapienza' - Italy  
Supervisor: Prf. F. De Luca.

**Skills:**

- **MRI medical imaging processing:** FSL, Freesurfer, SPM, Brain connectivity Toolbox, MRtrix
- **Programming:** Shell, Matlab, Python, C
- **Statistics:** R
- **Operating Systems:** Windows, Linux
- **Office Tools:** Microsoft Office, L<sup>A</sup>T<sub>E</sub>X

**Languages:**

- **Mother tongue:** Italian
- **Proficient:** French
- **Advanced:** English

**Awards:**

- **Prize of "Paediatric MR study group",** Joint Annual Meeting ISMRM-ESMRMB 2018 - Paris (France)
- **Award for best poster communication in imaging,** 23rd EDISS Scientific Day - Lyon (France), 2018
- **Prize in "IRM application",** SFRMBM 2017 - Bordeaux (France)

# Publications and Communications

## Publications

- "Topological modification of brain networks organization in children with high intelligence quotient: a resting-state fMRI study".  
**Suprano Ilaria**, Delon-Martin Chantal, Kocevar Gabriel, Stamile Claudio, Hannoun Salem, Achard Sophie, Badhwar Adampreet, Fournieret Pierre, Revol Olivier, Nusbaum Fanny, Sappey-Marinier Dominique.  
Frontiers in Human Neuroscience 2019; 13:241
- "Brain Structural Connectivity Correlates with Fluid Intelligence in Children: a DTI Graph Analysis".  
Kocevar Gabriel, **Suprano Ilaria**, Stamile Claudio, Hannoun Salem, Fournieret Pierre, Revol Olivier, Nusbaum Fanny, Sappey-Marinier Dominique.  
Intelligence 2019 72:67-75.
- "Structural Connectivity Correlates with High Intelligence Quotient Children".  
**Suprano Ilaria**, Kocevar Gabriel, Stamile Claudio, Hannoun Salem, Fournieret Pierre, Revol Olivier, Nusbaum Fanny, Sappey-Marinier Dominique.  
Frontiers in Psychology, 2019 (Under submission)

## Oral presentations

### Journées Lilloises de Neuropédiatrie 2018 - Lille

- "HPI: existe-t-il des particularités anatomo-fonctionnelles ?"  
**Suprano Ilaria**, Delon-Martin Chantal, Kocevar Gabriel, Stamile Claudio, Achard Sophie, Fourneret Pierre, Revol Olivier, Nusbaum Fanny, Sappey-Marinier Dominique

### Joint Annual Meeting ISMRM-ESMRMB 2018 - Paris

- "Reorganization of homotopic functional connectivity in two profiles of High Potential Children: a resting-state fMRI and DTI study"  
**Suprano Ilaria**, Delon-Martin Chantal, Kocevar Gabriel, Stamile Claudio, Achard Sophie, Fourneret Pierre, Revol Olivier, Nusbaum Fanny, Sappey-Marinier Dominique

### SFRMBM 2017 - Bordeaux

- "Analyse de la Connectivité Structurale Cérébrale en fonction du Quotient Intellectuel chez l'Adolescent"  
Kocevar Gabriel, Stamile Claudio, **Suprano Ilaria**, Hannoun Salem, Fourneret Pierre, Revol Olivier, Nusbaum Fanny, Sappey-Marinier Dominique

## Posters

### OHBM 2019 - Rome

- "Differential topological reorganization of functional connectivity in two high IQ children profiles"  
**Suprano Ilaria**, Delon-Martin Chantal, Kocevar Gabriel, Stamile Claudio, Achard Sophie, Fourneret Pierre, Revol Olivier, Nusbaum Fanny, Sappey-Marinier Dominique

**ISMRM 2019 - Montreal**

- "Graph-based Structural Connectivity is correlated with Children Intelligence Quotient Scores"

**Suprano Ilaria**, Delon-Martin Chantal, Kocevar Gabriel, Stamile Claudio, Achard Sophie, Fournieret Pierre, Revol Olivier, Nusbaum Fanny, Sappey-Marinier Dominique

**SFRMBM 2019 - Strasbourg**

- "Réorganisation des connectivités cérébrales fonctionnelles et structurales dans deux profils d'enfants à Haut Potentiel Intellectuel"

**Suprano Ilaria**, Delon-Martin Chantal, Kocevar Gabriel, Stamile Claudio, Achard Sophie, Fournieret Pierre, Revol Olivier, Nusbaum Fanny, Sappey-Marinier Dominique

**Joint Annual Meeting ISMRM-ESMRMB 2018 - Paris**

- "Reorganization of homotopic functional connectivity in two profiles of High Potential Children: a resting-state fMRI and DTI study"

**Suprano Ilaria**, Delon-Martin Chantal, Kocevar Gabriel, Stamile Claudio, Achard Sophie, Fournieret Pierre, Revol Olivier, Nusbaum Fanny, Sappey-Marinier Dominique

**ESMRMB 2017 - Barcelona**

- "Differential Hemispheric Brain Network Reorganization in two profiles of High IQ Children: a resting-state fMRI study"

**Suprano Ilaria**, Delon-Martin Chantal, Kocevar Gabriel, Stamile Claudio, Fournieret Pierre, Revol Olivier, Nusbaum Fanny, Sappey-Marinier Dominique

**ISMRM 2017 - Honolulu**

- "Topological Networks reorganization in two profiles of High Potential Children: a resting state fMRI study"

**Suprano Ilaria**, Delon-Martin Chantal, Kocevar Gabriel, Stamile Claudio,



Hannoun Salem, Fourneret Pierre, Revol Olivier, Nusbaum Fanny, Sappey-Marinier Dominique

### **SFRMBM 2017 - Bordeaux**

- "Réorganisation Topologique des Réseaux Fonctionnels dans Deux Profils d'Enfants à Haut Potentiel Intellectuel"

**Suprano Ilaria**, Delon-Martin Chantal, Kocevar Gabriel, Stamile Claudio, Hannoun Salem, Fourneret Pierre, Revol Olivier, Nusbaum Fanny, Sappey-Marinier Dominique



---

## Etude de la connectivité cérébrale par IRM fonctionnelle et de diffusion dans l'intelligence

---

L'idée que l'intelligence s'appuie non seulement sur des régions spécifiques du cerveau, mais également sur des réseaux cérébraux efficaces s'est récemment affirmée. Ces concepts nous ont amené à explorer le substrat neural de l'intelligence en utilisant des techniques avancées d'IRM avec la théorie des graphes. Après une étude IRMf méthodologique préliminaire, l'indice de réorganisation des réseaux a été mesuré. Une réorganisation fonctionnelle a été trouvée dans les deux groupes d'enfants à Haut Quotient Intellectuel (HIQ) avec des réorganisations plus importantes chez les Hétérogènes (Het-HIQ). Ensuite, l'analyse des faisceaux de fibres de substance blanche (SB) a permis d'estimer les métriques de diffusivité dans les faisceaux ainsi que la connectivité structurale. Avec l'augmentation du QI, nous avons observé une augmentation générale de la densité et une diminution de la transitivity et de la modularité du graphe. De plus, les corrélations entre les capacités intellectuelles et l'intégrité de la SB, mesurée avec les métriques de diffusion, ont été mesurées dans des faisceaux de fibres de SB. Ensuite, nous avons étudié les effets d'une stimulation cérébrale par une tâche de mémorisation sémantique au sein de la même population d'enfants HIQ. Cette analyse a montré des résultats significativement différents selon le groupe d'intelligence, en particulier au sein du group Het-HIQ. Enfin, nous avons appliqué ces méthodes à une population d'adulte pour analyser les réseaux cérébraux fonctionnels et structuraux en fonction du QI. Cette étude a montré certaines altérations des métriques globales et locales de la connectivité chez les adultes HIQ. Nous avons observé une diminution de l'assortativité et de la transitivity avec l'augmentation du QI. En conclusion, les techniques avancées d'IRM associées à l'analyse de graphes constituent une approche prometteuse pour une meilleure caractérisation des réseaux cérébraux en fonction du QI.

**Mots clés :** IRMf, DTI, Théorie des graphes, Connectome, Hub disruption index ( $\kappa$ ), Intelligence.

---

## A cerebral connectivity study by functional and diffusion MRI in intelligence

---

The idea that intelligence is embedded not only in specific brain regions, but also in efficient brain networks has grown up. These concepts have led us to investigate the neural substrate of intelligence using advanced MRI techniques in combination with a graph analysis. After a preliminary methodological fMRI study, an index of network reorganization, the "Hub disruption index", was measured. A functional brain network reorganization was found in both High Intelligence Quotient (HIQ) groups with a dominance in the Heterogeneous group (Het-HIQ). Then, the analysis of the white matter (WM) fiber-bundles allowed to estimate the diffusivity metrics and the structural connectivity. With the increase of IQ, we observed a general increase in density and a decrease in transitivity and modularity of the graph. Furthermore, relationships between intellectual abilities and enhanced WM integrity, as estimated by diffusivity metrics, were measured in WM fiber-bundles. In the same HIQ population, performing a memory task fMRI study we observed higher behavioral performances and increased functional activations. This study showed significant different results depending on intelligence group, in particular for the Het-HIQ group. Finally, the application of these methods in an adult population to analyze functional and structural brain networks allowed to highlight some changes in global and local metrics in HIQ subjects. We observed a decreased assortativity and transitivity with the enhancement of intelligence performances. In conclusion, these advanced MRI techniques associated with graph analysis may constitute a promising approach for a better characterization of brain networks and particularly in relation with intelligence abilities.

**Keywords:** fMRI, DTI, Graph theory, Connectome, Hub disruption index ( $\kappa$ ), Intelligence.

---

## INTITULE ET ADRESSE DE L'U.F.R. OU DU LABORATOIRE

CREATIS - CNRS UMR5220 - Inserm U1206 - Université de Lyon - Université Lyon1 - INSA-Lyon  
7 Av. Jean Capelle, 69621 VILLEURBANNE, France.